



MAY 6, 2023

# FEBRUARY 6, 2023 TÜRKIYE EARTHQUAKES: REPORT ON GEOSCIENCE AND ENGINEERING IMPACTS



**ODTÜ  
METU**

# February 6, 2023 Türkiye Earthquakes: Report on Geoscience and Engineering Impacts

A report prepared through international collaborations of the Earthquake Engineering Research Institute and Geotechnical Extreme Event Reconnaissance Association (USA) and the Earthquake Engineering Association and Earthquake Engineering Foundation of Türkiye.

## Report Coordinators/Editors

K. Önder Çetin, Middle East Technical University, Turkey

Jonathan D. Bray, University of California, Berkeley, USA

J. David Frost, Georgia Institute of Technology, USA

Ayşe Hortacısu, Applied Technology Council, USA

Eduardo Miranda, Stanford University, USA

Robb Eric S. Moss, California Polytechnic State University, USA

Jonathan P. Stewart, University of California, Los Angeles, USA

Earthquake Engineering Research Institute, LFE Program

GEER Association Report 082

<https://10.18118/G6PM34>

May 6, 2023



## GEER Field Team Members (Alphabetical Order)

Erhan Altunel	Eskisehir Osmangazi University
Bilal Umut Ayhan	Middle East Technical University
Patrick Bassal	Ohio State University
Jonathan Bray (Phase 3 Team Lead)	UC Berkeley
Kemal Önder Çetin (Phase 1 +2 Co-Team Lead)	Middle East Technical University
Kevin Clahan	Lettis Consultants Intl.
Emre Duman	Georgia Institute of Technology
David Frost (Phase 2 Co-Team Lead)	Georgia Institute of Technology
Sena Begum Kendir	Zemin Etüd vs Tasarım A.Ş.
Richard Koehler	University of Nevada Reno
Özgür Kozacı	Mott MacDonald
Jorge Macedo	Georgia Institute of Technology
Robb Eric S. Moss (Phase 1 Co-Team Lead)	California Polytechnic State University
Diane Moug	Portland State University
Menzer Pehlivan	Jacobs Inc.
Kristin Ulmer	Southwest Research Institute
Cengiz Yıldırım	Istanbul Technical University

### **Non-Traveling GEER Support Team (Alphabetical Order)**

Tristan Buckreis	University of California, Los Angeles
Renmin Pretell	University of California, Los Angeles
Youssef Hashash	University of Illinois Urbana-Champaign
Jorge Mario Lozano	Georgia Institute of Technology
Elliot Nichols	Georgia Institute of Technology
Jonathan Stewart	University of California, Los Angeles

### **EERI Field Team Members (Alphabetical Order)**

Önder Akıncı	Simpson, Gumpertz, & Heger
Merve Bayraktar	Hacettepe University
Altuğ Bayram	Promer
Riccardo Cappa (Lifelines Team Lead)	Simpson, Gumpertz, & Heger
Muhammet Ceylan	Gebze Technical University
Brent Chancellor	Wiss, Janney, Elstner Associates
Ahmet Çıtıptıoğlu	TAV Construction
Burcu Güldür Erkal	Hacettepe University
Rupa Garai	Skidmore Owings & Merrill
Bora Gençtürk	University of Southern California
Morgan Griffith	Exponent
Parth Gudhka	Imegcorp
Ricardo Henoeh	Skidmore Owings & Merrill
Jeff Hunt	Exponent
Ayhan Irfanoglu	Purdue University

Ezra Jampole	Exponent
Volkan Kara	Cerrahpaşa Medical School of Istanbul University
Robert Kraus	Wiss, Janney, Elstner Associates
Bret Lizundia	Rutherford + Chekene
Mike Mieler	Arup
Engin Nacaroglu	Pamukkale University
Menzer Pehlivan	Jacobs
Maryann T. Phipps	Estructure
Ali Roufegarinejad	Forell/Elsesser Engineers
Halil Sezen (Building Team Lead)	Ohio State University
Ali Sümer (Hospital Team Lead)	Department of Health Care Access and Information of California (HCAI)
Selçuk Toprak	Gebze Technical University
Yüksel Tonguç	Promer
Brad Wham	University of Colorado at Boulder
Gordon Wray	Degenkolb Engineers

## Executive Summary

The February 6th Kahramanmaraş events and the accompanying aftershocks were a once-in-a-century catastrophe that has greatly impacted Türkiye and Syria. The repercussions of these events will have a lasting effect on the region. The goal of this report is to document perishable data so that the entire earthquake community can improve the learning opportunities from these events, thereby ultimately facilitating the mitigation of risk from similar future events.

Türkiye lies at the junction of three tectonic plates which drives the significant seismicity of the region. The mainshock event of **M7.8** occurred on a portion of the plate boundary East Anatolian Fault and was followed approximately 9 hours later by a **M7.7** aftershock and many smaller aftershocks. Surface fault rupture was observed from these two events over a distance of roughly 460 km, with both ruptures presenting typical left-lateral strike-slip geomorphology and surface rupture patterns. The **M7.8** earthquake ruptured across three segments and two major releasing bends, and when compared to prior events on this fault indicate that sequencing and segmenting are not persistent in time. The field mapping and drone mapping of these surface fault ruptures will provide a wealth of data for informing fault rupture hazard modeling.

Ground motions from these events were recorded both near the fault ruptures and at distances up to 575 km on instruments in a variety of regional networks, the largest of which is AFAD in Türkiye. The **M7.8** and **M7.7** have produced the most comprehensive sets of strong motion recordings from strike-slip with magnitudes larger than 7.6. In particular, the **M7.8** mainshock and **M7.7** (6 Feb) and **M6.3** (20 Feb) aftershocks produced 311, 351, and 233 usable recordings. Manual, component-specific data processing optimized usable bandwidth while removing fling step displacements; work is ongoing for 44 mainshock records and about 10 records for each aftershock to preserve fling step. Source, path, and site metadata were compiled and are provided with ground motion intensity measures at a doi provided in Chapter 3. The data are compared to a global ground motion model (GMM) for active tectonic regions and a local, Türkiye-specific model. The global model has path misfits at distances > 200 km and underprediction bias at long periods. Event-specific semi-variogram models are developed to capture spatial variability for peak acceleration, peak velocity, and 5%-damped pseudo-spectral acceleration for a 1.0 sec oscillator period, which are used for ground motion estimation at sites of interest. The strong motion records produced by these events will facilitate studies of the characteristics of intense ground motions (PGV > 100 cm/s), including complex interactions between site and directivity effects, as well as studies of how such motions affect engineered structures by pairing observed intensity measures with seismic performance.

Liquefaction related ground failures were widespread in the damage zone. The geomorphology of the East Anatolian Fault region is that of a river valley following the fault, therefore river deposits in saturated conditions are prevalent and prone to seismic soil liquefaction. Additionally, there was widespread liquefaction in the coastal and port areas where saturated beach and river mouth deposits are present. Liquefaction resulted in damage to port facilities, building foundations, bridge foundations, lifelines, and other civil infrastructure in as many as 10 cities throughout the region.

As part of the reconnaissance efforts following the Kahramanmaraş earthquake sequence, the EERI Buildings Team visited the population centers that were most affected by the earthquakes including İskenderun, Samandağı, Kırıkhan, Antakya, Adana, Osmaniye, Kahramanmaraş, Gaziantep, Adıyaman, Gölbaşı, Malatya, Hassa, İslahiye and Nurdağı, covering a total distance of 3200 km in 6 days while collecting data in the field (Figure 5.3). The team focused on understanding the overall structural performance of buildings, including correlation with peak ground intensity at nearby ground motion recording stations. In addition to residential building performance, the team also documented and categorized the response of industrial facilities, commercial buildings, school buildings, and religious and historical structures.

The reconnaissance team collected information on 167 buildings in the region. These buildings are representative of the performance of buildings in the earthquake region constructed according to modern building codes (built after 2000). About 73% of the buildings visited were residential with the typical construction type consisting of reinforced concrete (RC) frames or with a combination of shear walls and moment frames as the lateral load resisting system. Most of these buildings that were visited were in the 6-10 story height range. In addition, some tunnel form shear wall construction was encountered in residential buildings. The team visited one RC core shear wall building with a steel gravity frame, some steel moment frame buildings, and two precast concrete industrial facilities. The historical buildings visited were mostly unreinforced masonry (URM). A combination of RC columns and flat slabs, locally referred to “asmolen”, where hollow blocks or bricks are embedded in the slab, are common in Türkiye in buildings constructed prior to 2018. These buildings performed poorly in the 1999 Duzce and Kocaeli earthquake and again in these earthquakes. In general, it was observed that the presence and increased amount of RC shear walls in a given building led to better structural performance and overall less damage. Almost no structural damage or performance issues with the foundations themselves were observed. However, in locations where liquefaction or soil failures occurred, many undamaged buildings sunk into soil, tilted as a rigid body experiencing permanent uniform drift caused by differential settlements.

Damage to nonstructural components including facades (masonry infill walls covered with insulation and a waterproof membrane, often with windows), interior partitions (masonry infill walls), rooftop equipment, ceilings, building contents, and stairs, are also documented.

Thirty-seven hospitals in the region were visited as part of the EERI Hospital Team reconnaissance efforts -six were seismically isolated, the rest were fixed-base. The operational status for each hospital 6 weeks after the main shock is documented, indicating that while hospitals constructed after 2010 were either partially or fully open, all or nearly all older buildings were closed during field visits. Furthermore, all seismically isolated hospitals (not under construction) were open. Little evidence of damage to structural systems was observed at hospital buildings constructed within the last 20 years; they were closed for service primarily due to damage to nonstructural systems.

Lifelines are essential facilities and structures that provide basic needs to communities such as transportation, energy, and water. Their continued operability after natural disasters such as earthquakes are key to the efficacy of emergency response, to the continued occupancy of buildings, and to the timely repair and rebuilding of cities and communities. EERI assembled a team specifically to conduct post-earthquake reconnaissance to document the seismic performance of lifelines in the region.

The transportation infrastructure was observed to have performed very well in these events. The EERI Lifelines Team observed two collapsed bridges, 8 bridges with severe damage, 13 bridges with moderate damage, and 75 bridges with light damage or no damage. Damage to roadways was primarily due to geotechnical issues such as embankment failure and lateral spreading next to rivers and locations where the road crossed the fault rupture. The team visited recently constructed airports in Gaziantep and Kahramanmaraş. The airport in Gaziantep remained operational after the earthquake sequence and sustained minor nonstructural damage; the airport in Kahramanmaraş airport was non-operational for two days after the earthquake sequence and re-opened the third day, primarily due to nonstructural damage.

The EERI Lifelines Team visited three of the largest coal power plants in the region. One had minor damage, the other two were still offline at the time of the visit. The overall performance of hydroelectric dams was very good. All the units were up and running once they received power back from the grid, which took 3 to 6 days depending on the location. Damage to the substation buildings typically included masonry infills falling onto equipment, cracks in beam-column panel zones, and nearby structures falling on the substation buildings. Several substation buildings collapsed. The team visited three LPG terminals and three LPG bottling and storing plants; they generally performed very well.



Damage to water and wastewater systems varied from significant to minor across the impacted region. The lives of many staff members were lost in the earthquake and one of the greatest challenges in the aftermath of the earthquakes was staff shortages. Performance of transmission and distribution systems in three major water utilities in the region is reported. In Hatay, it was reported that for 20 days following the earthquake sequence, potable water was supplied to the region via trucks and distributed water tanks. As of 19 March 2023, water was being supplied to most of the distribution system, however, the entire region was under a boil-water notice due to treatment quality concerns.

There were many earth dams throughout the region which provide water storage and flood control that were shaken by the earthquakes. Seven earth dams of this type were visited by GEER members after the events. These earth dams exhibited variable performance depending on the foundation conditions, construction type, and proximity to fault rupture. Damage such as fault rupture through a dam, soil liquefaction below and at the toe of dams, seismic compression of the earthfill, crest cracking and concrete spalling, and other damage patterns were documented. In general the outlet structures of the earth dams observed were intact and functional after the earthquakes.

Landslidings was not as prevalent in the observed areas as might be expected based on the ground shaking from these events and the topography in the region. Localized rock fall was observed in steeper mountainous terrain throughout the damage zone. One large slide, that did not impact civil infrastructure, was observed in the southern region and documented in these reconnaissance efforts.

The GEER and EERI teams were able to conduct reconnaissance only in the damaged regions of Türkiye. Limited information is available regarding earthquake effects in Syria through professional contacts in the country. It is reported that fault rupture did not cross the border, this strong ground shaking was the hazard imposed on Syrian infrastructure. The fact that this region has been in a civil war for the last decade means that prior to the the time of earthquakes, there was already much damage due to war. Nonetheless, the ground shaking resulted in significant damage to buildings similar to what was observed in the southern Hatay region of Türkiye adjacent to the Syrian border. Only limited discussion of the earthquake effects in Syria are included in Chapter 10 of this report.

The authors would like to express our profound sadness in the loss of lives and injured citizens. We offer our deepest condolences to the relatives of those who lost their lives during these earthquakes, and our hearts go out to all of Türkiye and Syria.

## Acknowledgments

The work of the GEER Association is supported in part by the National Science Foundation through the Engineering for Civil Infrastructure Program under Grant No. CMMI1826118. Any opinions, findings, and conclusions or recommendations expressed in this material are those of the authors and do not necessarily reflect the views of the NSF. Any use of trade, firm, or product names is for descriptive purposes only and does not imply endorsement by the U.S. Government. The GEER Association is made possible by the vision and support of the NSF Geotechnical Engineering Program Directors: Dr. Giovanna Biscontin, Dr. Richard Fragaszy, and the late Dr. Cliff Astill. GEER members also donate their time, talent, and resources to collect time-sensitive field observations of the effects of extreme events.

The Earthquake Engineering Research Institute is the leading non-profit membership organization that connects those dedicated to reducing earthquake risk. Its multidisciplinary members include engineers, geoscientists, social scientists, architects, planners, emergency managers, academics, students, and other like-minded professionals. EERI has been bringing people and disciplines together since 1948. Through the EERI Learning from Earthquakes (LFE) program, established 50 years ago, EERI conducts post-earthquake reconnaissance to accelerate and increase the learning from earthquake-induced disasters that affect the natural, built, social and political environments worldwide. The EERI Learning from Earthquakes program is funded through the support of EERI members and the generous contributions of individual donors to the LFE Endowment Fund. Additionally, for this EERI LFE reconnaissance mission, EERI received an anonymous donation to support the LFE response to these earthquakes and a number of companies and agencies provided additional financial support to cover travel expenses and allowed members of their staff to travel to Türkiye with EERI. In particular, we would like to thank (in alphabetical order): Arup, Degenkolb Engineers, Electric Power Research Institute (EPRI), Estructure, Exponent, Forell/Elsesser Engineers, Health Care Access and Information of California (HCAI), Imeg Corp, Jacobs, Rutherford + Chekene, Simpson, Gumpertz, & Heger, Skidmore Owings & Merrill, Wiss and Janney, Elstner Associates in the United States and to Promer and TAV Construction in Türkiye. Their financial support and commitment to the mission of the LFE program is greatly appreciated. The EERI Teams greatly benefitted from collaboration with METU/ODTÜ faculty member and President of the Earthquake Engineering Association of Turkey (TDMD) Prof. Murat Altuğ Erberik.

EERI and GEER are particularly grateful to members of the Advanced Team: Ayse Hortacsu and Ayhan Irfanoglu (from EERI) and Robb Moss and Özgür Kozacı (from GEER) that left for Türkiye on a very short notice and whose observations, perishable data and recommendations for logistics were of paramount importance to the planning of subsequent deployments.

The GEER team is grateful to METU/ODTÜ graduate students who were extremely helpful during the field deployments on logistical and technical matters. These include: Berkan Söylemez (PhD candidate), Elife Çakır (PhD candidate), Hayri Güzel (MS student), Arda Şahin (MS student), and Mehmet Türkezer (MS student). The team at SiteEye (Sahagözü) was instrumental in helping organize the data/images/information spatially and providing drone support throughout the GEER investigations. Thanks to Onur Pekcan and his students for facilitating GEER's access to this resource. Prof. Seyhan Fırat was most helpful to the GEER team in providing a tour of the damage in Gölbaşı, highlighting the most important lessons to learn from the events in that area. His knowledge and expertise was invaluable. We are sorry for his loss in the events, and appreciate his hospitality. Soner Özdemir was very helpful and informative at the Limak port, allowing the GEER team to document ground damage. The harbor masters at the İskenderun and Dörtüol harbors were welcoming and gracious, allowing us to document ground damage.

The work on ground motions benefitted from communications with officials at the AFAD Earthquake Department (in Turkish, T.C. İçişleri Bakanlığı Afet ve Acil Durum Yönetimi Başkanlığı, Deprem ve Risk Azaltma Genel Müdürlüğü, Deprem Dairesi Başkanlığı). We thank them for their assistance, and for sharing their invaluable ground motion data, especially given the extraordinary circumstances they faced following these devastating events. A number of individuals organized by EERI's LFE program volunteered to assemble ground motion information, maps and images for a selected number of cities to be visited by the EERI Advance team. These individuals are (listed alphabetically): Onur Deniz Akan, Patrick Bassal, Hector Davalos, Nathan Girmay, Dikshit Goel, Pablo Heresi, Maria Camila Lopez, Alan Poulos, Nicolas Quintero, Juliana Rivera, who were coordinated and assisted by Jorge Archbold and Eduardo Miranda. Additionally, the ground motion team (whose names are listed in Chapter 3) provided intensity measure estimates for use to different elements of the reconnaissance team. This requires estimation of site parameter  $V_{s30}$ , which was facilitated by graduate students Gökhan Şahin (Hacettepe University), Mustafa Koçkar (Hacettepe University), Mustafa Tolga Yılmaz (Middle East Technical University).

The following local experts joined the EERI Buildings Team during the site visits. Their help is greatly appreciated. Without their help it would not be possible to visit many of the sites in the field. Professors Murat Bikçe and Musab Erdem from İskenderun Technical University and their graduate students Alihan Atahan and Nebil İstanbullu joined us in İskenderun, Antakya, Samandağı and Kırıkhan. Jülide Yüzbaşı, PhD student at Çukurova University, joined the team in Hatay region and in Osmaniye. Practicing engineer Aytekin Uyduran showed us the sites in Osmaniye. Professor Mehmet Metin Köse and his graduate students Sıla Avgın, Ayşegül Koç, and

Muhammed Oğuzhanoglu from Kahramanmaraş Sütcü İmam University helped the team in Kahramanmaraş. Professor Sadik Bilen from Adıyaman University and Ahmet Yardımcı, engineer at Adıyaman municipality, joined us in Adıyaman. Professor Müslüm Murat Maraş from İnönü University joined the team and showed the sites in Gölbaşı and Malatya. In addition, Suat Yıldırım from Promer and Dr. Cem Haydaroglu from Arup, and Professor Aydın Demir from Sakarya University joined the team on March 13 and March 19, 2023, respectively. M. Fırat Aydın was immensely helpful to the EERI LFE Advance Team. The EERI Buildings Team would also like to acknowledge Renmin Pretell, Tristan Buckreis, and Professor Jonathan Stewart at University of California Los Angeles for providing estimates of peak ground accelerations and peak ground velocities for the 100+ sites we visited.

The EERI Hospitals team was supported by many individuals along the way. AFAD hosted the team in Ankara prior to field work. Thanks to Recep Cakir, Prof. Dr. Orhan Tatar, Tuba Kadirioglu, Murat Doruk Senturk. Suat Yildirim and Cem Sayar from Promer Engineering supported the team from their office in Ankara. Our day in Iskenderun was aided by Professors Murat Bikce and his PhD student Sahin Bankir from Iskenderun Technical University. Logistics coordination and additional hospital data were provided by Halil Sezen and Rupa Garai of the EERI Buildings Team. Thanks to the teams from Degenkolb Engineers lead by David Sommer and Jennifer Gross for sharing information collected from their reconnaissance trips. Rafael Alaluf from EQRM International, Inc answered our questions along the way. Jon Stewart and his team from UCLA provided the ground motion data for this report. Jennifer Thornburg, Jacqueline Bott, and Chen Rui from CGS provided us with additional ground motion data. Mahmoud Hachem from Earthquake Solutions joined our team on the ground for two days, making travel plans with short notice. Ayse Hortacsu provided her insights from her advanced reconnaissance trip. Maggie Ortiz-Millan and Eduardo Miranda from EERI's LFE program supported and helped organize the team. Additionally, thank you to the many hospital managers and staff who took time from their days to host the team, answer questions, give tours, and share their experiences.

The Lifelines Team thanks all the academics and professionals that contributed time, professional connections, and potential targets of interest in the planning stages of the reconnaissance investigation. These include Recep "Ray" Cakir, Polat Gülkan, Mehmet Çelebi, Onur Pekcan, Mutlu Gürler, Remzi Albayrak, Husna Karayazgan, Serkan Topal, and Adana city officials. Moreover, the team is grateful to the private and public utilities that supported the reconnaissance activities in the field and shared their knowledge of the infrastructure performance, including AFAD, İstanbul Metropolitan Municipality Extreme Event, Ankara Metropolitan Municipality Earthquake Risk Coordination and City Improvement Administration, Enerjisa, Toroslar, TEIAS/TORO, LPG and fuel providers, Kahramanmaraş Water and Sewerage

Administration (KASKİ), Gaziantep Water and Sewer Authority (GASKİ), and Hatay Water and Sewerage Administration (HATSU).

# Table of Contents

Executive Summary.....	4
Acknowledgements.....	8
<b>Table of Contents.....</b>	<b>12</b>
<b>1.0 Introduction.....</b>	<b>17</b>
1.1 Event Overview.....	17
1.2 Scope of Reconnaissance.....	20
1.3 Overview of Urban Damage.....	21
1.3.1 Malatya.....	22
1.3.2 Doğanşehir.....	22
1.3.3 Elbistan.....	23
1.3.4 Adıyaman - Gölbaşı.....	23
1.3.5 Pazarcık.....	23
1.3.6 Kahramanmaraş.....	23
1.3.7 Gaziantep.....	23
1.3.8 İskenderun.....	24
1.3.9 Antakya.....	24
1.3.10 Diyarbakır.....	24
1.3.11 Elazığ.....	24
<b>2.0 Geologic Setting and Fault Rupture.....</b>	<b>25</b>
2.1 Tectonic Setting.....	26
2.2 Surface Fault Rupture.....	29
2.2.1 Rupture Terminations.....	30
(a) Kahramanmaraş Earthquake Rupture Termination.....	30
(b) Sürgü-Çardak Earthquake Rupture Termination.....	38
2.2.2 Narlı fault rupture.....	41
2.2.3 East Anatolian fault.....	45
2.2.4 Sürgü-Çardak fault.....	54
2.2.5 Summary of Geologic Setting and Fault Rupture.....	62
<b>3.0 Ground Motions.....</b>	<b>63</b>
3.1 Ground Motion Networks.....	63
3.2 Data Review and Processing.....	65
3.3 Metadata Compilation.....	72
3.3.1 Source and Path.....	72
3.3.2 Site Parameters.....	76

3.4 Comparisons of Data to Global and Local GMMs.....	77
3.5 Ground Motion Estimation for Sites without Recordings.....	82
3.5.1 Semi-Variogram Model.....	82
3.5.2 Within-Event Residual Maps.....	85
3.5.3 Ground Motion Estimation Procedure.....	90
3.6 Observations Near Ground Motion Stations.....	90
4.0 Liquefaction and Lateral Spreading.....	95
4.1 Gölbaşı, Adıyaman.....	95
4.1.1 Regional and Site Observations - Gölbaşı, Adıyaman.....	95
4.1.2 Building Tilt and Settlement - Gölbaşı, Adıyaman.....	107
(a) Two 2-story residential buildings on Zübeyde Hanım Caddesi.....	107
(b) Two 5-story apartment buildings on 511 Street.....	110
4.2 İskenderun, Hatay.....	112
4.2.1 Regional and Site Observations - İskenderun, Hatay.....	112
4.2.2 Detailed Lateral Spreading Measurements - İskenderun, Hatay.....	126
4.2.3 Lateral Ground Displacements near Çay District Mid-Rise Buildings - İskenderun, Hatay.....	133
4.2.4 Post-earthquake flooding - İskenderun, Hatay.....	139
4.2.5 U-box D817 wall underpass flooding and performance - İskenderun, Hatay.....	142
4.2.6 Building Settlement and Tilting- İskenderun, Hatay.....	144
(a) No. 34 Ersoz, Bahçeli Sahil Evler Caddesi.....	144
(b) No. 16 Kazım Karabekir Caddesi, Pallet Hookah.....	145
(c) Four buildings in Çay, İskenderun, Hatay: No. 26 and 28 Atatürk Boulevard, No. 14 and 16 Bahçeli Sahil Evler Caddesi.....	146
(c) No. 33 Mareşal Fevzi Çakmak Caddesi.....	148
4.3 Dört Yol, Hatay.....	150
4.4 Demirköprü, Hatay.....	155
4.5 Türkoğlu, Kahramanmaraş.....	160
4.6 Antakya, Hatay - Bridge Damage.....	163
4.6.1 D817 Bridge crossing the Orontes River.....	163
4.6.2 Utku Acun Cadiz Bridge crossing the Orontes River.....	166
4.6.3 Bekir Karabacak Koprusu Bridge crossing the Orontes River.....	167
4.6.4 Hatay “Stadium” Bridge crossing the Karasu River.....	170
4.6.5 Hatay “Hospital” Bridge crossing the Karasu River.....	172
<b>5.0 Performance of Buildings.....</b>	<b>173</b>
5.1 Introduction.....	173
5.2 Breadth and Depth of Observations.....	179
5.3 System Level Building Performance.....	185

5.3.1 Shear Wall and Beam-Column Frame System.....	185
5.3.2 Tunnel Form Shear Wall System.....	187
5.3.3 Steel Framed System.....	188
5.3.4 Vertical Irregularities.....	190
5.3.5 Pounding Effects.....	191
5.3.6 Settlement and Overturning due to Liquefaction.....	193
5.4 Structural Performance of Reinforced Concrete Components.....	194
5.4.1 Floor Slabs and Asmolen.....	194
5.4.2 Beams in Buildings with Shear Walls and Beam-Column Frames.....	196
5.4.3 Coupling Beams and Deep Beams.....	197
5.4.4 Beam-Column Joints and Column-Foundation Joints.....	198
5.4.5 Columns.....	199
5.4.6 Shear Walls.....	201
5.4.7 Foundations.....	204
5.5 Historical Buildings.....	204
5.6 Other Structures.....	209
5.6.1 Base Isolated Buildings.....	209
5.6.2 School, Library and Courthouse Buildings.....	212
5.6.3 Religious Buildings.....	216
5.6.4 Industrial Buildings.....	217
5.7 Non-Structural Components or Contents.....	220
5.7.1 Façades.....	220
5.7.2 Interior partitions.....	230
5.7.3 Rooftop equipment and structures.....	232
5.7.4 Ceilings.....	234
5.7.5 Building contents.....	237
5.7.6 Stairs.....	241
<b>6.0 Hospitals.....</b>	<b>244</b>
6.1 Breadth and Depth of Observations.....	244
6.2 Structural Performance.....	250
6.2.1 Foundations.....	256
6.3 Non-Structural Performance.....	258
6.4 Seismically-Isolated Building Performance.....	263
6.5 Post-earthquake Operation and Return to Function.....	270
6.6 Key Observations.....	272
6.6.1 Pre-Disaster Planning and Design.....	272



6.6.2 Immediate Post-Earthquake Hospital Functionality (First 15 Minutes).....	273
6.6.3 Immediate Post-Earthquake Hospital Functionality (First 24 Hours).....	273
6.6.4 Post-Earthquake Restoration of Services (First Six Weeks).....	274
6.7 Parallels to California Hospital Seismic Compliance.....	274
6.8 Preliminary Recommendations.....	275
6.8.1 Pre-Earthquake Planning and Design.....	276
6.8.2 Immediate Post-Earthquake Hospital Functionality (First 15 Minutes).....	277
6.8.3 Immediate Post-Earthquake Hospital Functionality (First 24 Hours).....	278
6.8.4 Post-Earthquake Restoration of Services (First Six Weeks).....	278
6.8.5 Future Information Gathering Needs.....	279
<b>7.0 Performance of Lifelines.....</b>	<b>280</b>
7.1 Introduction.....	280
7.2 Data Collection Methods.....	281
7.3 Transportation Systems.....	283
7.3.1 Bridges/Viaducts.....	283
7.3.2 Tunnels.....	287
7.3.3 Roadways.....	288
7.3.4 Airports.....	289
7.4 Energy Systems.....	292
7.4.1 Coal and Gas Power Plants.....	292
7.4.2 Hydroelectric Dams.....	299
7.4.3 Electrical Substations.....	302
7.4.4 Transmission and Distribution Overhead Systems.....	304
7.4.5 Energy Transmission and Distribution Facilities.....	305
7.4.6 LPG Storage and Distribution Facilities.....	306
7.4.7 Petrol Stations.....	310
7.4.8 Wind Turbines.....	312
7.5 Water and Wastewater Systems.....	312
7.5.1 Water Utilities, Transmission, and Distribution Systems.....	313
(a) Kahramanmaraş Water and Sewerage Administration (KASKİ).....	313
(b) Gaziantep Water and Sewer Authority (GASKİ).....	315
(c) Hatay Water and Sewerage Administration (HATSU).....	316
7.5.2 Water Towers.....	318
7.5.3 Water Treatment Plants.....	319
7.5.4 Wastewater Treatment Plants.....	324
7.6 University Facilities.....	330

7.6.1 Mustafa Kemal University (MKU) in Hatay.....	330
7.6.2 Gaziantep University.....	334
7.6.3 Kahramanmaraş Sütçü İmam University (KSU).....	336
Appendix A to Chapter 7 - GROUND MOTIONS AT SITES VISITED BY THE LIFELINES TEAM..	338
<b>8.0 Performance of Flood/Irrigation Earth Dams.....</b>	<b>348</b>
8.1 Sultansuyu Dam.....	349
8.2 Sürgü Dam.....	351
8.3 Kartalkaya Dam.....	352
8.4 Arıklıkaş Pond.....	355
8.5 Yarseli Dam.....	357
8.6. Reyhanlı Dam.....	360
8.7. Erkenek Dam.....	361
<b>9.0 Landslides and Rock Falls.....</b>	<b>364</b>
9.1 Landslides.....	364
9.2 Rock Fall.....	366
<b>10.0 Impacts in Syria.....</b>	<b>369</b>
<b>11.0 Future Studies and Opportunities.....</b>	<b>372</b>
References.....	376

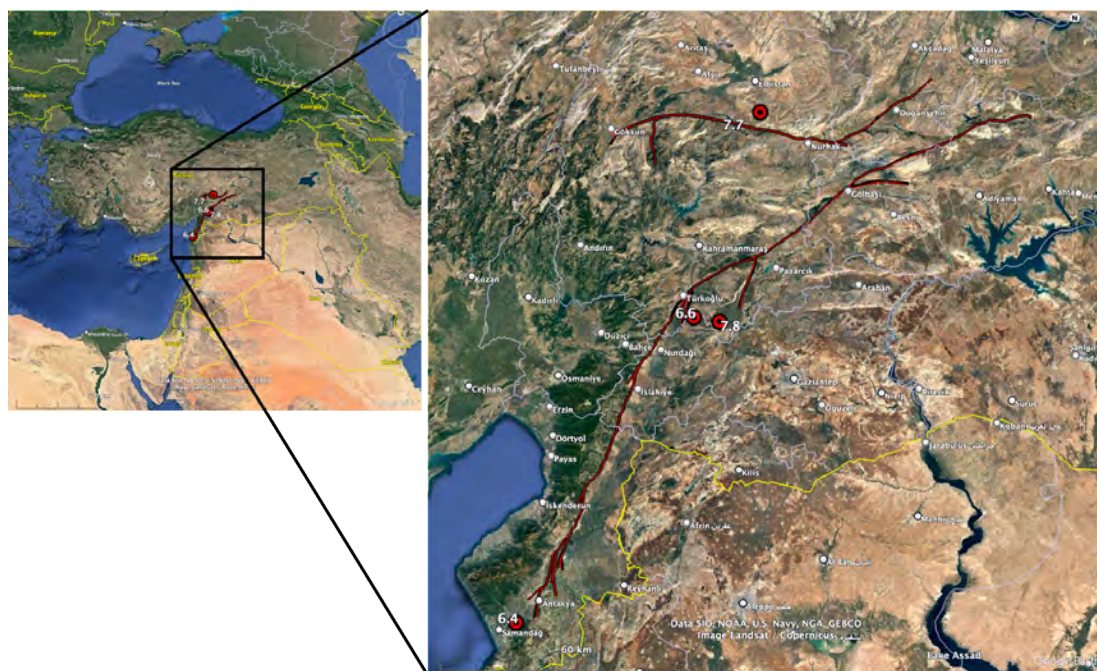
# 1.0 Introduction

*Onder Cetin, Robb Moss, J. David Frost, Jonathan P. Stewart*

## 1.1 Event Overview

A moment magnitude (**M**) 7.8 earthquake occurred on East Anatolian Fault (EAF), Türkiye, on February 6, 2023, at 04:17 local time (01:17 GMT). The magnitude, epicentral coordinates and other source information used in this report, are from the [Global CMT catalog](#) unless otherwise noted. The earthquake's epicenter was located at 37.288°N, 37.043°E, in Pazarcık-Kahramanmaraş-Türkiye, approximately 40 km northwest of Gaziantep and 33 km southeast of Kahramanmaraş. The focal depth was reported as 8.6 km (AFAD). In the rest of this report this event will be referred to as the **M7.8 Kahramanmaraş** event.






Approximately nine hours later at 13:24 local time (10:24 GMT) a major aftershock of **M7.7**, with epicenter coordinates at 38.089°N, 37.239°E in Ekinözü-Elbistan-Kahramanmaraş-Türkiye, occurred. The epicenter of this event is located at approximately 98 km northwest of Adıyaman, and 62 northeast of Kahramanmaraş, with a focal depth of 7.0 km (AFAD). In the rest of this report this event will be referred to as the **M7.7 Elbistan** event. Figure 1.1 represents the location of epicenters with the spatial distribution of aftershocks along with the ruptured fault zone.



**Figure 1.1.** Map of Türkiye (Google Maps). The epicenter of the February 6, 2023, Kahramanmaraş (**M7.8**) and Elbistan (**M7.7**) earthquakes shown along with other aftershocks and surface fault rupture.

Table 1.1 and 1.2 summarize the faulting mechanism, magnitude, and depth of these two events recorded by different national and international agencies. The focal mechanism indicated by different agencies is consistent with the East Anatolian Fault (EAF) characteristics, so the mechanism is a left lateral strike-slip.

**Table 1.1.** Characteristics of **M7.8** Kahramanmaraş mainshock

Institution	Focal Mechanism	Depth (km)	M
AFAD <sup>1</sup>		8.6	7.7
KOERI <sup>2</sup>		10	7.7
USGS <sup>3</sup>		17.5	7.8
EMSC <sup>4</sup>		10	7.7
GCMT <sup>5</sup>		14.9	7.8

<sup>1</sup>Turkish Prime Ministry-Disaster and Emergency Management Presidency






<sup>2</sup>Kandilli Observatory and Earthquake Research Institute

<sup>3</sup>United States Geological Survey

<sup>4</sup>European Mediterranean Seismological Centre

<sup>5</sup>Global Centroid Moment Tensor Catalog

**Table 1.2.** Characteristics of **M7.7** Elbistan aftershock

Institution	Focal Mechanism	Depth (km)	M
AFAD <sup>1</sup>		7.0	7.6
KOERI <sup>2</sup>		10	7.6
USGS <sup>3</sup>		13.5	7.5
EMSC <sup>4</sup>		15	7.6
GCMT <sup>5</sup>		12	7.7

<sup>1</sup>Turkish Prime Ministry-Disaster and Emergency Management Presidency

<sup>2</sup>Kandilli Observatory and Earthquake Research Institute

<sup>3</sup>United States Geological Survey

<sup>4</sup>European Mediterranean Seismological Centre

<sup>5</sup>Global Centroid Moment Tensor Catalog

Historic destructive earthquakes which took place on the EAF in the last 60 years are listed as follows (Figure 1.2):

- Bingöl Earthquake (**M 6.9**), May 1971
- Lice Earthquake (**M 6.7**), September 1975
- Sürgü Earthquake (**M 6.1**), May 1986
- Bingöl Earthquake (**M 6.4**), May 2003
- Elazığ-Kovancılar Earthquake (**M 6.1**), March 2010
- Elazığ Sivrice Earthquake (**M 6.8**), January 2020

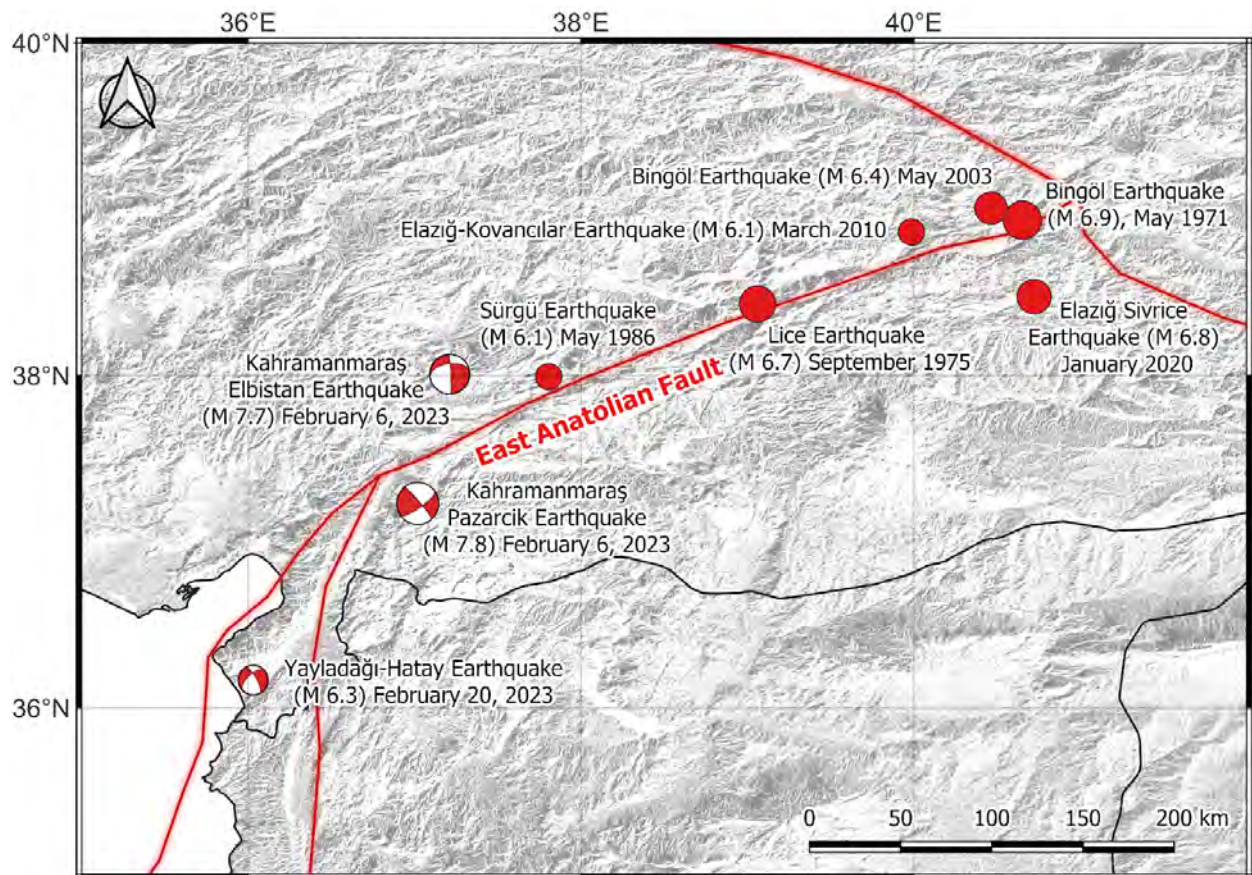


**Figure 1.2.** Locations of 2023 and historic earthquakes along the East Anatolian Fault

These 2023 Türkiye earthquakes affected more than 15 million people in the cities of Kahramanmaraş, Adıyaman, Antakya/Hatay, Osmaniye, Malatya, Gaziantep, Şanlıurfa, Diyarbakır, Adana, Elazığ, and Kilis and caused intense shaking and damage. The approximate number of casualties exceeded 45,000, and more than 120,000 buildings collapsed or were heavily damaged (AFAD, 2023).

Over 11,020 aftershocks occurred in the earthquake region through the 1st of March within a 200 km epicenter distance. Among them, more than 400 of these aftershocks exceed **M** 5.0. An independent **M** 6.3 earthquake occurred in Yayladağı-Hatay at 36.037°N, 36.021°E on February 20 with a focal depth of 21.73 km (AFAD).

AFAD operates 280 strong-motion stations within 436 km from the zone of energy release, and these stations successfully recorded the February 6, 2023, Kahramanmaraş (**M** 7.8) earthquake. For this event, the largest recorded median-component (RotD50) peak ground acceleration (PGA) was 2.21g at Station TK 4614, Pazarcık. The largest median-component PGA for the Elbistan (**M** 7.7) aftershock was 0.59 g at Station 4612, Kahramanmaraş, Göksun. These accelerations are based on the processing described in Chapter 3.

As the authors, we are deeply sorry for the loss of lives and injured citizens. We would like to offer our deepest condolences to the relatives of those who lost their lives during these earthquakes.

## ***1.2 Scope of Reconnaissance***

Shortly following these events, leaders of the EERI Learning from Earthquakes program and GEER Association PIs began holding meetings to plan the appropriate scale and timing of a reconnaissance response. We were in regular communication with researchers in Türkiye, including engineers and geologists primarily coordinated by Onder Cetin and Murat Altuğ Erberik at METU, and by Alper İlki at ITU and Erhan Altunel at Eskisehir Osmangazi University who had already begun to deploy to the field in the initial days following the event.

From an organizational perspective, GEER and EERI decided that a combined Turkish-American response was the right approach, and collaboration agreements were reached with the Earthquake Engineering Association and Earthquake Engineering Foundation of Türkiye one week following the mainshock. These efforts were openly communicated with other reconnaissance organizations within the US who were welcome to join in, but it was GEER and EERI that ultimately committed to a coordinated field response.

GEER and EERI formed advance teams (Phase 1) consisting of Ayse Hortacsu and Ayhan Irfanoglu (from EERI) and Robb Moss and Özgür Kozacı (from GEER) that deployed February 12 through February 22 and worked with over a dozen collaborators in Türkiye, mainly organized and coordinated by Altuğ Erberik (EERI) and Önder Çetin (GEER). The goal of the advance team was mainly to assess the scale of the reconnaissance effort that would be needed to collect the most valuable perishable data. That information was integral to the planning of subsequent

deployments, which began with a Phase 2 GEER team then deployed to the field Feb 28 to Mar 4, led by David Frost, and with the members shown in the frontmatter. Shortly thereafter, EERI deployed three teams to the field to focus on building structures, lifelines, and hospitals, with the members indicated in the frontmatter. The EERI buildings, lifelines, and hospitals teams were led by Halil Sezen, Riccardo Cappa, and Ali Sumer, respectively. Finally, a GEER Phase 3 team led by Jonathan Bray deployed March 27 to April 1 to focus on liquefaction issues in ports and detailed studies of liquefaction effects on buildings.

All of the GEER and EERI team members received ethics training (<https://converge.colorado.edu/resources/training-modules/>) and were provided instruction on mission (perishable data collection that would be useful to subsequent research) and the need for data to be posted and shared. This has been done both with Designsafe (<https://www.designsafe-ci.org/>) and with a preferred application of Turkish partners, SiteEye (<https://app.sahagozu.com/>).

### ***1.3 Overview of Urban Damage***

Here we provide a general overview of the types of damage observed in each of the urban areas including whether damage was structural, geotechnical, fault related, etc. A map showing the locations of the urban areas is provided in Figure 1.3. Additional details are provided in subsequent chapters, mainly Chapter 4 (liquefaction) and Chapter 5 (performance of buildings).

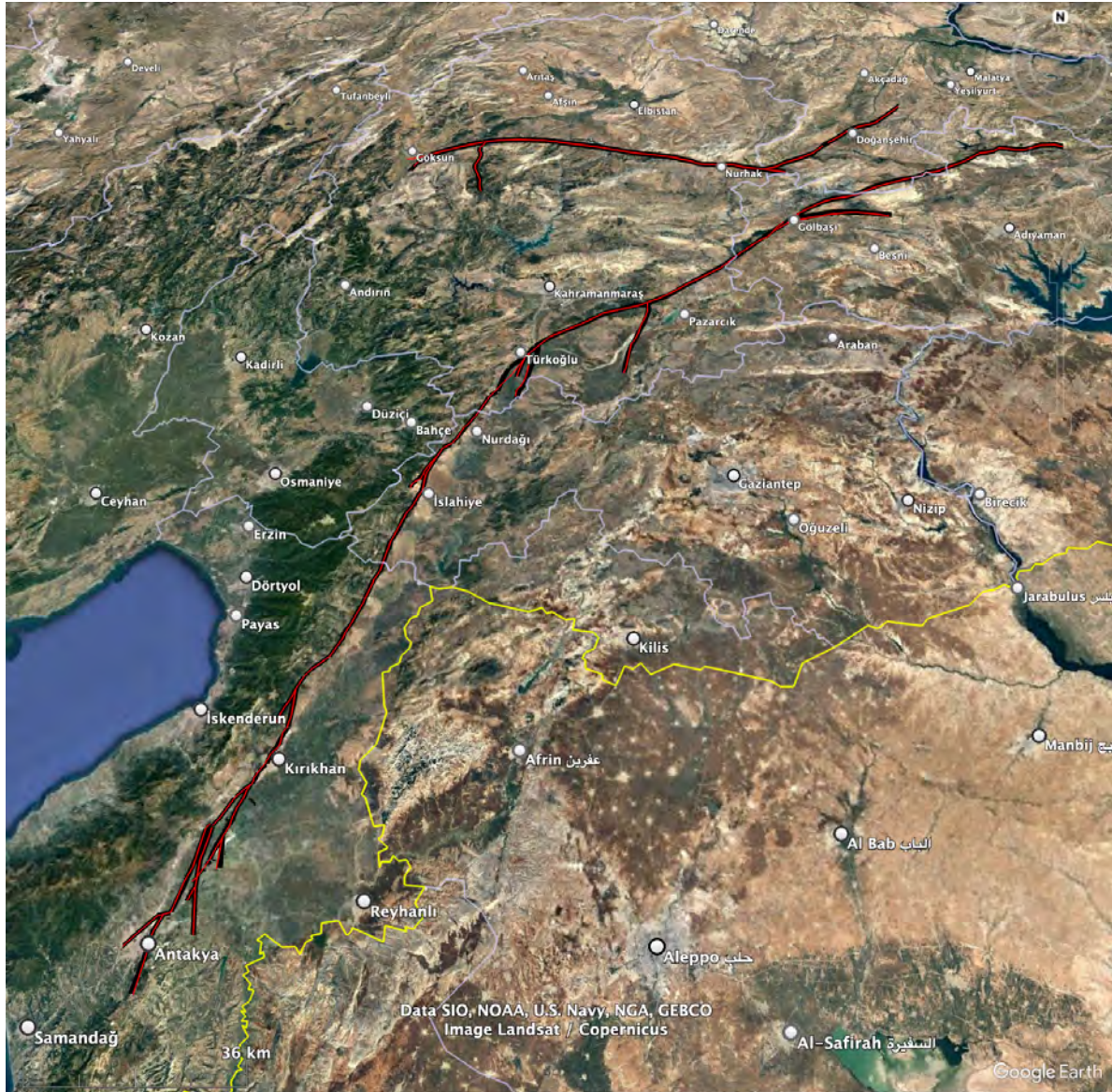


**Figure 1.3.** Map showing locations of towns described in the following text along with surface fault rupture from the earthquakes (Google Maps).

**1.3.1 Malatya**

Malatya is located in the northeast of Kahramanmaraş and was one of the highly affected cities by the events. Site observations revealed that a high rate of heavily damaged or collapsed buildings is attributed to the old building stocks or poor structural design quality.

**1.3.2 Doğanşehir**

This town is located in the region between both ruptured faults. The Erkenek dam is in the vicinity which experienced surface rupture through the embankment from the Eastern Anatolian Fault. Fault rupture through the surrounding roads and strong ground shaking damage to structures were observed in this town.



### **1.3.3 Elbistan**

Elbistan is located to the eastern end of the Sürgü-Çakmak fault zone. Significant structural damage and collapse were observed, but no ground failures due to liquefaction or other soft soils were observed. It is in a mountainous area, where the profile is composed of rock and stiff/dense soil units.

### **1.3.4 Adıyaman - Gölbaşı**

Almost 60% of the building stock in the city center collapsed during these two events, and the majority of the remaining buildings were heavily damaged. In the city center, no liquefaction manifestation was reported, but almost every building by the Golbasi lake was exposed to liquefaction-induced ground displacements and deformations in the forms of settlement and lateral spreading, etc.

Seismic soil liquefaction led to the loss of bearing capacity in some residential buildings. Tilted and overturned buildings were documented. Liquefaction-induced bearing capacity failures were more common in 5-7 story buildings, as compared to one to three-story ones. In addition, rock falls involving large blocks were also mapped by Karamağara locality. No loss of life due to the rockfalls was reported, but the roads were closed, and transportation was disrupted.

Along with liquefaction, surface fault rupture was observed through the city. The left step of left-lateral faulting resulted in *en echelon* faulting which ruptured through the city and was evident alongside liquefaction and lateral spreading.

### **1.3.5 Pazarcık**

Pazarcık is located by the epicenter of the first event, and is also located near the subevent that triggered the main event. Moderate levels of structural damage were observed. Surface fault rupture was observed on the East side of the highway, as well as crossing the highway in many locations to the South of Pazarcık.

### **1.3.6 Kahramanmaraş**

Kahramanmaraş is located in the southern-central part of Türkiye with a population of more than one million citizens. The region has many tectonic-based alluvium plains, whose boundaries are controlled by surrounding faults.

Although the collapsed and heavily damaged building rate is high in the region, no significant geotechnical-related damage was observed. The structural damage is generally associated with poor construction quality and detailing combined with the strong ground motion intensity. Some rockfalls and landslides were mapped along the main roads. In nearby Türkoğlu, surface manifestations of soil liquefaction and lateral spreading were observed by Aksu River.

### **1.3.7 Gaziantep**

Gaziantep is located in southern Türkiye with a population of over 2.5 million. At least 25 residential buildings collapsed or were heavily damaged during the earthquake in the city center. The stone walls of the historical Gaziantep castle (constructed by the ancient Hittite

Empire during the 2nd and 3rd centuries) were severely damaged. No surface manifestation of liquefaction was observed in the city center, but slope failures occurred in several spots.

Nurdağı district is located 68 km away from the city center of Gaziantep towards the west and is a transportation hub providing connections in the north-south and east-west. Surface faulting and structural damage were widely observed in the town. Soil and rock mass failures in the form of landslides and rockfalls were mapped nearby.

İslahiye is another district in Gaziantep approximately 10 km south of Nurdağı , where a high rate of collapsed or heavily damaged buildings was reported after the two earthquakes. Here examples of geotechnical damage were documented in the form of slope instability, rockfall, lateral spreading, and excessive settlements.

### **1.3.8 İskenderun**

İskenderun is a city of roughly 250,000 people that was heavily affected by events. The near surface is composed of Quaternary-aged alluvium. Many examples of soil ejecta and lateral spreading were observed. Damaged, tilted, or settled buildings were documented due to loss of bearing capacity after liquefaction. The surrounding ports were also heavily damaged due to liquefaction and lateral spreading. The harbor in İskenderun is where a cruise ship was docked in order to shelter the unhoused citizens after the earthquakes.

### **1.3.9 Antakya**

Antakya, which was the ancient city of Antioch, is located in the Hatay district and was damaged the most severely of any Turkish city in these events. More than 50% of the city's buildings were destroyed, with another 30% of the buildings experiencing sufficient damage that they will have to be demolished. On the order of 3000 buildings collapsed killing upwards of 20,000 people in this city alone. The main 7.8 event resulted in significant ground shaking in this region, and the subsequent 6.4 aftershock was located close by causing more strong ground shaking. Significant liquefaction and lateral spreading was observed nearby in the Hatay airport area and other regions surrounding Antakya. Due to the level of destruction and ongoing rescue operations the GEER Advance Team did not initially visit the city of Antakya. Subsequent visits were performed by EERI and GEER Phase II team.

### **1.3.10 Diyarbakır**

Diyarbakır is in the southeast part of Türkiye, and the near surface is generally rock-like conditions. The limited number of building collapses (less than 10 buildings) is mainly associated with poor construction or material quality. Neither slope stability failures nor surface manifestations of liquefaction was observed in the city.

### **1.3.11 Elazığ**

Elazığ is the neighboring city to Malatya in the east. Only one building collapsed due to the earthquakes. No geotechnical failures were reported.

## 2.0 Geologic Setting and Fault Rupture

*Ozgur Kozaci, Richard D. Koehler, Kevin Clahan*

Two mobilizations included the first author and Erhan Altunel (Advance Team geologists) and the 2nd and 3rd authors with Cengiz Yıldırım (Phase II Team geologists and geomorphologist) with the goal of documenting the surface rupture characteristics. The locations of their fault investigations are shown in Figure 2.1. The Advance Team focused on northern and southern M7.8 Kahramanmaraş earthquake rupture terminations, the connection between the Sürgü-Çardak and East Anatolian faults and fault rupture impacts on the critical infrastructure including transmission pipelines, electric transmission corridors, levees and built environment such as Hatay Airport and bridges. The Advance Team also identified a list of priorities for the Phase II team to focus on during their reconnaissance. Subsequently, the Phase II team focused on systematic mapping of ruptures and displacements associated with M7.8 Kahramanmaraş and M7.7 Elbistan earthquakes.

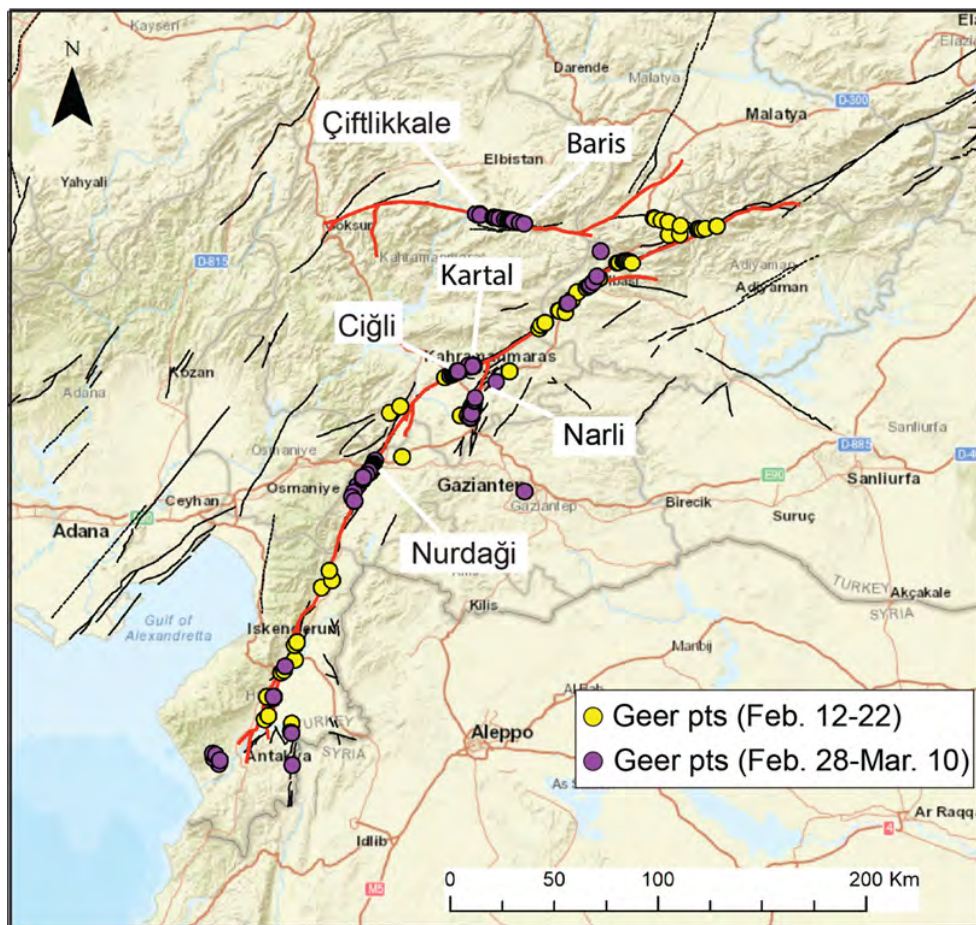


**Figure 2.1.** Fault Rupture Team observation points from the GEER field investigation. Red lines are the simplified rupture traces from the U.S. Geological Survey (Reitman et al., 2023). Thin black lines are previously mapped faults from the Active Fault Map of Turkey (Emre et al., 2013).

The reconnaissance results include hundreds of geo-located observations along the main rupture traces and affected areas. In total, the geologic reconnaissance teams observed over 300 km of fault surface rupture and mapped nearly 80 km of the ruptures in detail. Left-lateral surface displacements along the M7.8 East Anatolian fault rupture were remarkably consistent, 3 to 5 m, but diminished to the south near Antakya to around 0.5 m. The M7.7 event produced the largest recorded left-lateral surface displacements of consistent 6.5 to 8 m (max observed 8.6 m).

## 2.1 Tectonic Setting

Türkiye, most of which is located on the Anatolian Block, lies at the triple junction between the Eurasian, African, and Arabian plates (Figure 2.2). The Anatolian block is bounded by the North Anatolian Fault (NAF) in the north, the East Anatolian Fault (EAF) in the east, Hellenic and Cyprus subduction zones in the south and an extensional regime in the west together which accommodate the relative counterclockwise rotation and westward motion between the three surrounding plates. The events on February 6, 2023 initiated on Narli Fault, a splay of the EAF which then propagated along the EAF in a bilateral manner from the center out to the NE and SW resulting in a M7.8. approximately 9 hours later another event occurred on the Sürgü-Çardak faults resulting in a M7.7.

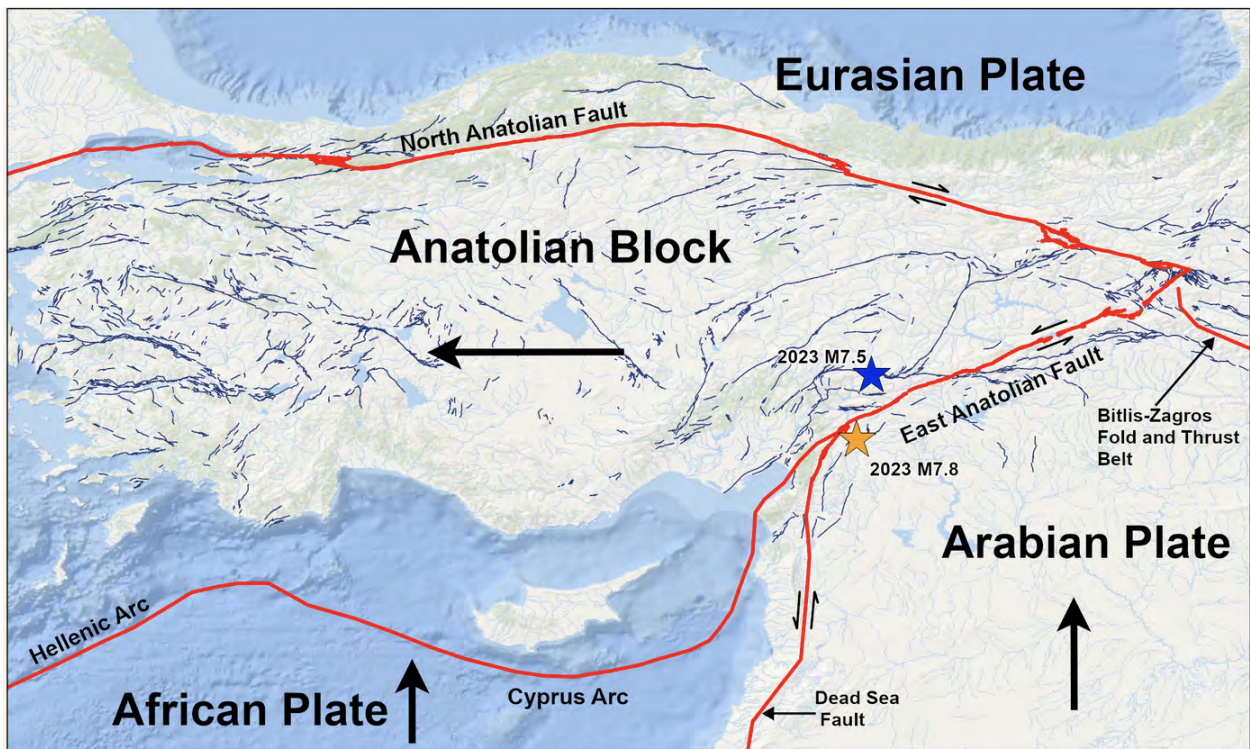


**Figure 2.2.** (USGS) Tectonic plate and fault map of the region ([link](#)). Red lines denote faults along the plate boundaries. Gray lines denote other faults.

The East Anatolian fault is an ~700-km-long left-lateral strike-slip fault. Geomorphic, paleoseismic, and geodetic studies indicate a slip rate of 10 mm/yr. Six segments were previously defined based on structural complexities (Figure 2.3). The 2023 earthquake rupture extended across three previously defined segments and through two major restraining bends.

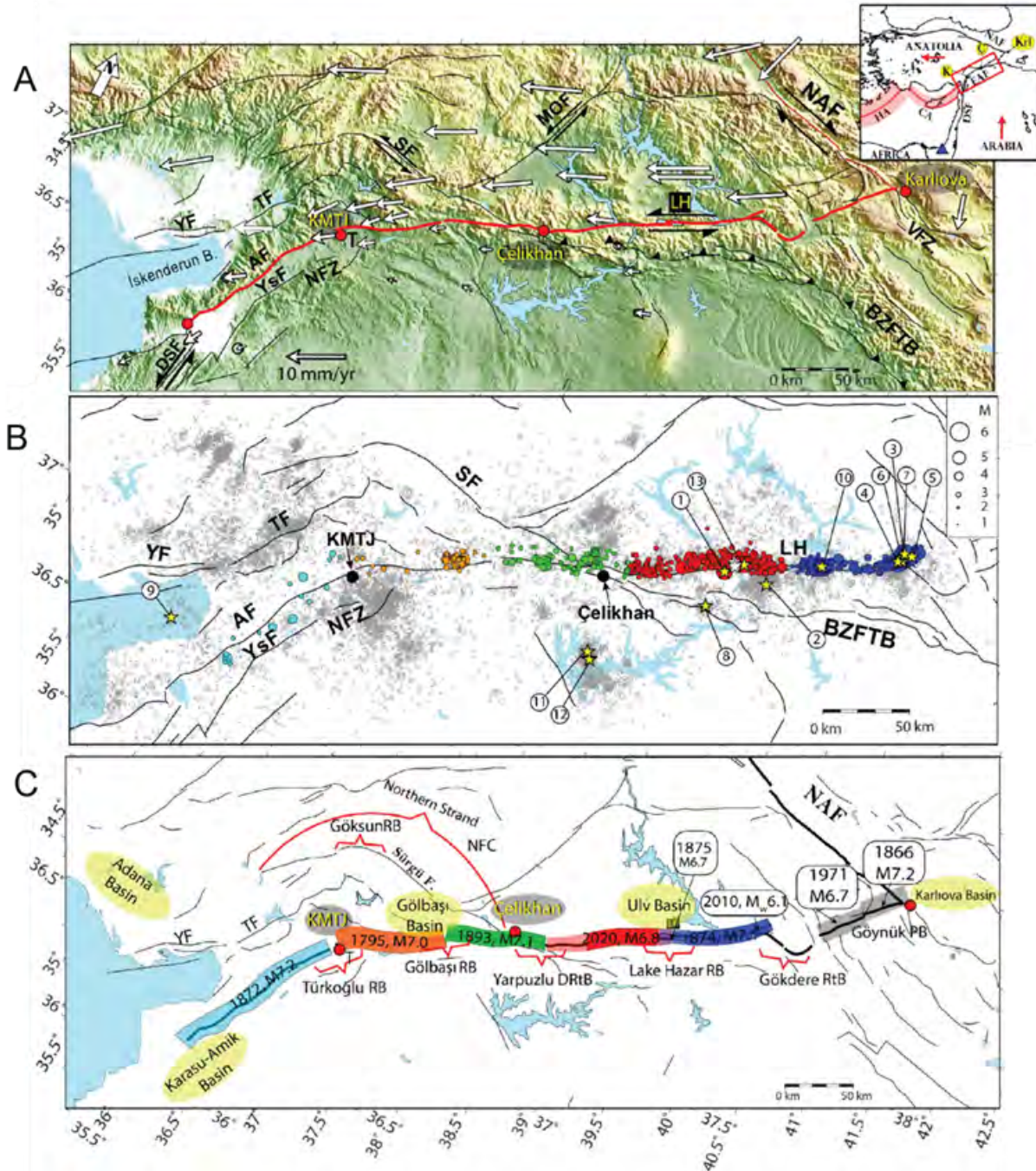


**Figure 2.3.** Maps of the East Anatolian fault from Guvercin et al. (2022) showing (A) Geodetically measured crustal velocities (white arrows) of Anatolia relative to a fixed Arabian plate, (B) seismicity from 2007-2019 colored by inferred segment, and (C) inferred extent of historical earthquakes.

These events are all primarily left-lateral strike slip in mechanism and resulted in a rather complex rupture pattern. The depths of these events are on the order of 10km. The main events and aftershock patterns are shown in Figure 2.4 and a snapshot of the rupture dynamics are shown in Figure 2.5.

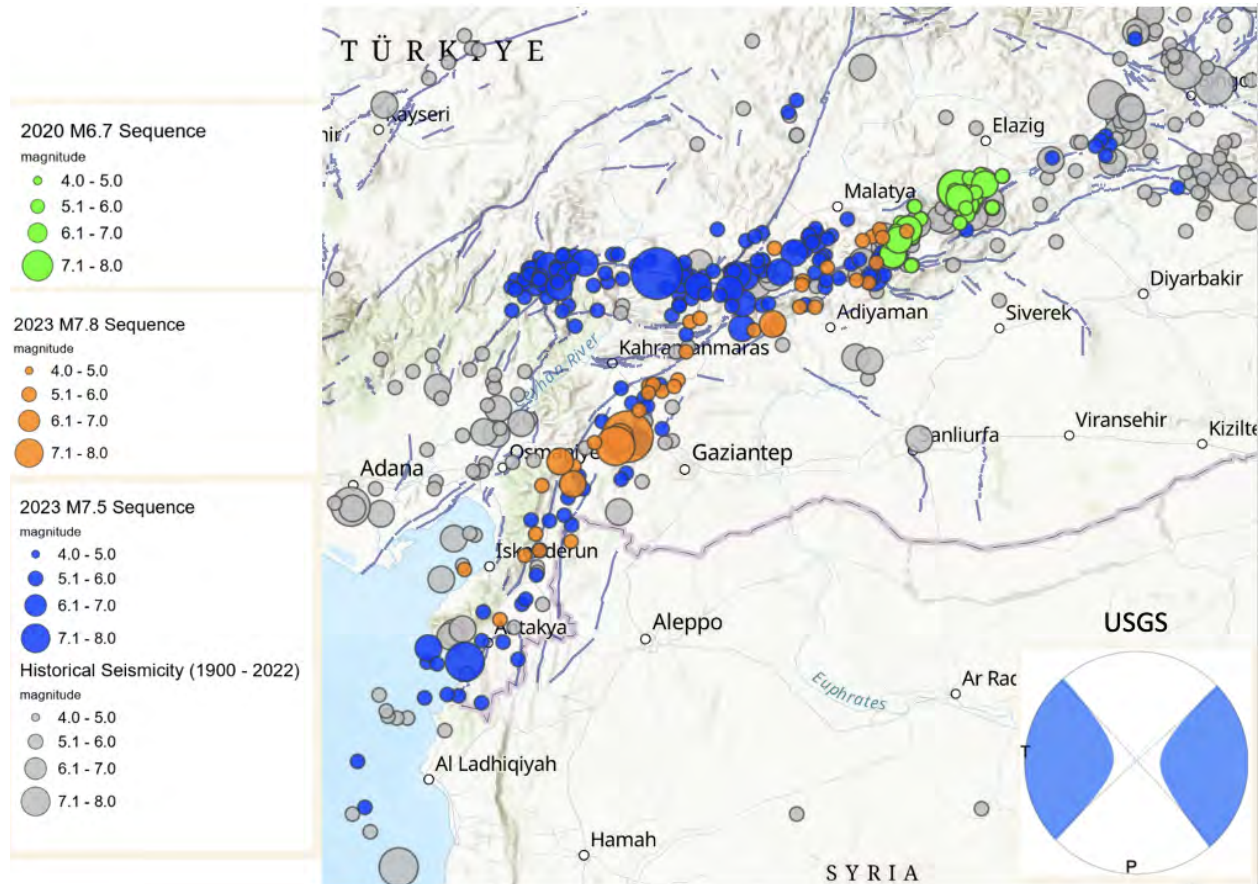


**Figure 2.4.** Locations and sizes of events in the sequence (USGS).

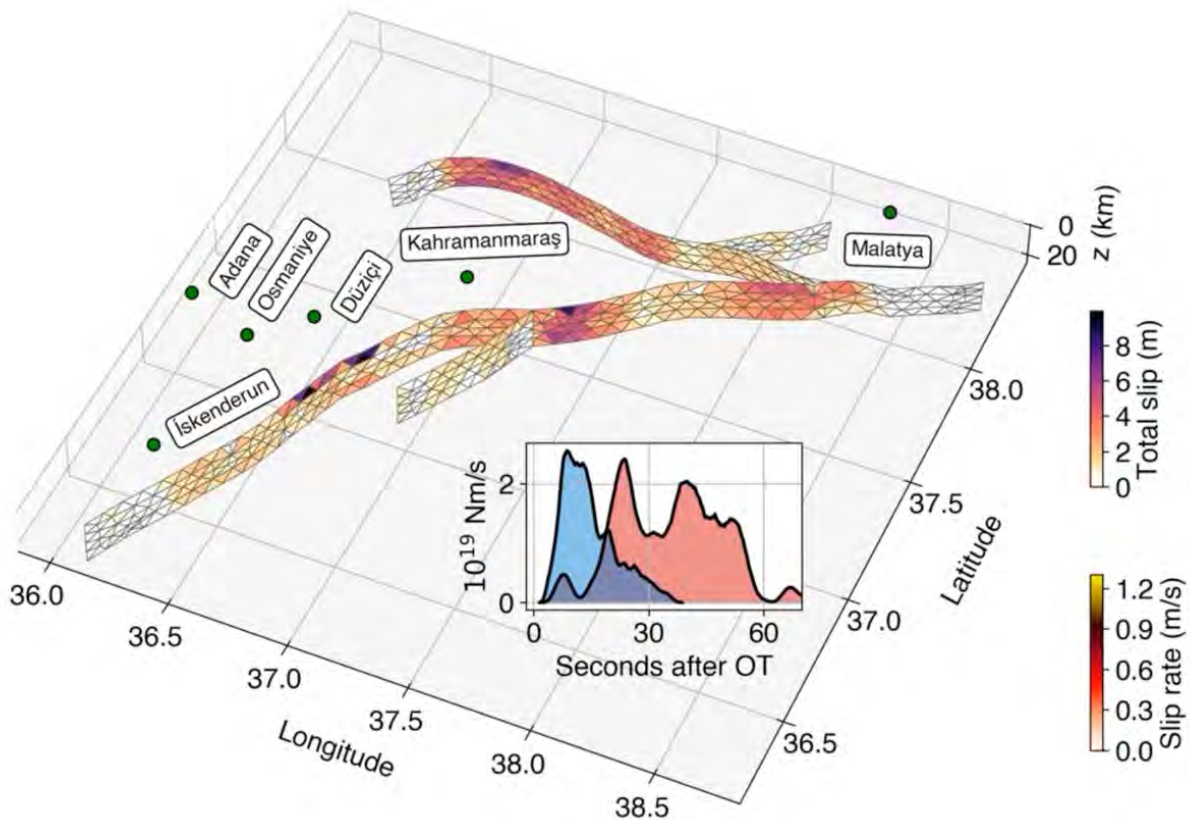


**Figure 2.5.** Preliminary finite fault model from Diego Melgar. Accessed from <https://twitter.com/i/status/1627723600282419200>

## 2.2 Surface Fault Rupture

Reconnaissance efforts started with documenting the rupture terminations of both faults, and then proceeded to document the surface rupture along the lengths of both faults. The discussion in this chapter follows suit.

Both ruptures are characterized by classic strike-slip geomorphology (right-stepping *en echelon* scarps, moletracks, linear depressions, shutter and pressure ridges, linear swales, saddles, and side-hill benches). Less common rupture locations include breaks across the tops of shutter ridges and bedrock slopes, and through complex arrays of *en echelon* pressure ridges. The ruptures typically followed tectonic geomorphic features that most likely would have been recognized in pre-rupture mapping, however some locations would have been difficult to predict. The mapping results provide information that helps better understand the locations of fault rupture with implications for improving surface fault rupture hazard assessments important for infrastructure design.

### 2.2.1 Rupture Terminations

Mapping rupture terminations is important for confirming the rupture extent determined via remote sensing methods and evaluating the possibility of triggering relations with the adjacent unruptured fault sections.

#### (a) Kahramanmaraş Earthquake Rupture Termination

Surface rupture of the M7.8 Kahramanmaraş earthquake begins to die out around Hatay Airport in the south. North of the Hatay Airport surface rupture is approximately 100 m wide and displays approximately 75 cm left lateral and 23 cm vertical displacements on individual strands (Figures 2.6 to 2.8). Approximately 4.7 km south of the airport the surface rupture extends over an approximately 3.8 km wide distributed fault zone where no discernable offsets could be measured on individual strands (Figures 2.9 and 2.10).

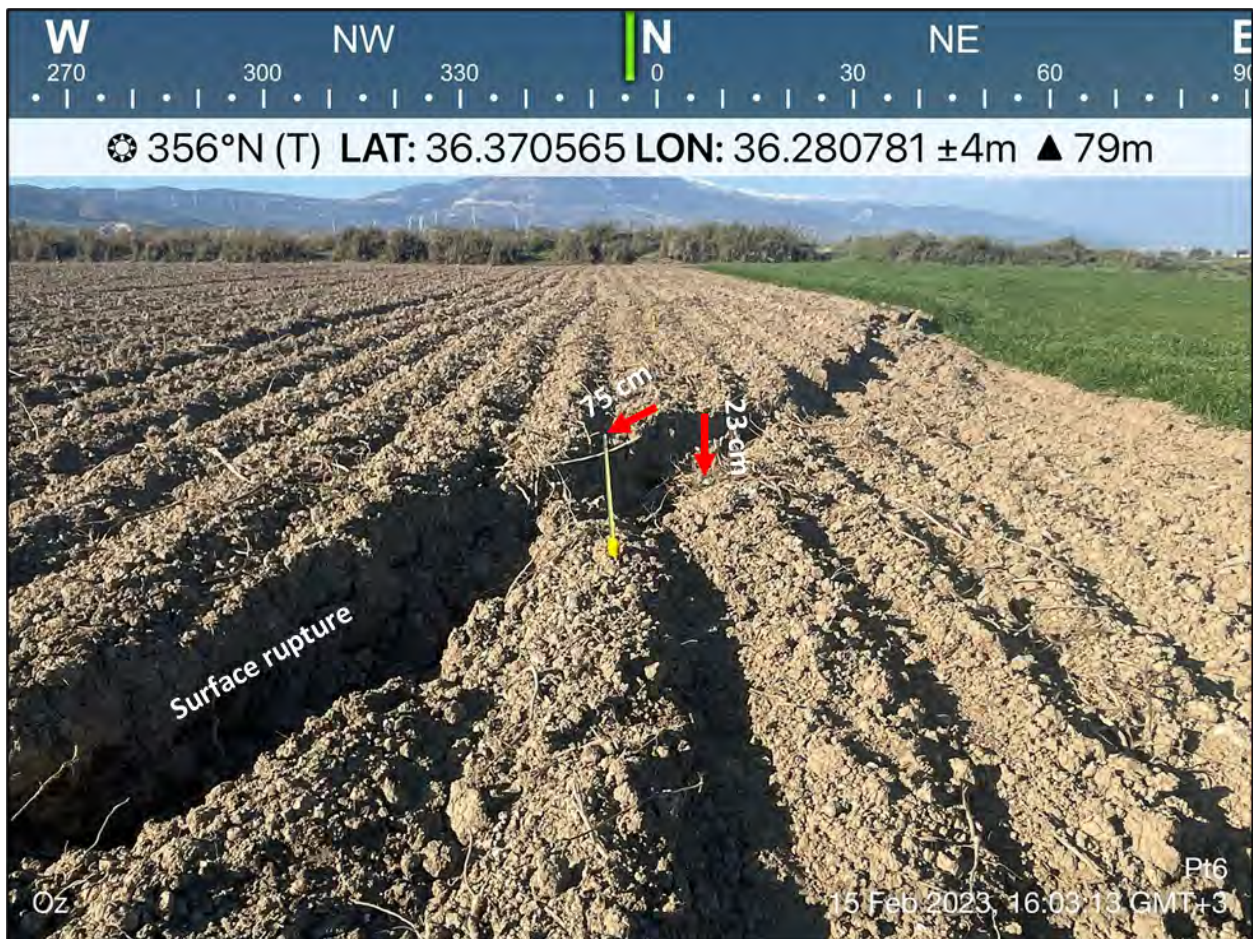


**Figure 2.6** February 6, 2023 M7.8 Kahramanmaraş earthquake surface rupture in the recently tilled field 300m north of Hatay Airport. Note the 75cm left lateral and 23cm vertical displacement at this location.





**Figure 2.7.** February 6, 2023 M7.8 Kahramanmaraş earthquake surface rupture at the Hatay Airport north fence. Note the left-stepping en-echelon left-lateral surface rupture with down-to-the-east vertical component. Lat/Long: 36.366992°N, 36.279822°E. Photo taken February 15, 2023.



**Figure 2.8.** February 6, 2023 M7.8 Kahramanmaraş earthquake surface rupture expressed as an approximately 2.1-km-wide deformation zone with secondary fault rupture displacements on the order of centimeters and localized depression. Photo looking along the Hatay Airport access road.



**Figure 2.9.** Aerial reconnaissance of the February 6, 2023 M7.8 Kahramanmaraş earthquake surface rupture south of the Hatay Airport.



**Figure 2.10.** February 6, 2023 M7.8 Kahramanmaraş earthquake surface rupture crossing a levee south of the Hatay Airport.

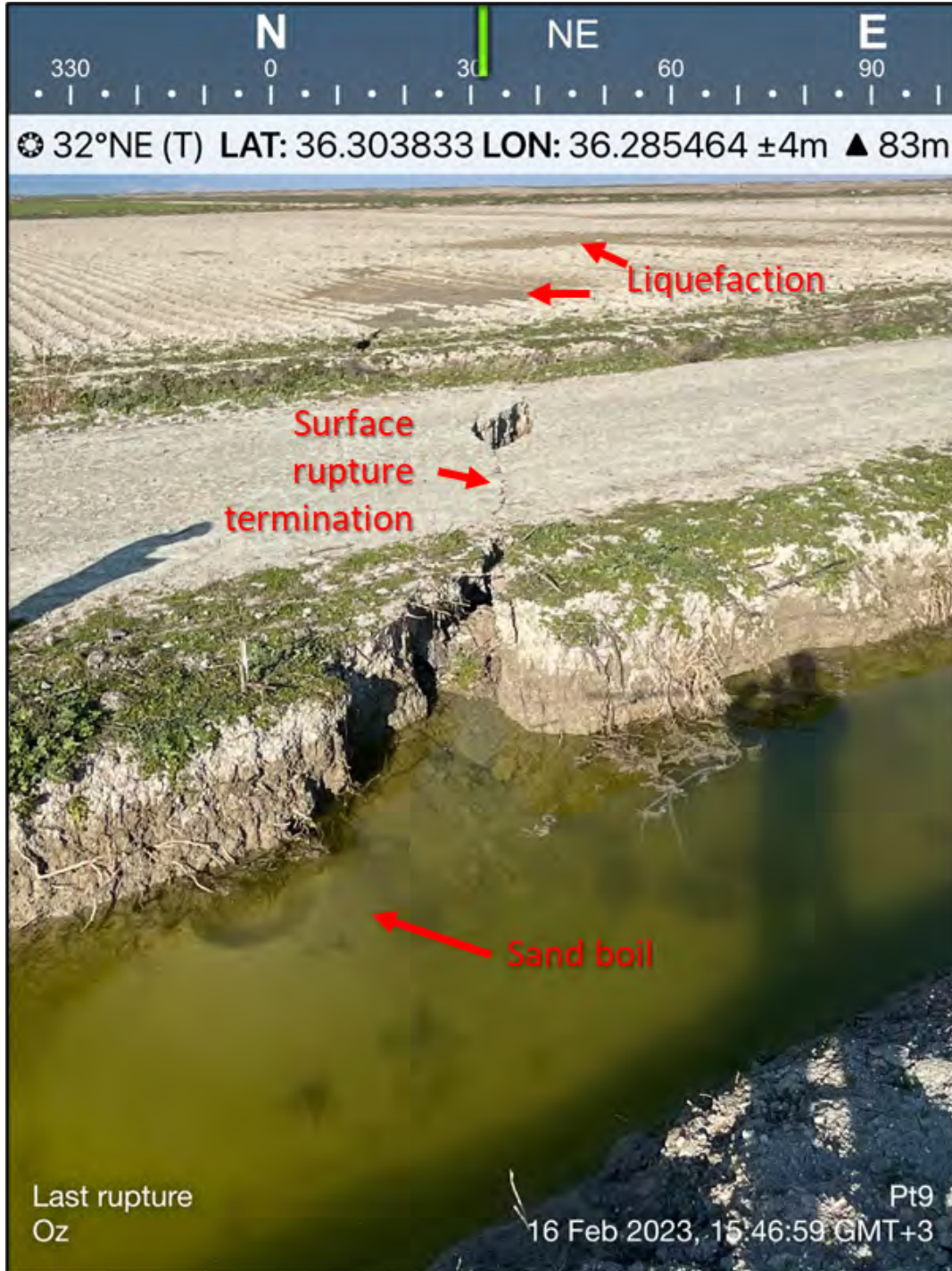


**Figure 2.11.** February 6, 2023 M7.8 Kahramanmaraş earthquake surface rupture dies out approximately 3.7km southeast of the Hatay Airport. At this location surface rupture is expressed as a crack with no discernable displacement but still displays en-echelon surface trace characteristics along with liquefaction features (sand boils).

Northern continuation of the February 6, 2023 M7.8 Kahramanmaraş earthquake surface rupture was extended to the Balıkburnu Village of Çelikhan (Figures 2.12 and 2.13).



**Figure 2.12.** Left lateral offset of Çelikhan-Sürgü Road in Balıkburnu Village. Note that electric and telephone poles are bent and tilted only within the fault zone and its vicinity.

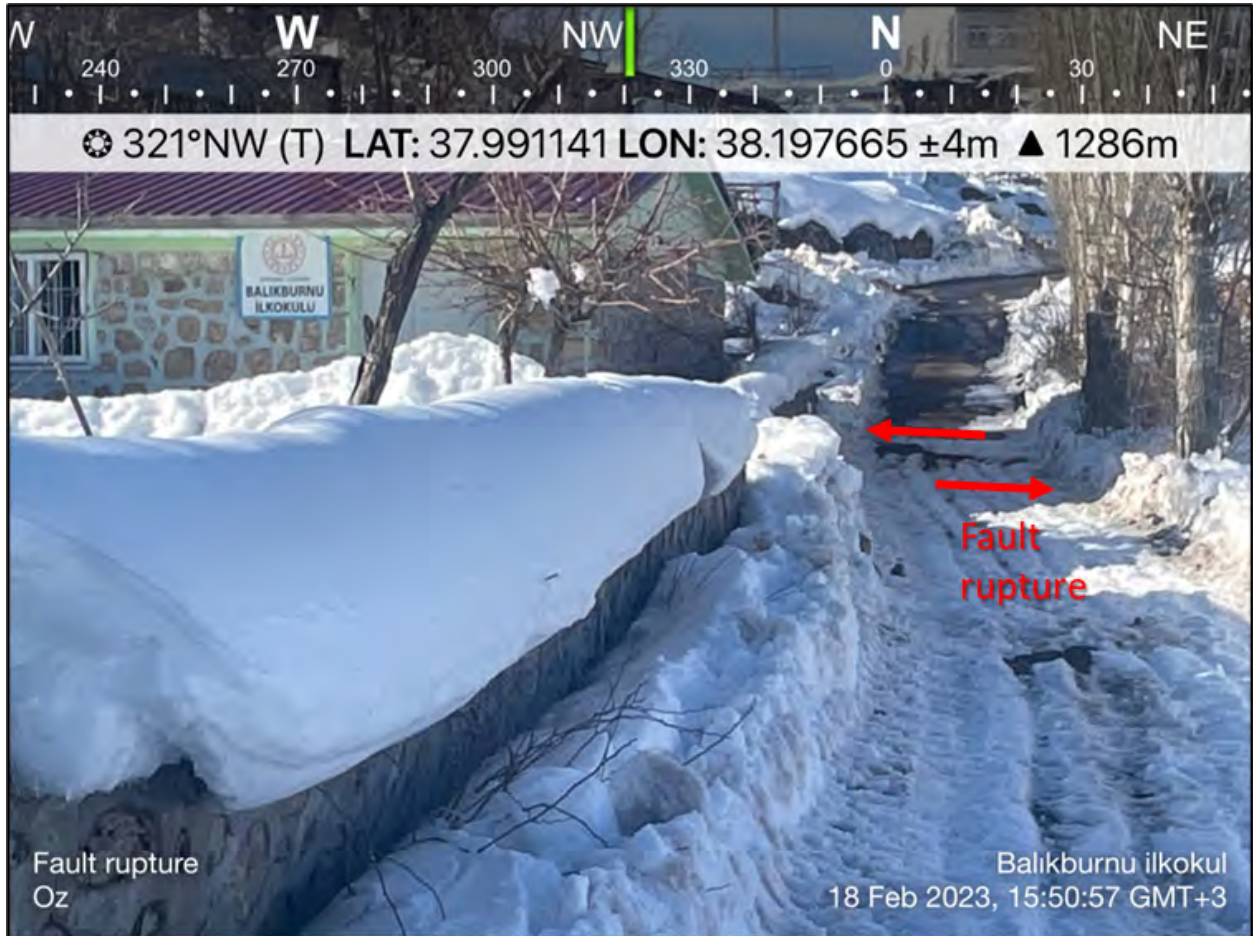
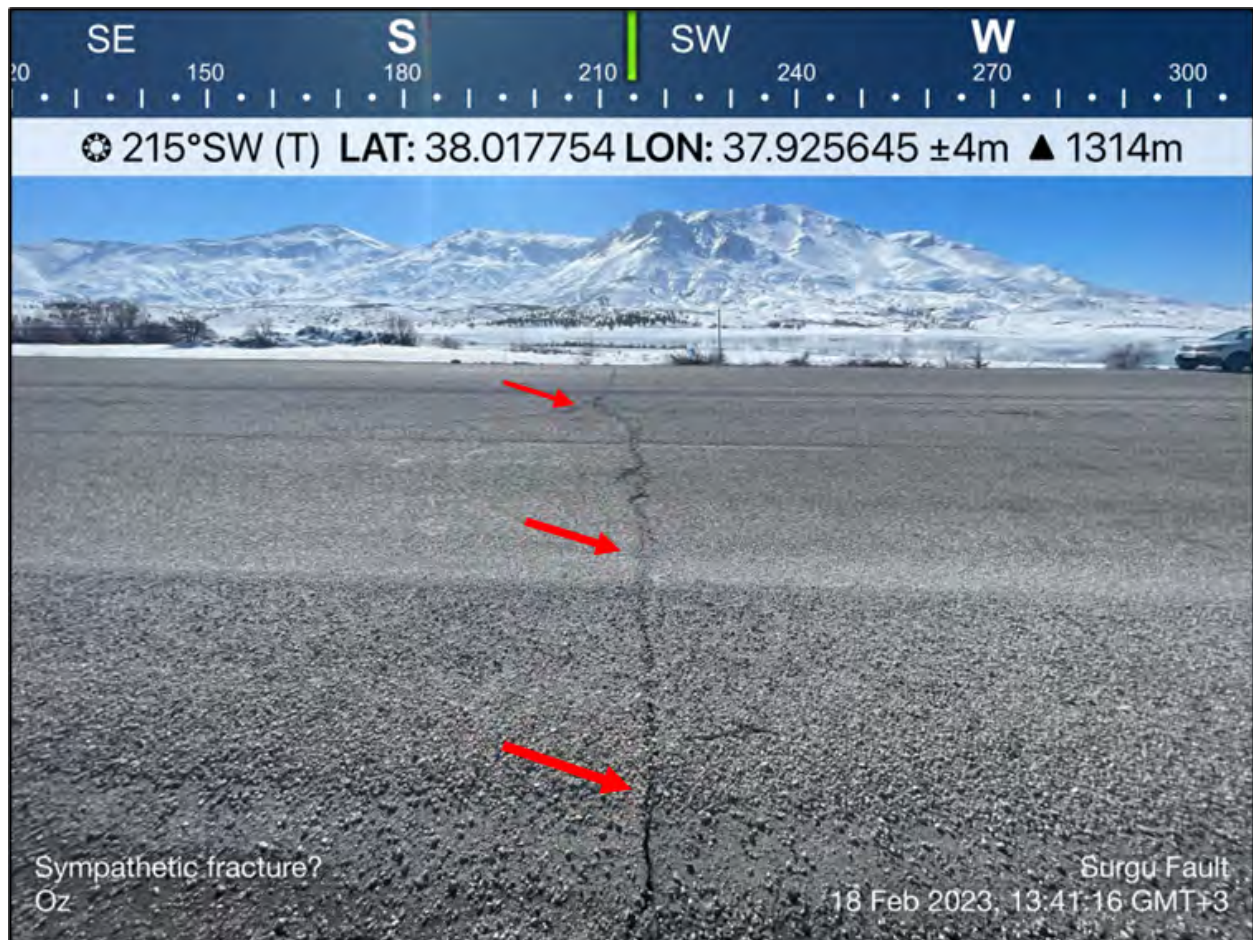


Figure 2.13. Approximately 1.4m left lateral offset stone wall of Balıkburnu Village Elementary School.

**(b) Sürgü-Çardak Earthquake Rupture Termination**

The GEER Advance Team also field checked the eastward extension of the Sürgü-Çardak fault rupture towards the East Anatolian fault rupture and confirmed that the surface rupture along the Sürgü-Çardak fault does not extend eastward and connect with the East Anatolian fault. Only a sympathetic fracture within the road pavement with no displacement was observed at the mapped fault trace of the Sürgü fault (Figure 2.14).



**Figure 2.14.** A sympathetic fracture on the road pavement was observed at the mapped surface trace location of the Sürgü fault; however, no displacement or continuation of the fracture exists.

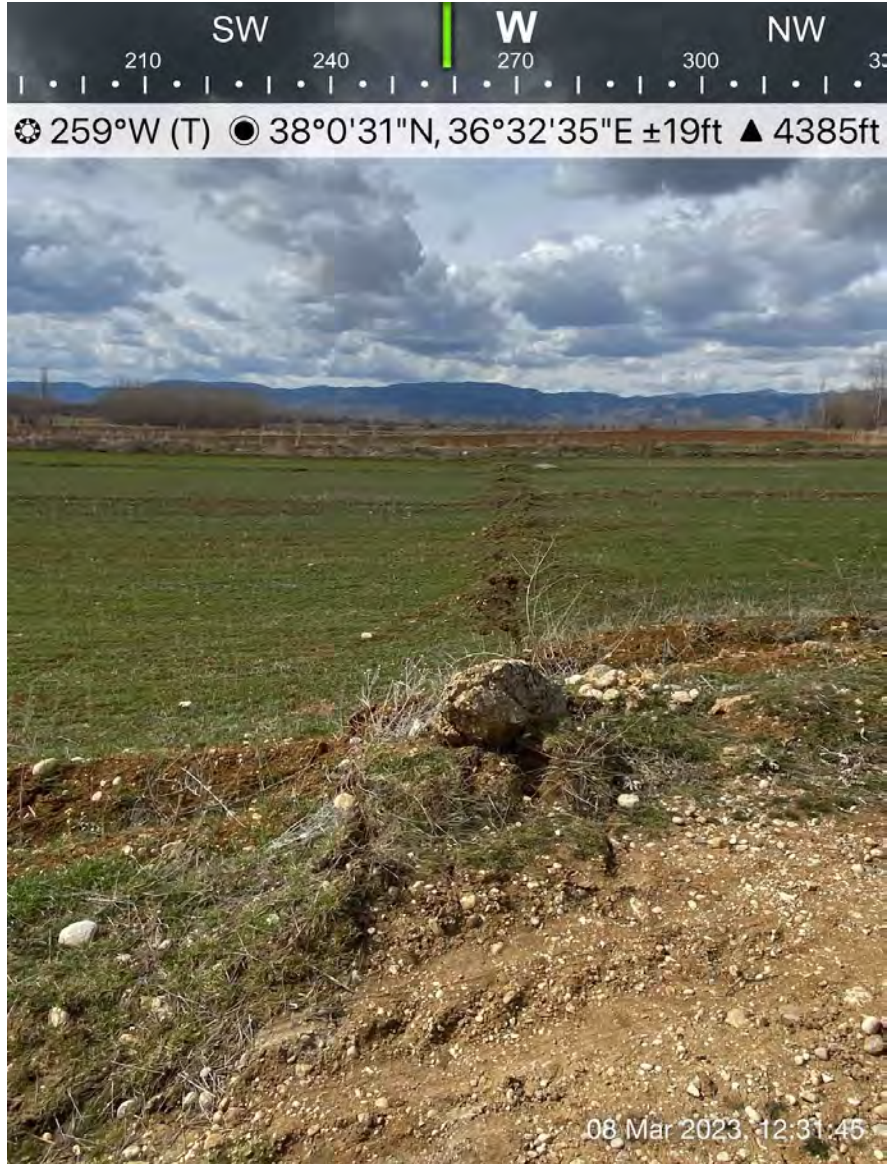
The western extent of surface rupture of the M7.7 Sürgü-Çardak earthquake terminates approximately 2 km immediately south of the town of Göksun. The rupture crosses the main highway (D825) and terminates approximately 300 m west of the highway in a field where it left laterally offsets an above ground aqueduct approximately 15 cm (Figure 2.15). The western termination of the roughly east-west trending Sürgü-Çardak fault manifested as a widening 2 -6 m wide zone of right stepping en-escalon shears approximately 0.5 m long that appeared to “horsetail” at its westernmost point (Figure 2.16).



Within approximately 300 meters of the western termination of the Sürgü-Çardak fault, the fault trace followed a narrow (1-2 m wide), linear path through farm land (Figure 2.17). The fault showed 35 cm of left lateral displacement and approximately 5 to 15 cm of vertical displacement (north side up). As the fault trace heads east, displacement quickly increases to 3 to 4 m left lateral within approximately 13 km of the western termination point (Figure 2.18). The GEER Team A concluded its reconnaissance of the western Sürgü-Çardak fault near the town of Findik.



**Figure 2.15. (LEFT)** The westernmost point of the M7.7 Sürgü-Çardak earthquake south of the town of Goksun. The fault left-laterally offset an above ground aqueduct 15 cm near its termination. **Figure 2.16. (RIGHT)** Right stepping en-escalon fault shears appeared to “horsetail” at its westernmost extent.



**Figures 2.17.** Approximately 300 m east from the western termination of the M7.7 Sürgü-Çardak earthquake, the fault is a narrow, linear feature with 35 cm of left lateral offset and 5 -15 cm of vertical offset (north side up).

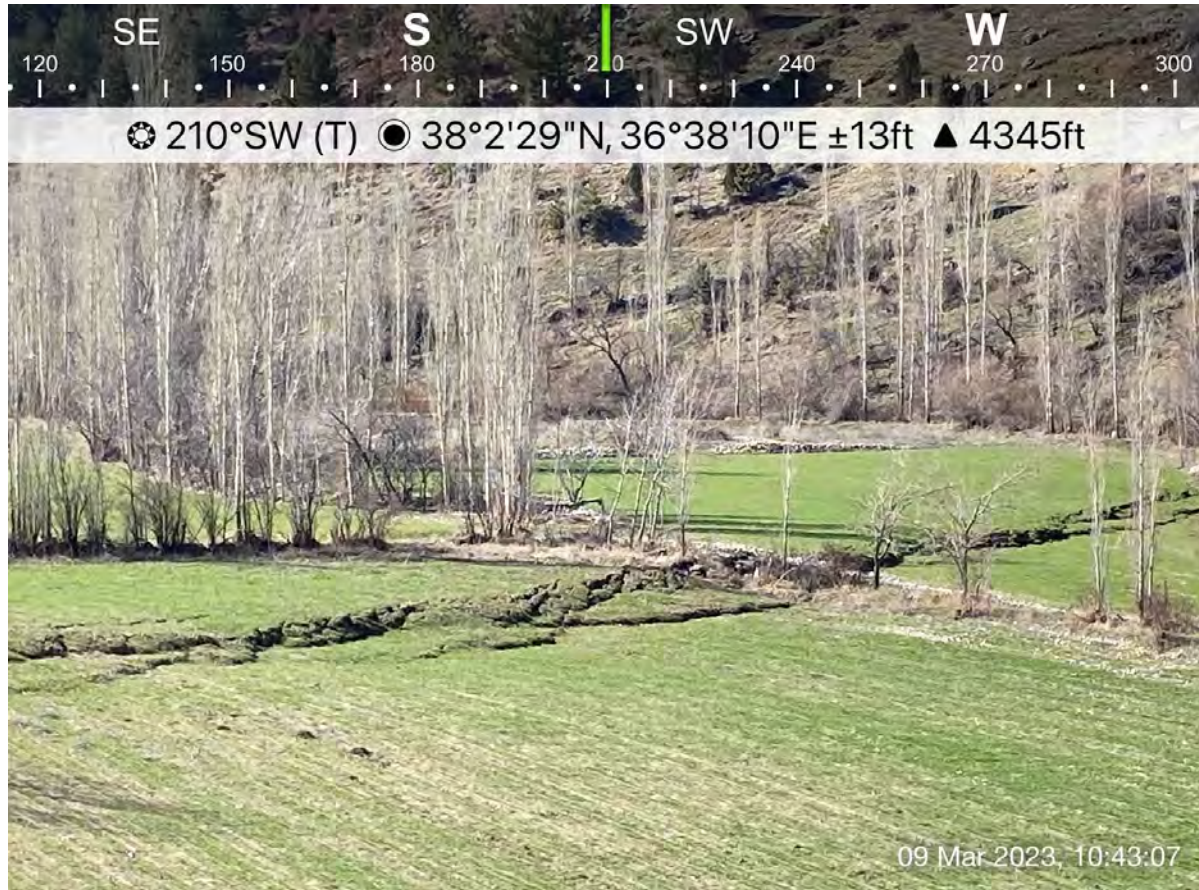


**Figure 2.18.** The Sürgü-Çardak fault displacement quickly increases to over 3 and 4 m within 13 km of the western termination.

### 2.2.2 Narlı fault rupture

The epicenter of the M7.8 earthquake was along the Narlı fault, a relatively short fault subparallel to the East Anatolian fault. Geer Team A investigated the surface rupture along the Narlı fault for a distance of ~10 km from the village of Dedepaşa in the south to the junction of the rupture with the alluvial floodplain of the Aksu River north of the village of Narlı (Figures 2.1 and 2.19). In this area, the rupture is oriented 010-020 and extends along the middle of a broad flat alluvial valley, the Narlı plain. The valley contains several terraces separated by low terrace risers (<2 m), however evidence of prior rupture along the rupture trace was not observed. It is unclear whether this is because the terrace deposits are younger than the last rupture or if tectonic features have been obscured by farming activities that are pervasive in the valley. A discontinuous fault is depicted on the active fault map of Türkiye (Emre et al., 2013) along the eastern margin of the valley, however the range front lacks prominent tectonic geomorphic features and the inferred structure did not rupture in 2023. North of the Aksu River, the rupture projects into mountainous terrain with limited access precluding direct observation of the rupture, however it may extend an additional 12 km to an intersection with the East Anatolian fault east of Kartal. In general, the fault is primarily expressed as right-stepping en echelon

scarps, moletracks, and linear depressions and grabens (Figure 2.20). Left-lateral surface displacements increase from 0.25 cm in the south to >3 m in the north.

North of the village of Dedepaşa, the rupture is characterized by horsetail splays and right-stepping en echelon fractures. Individual overlapping fractures are associated with steps of <3 m. Left-lateral displacements observed across farm roads, drainage canals, and plow lines in the agricultural fields range between 20 and 50 cm and typically have 10-25 cm down-to-the-west vertical scarps.

From about 2 km north of Dedepaşa to the rupture's intersection with Highway D835, the rupture continues in a right-stepping en echelon pattern with intermittent moletracks, however displacements increase. In this area, left-lateral displacements range from 45 to 110 cm and vertical displacements range from 30 to 120 cm down-to-the-west. Individual rupture traces are about 25-30-m-long and separated from adjacent traces by steps of ~2 to 8 m. The total width of the zone of deformation ranges from 3- 6 m. Open fissures along these ruptures are up to 90 cm deep and 20-40 cm wide. In one location the fault bends to an orientation of 315-320 (Lat/Long: 37.347364N, 37.135503E) where it is associated with a vertical scarp of 1.2 m and open fissures 2-m-wide and 2-m-deep.

The main rupture steps right ~200 m (east) where it crosses Highway D835. Here it is associated with a distributed zone (~50-m-wide) characterized by multiple subparallel right-stepping fractures with minimal lateral displacement. Extensive cracking and failure of the western highway road fill prism was observed including cracks along the crest up to 10 meters long, 20 cm deep, and 40 cm wide. At the time of the reconnaissance the highway was actively being repaired.

North of Highway D835 and across agricultural fields east of the city of Narlı the rupture alternates between narrow and wide zones of deformation. Narrow zones are typically 10-25-m-wide and characterized by 25-30-m-long right-stepping en echelon ruptures separated by steps of 4-8 m with occasional steps of >40 m (Figure 2.21). Left-lateral displacements on these ruptures are up to 3 m with down-to-the-west vertical scarps of 0.5-1 m. These narrow zones of deformation are also associated with linear pop-up mounds and small grabens. The dimensions of these features are typically ~50-m-long by 10-m-wide with approximately 2-3 m of left-lateral displacement accommodated across faults bounding their eastern and western sides. Wide zones of deformation include a distributed zone (140-m-wide) of 3 to 4 parallel ruptures that together accommodate ~ 3 m of left-lateral displacement (Lat/Long: 37.391037°N, 37.150103°E) and a large graben approximately 250-m-long by 40-m-wide (Lat/Long: 37.371944N, 37.146389E) (Figure 2.22). The fault that bounds the eastern side of the graben is associated with ~2 m left-lateral displacements of farm ditches and a 1.6-m-high west-facing vertical scarp. The western bounding fault of the graben is associated with 0.7 to 1.2 m of left-lateral displacement and a 0.25-0.5 m east-facing scarp. Both bounding faults exhibit a right-stepping en echelon pattern.

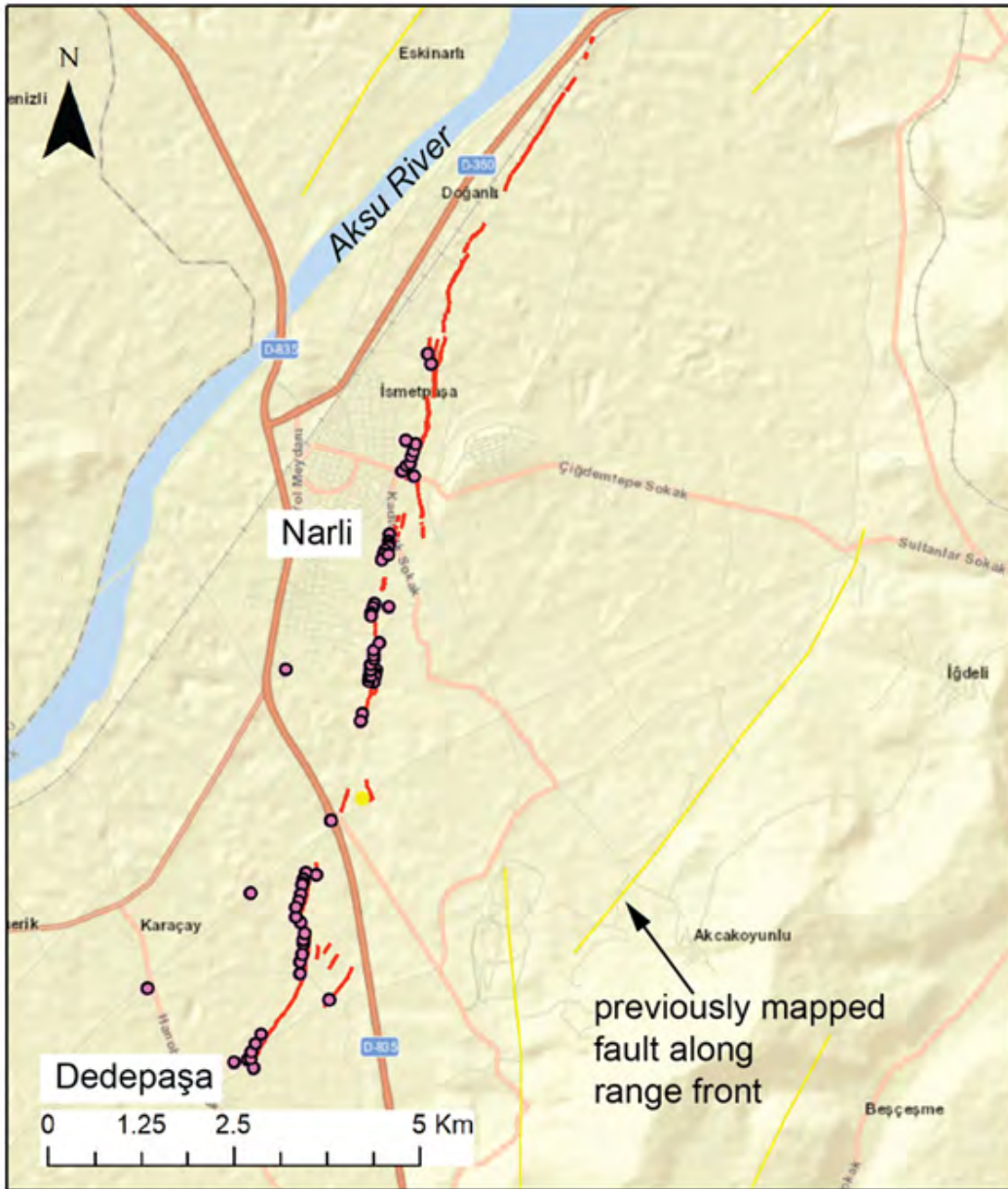


**Figure 2.19.** Map of geological observation points along the Narlı fault in the vicinity of Narlı. Red lines are rupture traces interpreted from post-event imagery (Reitman et al., 2023). Yellow lines are previously mapped faults from the Active Fault Map of Turkey (Emre et al., 2013).

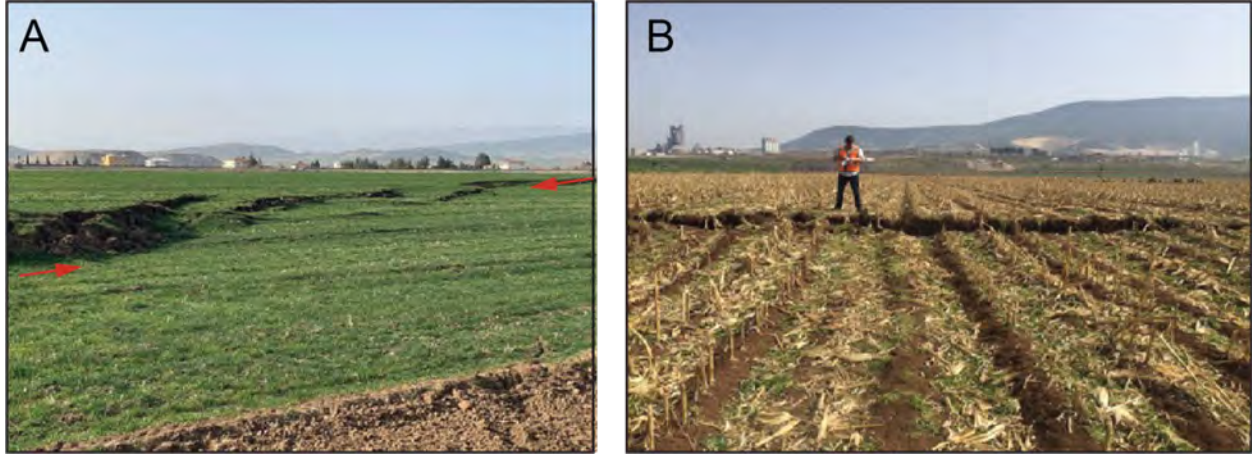


**Figure 2.20.** (A) Right-stepping en echelon rupture, typical geomorphic expression of the rupture across the Narlı plain. Lat/Long: 37.4025°N, 37.152778°E. Photo date: March 1, 2023. (B) Typical offset furrows in onion fields. Lat/Long: 37.343611°N, 37.136944°N. Photo date: February 28, 2023.

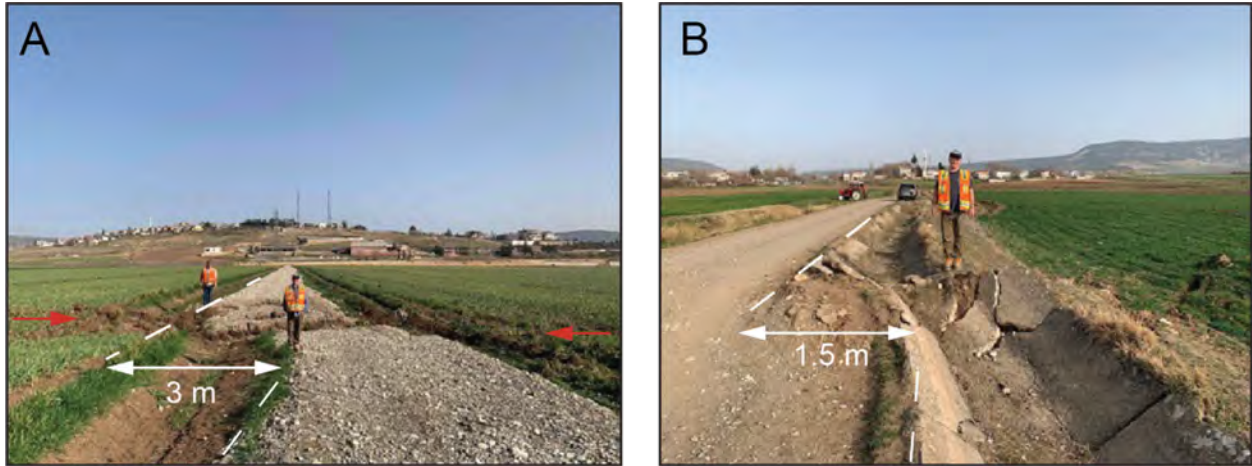


**Figure 2.21.** (A) Left-laterally offset farm road, 3 m lateral and 80 cm vertical. Lat/Long: 37.393917°N, 37.151171°E. Photo date: March 1, 2023. (B) Left-laterally offset road and drainage ditch, 1.5 m. Lat/Long: 37.378527°N, 37.146124°E. Photo date February 28, 2023.

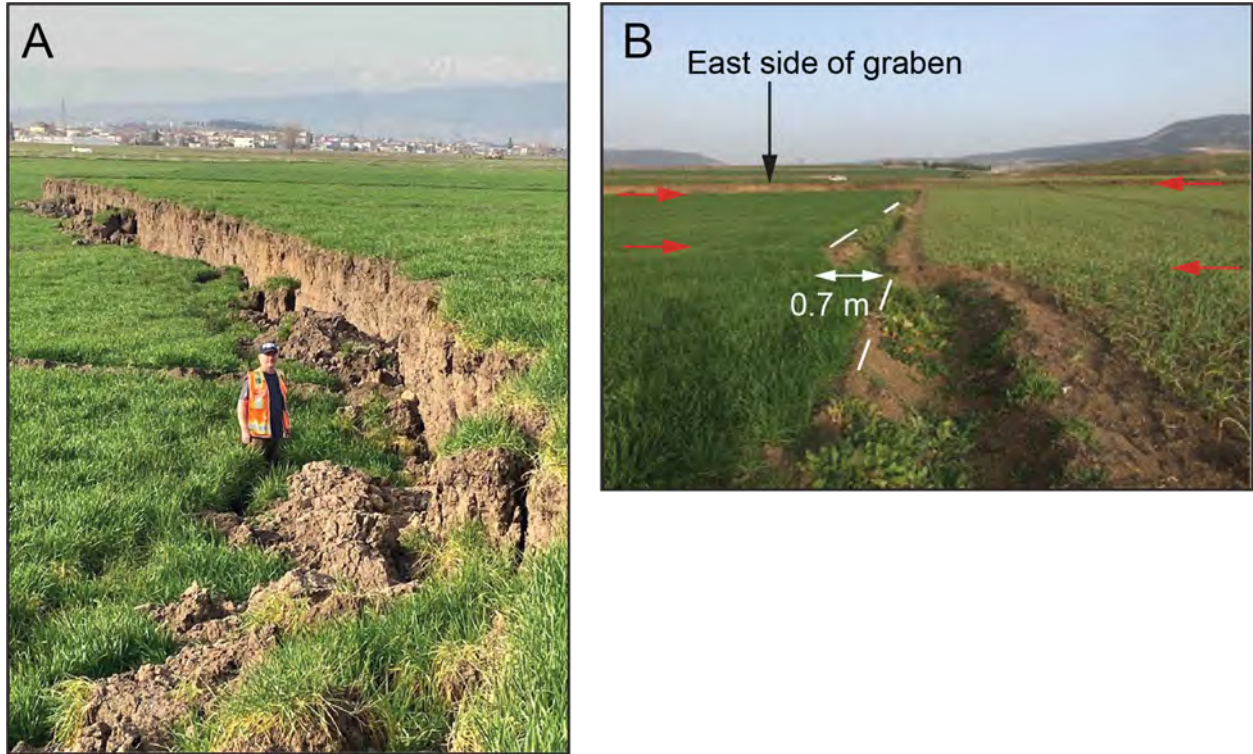


**Figure 2.22.** (A) Vertical Scarp (1.6 m) along the east side of a large graben. Left-lateral offsets of farm ditches perpendicular to the scarp are ~2 m. Fissures adjacent to scarp about 0.5 m deep. Lat/Long: 37.371944°N, 37.146389°E. (B) View to the east across graben showing 0.7 m left-lateral offset across the western bounding fault of the graben. Vertical scarp along east side of graben in (A) in the background. Lat/Long: 37.371944°N, 37.145556°E. Photographs taken February 28, 2023.

### 2.2.3 East Anatolian fault

Along the East Anatolian fault, the distribution of slip and geomorphic expression along the central part of the M7.8 rupture was assessed along two transects including a 25-km-long section between İslahiye and Nurdağı (herein Nurdağı transect) and a ~12 -km-long section from Highway D835, through the village of Çiğli to the vicinity of the village of Kartal (Herein Çiğli transect) (Figures 2.23 and 2.24). The rupture was also observed near the villages of Balkar and Ozan. In general, the rupture extends along typical tectonic geomorphic landforms in relatively narrow zones, however in some locations it is expressed across bedrock hillslopes and shutter ridges in broadly distributed zones. Observed left-lateral displacements range from 2.5 to 4.4 m, however considering parallel splays and distributed deformation the total displacement along the central part of the rupture may approach 6 m.

Within the Nurdağı transect, between İslahiye and Nurdağı the East Anatolian fault extends along the eastern margin of the Amanos Mountains and is expressed as a prominent range front oriented 020-030 associated with large shutter ridges (Figure 2.23). North of İslahiye, the

rupture occurred along two subparallel overlapping faults separated by about 1 km. The eastern trace extends across flat alluvial deposits and is associated with 1.5 m left-lateral displacement and west-facing scarps 25-50-cm-high. The western trace is associated with 1.3-1.8 m left-lateral displacements and 80-cm-high east-facing scarps. Tectonic geomorphic features along the western trace include right-stepping scarps and sag ponds. The combined lateral displacement across the two traces is ~3.3 m. To the north the western trace projects along the range front to the village of Fevzipaşa where it is expressed as parallel breaks distributed across the lower 20 m of the slope.

Within the village of Fevzipaşa, the rupture is distributed across a bedrock shutter ridge and characterized by multiple parallel breaks. Nearly every structure on the ridge was destroyed, consistent with focused ground motions and ridgetop shattering. North of the ridge, the rupture converges onto a trace associated with 3.9 m of left-lateral displacement that extends along the lower bedrock slope of the range front. In the village of Kozdere, right-stepping en echelon ruptures with left-lateral displacements up to 2 m project along the western side of a bedrock shutter ridge (Figure 2.25). North of the ridge, the rupture is distributed across a 100-m-wide zone and projects into a long linear valley within bedrock that extends into the mountain front. Limited road access precluded direct observation of the rupture in this area, however the valley is clearly expressed on DEMs and GoogleEarth imagery and is the most likely location of the rupture west of the village of Karaburçlu (Figure 2.23). From here, the rupture steps or bends approximately 700 m to the range front where it is expressed as at least two parallel rupture traces. In the village of Gökçedere, two traces separated by about 60 m extend within bedrock along the range front and each are associated with about 1.1 to 1.4 m of left-lateral displacement (Figure 2.26).

Within alluvial fans adjacent to the range front west of Nurdağı, the rupture is characterized by moletrack ruptures up to 10-m-wide and right-stepping en echelon fractures up to 1-m-deep. Left-lateral displacements along these ruptures observed across fence lines, roads, and sidewalks range from 2.5 to 3 m (Figure 2.27). To the north, the rupture extends along the western side of a large shutter ridge within a linear valley in the Nurdağı suburb of Kurudere. Here the rupture is confined to a relatively narrow zone and is associated with right-stepping en echelon breaks, moletracks, left-lateral displacements of 3.1 m, and west-facing 0.5 m vertical scarps. Fissures along this zone are up to 1-m-wide and 0.75-m-deep (Figure 2.28).

Ruptures along the Çiğli transect northeast of Highway D835 extend 065 across a broad alluvial valley, through the village of Çiğli, and project northeast into the mountains towards the village of Kartal (Figure 2.24). Northeast of the crossing with Highway D835, the rupture extends along the northwest side of a linear pressure ridge consistent with long term tectonic displacement. Here it displaces farm roads and concrete drainage ditches left-laterally 3.9 m and up to 60 cm up-to-the-southeast (Figure 2.29). The rupture is expressed as right-stepping 2 to 6 m wide moletracks up to 1-m-high. At Çiğli village, the moletrack scarps buckle paver roads and directly intersect houses and lateral offsets were difficult to ascertain. In one location in the center of the village, the rupture extends along a linear headwater valley where it is associated with a 1 m uphill-facing scarp and a stream channel offset of 3.4 m (Figure 2.30a). At the eastern end of



the village, the rupture is expressed as a 16-m-wide graben bound by 70-cm-high vertical scarps that together accommodate about 2 m of left-lateral displacement. East of Çiğli, the rupture steps ~100 m to the southeast where it is expressed in a broadly distributed zone consisting of a series of right-stepping en echelon ridges and subparallel linear drainages (Figure 2.30b). Surface scarps extend at an orientation of 060 along the southwestern side of each ridge and bend to 030 wrapping into narrow drainages between the ridges. Left-lateral displacements here are up to 2.5 m and vertical scarps range between 0.05 to 1.5 m. The total width of the zone of stepping ridges is about 500 m. To the northeast, several long linear valleys extend towards the village of Kartal, however mountainous terrain and limited road access prevented direct observation of the rupture there.

Directly south of the village of Kartal, the fault extends across a wind gap drainage divide separating two linear river valleys. West of the divide, the rupture consists of a 25-30 m wide zone of two parallel traces associated with 1.5-2-m-high north-facing scarps. The two traces converge forming a 4-m-wide moletrack that displaces planted olive tree rows left-laterally 4.4 m (Figure 2.31). Within bedrock terrain in the headwaters of the valley the rupture forms a large uphill-facing fault plane scarp in bedrock that is about 2 m high (Figure 2.31). East of the divide, the rupture extends along alluvial fill terraces and a low linear ridge along the north margin of the linear river valley (Figure 2.32). Here, the rupture consists of several traces distributed across a 20-m-wide zone. The ruptures are associated with 0.5-1-m-high north- and south-facing scarps. Left-laterally offset fence lines, rock walls, and agricultural field margins indicate that the total displacement across the zone is 2.6 to 3.5 m.

Southwest of Gölbaşı near the village of Balkar, the rupture extends along the southeastern side of several prominent linear pressure ridges (Figure 2.33). Several low gradient antecedent alluvial fans spread from southeast to northwest through wind gaps in the pressure ridges indicating long term tectonic activity. In this area, the rupture is characterized by 4-m-wide moletracks and right-stepping fissures distributed across a zone of deformation ~10-m-wide. Fissures are typically 1.5-m-deep, 2-3-m-wide, and 10-m-long. Left-lateral offsets of rock walls, farm roads, and fence lines range from 2.2 to 3.8 m. Vertical scarps up to 1.2 m face both southeast and northwest, but are consistently up on the northwest along the margins of the pressure ridges consistent with long term uplift. Minor parallel ruptures associated with <50 cm of left-lateral displacement horsetail up the southeastern slopes of the pressure ridges.

Northeast of Gölbaşı, the rupture occurred on two major subparallel traces. Clear continuous surface rupture was identified on post-event WorldView imagery for a distance of 5 km along the 055 oriented northern trace and 7.5 km along the 075 oriented southern trace (Reitman et al., 2023). These traces bound the Gölbaşı basin, a pull apart basin that contains a large lake, Gölbaşı Gölü. The northern trace projects along the linear northwestern margin of the lake, crosses highway D360 near the village of Ozan, and continues to the northeast along a prominent linear valley. The rupture was observed in a field southwest of the highway crossing where it is characterized by a subtle 1-2 m-wide, 20-30-cm high moletrack associated with offset drainage channels and planted tree rows with 1.9 m of left-lateral displacement (Lat/Long: 37.817859N, 37.680148E). A clear scarp observed in pre-event imagery indicates

prior rupture on this part of the fault. The southern trace projects through the central part of the city of Gölbaşı (contributing to the intense damage there) and extends to the northeast within a long linear valley. This trace was not investigated during the reconnaissance, however satellite displacement data suggest left-lateral displacement of <2 m (Reitman et al., 2023). Thus, the combined displacement across both traces suggests a total displacement of ~4 m for this part of the rupture distributed across a width of ~2.5 km.

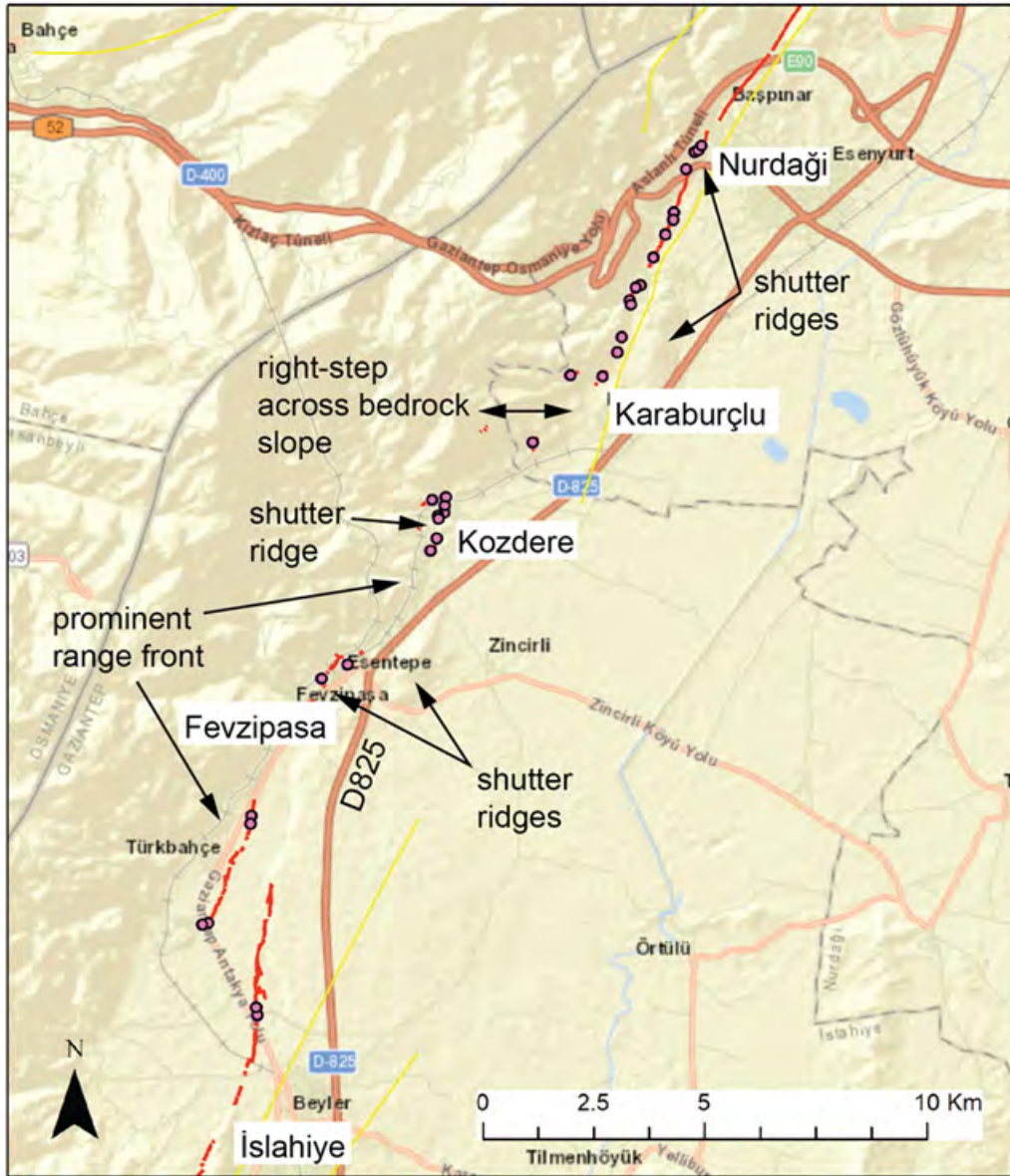


**Figure 2.23.** Map of geological observation points along the East Anatolian fault between the cities of İslahiye and Nurdağı. Red lines are rupture traces interpreted from post-event imagery (Reitman et al., 2023). Yellow lines are previously mapped faults from the Active Fault Map of Türkiye (Emre et al., 2013).

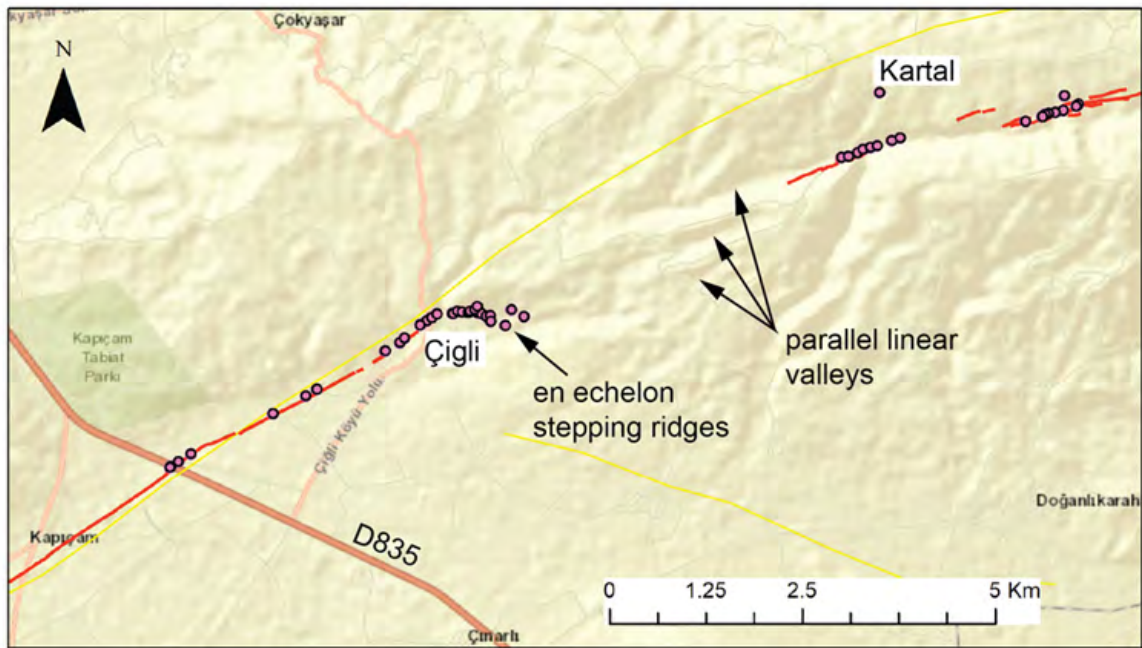


**Figure 2.24.** Map of geological observation points along the East Anatolian fault near the villages of Çiğli and Kartal. Red lines are rupture traces interpreted from post-event imagery (Reitman et al., 2023). Yellow lines are previously mapped faults from the Active Fault Map of Türkiye (Emre et al., 2013).

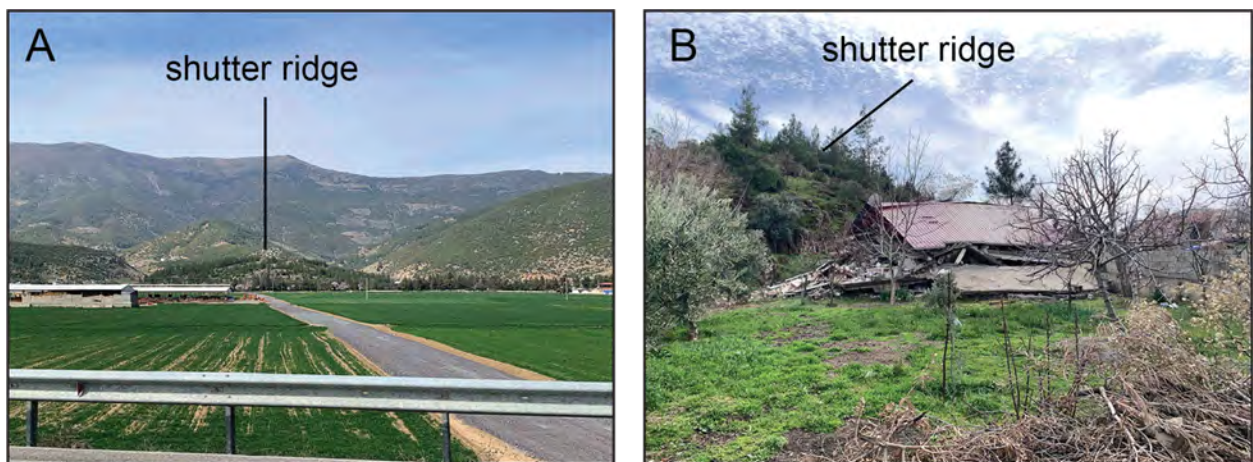


**Figure 2.25.** Classic rangefront morphology including shutter ridges and faceted spurs in the village of Kozdere. Rupture extends along the rangefront on the right and behind the shutter ridge in the center of the photograph. Lat/Long: 37.120278°N, 36.676111°E. (B) Collapsed house on the south side of the shutter ridge in (A). Lat/Long: 37.127222°N, 36.666667°E. Photographs taken March 5, 2023.



**Figure 2.26.** Distributed rupture along bedrock hillside south of Gökçedere. Lat/Long: 37.164314°N, 36.706504°E. Photograph date March 5, 2023.



**Figure 2.27.** Photographs of offsets west of Nurdağı. (A) 3 m displacement of road and sidewalk. Lat/Log: 37.176332°N, 36.714138°E. (B) 2.8 m displacement of gravel road. Lat/Long: 37.172828°N, 36.712396°E.



**Figure 2.28.** Photographs of the rupture west of the city of Nurdağı. (A) Rupture extending along western side of shutter ridge (east of range front). Left lateral offset of paver road and fence line, 2.8 m. Lat/Long: 37.186944°N, 36.719444°E. (B) Left-lateral offset of paver road, 3 m. Lat/Long: 37.186366°N, 36.719098°E. Photographs taken March 5, 2023.

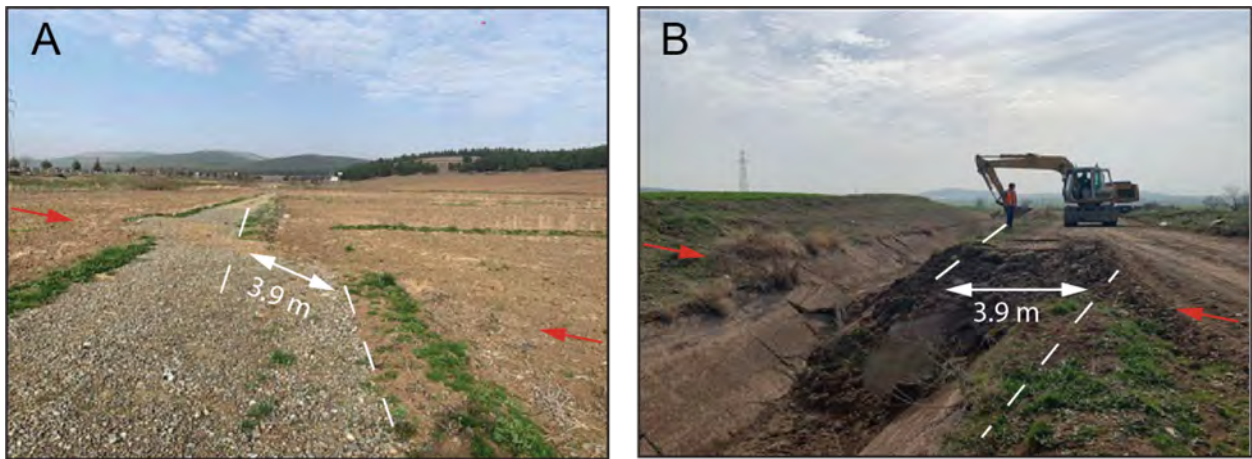


**Figure 2.29.** Photographs of rupture east of Highway D835 and west of the village of Çiğli. (A) Left-laterally offset gravel farm road, 3.9 m. Lat/Long: 37.480278°N, 37.043056°E. (B) Left-laterally offset drainage ditch, 3.9 m. Vertical displacement 60 cm up to the south. Backhoe present at the time of observation was beginning repairs. Lat/Long: 37.484722°N, 37.053889°E. Photographs taken March 2, 2023.

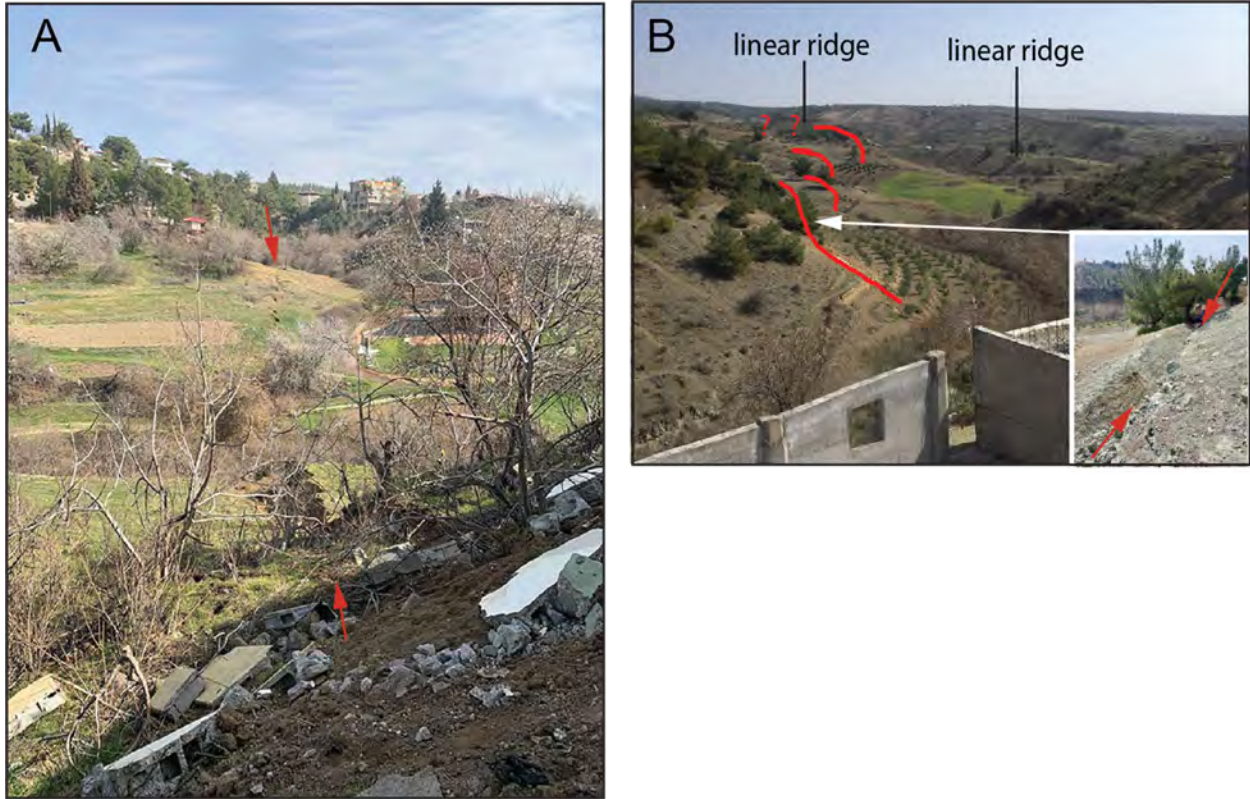


**Figure 2.30.** Photographs of the rupture in the village of Çiğli. (A) Uphill-facing fault scarp and moletrack within Çiğlivillage. Lat/Long: 37.491389°N, 37.069167°E. (B) Right-stepping scarps and ridges along the eastern side of Çiğlivillage. Lat/Long: 37.493889°N, 37.073333°E. Inset shows uphill-facing fault scarp and fault plane exposed across hillside. Lat/Long: 37.494167°N, 37.075556°E. Photographs taken March 2, 2023.

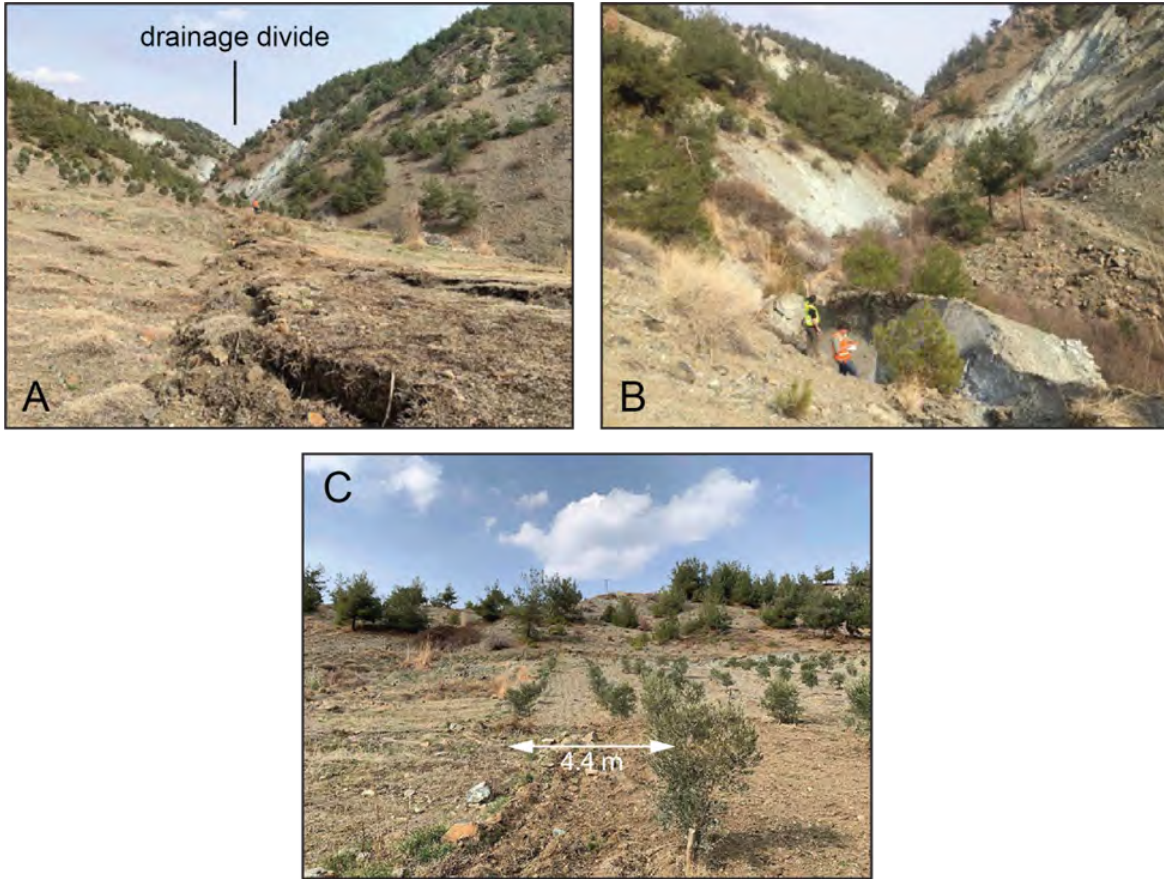


**Figure 2.31.** Photographs of rupture south of Kartal. (A) Moletrack rupture (4-m-wide, 1.5-m-high) projecting towards drainage divide. Lat/Long: 37.509167°N, 37.123056°E. (B) Uphill-facing fault scarp exposing fault plane (oriented 070, 58N). Lat/Long: 37.509722°N, 37.124167°E. (C) Left-laterally offset olive tree rows, 4.4 m. Lat/Long: 37.509167°N, 37.123611°E. Photographs taken March 2, 2023.

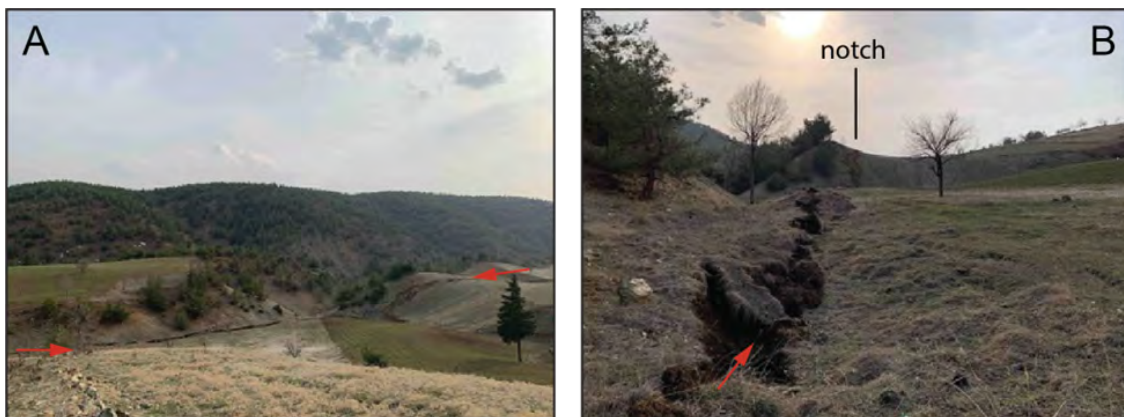


**Figure 2.32.** Photographs of rupture extending across fluvial terraces within the drainage divide of a long linear valley east of Kartal. (A) View to the south. Lat/Long: 37.514167°N, 37.146111°E. (B) View to the west. Moletrack rupture projects across topographic notch in the background. Lat/Long: 37.512778°N, 37.146389°E. Photographs taken March 2, 2023.

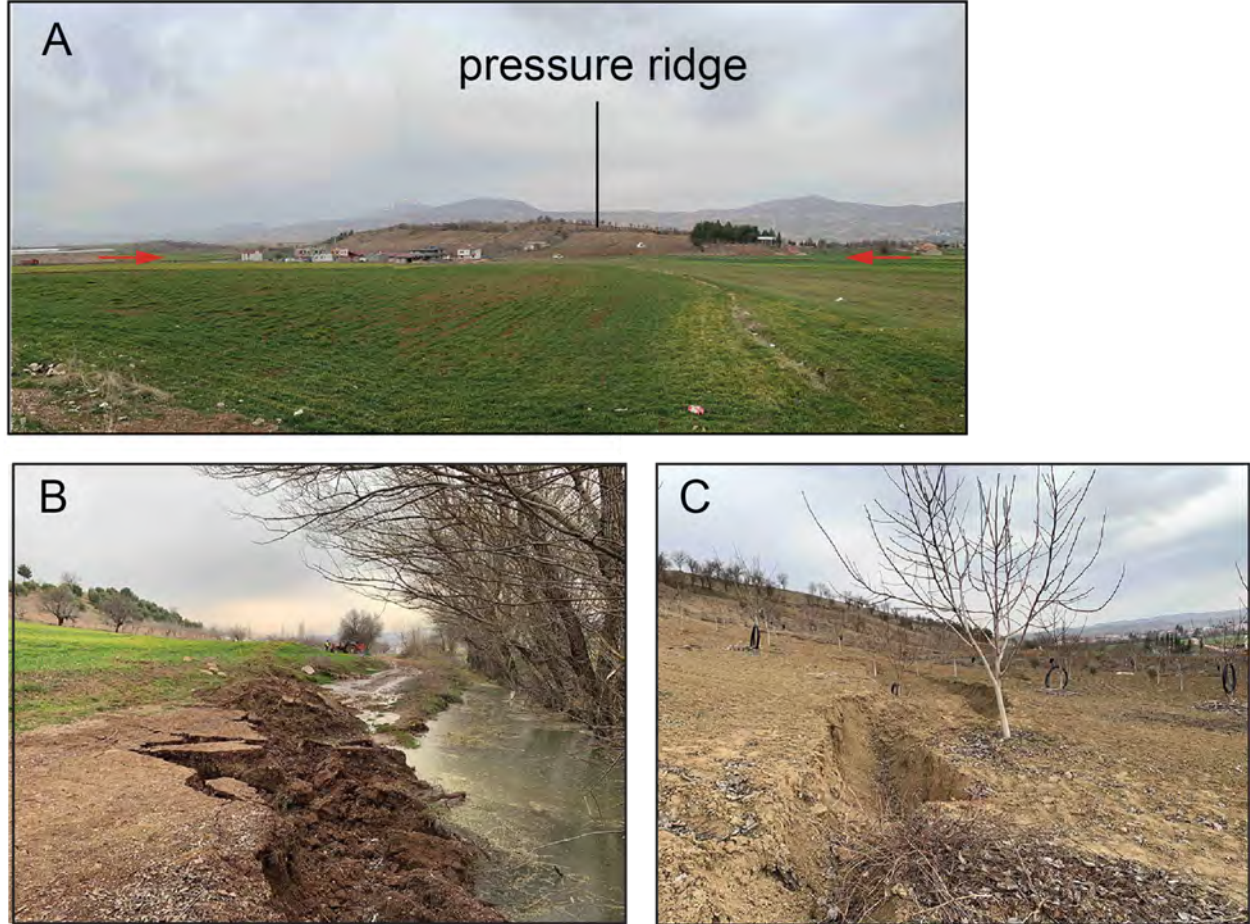


**Figure 2.33.** (A) Northeast trending pressure ridge in the middle of a large alluvial valley west of Balkar. Photo taken from Highway at Lat/Long: 37.725989°N, 37.559038°E. (B) Moletrack rupture projecting towards southeast side of pressure ridge associated with ponded water and up-to-northwest displacement of ~1 m. Lat/Long: 37.726389°N, 37.55°E. (C) Right-stepping fissures approximately 1.5 m deep and 10 m long extending along southeast side of pressure ridge. Tire tracks across rupture left-laterally offset 2.8 m. Lat/Long: 37.7275°N, 37.553333°E. Photographs taken March 3, 2023.

#### 2.2.4 Sürgü-Çardak fault

Geologic observations on fault displacements and tectonic geomorphology were collected along the M7.5 Elbistan rupture (Çardak-Sürgü fault) along a 26-km-long transect between the village of Çiftlikkale and Nurhak (Figure 2.34). In this area, the fault is oriented 100° and extends across rugged mountainous terrain. It is expressed by aligned linear valleys, saddles, and sidehill scarps in bedrock, triangular faceted range fronts, and moletrack scarps that extend across alluvial fans. The fault trace is also associated with several large right steps of >200 m. The largest observed displacements of the 2023 earthquake sequence occurred along this fault and



were relatively consistent across the section investigated ranging between ~6-8 meters. Long-term progressive displacement is evident from mountain front stream channels that are left-laterally displaced on the order of 100-200 m.

West of the village of Çiftlikale, the rupture extends obliquely across a Holocene terrace along a small stream where it is characterized by a 4 to 5-m-wide moletrack ranging in height from 0.5 to 2 m. Along the north bank of the stream a concrete wall is left-laterally displaced 7.8 m across a narrow rupture trace associated with a 60 cm up-to-the-north scarp (Figure 2.35). East of the wall, the rupture projects along the southern side of a linear bedrock ridge as a 0.25-0.5-m-high south-facing scarp. Where this scarp crosses an erosion gully the rupture forms an uphill-facing bedrock scarp that exposes the fault plane (Figure 2.35). The fault plane is oriented 092 and dips 65°N. Although clear piercing lines were not present, the wall of the gully is left-laterally displaced ~7 m. Farther to the east, the rupture projects into the mountains along a long linear valley. A massive landslide headscarp extends along the crest of the mountain that bounds the north side of the valley and movement of the slide is inferred to be related to strong ground shaking (Figure 2.36).

Directly west of the village of Gözpinar, the fault makes a >200 m right step from an intermountain linear valley to the mountain front (Figure 2.37a). Although the fault is primarily in bedrock here it is clearly expressed along the mountain front by left-deflected streams, aligned saddles, and faceted spurs. Across one saddle the rupture forms a large 8-m-wide, 2-3-m-deep graben and displaces a dirt power line road left-laterally 8.6 m (Figure 2.37b). Several power poles were destroyed during the earthquake and these were actively being repaired during the reconnaissance. East of this graben, the rupture extends along a short linear swale into a stream channel where it is expressed as a 1-2-m-high north-facing scarp (Figure 2.37c). The west wall of the channel is offset ~60 m and the cumulative left deflection of the channel is ~200 m indicating progressive deformation. Across the next saddle to the east, the rupture is expressed as a graben and a 35-m-wide zone of right-stepping breaks (Figure 2.38a). A bedrock offset along the western side of this saddle exposes the fault plane and is associated with 8.2 m of left-lateral displacement (Figure 2.38b). Where the rupture extends along steep faceted bedrock slopes in this section it is typically expressed as several parallel traces that anastomose, right-step, and splay upslope.

About 1 km east of Gözpinar the fault projects out of the mountains and parallels the range front for ~4.7 km to Barış. In this section, the rupture extends across relatively young (Holocene?) alluvial fans that show little evidence of previous rupture. Within the village of Değirmenkaya, the zone of deformation is at least 50-m-wide and associated with right-stepping en echelon moletracks up to 1.6-m-high. Left-lateral displacements here are up to 8 m and typically partitioned across several splays. East of the village, the rupture continues with similar expression and the width of deformation ranges from ~3 to 80 m. In wider zones the deformation is typically partitioned across several overlapping traces. The rupture exhibits both north- and south-facing scarps and moletracks up to 1.5-m-high and left-lateral displacements of rock walls and fence lines range from 5.4 to 7.3 m (Figure 2.39). A road at the western edge of Barış is left-laterally displaced 7.9 m across a 2-m-high south-facing scarp. Within Barış, the

rupture extends along the north side of a house that was relatively undamaged. A concrete wall in the backyard was displaced  $\sim 6.5$  m (Figure 2.40).

From Barış, the rupture continues east along the range front and maintains consistent displacements of 6 to  $>7$  m across young (Holocene?) alluvial fans. About 3 km east of Barış, a rock wall at the edge of an agricultural field is displaced 7.3 m left-laterally across a narrowly confined moletrack that is 2-m-wide and 0.75-m-high (Figure 2.41a). East of this site, the rupture extends across a series of progressively older deeply incised alluvial fans (late Pleistocene to possibly middle Pleistocene in age). Tonal lineaments, springs, and scarps observed on pre-event GoogleEarth imagery align with the rupture and provide evidence of paleo ruptures across these fans. This area may represent a site for future geochronologic and paleoseismic studies aimed at constraining a geologic slip rate and earthquake recurrence. Farther east, the rupture projects into a linear bedrock inter mountain valley. The lack of road access prevented inspection of the rupture there, however it is inferred to extend approximately 2-3 km north of Nurhak (Figure 2.41b).

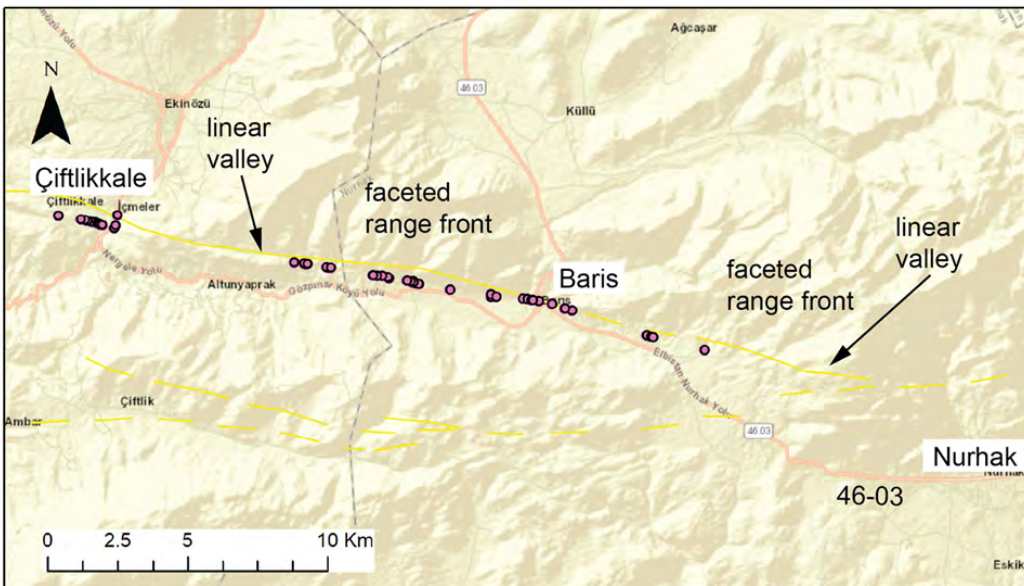


**Figure 2.34.** Map of geological observation points along the Çardak-Sürgü fault between Çiftlikkale and Nurhak. Yellow lines are previously mapped faults from the Active Fault Map of Turkey (Emre et al., 2013).



**Figure 2.35.** Photographs of rupture near the village of Çiftlikkale. (A) Left-laterally offset concrete wall along stream margin (7.8 m) and lidar scan of the feature. Lat/Long: 38.030556°N, 37.166111°E. (B) Uphill-facing scarp and fault plane extending along the south side of linear bedrock ridge. Lat/Long: 38.029722°N, 37.168611°E. Photographs taken March 3, 2023.



**Figure 2.36.** Photograph of rupture extending along linear valley south of Çiftlikkale. Uphill-facing bedrock scarp (fault plane) shown in Figure 2.35 is in the middle of photograph. A large landslide headscarp extends across the entire hillside east of town and slope movement is inferred to have occurred during the earthquake. Lat/Long: 38.029444°N, 37.161944°E. Photograph date March 3, 2023.

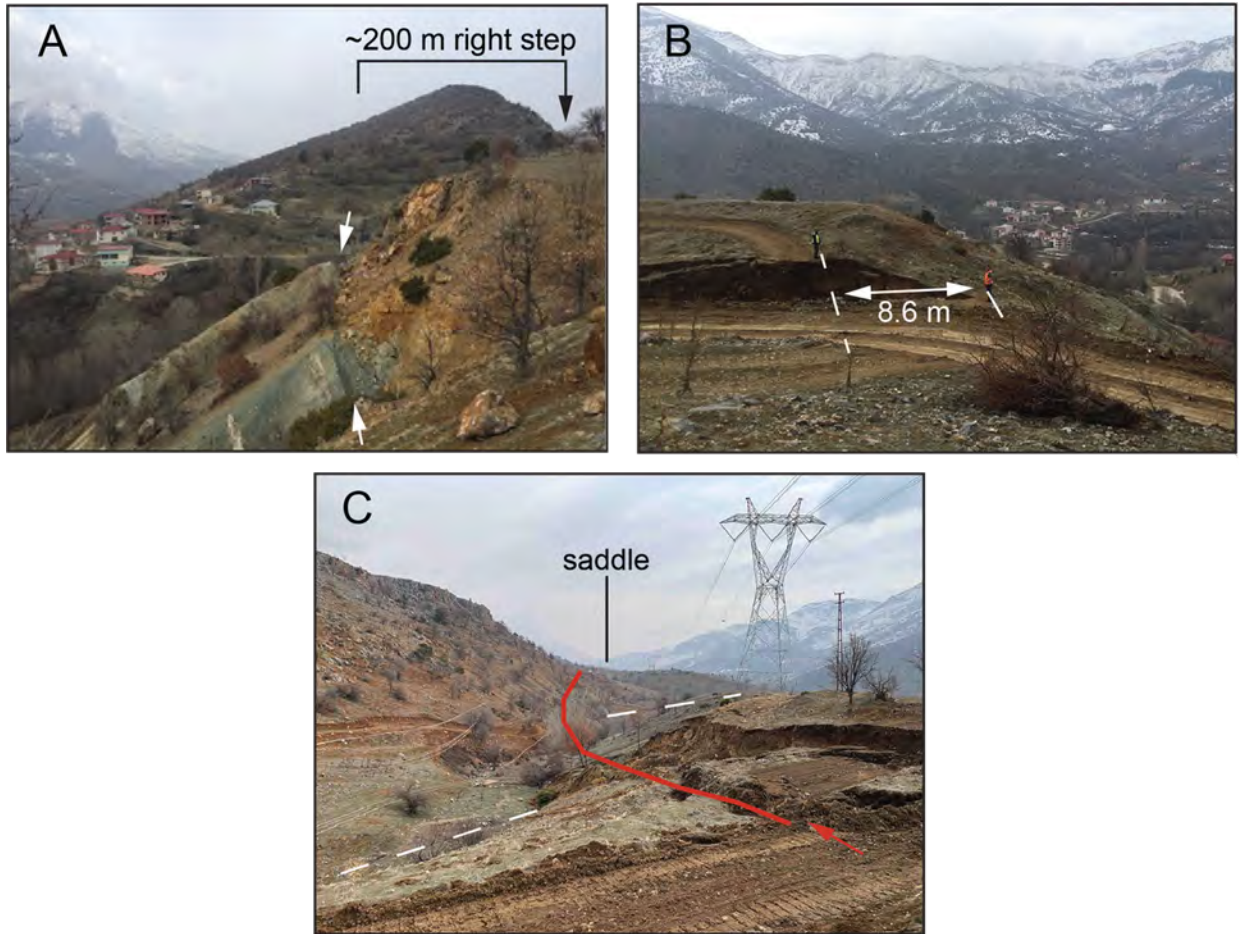


**Figure 2.37.** Photographs of the rupture extending across saddle and hillside near the village of Gözpınar. (A) Graben extending across saddle associated with 8.6 m left-lateral rupture of dirt road. Lat/Long: 38.02°N, 37.233333°E. (B) Uphill-facing scarp in bedrock. Large right-steps are common in the mountainous terrain in this area. Lat/Long: 38.020278°N, 37.233333°E. (C) Long-term offset of channel (thalweg approximated by white dashed line) and side-hill scarp that projects across saddle to the east. Lat/Long: 38.02°N, 37.234722°E. Photographs taken March 4, 2023.

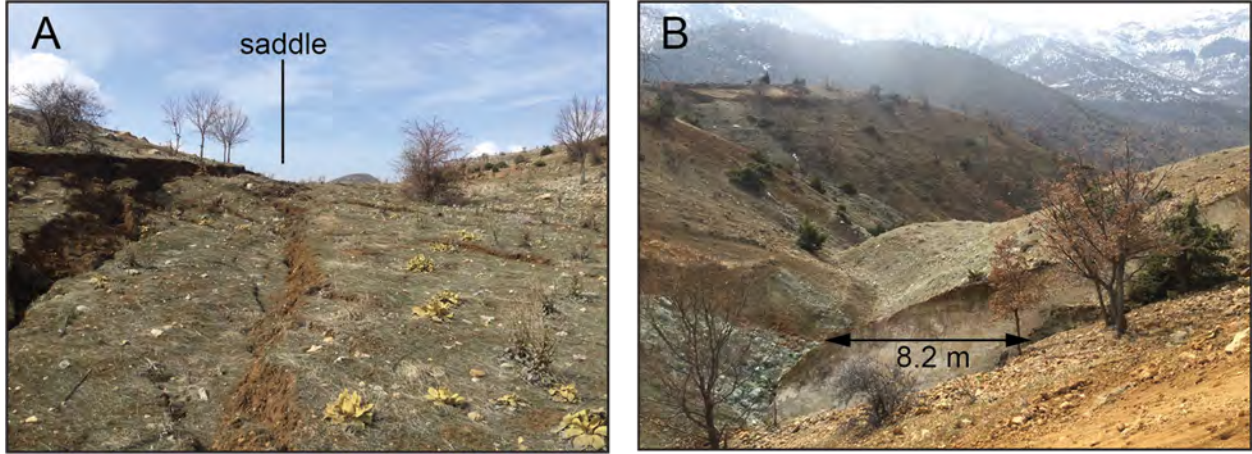


**Figure 2.38.** (A) Graben cutting across saddle (Lat/Long: 38.019130°N, 37.241423°E) and (B) bedrock scarp associated with 8.2 m of left-lateral displacement (Lat/Long: 38.019241°N, 37.240900°E) near the village of Gözpinar. Photographs taken on March 4, 2023.

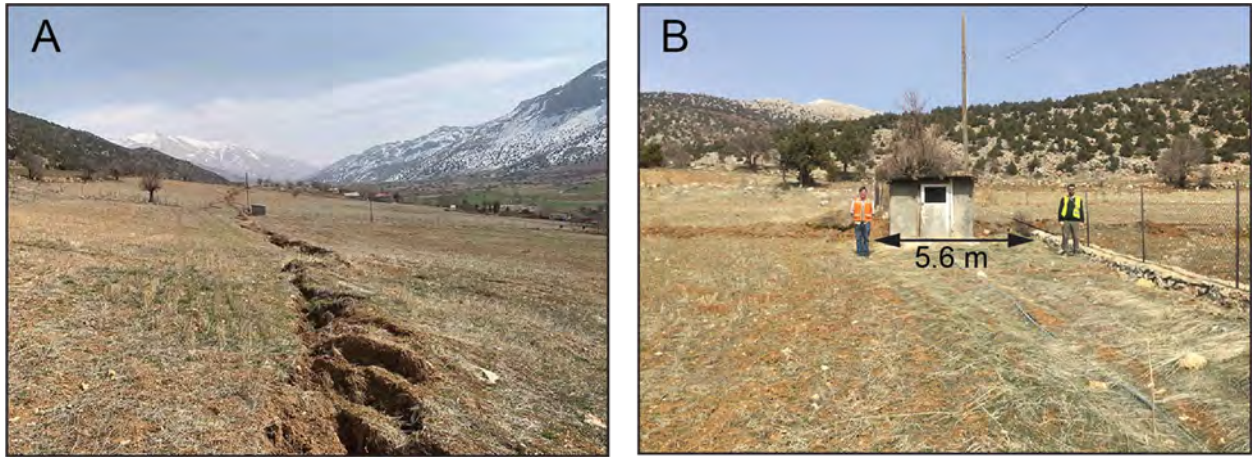


**Figure 2.39.** Photographs of the rupture extending across an alluvial fan west of Barış. (A) Right-stepping en echelon mole track scarp, zone of deformation relatively narrow ~5-m-wide. Lat/Long: 38.015556°N, 37.269444°E. (B) Left-laterally offset concrete wall and fence line, 5.6 m. Lat/Long: 38.014722°N, 37.270278°E. Photographs taken March 3, 2023.



**Figure 2.40.** Photographs of rupture in the village of Barış. (A) Rupture extending along the north side of a house that was relatively undamaged. Lat/Long: 38.010833°N, 37.306944°E. (B) Left-laterally offset concrete wall (6.5 m) in the backyard of the house in (A). Lat/Long: 38.010556°N, 37.3075°E. Photographs taken March 4, 2023.

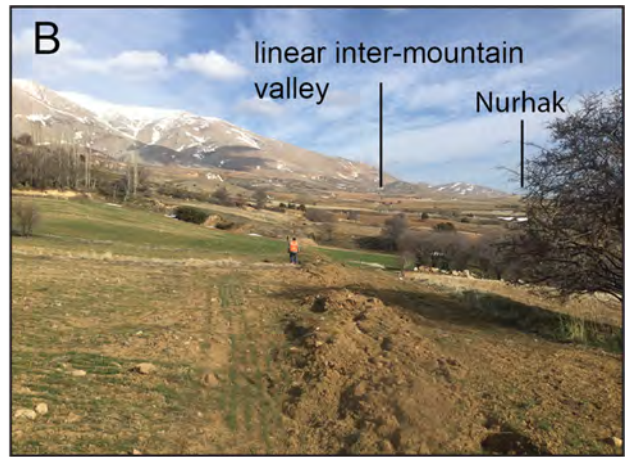


**Figure 2.41.** Photographs of the rupture approximately 3 km east of Barış. (A) 7.3 m left lateral displacement of rock wall along agricultural field margin. (B) View to the east from (A) showing the projection of the rupture into a linear bedrock valley. For both photographs, Lat/Long: 38.001971°N, 37.343925°E. Photographs taken March 4, 2023.

### **2.2.5 Summary of Geologic Setting and Fault Rupture**

The mapping results provide information that helps better understand the locations of fault rupture with implications for improving surface fault rupture hazard assessments important for infrastructure design. Although most ruptures followed tectonic geomorphic features that most likely would have been recognized in pre-rupture mapping, some locations would have been difficult to predict.

Both ruptures are characterized by classic strike-slip geomorphology (right-stepping en echelon scarps, moletracks, linear depressions, shutter and pressure ridges, linear swales, saddles, and side-hill benches). Less common rupture locations include breaks across the tops of shutter ridges and bedrock slopes, and through complex arrays of en echelon pressure ridges.

Structural geometric complexities and historic ~M7 earthquakes have previously been used to define segments along the East Anatolian fault. The 2023 M7.8 earthquake ruptured across three segments and two major releasing bends. Thus, the rupture segments are not persistent in time.

The mapping observations provide field validation of the location of ruptures and the distribution of slip estimated by remotely sensed methods, as well as highlight challenges in assessing surface fault rupture hazards.



## 3.0 Ground Motions

*Tristan E. Buckreis, Baran Güryuva, Abdullah İçen, Oğuz Okçu, Abdullah Altındal, Mehmet Fırat Aydın, Renmin Pretell, Abdullah Sandikkaya, Özkan Kale, Aysegul Askan, Scott J. Brandenburg, Tadahiro Kishida, Sinan Akkar, Önder Cetin, Yousef Bozorgnia, Jonathan P. Stewart*

The 2023 Türkiye/Syria earthquake sequence occurred in a region that was known to have major active faults and which had been instrumented north of the Türkiye-Syria border. As a result, the events were well recorded both near the fault and at distances up to 575 km. This chapter describes available recordings as of the present date (April 2023); manual, component-specific data processing that was performed to optimize usable bandwidth; metadata compilation according to uniform protocols; data comparisons to a global ground motion model (GMM) for active tectonic regions and a local, Türkiye-specific model; and analyses of spatial variability of three ground motion intensity measures (peak acceleration, peak velocity, and 5%-damped pseudo-spectral acceleration for a 1.0 sec oscillator period), which are useful for ground motion estimation at sites without recordings.

Several previous ground motion compilations have been presented since the 6 February 2023 mainshock (Baltzopoulos et al. 2023; Garini and Gazeta 2023; Gülerce et al. 2023; Kale et al. 2023). The work presented in this chapter clearly has some overlap in intent, but there are differences in the scope including the use of recently-released data from the AFAD network that corrects errors from earlier releases, the application of PEER/NGA protocols for data processing and metadata compilation, and the presentation of data for three events that were of primary interest to reconnaissance teams (6/2/2023 **M7.8** mainshock, 6/2/2023 **M7.8** aftershock, and 20/2/2023 **M6.3** aftershock). Moreover, the data compiled in the present work is published to a doi for public use by the EERI and GEER reconnaissance teams, researchers engaged in Next Generation Attenuation projects, and other interested researchers. The doi for data distribution follows: <https://doi.org/10.17603/ds2-t115-bk16> (Buckreis et al. 2023).

### 3.1 Ground Motion Networks

Networks that produced recorded ground motions are mainly located in Türkiye, Syria, and Lebanon. Table 3.1 summarizes the networks and the numbers of recordings that have been retrieved as of this writing for the **M7.8** mainshock and the **M7.7** and **M6.3** aftershocks. Records from the **M6.3** event were considered in this data compilation due to media reports of some structural collapses during the aftershock.

The Disaster and Emergency Management Authority (AFAD) in Türkiye operates the

[Turkish National Strong Motion Network \(TNSMN\)](#) and the [Turkish National Seismic Network \(TNSN\)](#). The TNSMN is a strong motion network, consisting mainly of accelerometers, while the TNSN are mainly broadband seismometers. TNSMN and TNSN stations are mainly distinct in terms of instrument locations, although some are co-located. These networks produced the majority of recordings from the earthquake sequence, including all of the near-fault records. The principal additional network is the Kandilli Observatory and Earthquake Research Institute, which operate stations mainly in northern parts of Türkiye.

**Table 3.1.** Networks that recorded Türkiye-Syria earthquake sequence

<b>Network</b>	<b># Stations in Network</b>	<b># Recs M 7.8</b>	<b># Recs M 7.7</b>	<b># Recs M 6.3</b>
Turkish National Strong Motion Network	817	285	320	148
Turkish National Seismic Network	267	3	6	55
Kandilli Observatory and Earthquake Research Institute <sup>1</sup>	243	21	21	18
Cyprus Broadband Seismological Network	13	2	4	7
GEOFON Program, GFZ Potsdam, Germany <sup>2</sup>	121	0	0	2
International Miscellaneous Stations	322	0	0	2
Global Seismograph Network	92	0	0	1
Syrian National Seismic Network <sup>3</sup>	27	–	–	–
Lebanon National Centre for Geophysical Research <sup>4</sup>	12	–	–	–

<sup>1</sup> Cambaz et al. (2019)

<sup>2</sup> <https://geofon.gfz-potsdam.de/>

<sup>3</sup> Dakkat et al. (2005)

<sup>4</sup> National Centre for Geophysical Research (2019)

The networks operating in Syria and Lebanon are indicated in Table 3.1. We have been in contact with personnel operating those networks via colleague Salah Sadek at the American

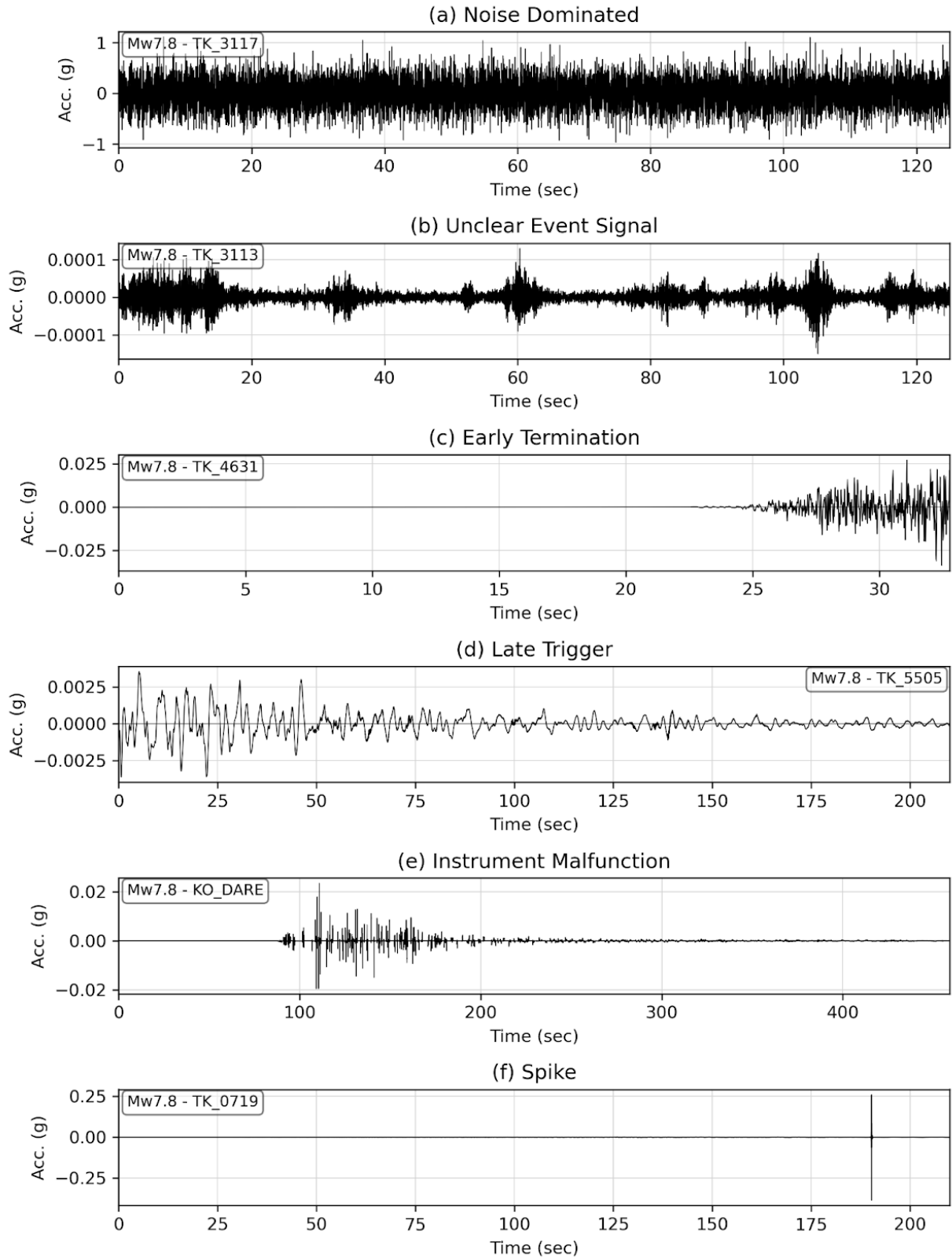
University of Beirut. Both networks report having recordings from these events but the data has not been released and we are unaware of a specific time table for doing so. The Syria stations would be relatively near-source for the **M7.8** mainshock and **M6.3** aftershock, whereas the Lebanon stations would occur at distances on the order of 160 - 365 km. Our current understanding is that the instruments within these networks are mainly seismometers (recordings of velocity).

### **3.2 Data Review and Processing**

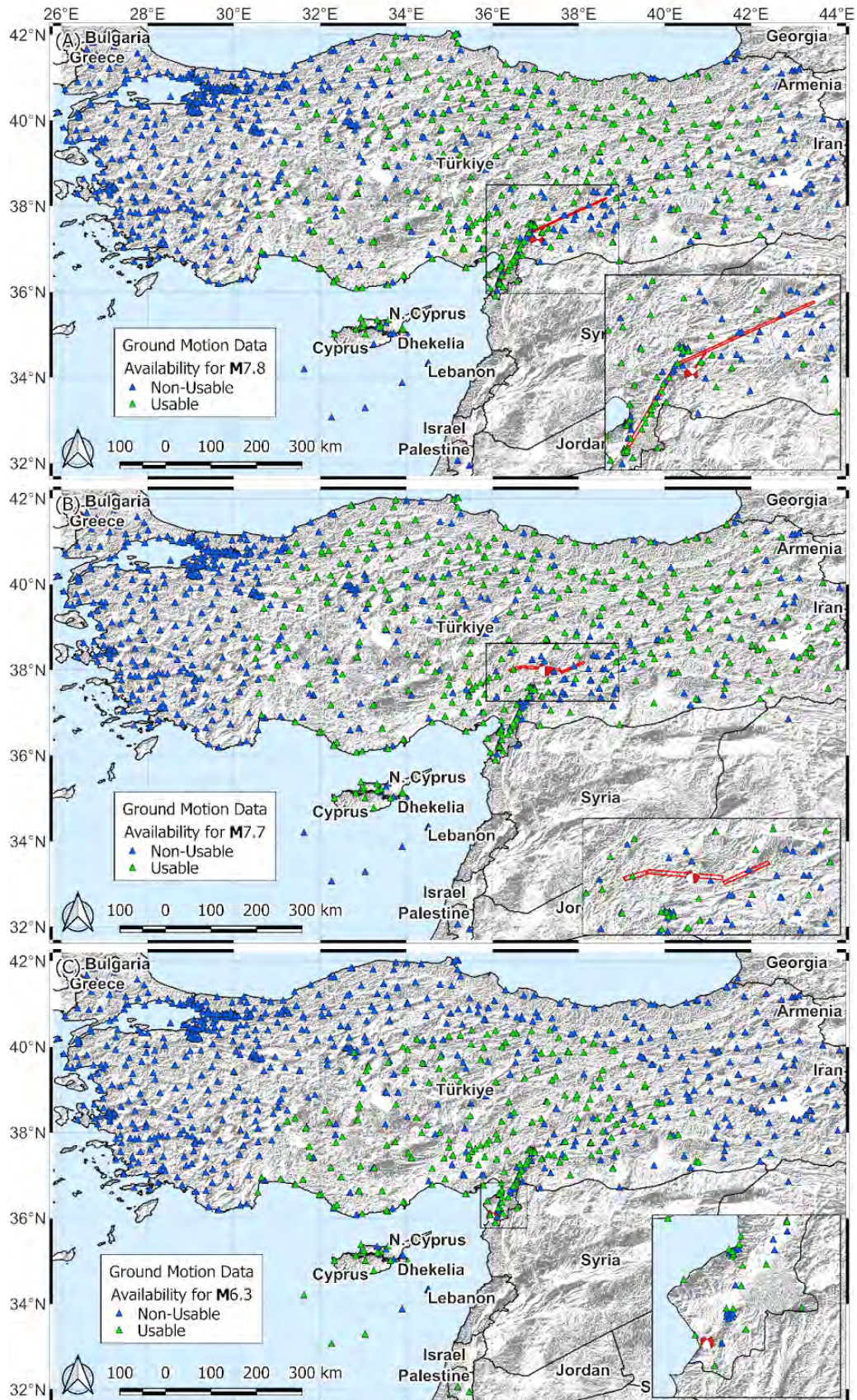
Raw (unprocessed) waveforms for each event of interest were obtained from the Earthquake Data Center System of Türkiye (TDVMS; <https://tdvms.afad.gov.tr/>) and the Incorporated Research Institutions for Seismology (IRIS). Data were initially screened to remove duplicate records. The current dataset was downloaded in late March, to obtain unprocessed and baseline-uncorrected records not previously available. An initial visual review was performed to identify and remove records with non-usable data, which include noise-dominated, unclear event signal, early termination, late trigger, instrument malfunction, and spike records (Figure 3.1).

Figure 3.2 presents maps of all seismic stations in the region distinguished (in terms of the mapped symbols) between those with usable and non-usable data for the three events of interest. Many of the recordings from the **M7.8** event exhibited early termination (Figure 3.1c), likely a result of power failure during the strong shaking. Most seismometers (instrument code “H”) were unable to record the strong shaking during the **M7.8** and **M7.7** events (Figure 3.1e), so recordings for these events are mostly from accelerometers (instrument code “N”) and seismometers at far distances (> 100 km). Unfortunately, there were no usable recordings near Gölbaşı, Şekeroba, and Çelikhan and few near İskenderun and Kahramanmaraş for the **M7.8** and **M7.7** events. Few usable records were obtained in the source region (near Antakya) for the **M6.3** aftershock. At the time of writing, a total of 311, 351, and 233 usable records at stations as far as 575 km, 536 km, and 500 km were identified for the **M7.8**, **M7.7**, and **M6.3** events, respectively.

Near-fault rupture waveforms for the **M7.8** event were unique in that they sometimes included multiple wave packets, as shown in Figure 3.3. We did not attempt to separate these waveforms, and chose to use the entire ground motion time series during processing and intensity measure computations.



**Figure 3.1.** Example time-series for non-usable records: (a) noise-dominated, (b) unclear event signal, (c) early termination, (d) late trigger, (e) instrument malfunction, and (f) spike.



**Figure 3.2.** Maps of locations of seismic stations colors indicate usable (green) and non-usable (gray) data for (a) **M7.8**, (b) **M7.7**, and (c) **M6.3** events.

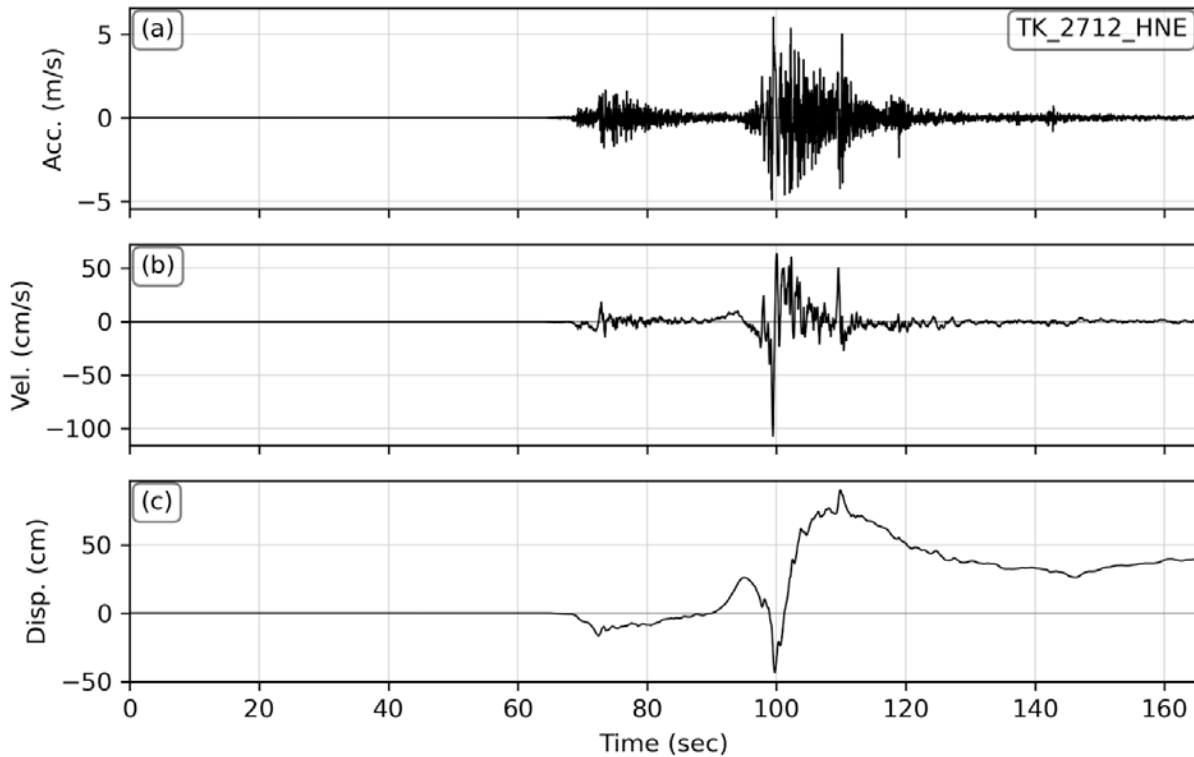


**Figure 3.3.** Example unprocessed time-series for east component of station TK 2712 from the **M7.8** mainshock illustrating multiple wave packets; (a) acceleration, (b) velocity, and (c) displacement.

Each of the three-component records were processed individually according to standard protocols developed during the Pacific Earthquake Engineering Research center (PEER) Next Generation Attenuation (NGA) projects (e.g., Goulet et al. 2021). The procedure consists of applying a baseline correction and high- (and sometimes low-) pass Butterworth filters in the frequency domain. Corner frequencies are selected by visual inspection of the Fourier amplitude spectra (FAS), ratio of the signal-to-noise FAS (SNR), and reasonableness of the displacement time-series. The lowest high-pass corner frequency which satisfies a minimum SNR threshold and produces a reasonable displacement time-series is selected.

This procedure removes any static displacement that might otherwise be present in near-field records, which is the case for many records from the **M7.8** and **M7.7** events. Processing that includes preservation of the fling has been started by the authors and other investigators, but is not maturely developed enough for presentation in this report and will be addressed in later publications. When using standard processing that does not allow for permanent displacement with records for which such displacements are present, unique challenges arise in the selection of high-pass corner frequencies,  $f_{c,HP}$ . The difficulty is well illustrated by the TK 4615 (north component) record in Figure 3.4, where the different panels show acceleration, velocity and

displacement. This station is located about 2 km from the **M7.8** rupture. In each panel, time series are shown for the unprocessed record, and the record subjected to a relatively modest high-pass filter ( $f_{c,HP}=0.016$  Hz) that preserves much of the low-frequency energy and a more aggressive high-pass filter ( $f_{c,HP}=0.053$  Hz). These filter corners were selected considering different objectives: (1) the relatively modest filter ( $f_{c,HP}=0.016$  Hz) aimed to preserve the velocity pulse between 68 and 75 sec, which is associated with the downward (negative displacement) fling step; (2) the more aggressive filter ( $f_{c,HP}=0.053$  Hz) aimed to remove long-period displacement wobble that occurs when the pulse features are preserved. An alternative way to remove the long-period features would be to fit a velocity pulse function and subtract it from the recording (Shahi and Baker 2014), which was not applied in the present work.

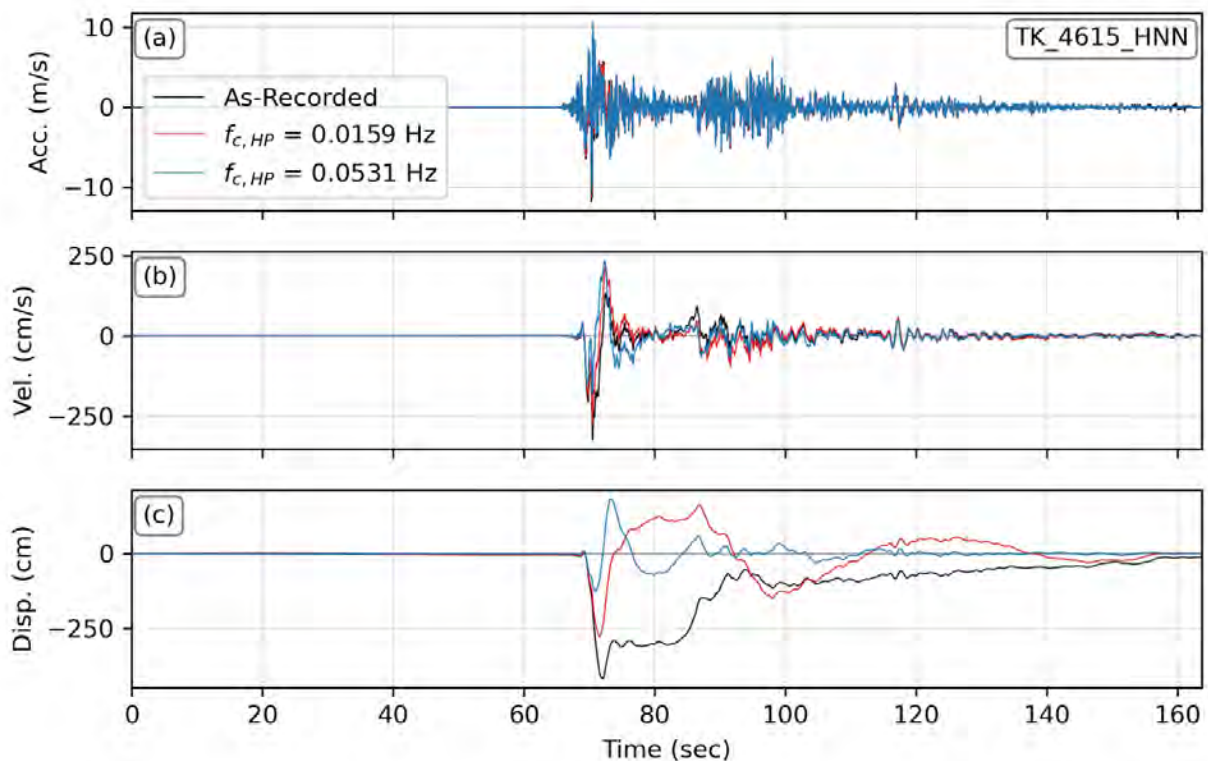


**Figure 3.4.** Example time-series plots illustrating sensitivity of high-pass corner selection during signal processing for north component of station TK 4615 corresponding to the **M7.8** mainshock: (a) acceleration, (b) velocity, and (c) displacement. Unprocessed shown by black curve,  $f_{c,HP} = 0.0159$  Hz shown in red, and  $f_{c,HP} = 0.0531$  Hz shown in blue.

As illustrated in Figure 3.4, there are different objectives that guide the selection of  $f_{c,HP}$  in the present context. The first approach has the advantage of preserving an important component of the ground motion (velocity pulse) but the disadvantage of artificial displacement wobble, while the second approach removes these features. It is not possible to preserve the velocity pulse

and obtain reasonable displacements. These considerations affect 44, 11, and 10 ground motions from the **M 7.8** mainshock, and the **M7.7** and **6.3** aftershocks, respectively, based on visual assessments during record processing. When processing near-field records, we chose to prioritize preservation of the velocity pulse over the reasonableness of the displacements.

The longest usable period of the ground motion is defined as  $T < 1/(1.25f_{c,HP})$ , where  $f_{c,HP}$  is the greater of the two horizontal high-pass corner frequencies selected during signal processing for combined horizontal components (e.g., RotD50 as given by Boore 2010). Figure 3.5 presents the number of usable combined horizontal components as a function of oscillator period for the three events of interest. The **M6.3** event has a more rapid rate of decay of number of usable records with period for  $T > 5$  sec than the **M7.8** and **M7.7** events, which likely results from the reduced long period energy from this smaller magnitude event. The reduced long-period energy increases the likelihood that records will be noise-dominated at these long periods.

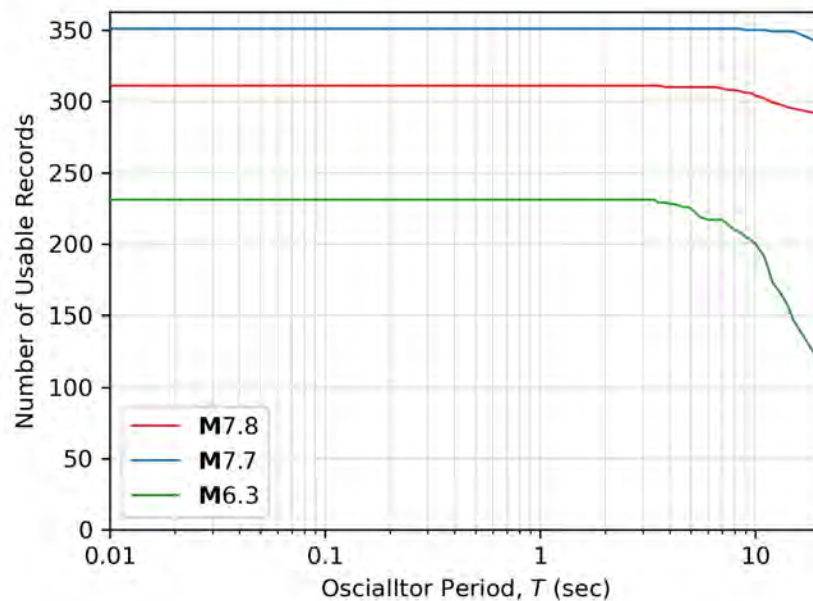


**Figure 3.5.** Number of usable records vs period for the **M7.8**, **M7.7**, and **M6.3** events. Longest usable period defined as  $1/(1.25f_{c,HP})$ , where  $f_{c,HP}$  is the maximum of the two horizontal components.

Figure 3.6 presents plots of the spatial distribution of RotD50 PGA for the three events of interest. Locations of stations without usable records are also shown in gray. Tables in the aforementioned doi present the selected  $f_{c,HP}$  and RotD50 PGA and PGV for all usable records.



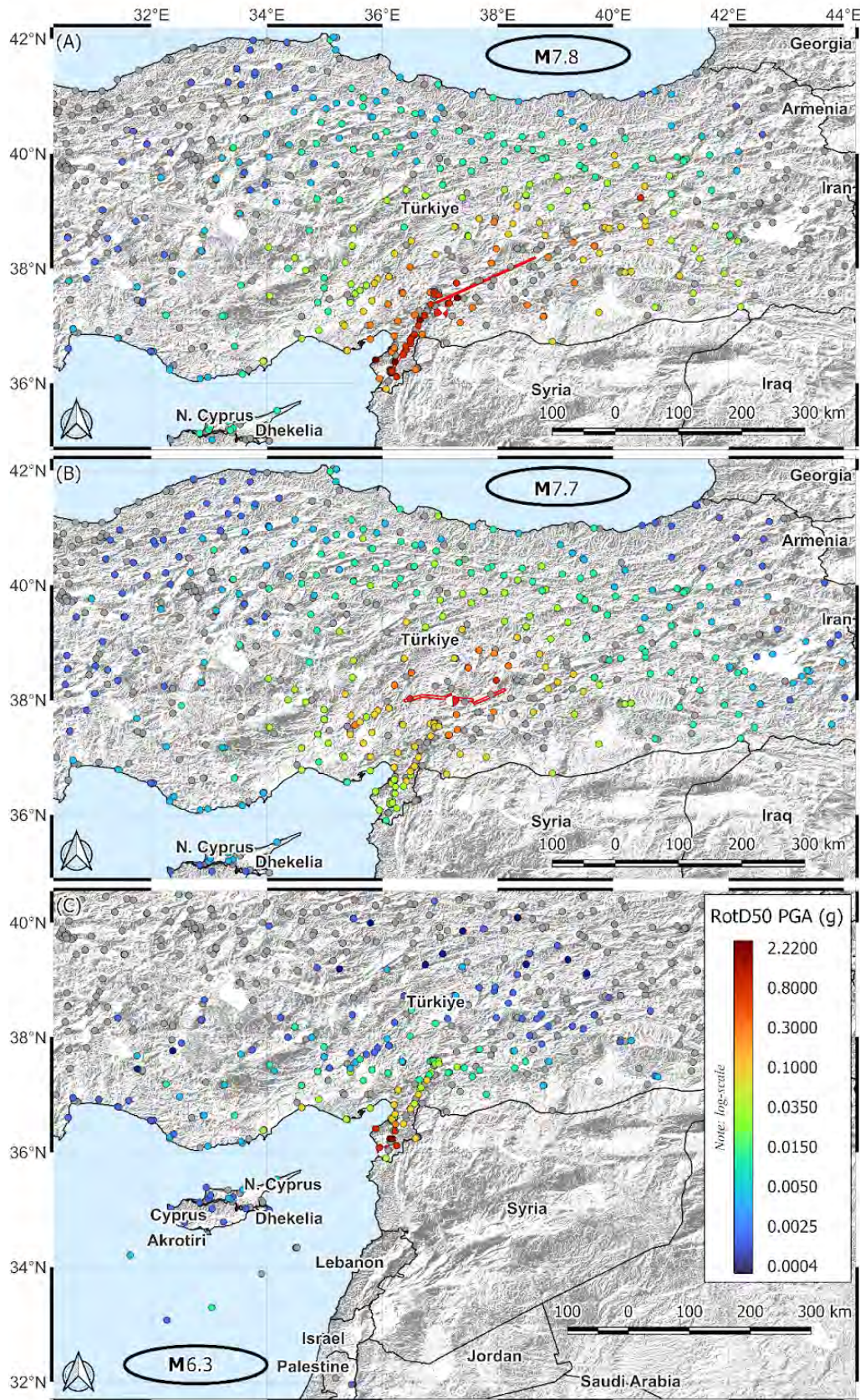


**Figure 3.6.** Maps of locations of seismic stations colored by RotD50 PGA values for (a) M7.8, (b) M7.7, and (c) M6.3 events.

### 3.3 Metadata Compilation

#### 3.3.1 Source and Path

The Global Centroid Moment Tensor (CMT) project (Ekström et al. 2012) origin times, **M** values, and nodal plane solutions are preferred because they are derived using global recordings that average out radiation pattern variability and provide between-region consistency. However, GCMT hypocenter locations correspond to the center of the earthquake moment distribution in time and space, which may not align well with the location of the initial slip. Therefore, the preferred locations are adopted from the USGS National Earthquake Information Center (NEIC). Table 3.2 summarizes the compiled moment tensor metadata for the **M7.8**, **M7.7**, and **M6.3** events. The strike, dip and rake angle provided in Table 3.2 are based on the solution that best aligns with the known orientation strike of the East Anatolian Fault.

**Table 3.2.** Source metadata for the Türkiye-Syria earthquake sequence

Origin Time (UTC)	Longitude (deg)	Latitude (deg)	Depth (km)	M	$M_0$ (dyne-cm)	Strike (deg)	Dip (deg)	Rake (deg)
2023-02-06 01:18:10	37.019	37.230	10	7.8	6.10E27	54	70	11
2023-02-06 10:24:59	37.211	38.008	13.1	7.7	4.97E+27	261	42	-8
2023-02-20 17:04:29	36.030	36.167	16	6.3	3.29E+25	227	45	-16

Finite fault models (FFMs) for the **M7.8** and **M7.7** events are presented by USGS (2023), the surface projections of which are illustrated in Figure 3.7. These models contain broad regions with relatively little slip, in addition to concentrated areas of high slip, therefore trimming is needed. Accordingly, the FFMs were trimmed by applying a threshold of 15% of the maximum slip (consistent with Zimmaro et al. 2018 and Contreras et al. 2022), in which a rectangle is drawn around the high slip areas. The trimming applied for the **M7.8** and **M7.7** FFMs are illustrated in Figures 3.8 and 3.9, respectively. The only exception to the 15% criterion is for segment 1 of the **M7.8** FFM, which was extended to intersect segment 2. Table 3.3 summarizes the rectangular representations of each trimmed FFM, parameterized by the location of the upper-left corner (ULC), dimensions, strike, and dip. The ULC is identified by viewing the fault from the hanging wall, as defined by Aki and Richards (1980).

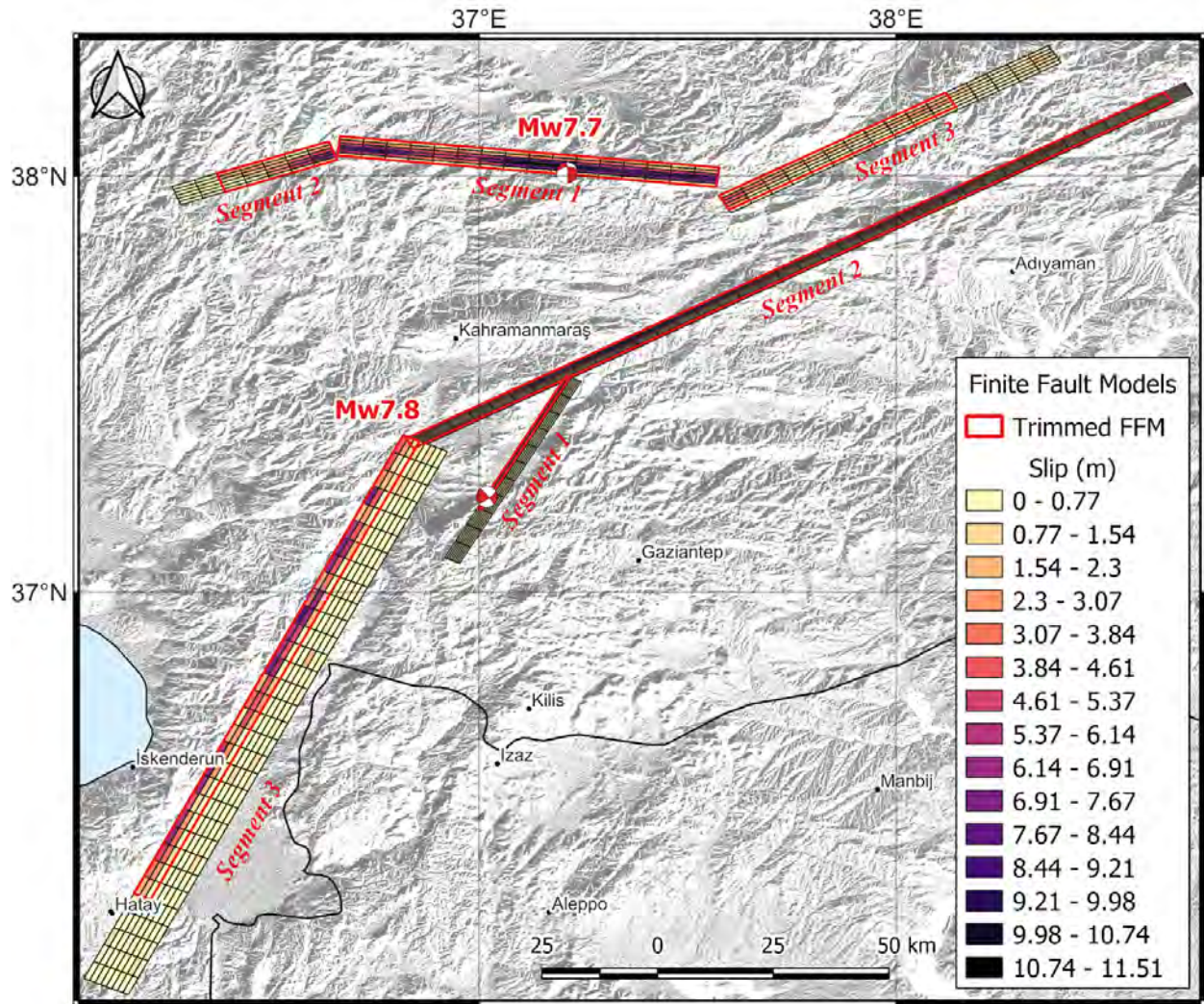


**Figure 3.7.** Finite fault models reported by the USGS (2023) for the M7.8 and M7.7 events; trimmed representations shown by red outlines.

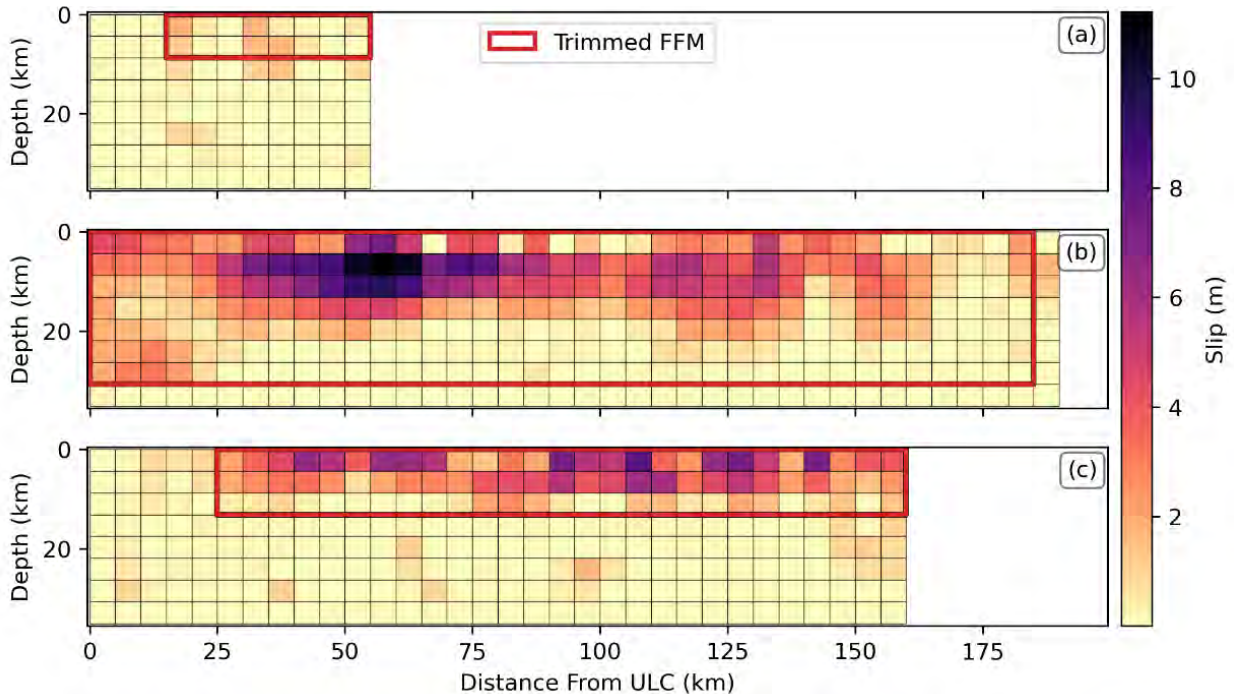


**Figure 3.8.** M7.8 finite fault model reported by USGS (2023); (a) segment 1, (b) segment 2, and (c) segment 3. Trimmed model corresponds to parts of the rupture surface with slip > 15% of the maximum slip (11.21 m).

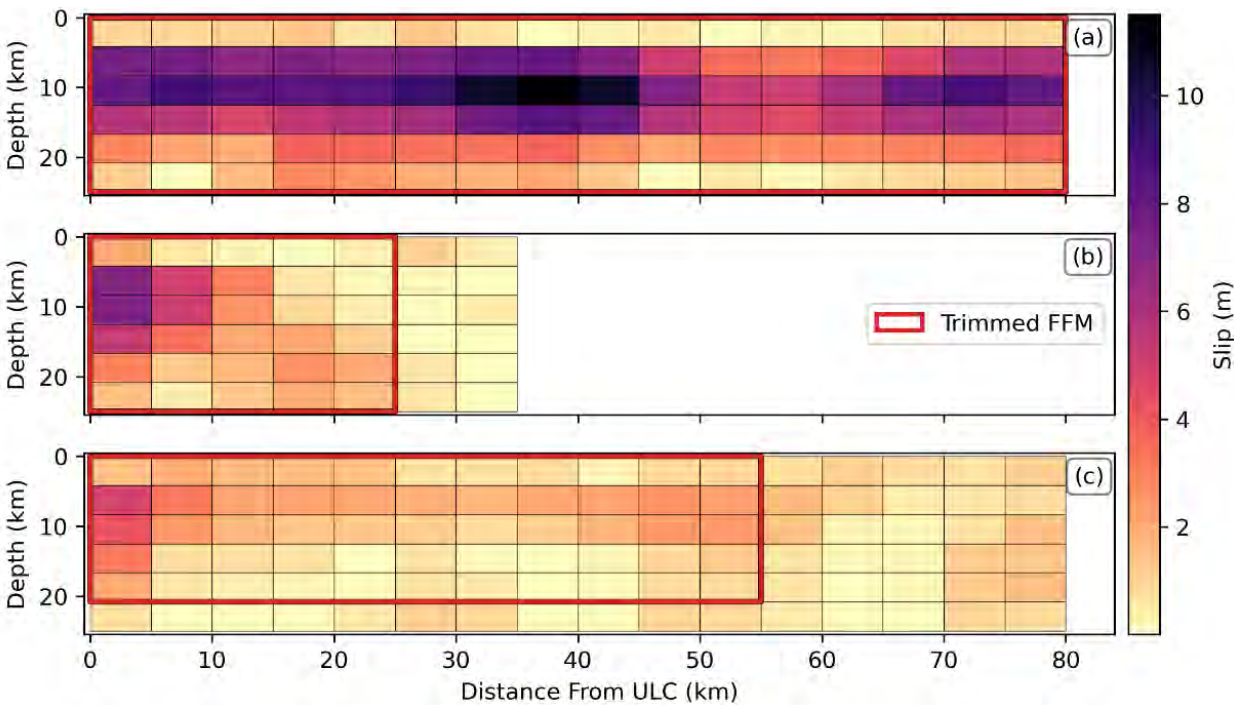


**Figure 3.9.** M7.7 finite fault model reported by USGS (2023); (a) segment 1, (b) segment 2, and (c) segment 3. Trimmed model corresponds to parts of the rupture surface with slip > 15% of the maximum slip (11.51 m).

**Table 3.3.** Summary of the trimmed FMMs for the **M7.8** and **M7.7** events

<b>M</b>	<b>Segment</b>	<b>ULC Longitude (deg)</b>	<b>ULC Latitude (deg)</b>	<b>ULC Depth (km)</b>	<b>Length (km)</b>	<b>Width (km)</b>	<b>Strike (deg)</b>	<b>Dip (deg)</b>
7.8	1	36.9979	37.2035	1.5476	39.9675	10.1089	28	85
7.8	2	36.8254	37.3698	0.0000	184.8870	34.8321	60	85
7.8	3	36.1724	36.2771	0.0000	135.0800	15.1741	25	75
7.7	1	37.5969	37.9740	0.0000	80.2456	29.8827	276	80
7.7	2	36.6600	38.0390	0.0000	25.0673	29.9808	250	80
7.7	3	37.5753	37.9531	0.0000	55.0569	24.9879	60	80

No FFM is currently available for the **M6.3** event, therefore the simulation procedure described in Contreras et al. (2022) was performed using the CCLD5 program to obtain rupture surface parameters. **M**-dependent relations provided by Leonard (2014) for shallow-crustal events in active tectonic regimes are used to estimate the rupture area and aspect ratio as part of this simulation procedure. These simulations were performed with a constrained strike based on the moment tensor solution, using the strike that aligns with the East Anatolian fault. Table 3.4 summarizes the simulated rupture representation for the **M6.3** event.

**Table 3.4.** Summary of the simulated rupture surface for the **M6.3** event

<b>M</b>	<b>Segment</b>	<b>ULC Longitude (deg)</b>	<b>ULC Latitude (deg)</b>	<b>ULC Depth (km)</b>	<b>Length (km)</b>	<b>Width (km)</b>	<b>Strike (deg)</b>	<b>Dip (deg)</b>
6.3	1	36.1256	36.1860	11.6960	17.2359	6.9537	227	45

Source-to-site distances were evaluated using the rupture surface representations given in Tables 3.3 and 3.4 using the P4CF routine (Chiou 2021). The recorded distance metrics include the closest distance from the site to any point on the rupture surface ( $R_{RUP}$ ), closest distance from the site to any point on the surface projection of the rupture surface ( $R_{JB}$ ), distance measured perpendicular to the fault strike from the surface projection of the top edge of the rupture surface ( $R_x$ ), distance measured parallel to the fault strike from the midpoint of the

surface projection of the rupture surface ( $R_v$ ), the root-mean-square distance ( $R_{rms}$ ), the epicentral distance ( $R_{epi}$ ), and the hypocentral distance ( $R_{hyp}$ ). These distances are provided for each recording site with usable recordings in tables in the doi.

### 3.3.2 Site Parameters

The site parameter that is required to facilitate model-data comparisons (Section 3.4) is the time-averaged shear wave velocity in the upper 30 m of the site ( $V_{s30}$ ).  $V_{s30}$  values are compiled for the 470 distinct stations that recorded usable data from the **M7.8**, **M7.7**, and/or **M6.3** events. The AFAD website reports  $V_{s30}$  values computed from  $V_s$  profiles measured using geophysical techniques (MASW and ReMi) for 234 of the stations, as shown in Figure 3.10.  $V_{s30}$  values at 24 of those stations (TK 0125, TK 0201, TK 0603, TK 1201, TK 2401, TK 2518, TK 3113, TK 3116, TK 3133, TK 3143, TK 3144, TK 3301, TK 3801, TK 4614, TK 4628, TK 5001, TK 5201, TK 5505, TK 5508, TK 5801, TK 5804, TK 6004, TK 6302, and TK 6901) were updated relative to those on the AFAD website. These updates were motivated by some errors (specifically, inconsistencies with the 1D layered earth models at some stations). The corrections of these errors adjusted the  $V_s$  profiles and the  $V_{s30}$  values.

Proxy-based  $V_{s30}$  models are used to assign  $V_{s30}$  values at locations which lack site characterization data. The Zhou (2023) proxy model based on topographic slope and kriging interpolation of  $V_{s30}$  values computed from measured  $V_s$  profiles and the Yilmaz et al. (ongoing project) geology and topography based models are used at stations within Türkiye. Outside of Türkiye,  $V_{s30}$  values are assigned using the topographic slope based proxy model proposed by Wald and Allen (2007).

$V_{s30}$  values computed from  $V_s$  profiles or estimated from proxy-based models are provided for each recording station with usable recordings in tables in the doi.

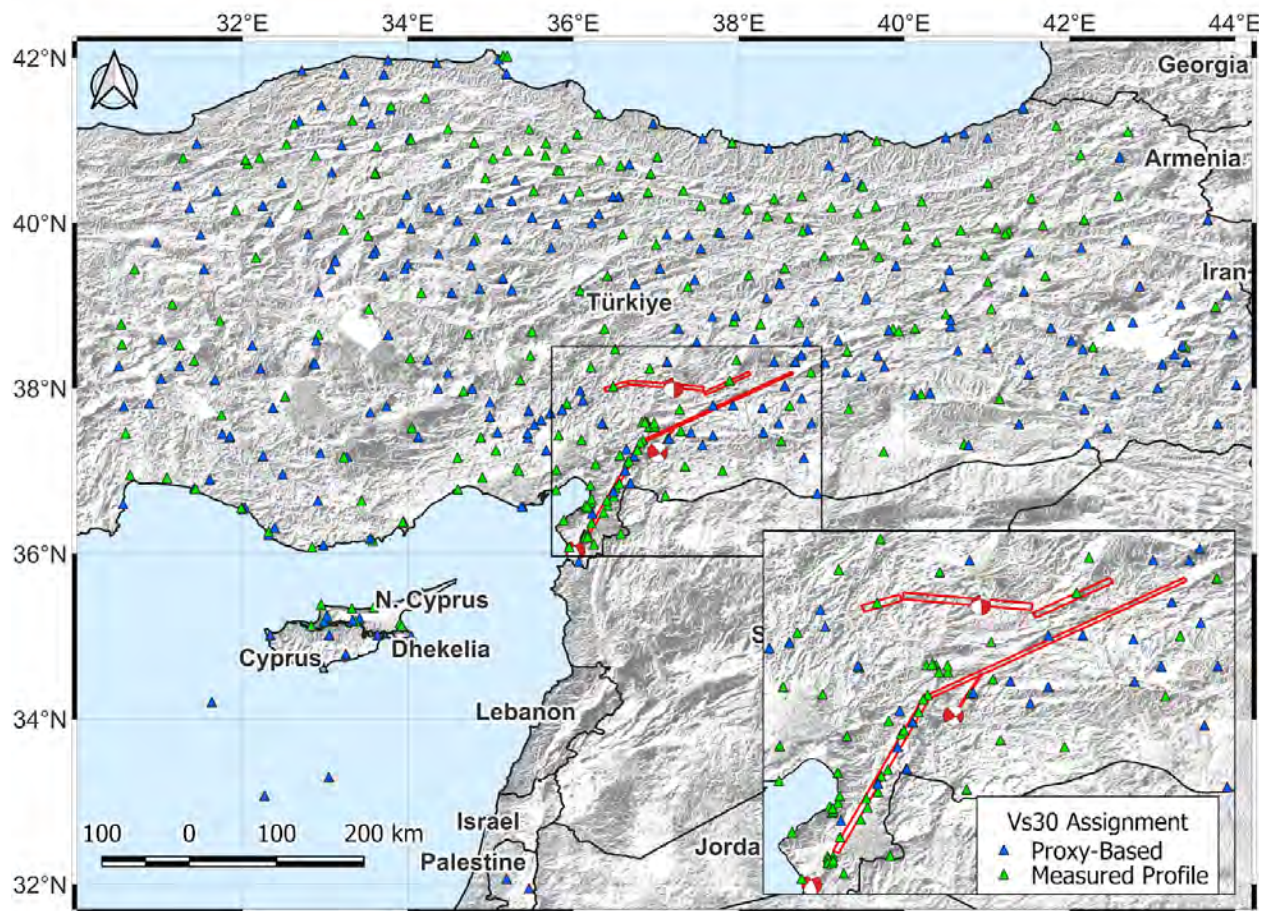


**Figure 3.10.** Locations of stations where  $V_{s30}$  is assigned using proxy-based methods (blue) or computed from measured  $V_s$  profiles (green).

### 3.4 Comparisons of Data to Global and Local GMMs

We compare recorded data with the following GMMs for shallow crustal regions: (1) a global model - Boore et al. (2014; hereafter BSSA14) and (2) a Türkiye-specific model by Kale et al. (2015; hereafter KAAH15). The BSSA14 model can be applied with or without regional adjustments that affect the rate of anelastic attenuation, being relatively low for Türkiye (slower attenuation) and relatively high for Italy (faster attenuation). Without a regional adjustment, the model is considered applicable to California, New Zealand, and Taiwan. Additional NGA-West2 GMMs may be considered in future work.

The GMMs provide predictions of ground shaking intensity given  $M$ , rupture mechanism/style-of-faulting (strike-slip for all three events),  $R_{JB}$ , and  $V_{s30}$ . BSSA14 has basin adjustments for iso-surface depths (i.e.,  $z_{1.0}$ ), however given that this site parameter is

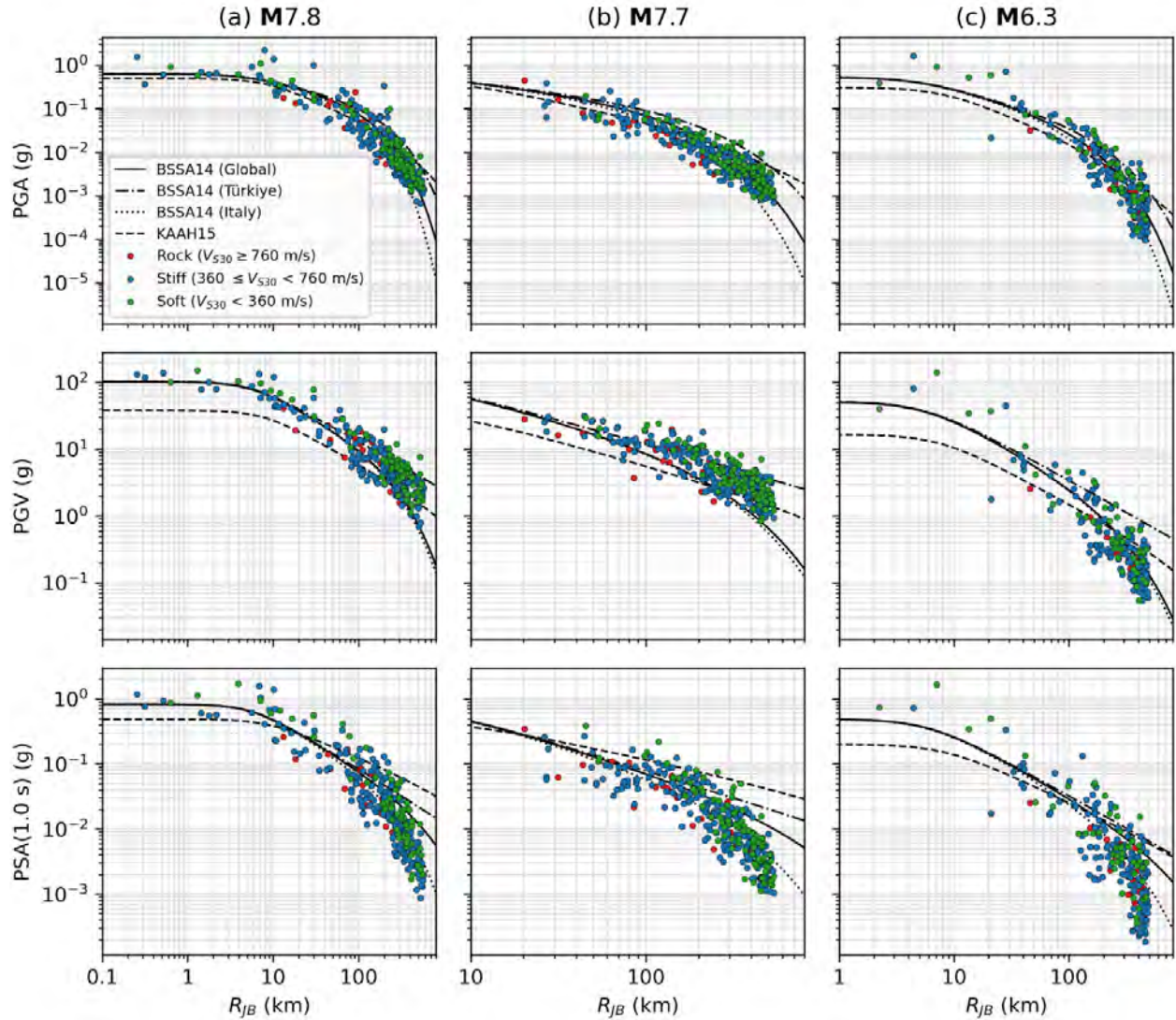
unavailable for the vast majority of sites, we choose not to apply any basin adjustments during this analysis (i.e., the differential depth  $\delta z_1 = 0$ ).

Figure 3.11 shows the distance-dependence of RotD50 PGA, PGV, and PSA(1.0 sec) for the **M7.8**, **M7.7**, and **M6.3** events. Recorded data are subdivided into three categories: (1) rock ( $V_{s30} \geq 760$  m/s), (2) stiff soil ( $360 \leq V_{s30} < 760$  m/s), and (3) soft soil ( $V_{s30} < 360$  m/s). The median predictions for a site with  $V_{s30} = 360$  m/s for each of the GMMs are also shown.

Figure 3.11 shows that all GMMs fit the observed PGA data reasonably well out to distances of about 200 km. For PGV and PSA(1 sec) the global and Italian regionalized versions of BSSA14 are nearly identical, and fit the data best up to distances of approximately 100 km, where the Italian version starts to attenuate faster at larger distances. The slower attenuation of the BSS14 model with Türkiye regionalization over-predicts at distances beyond approximately 100 - 200 km. The KAAH15 significantly underpredicts PGV in the near-field, and because the model does not include anelastic attenuation it over-predicts PGV and PSA(1 sec) at far distances.

The poor predictions of the BSSA14 model with the Türkiye regional adjustment may initially be surprising. However, the Turkish data considered in the development of that model was mainly from the northern part of Türkiye, near the North Anatolian Fault. This region corresponds to the Eurasian and Anatolian Blocks (Figure 2.2), whereas the present data is in the south of Türkiye near the interface of the Anatolian and Arabian plates. The results suggest that different crustal properties are encountered in the two parts of Türkiye, which is likely a consequence of the different crustal blocks. For subsequent analyses, we use the global version of the BSSA14 model.





**Figure 3.11.** Observations vs distance colored by site condition (rock, stiff-soil, or soft-soil) for (a) **M7.8**, (b) **M7.7**, and (c) **M6.3** events. Predictions shown for global BSSA14, regional BSSA14, and KAAH15 GMMs for a  $V_{S30}$  of 360 m/s.

To better evaluate the performance of these GMMs relative to the data, we compute total residuals ( $R_{ij}$ ), considering the appropriate path and site conditions as follows:

$$R_{ij} = \ln(Y_{ij}) - \ln(y_{ij}) \quad (3.1)$$

where  $Y_{ij}$  is the value of the observed ground motion intensity measure (e.g., PGA, PGV, etc.) from station  $i$  for event  $j$ , and  $y_{ij}$  is the median GMM prediction. Figure 3.12 presents plots of  $R_{ij}$  versus distance for BSSA14 (global) and KAAH15 GMMs. Binned means are also shown for  $R_{ij}$  along with their 95% confidence intervals, using approximately seven intervals for each log-cycle

(intermittent bin sizes are used at short distances due to sparsity of data). Only data from free-field sites are shown (data from 16 instrumented dam sites are screened out due to the potential of impactful soil-structure-interaction effects).

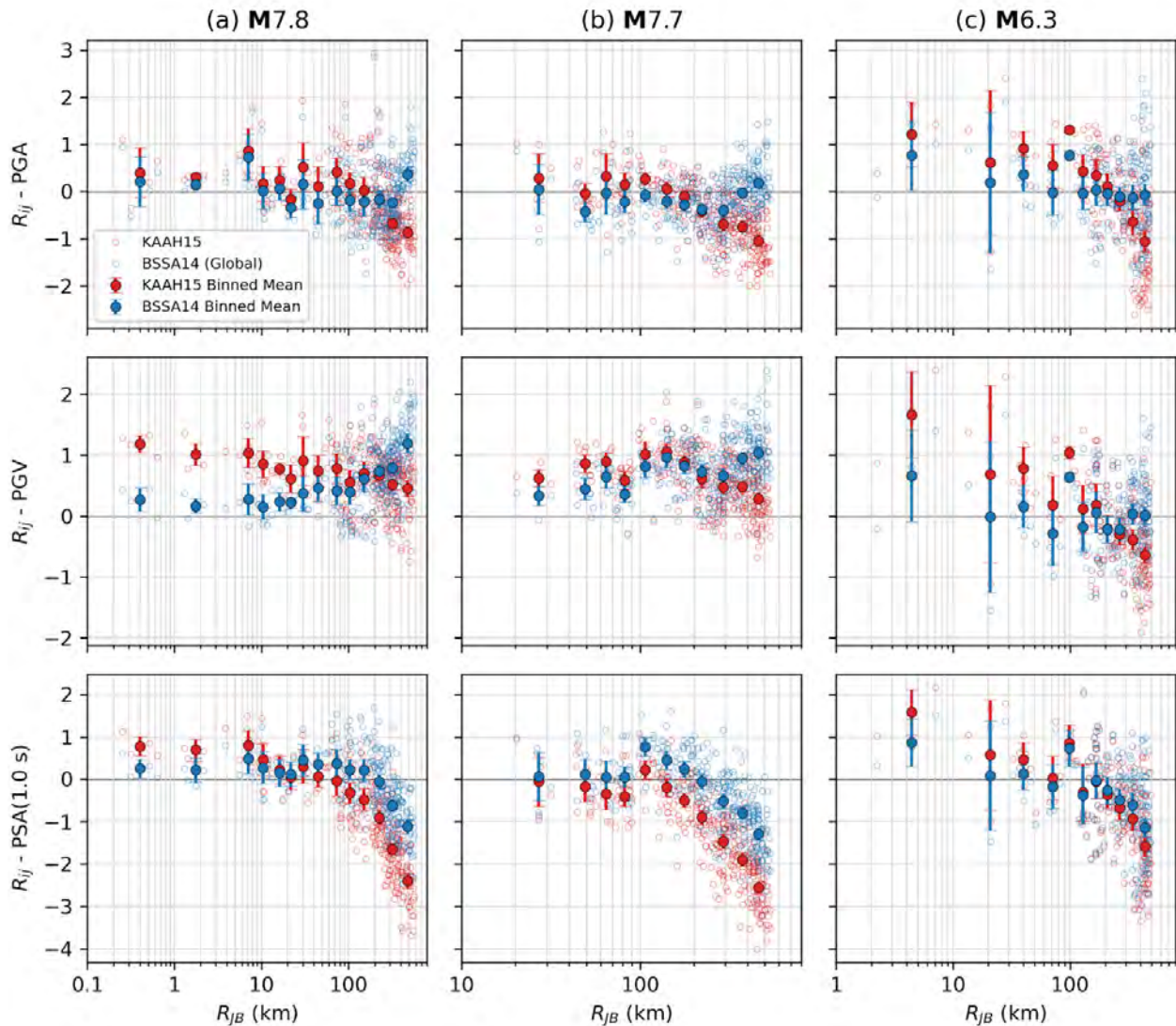


**Figure 3.12.** Total residuals vs distance for (a) **M7.8**, (b) **M7.7**, and (c) **M6.3** events. Residuals computed for PGA, PGV, and PSA(1.0 sec) for the global BSSA14 and KAAH15 GMMs.

The plots shown in Figure 3.12 support the initial observations drawn from Figure 3.11, namely the existence of complex path effects which result in relatively poor fits between the GMMs and observed data at large distances (generally  $R_{JB} > 200$  km). BSSA14 performs the best at distances less than approximately 200 km, beyond which uncaptured path effects are apparent. KAAH15

performs comparably, except for a tendency to underpredict PGV over a wide distance range, and the other intensity measures at short-to-moderate distances.

Event terms ( $\eta_{Ei}$ ), which represent the event-specific bias, can be approximated as the average  $R_{ij}$  for each event. To avoid mapping potential bias from the uncaptured path effects into the estimation of  $\eta_{Ei}$ , only observations within 200 km are used. Figure 3.13 presents plots of  $\eta_{Ei}$  and their standard errors for PGA, PGV, and PSA at periods ranging from 0.01 sec to 4 and 10 sec for KAAH15 and BSSA14, respectively.

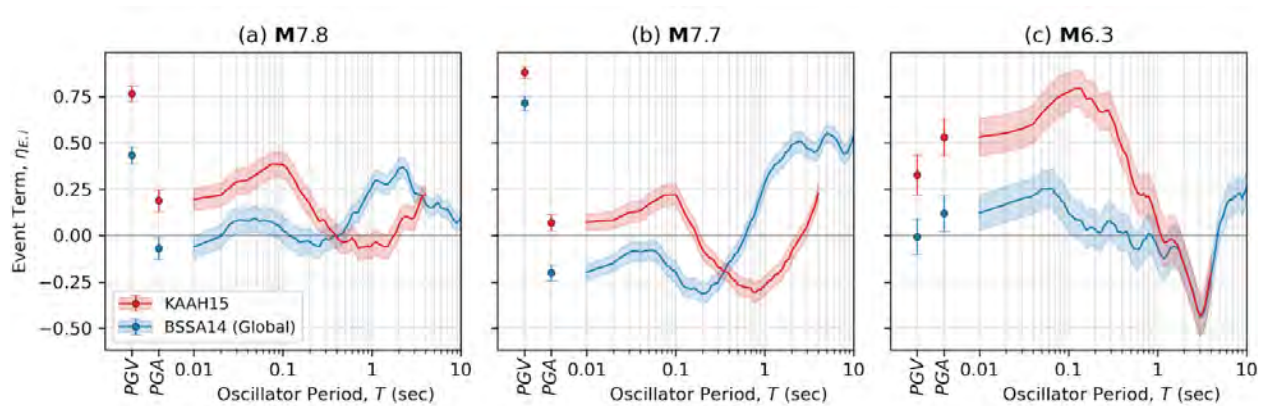


**Figure 3.13.** Event terms vs oscillator period for (a) **M7.8**, (b) **M7.7**, and (c) **M6.3** events computed using the global BSSA14 and KAAH15 GMMs.

The results in Figure 3.13 show that the BSSA14 model under-predicts long-period motions ( $> 0.5$  sec) and PGV for the larger events (positive  $\eta_{Ei}$ ). On the other hand, it generally captures shorter period motions and PGA with little bias. The KAAH15 model is relatively effective at long periods but has underprediction bias at short-to-moderate periods ( $T < 0.2$  sec). The source effects from the **M6.3** event were reasonably captured by BSSA14 over the entire period range investigated but under-predicted by KAAH15.

Underpredictions by GMMs at some stations may have been influenced by directivity and/or basin effects that affect the ground motions but that are not accounted for directly in the model. While models for the 3D sedimentary structure of basins are not available in the study region at the present time, some locations like Hatay (Station # 3129, 3126, and 3125) are located in what can geologically be recognized as a basin and exhibit long period ground motion features that are often found for basin sites (e.g. Figure 3.14). Future research will seek to isolate the effects of site response, and potentially directivity, on the attributes of the ground motions at these and other stations.

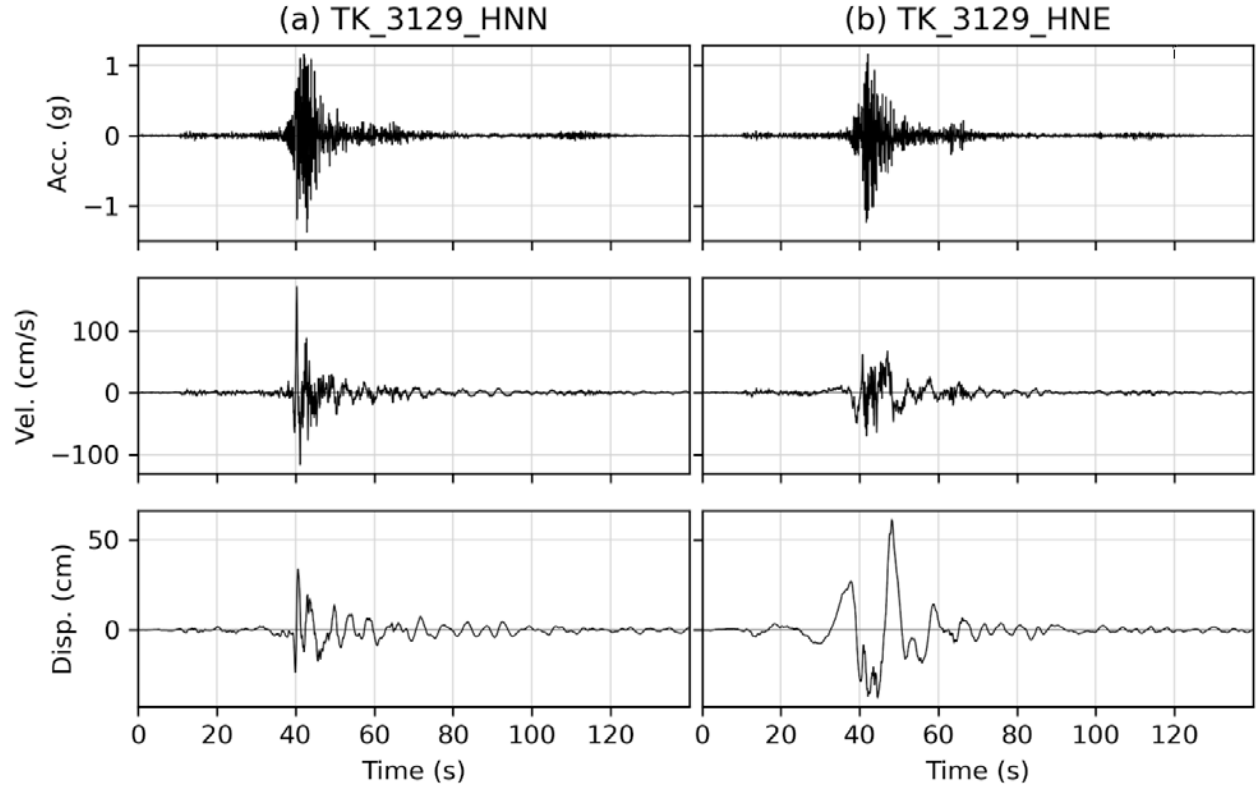


**Figure 3.14.** Plots of acceleration, velocity, and displacement for Hatay station (TK 3129); (a) north-south component; (b) east-west component.

### 3.5 Ground Motion Estimation for Sites without Recordings

#### 3.5.1 Semi-Variogram Model

Semi-variogram models are developed to characterize the spatial correlation structure of PGA, PGV, and PSA(1.0 sec) for the **M7.8** mainshock, and the **M7.7** and **M6.3** aftershocks. Empirical semi-variograms are first developed using within-event residuals ( $\delta W_{ij}$ ) for the ground motion intensity measures as computed using the BSSA14 global model, calculated as:

$$\delta W_{ij} = R_{ij} - \eta_{Ei} \quad (3.2)$$

These within-event residuals are then used to compute empirical semi-variograms,  $\gamma^e$ , using the relation below (e.g., Jayaram and Baker, 2009):

$$\gamma^e(h) = \frac{1}{2N(h)} \cdot \sum_{k=1}^{N(h)-1} \sum_{l=k+1}^{N(h)} [\delta W(x_k) - \delta W(x_l)]^2 \quad (3.3)$$

Where  $h$  is the separation distance between two stations with a tolerance  $\Delta h/2$ , where  $h \pm \Delta h/2$  is a bin represented by a point in the empirical semi-variogram,  $N(h)$  is the number

of seismic station pairs within a bin, and  $\delta W(x_i)$  is the within-event residual for station “ $i$ ”. The tolerance  $\Delta h$  is selected such that  $N(h) \geq 10$  for all points the semi-variogram. Due to the problems with the GMMs at large distances, as well as the focus of the reconnaissance being on near-fault sites, we only use data from recording stations with  $R_{jB} < 200$  km.

The empirical semi-variograms are then fit using a selected semi-variogram model. An exponential semi-variogram model form is applied (e.g., Baker and Chen, 2020):

$$\gamma^m(h) = \phi^2 \cdot \left[ 1 - \exp\left(-3 \cdot \frac{h}{b}\right) \right] \quad (3.4)$$

where  $b$  is the semi-variogram range (i.e. the distance range where correlation is appreciable), and  $\phi^2$  is the semi-variogram sill, equivalent to the within-event residuals’ standard deviation at separation distances longer than  $b$ . A Bayesian updating approach (Pretell et al., in progress) is used to compute semi-variogram models that capture the scatter in the empirical semi-variograms. This Bayesian approach allows for integrating prior knowledge about GMMs (particularly, models for  $\phi^2$ ) and attributes of semi-variogram models for different GMIMs. Figures 3.15-3.17 present 1000 semi-variogram models developed for the peak ground acceleration (PGA), peak ground velocity (PGV), and pseudo-spectral accelerations (PSA) at 1.0 sec, for the **M7.8** mainshock event. The maximum a posteriori or mode semi-variogram, i.e., the most likely model, is also presented and used for generating maps of within-event residuals.

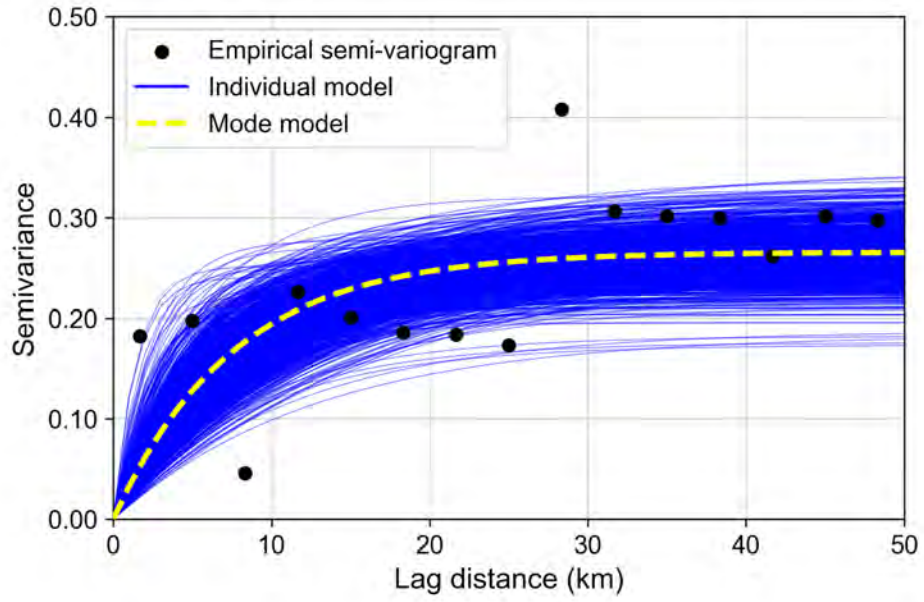


**Figure 3.15.** Semi-variogram models for PGA, M7.8 mainshock.

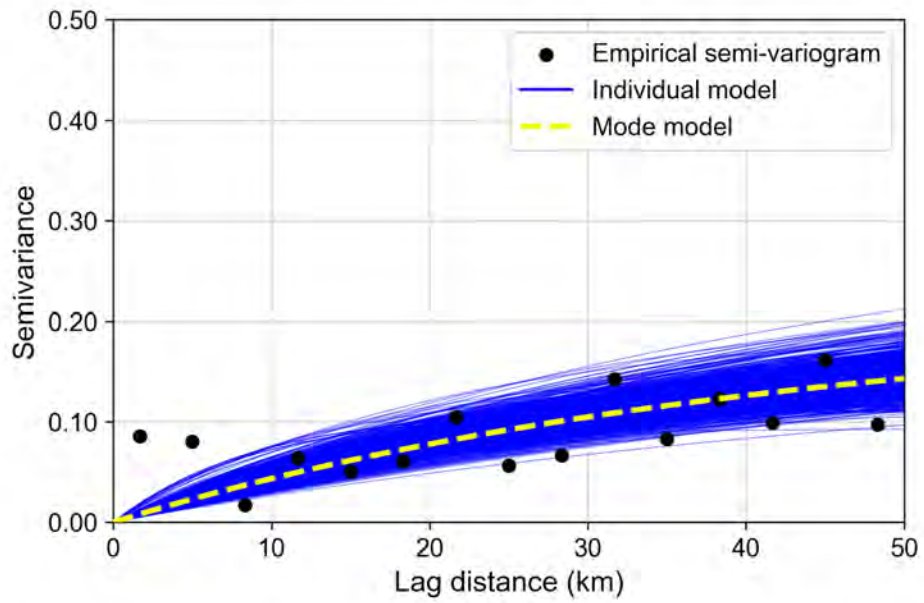


**Figure 3.16.** Semi-variogram models for PGV, M7.8 mainshock.

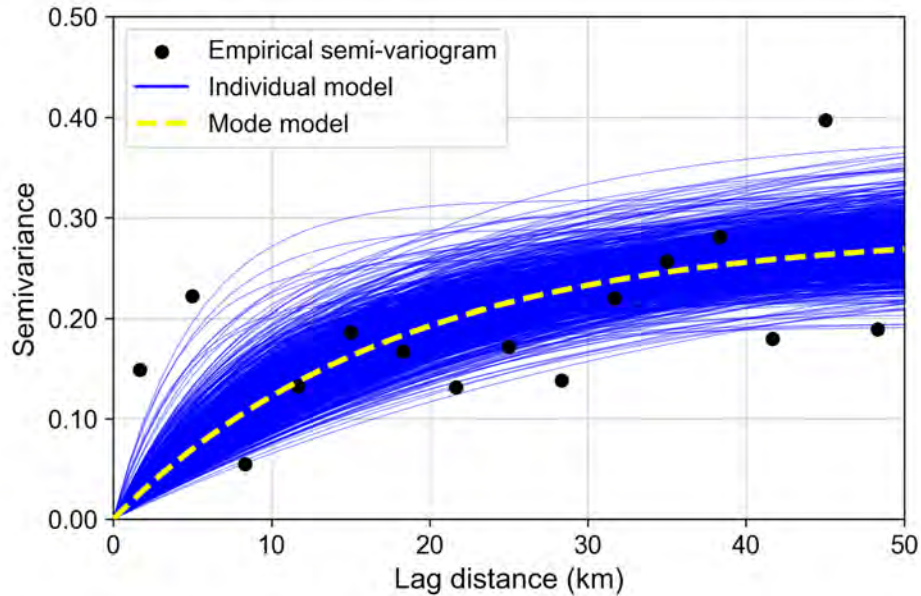


**Figure 3.17.** Semi-variogram models for PSA(1.0 sec), M7.8 mainshock.

### 3.5.2 Within-Event Residual Maps

Within-event residual maps are generated for PGA, PGV, and PSA(1.0 sec). Within-event residual maps inform about the expected deviation in natural logarithm units from ground motion model-based estimates at unsampled locations, i.e., locations without a seismic station. The within-event residuals are estimated based on the observed within-event residual at seismic stations using Kriging interpolation and the semi-variogram models developed to characterize the ground motion correlation structure for each earthquake.

Ordinary Kriging is used to estimate the mean within-event residual and the associated standard deviation of the interpolation error at unsampled locations. The interpolation errors, estimated as part of the Kriging step, are due to the closeness of a given unsampled location to the closest seismic station. Locations close to a seismic station have lower standard deviation, while locations further apart from seismic stations have a higher standard deviation. The standard deviation of the interpolation error at recording stations is zero.

The within-event residuals are estimated to capture the uncertainty due to the semi-variogram model and the interpolation error. First, the 1000 Bayesian semi-variogram models are used to calculate the mean and standard deviation within-event residuals at unsampled locations. Second, each one of 1000 mean-standard deviation pairs at an unsampled location is used to define a normal distribution and draw 1000 within-event residuals. This procedure results in  $10^6$  within-event residuals. Lastly, the mean and standard deviation of the  $10^6$  values are calculated

at each unsampled location and considered as representative. Figures 3.18 to 3.20 show the maps for the mean within-event residuals for PGA, PGV, and PSA(1.0 sec) for the **M7.8**, **M7.7**, and **M6.3** events, respectively. These maps are generated using the mode semi-variogram models.

The maps shown in Figures 3.18 to 3.20 demonstrate interesting spatial patterns of residuals. Keeping in mind that the **M7.8** mainshock is on the East Anatolian Fault that serves as the boundary between the Anatolian Block to the northwest and the Arabian block to the southeast, we generally find negative residuals on the Anatolian block and positive residuals on the Arabian block. This suggests that the global BSSA14 model overpredicts on the Anatolian block and underpredicts on the Arabian block. These patterns are fairly consistent across the three events. Such effects could be accounted for in future GMMs that account for different attenuation features in different crustal blocks.



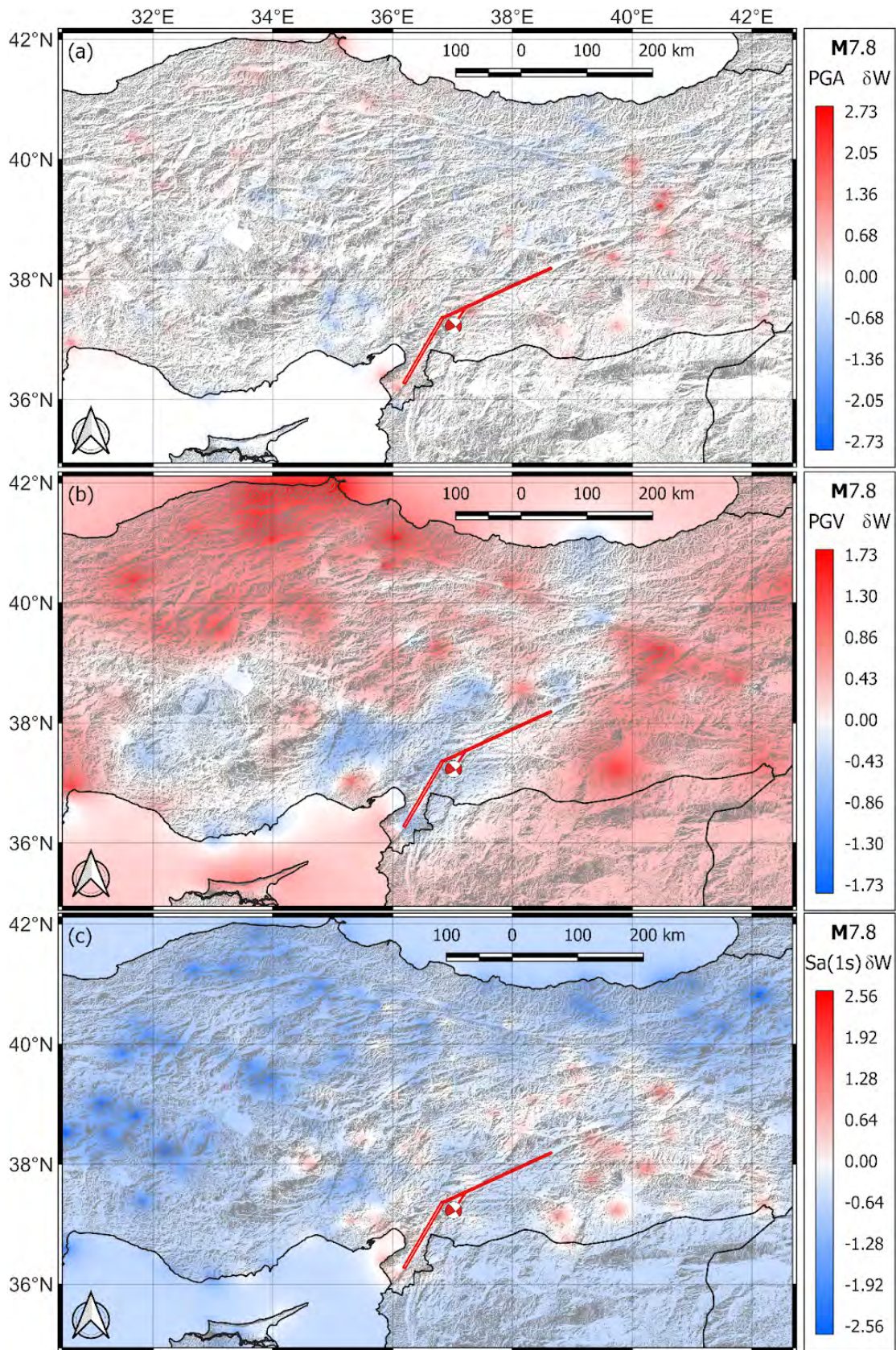


**Figure 3.18.** Mean within-event residual for (a) PGA, (b) PGV, and (c) PSA(1.0) for the  $M7.8$  event.

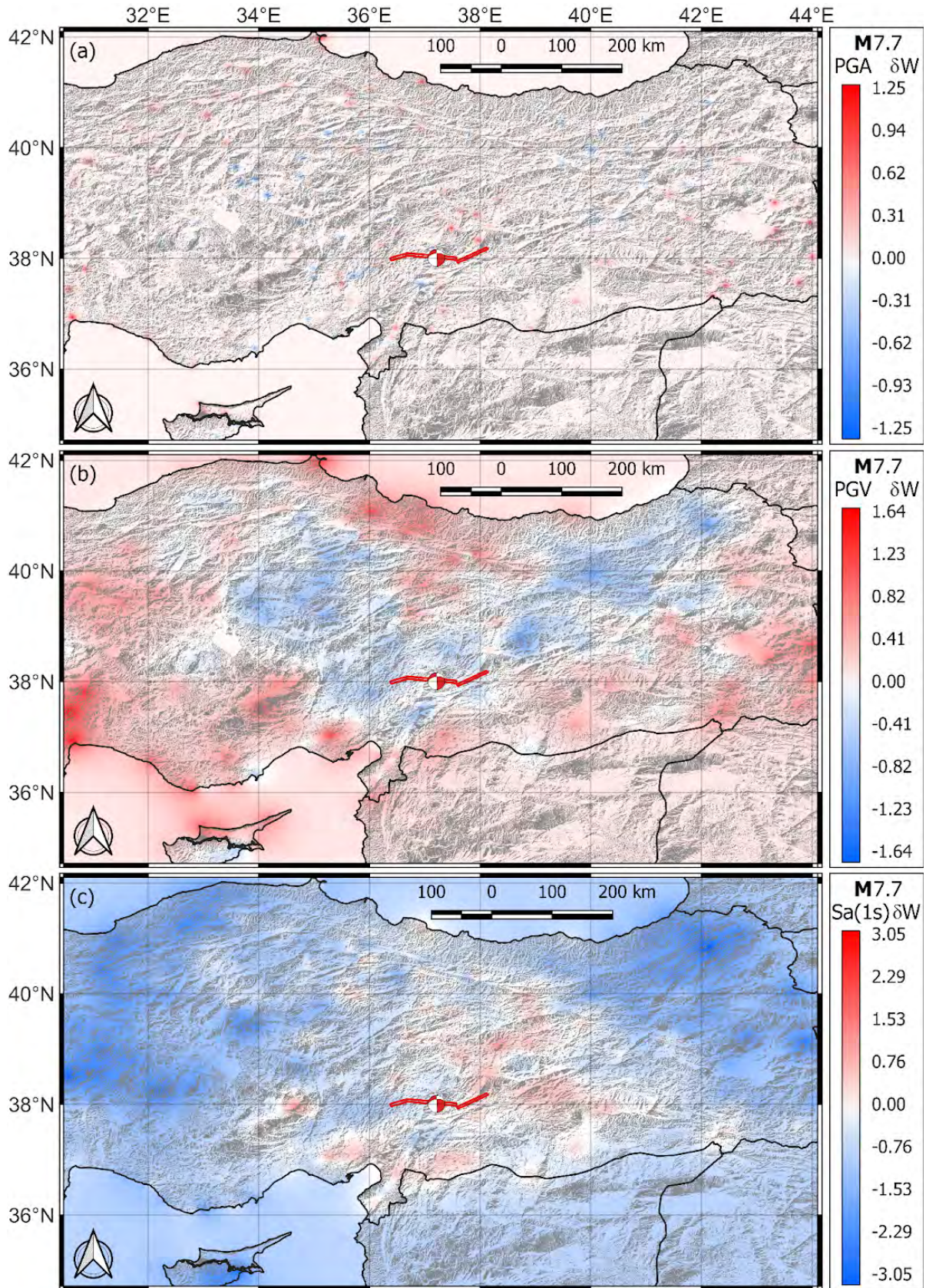
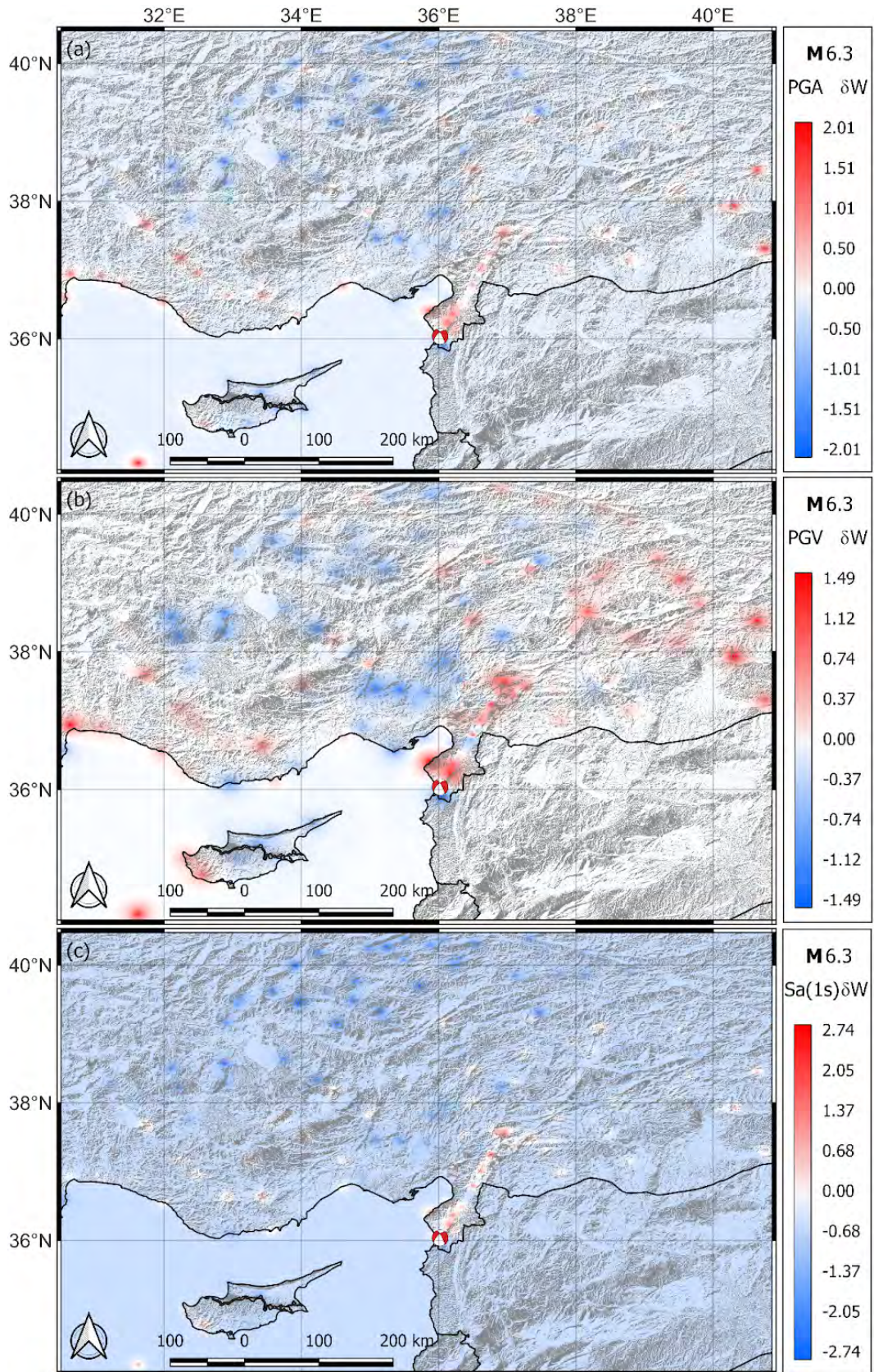


Figure 3.19. Mean within-event residual for (a) PGA, (b) PGV, and (c) PSA(1.0) for the M7.7 event.



**Figure 3.20.** Mean within-event residual for (a) PGA, (b) PGV, and (c) PSA(1.0) for the  $M 6.3$  event.

### 3.5.3 Ground Motion Estimation Procedure

Mean ground motion estimates ( $\hat{y}$ ) can be obtained at sites without instrumentation using BSSA14 median predictions, within-event residuals maps (Section 3.5.2), and event terms (Figure 3.13) as follows:

$$\ln(\hat{y}_{ij}) = \ln(y_{ij}) + \eta_{E,i} + \delta W_{ij} \quad (3.5)$$

where the computation of  $y_{ij}$  requires estimation of  $V_{S30}$  and  $R_{jB}$  for the site. Uncertainties in the ground motion are also provided that account for aleatory variability in the Kriged within-event residual and epistemic uncertainty in the same parameter that is related to the multiple possible semi-variogram models.

Eq. (3.5) has been used to estimate RotD50 PGA, PGV, and PSA (1.0s) for sites of interest. These estimates are presented and discussed in Chapters 4 to 8.

### 3.6 Observations Near Ground Motion Stations

Members of the GEER Phase 2 team (Jorge Macedo, Menzer Pehlivan, Kristin Ulmer) visited select ground motion recording stations. Table 3.6 presents the team's observations of the site conditions and the damage near the stations, and Figure 3.21 shows locations of the 12 stations that were visited. Where possible, the structural damage index and ground failure index used in reconnaissance following the 1999 Adapazari, Turkey earthquake (Bray and Stewart 2000) were used to describe the level of damage in the surrounding area. These indices are summarized in Tables 3.7 and 3.8.

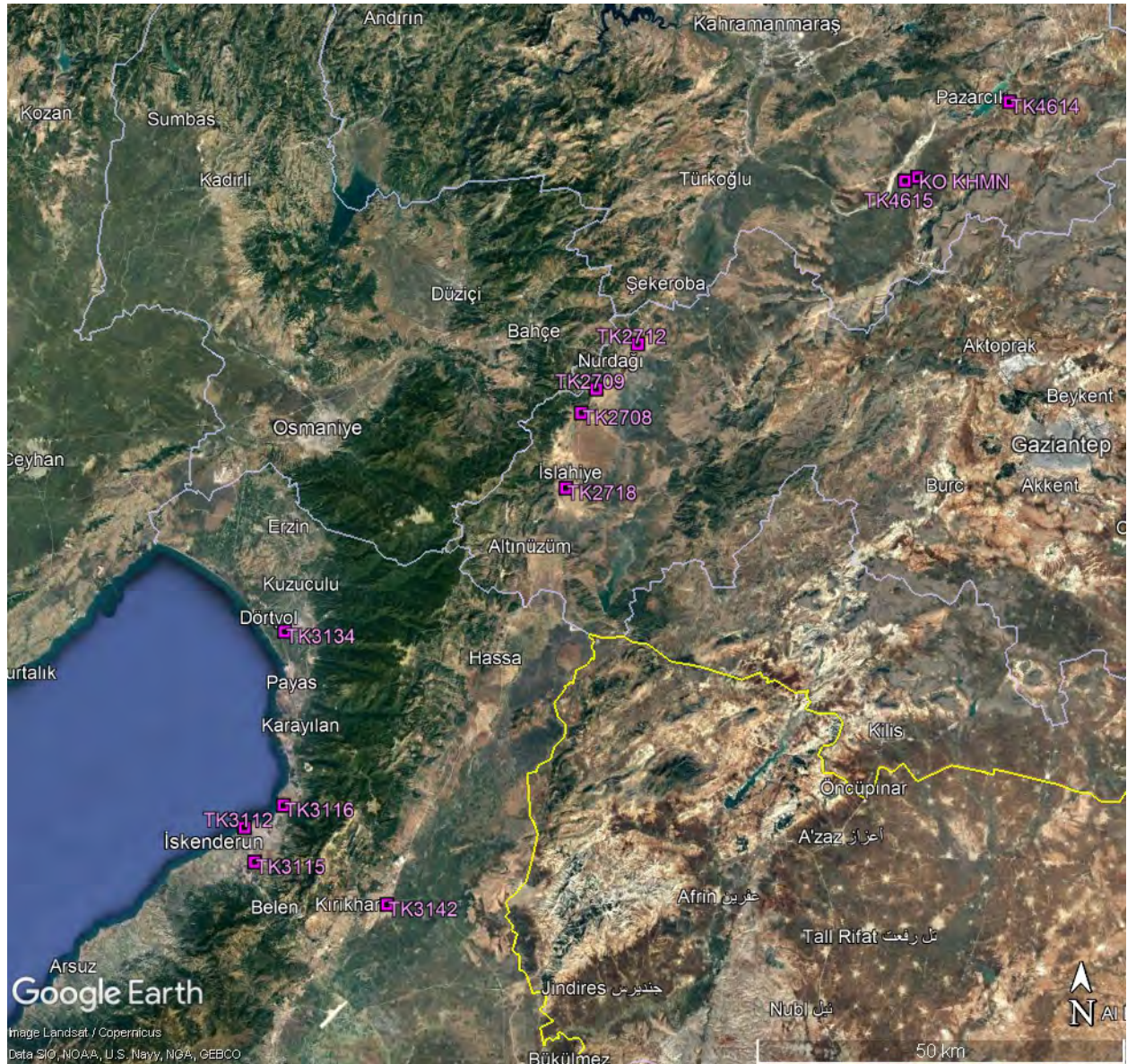


**Figure 3.21.** Map showing locations of ground motion stations visited by GEER Team 2.

**Table 3.6.** Field observations near strong ground motion stations

Station Name	Date Visited	Latitude	Long.	PGA <sup>1</sup> (g)	PGA <sup>2</sup> (g)	Observations
TK 4615	March 1, 2023	37.3868	37.1380	0.615	0.068	The GMRS is located in the garden of a logistic warehouse facility in a standalone concrete building. Across the street from the GMRS is an open excavation with almost vertical cuts that stayed intact after the ground shaking. The open excavation is due to Narlı 26 January Elementary School that was demolished to be reconstructed. Team collected soil samples for laboratory testing. Warehouse next to the station (1-story) appeared undamaged, the wall around the perimeter of the lot was collapsed. There were many damaged buildings (some with cracks, others collapsed) in the neighborhood but not immediately next to the station
KO KHMN	March 1, 2023	37.3916	37.1574	0.632	#N/A	The GMRS is located up on a hill, within 5km from the fault trace near Narlı. The single family, 2- to 3- story houses, and transmission tower nearby performed well. Railroad bridge and embankment at the bottom of the hill performed well. Team observed some damage to a retaining wall supporting the railroad bridge on the west facing side.
TK 4614	March 1, 2023	37.4851	37.2977	2.212	0.164	The GMRS is located near a health center operated by the government. We believe it housed the recording device but we were not able to go in to confirm. The one-story building had very minor damage (D1) and no apparent ground failure (GF0). Damage does not seem consistent with recorded PGA of 2.2 g during the Kahramanmaraş-Pazarçık (Mw 7.7) event. The neighborhood immediately around the station and the general Pazarçık area experienced significant damage with the majority of multi-story structures collapsed or heavily damaged.
TK 2712	March 2, 2023	37.1840	36.73283	0.587	#N/A	The GMRS is located in a school yard. The school has 4 stories and a basement. Only minor damage is observed in the school building with mostly minor cracks, some tiles fell off the walls near the base of the building, some interior cracks that the team could see through the window, the roof slid to NW direction (D2). Some ground settlement around the building was observed, the stairs settled around 5 inches compared to the building (GF2).
TK 2709	March 2, 2023	37.12852	36.67048	#N/A	#N/A	The GMRS is located next to a playground in a small village. Local woman said she couldn't walk straight during the earthquake, and bounced from one wall to another. No ground failures (GF0) or significant building damage (D0-D1) that we could see in the area. Most structures were small, 1-2 story residential buildings.

TK 2708	March 2, 2023	37.09933	36.64837	1.517	#N/A	The GMRS was observed through a fence, but was not directly accessible. No evidence of ground failure near the station (GF0). Two buildings were nearby, one East and one West of the station. East of station (school): 4 stories, partial story on top, had noticeable damage but still standing (D2). West of station: almost no damage we could see from a distance (D0).
TK 2718	March 2, 2023	37.00777	36.6266	0.651	0.041	The GMRS is located next to a religious school (Mevlana İmam Ortaokulu). Building was standing, plentiful cracks on exterior (D2-D1). No apparent ground deformation (GF0).
TK 3142	March 2, 2023	36.49797	36.36612	0.685	0.015	The GMRS is located next to a 1-story school with minor damage on the exterior walls, but locals said the roof had shifted and was fixed before we arrived (D1). Appears to be a soil site. No apparent ground failure, although hard to tell if there was any ejecta given the playground sand covering the ground. Locals said no sand boils appeared (GF0). Buildings across the street and in the neighborhood with 6-8 stories suffered more damage but still standing (D2). A local pointed out a building that had tilted, ~7.5inch uplift on the W side of the building toward the NE direction.
TK 3112	March 2, 2023	36.58829	36.14839	#N/A	#N/A	On the other side of the soccer field from the GMRS, a large sand boil (~21 ft by 9 ft by 3 inch deep) was observed by a well (~8 inch diameter). Did not see sand boils on the rest of the soccer field. No visible signs of liquefaction or other ground failure next to the GMRS (GF0). A security guard said that water overflowed in the water treatment tanks next to the GMRS. 4-story buildings in the area seemed to perform well. No obvious evidence of liquefaction in the neighborhood immediately around the GMRS.
TK 3115	March 2, 2023	36.54634	36.16459	0.293	0.026	The GMRS is located at high elevation on a ridge. No obvious signs of ground failure (GF0). Most buildings nearby (~6 stories, residential) are still standing, but suffered significant damage.
TK 3134	March 3, 2023	36.82763	36.20388	0.229	0.036	Building on the north side of the GMRS appears undamaged from the outside. Building on the south side of the station also appears undamaged from the outside, but a local said the interior columns are compromised, so the building is not inhabited.
TK 3116	March 3, 2023	36.61618	36.20661	0.176	0.019	GMRS is on the slope of a hill, no obvious signs of ground deformation (GF0). A 1-story house nearby had no damage and a 6-story building across the street did not have obvious external damage (D0).

<sup>1</sup>Kahramanmaraş-Pazarcık (M7.8 event); <sup>2</sup>Kahramanmaraş-Elbistan (M7.7 event)

**Table 3.7.** Structural damage index (from Bray and Stewart 2000)

Index	Description	Interpretation
D0	No Observable Damage	No cracking, broken glass, etc.
D1	Light Damage	Cosmetic crackgin, no observable distress to load-bearing structural elements
D2	Moderate Damage	Cracking in load-bearing elements, but no significant displacements across these cracks
D3	Heavy Damage	Cracking in load-bearing elements with significant deformations across the cracks
D4	Partial Collapse	Collapse of a portion of the building in plan view (i.e., a corner of a wing of the building)
D5	Collapse	Collapse of the complete structure or loss of a floor

**Table 3.8.** Ground failure index (from Bray and Stewart 2000)

Index	Description	Interpretation
GF0	No Observable Ground Failure	No settlement, tilt, lateral movement, or boils
GF1	Minor Ground Failure	Settlement less than 10 cm; tilt of > 3-story buildings less than 1 degree; no lateral movements
GF2	Moderate Ground Failure	Settlement between 10 to 25 cm; tilts of 1-3 degrees; small lateral movements less than 10 cm
GF3	Significant Ground Failure	Settlement greater than 25 cm, tilts greater than 3 degrees; lateral movements greater than 25 cm



## 4.0 Liquefaction and Lateral Spreading

*Onder Cetin, Robb Moss, Umut Ayhan, Jorge Macedo, David Frost, Kristin Ulmer, Menzer Pehlivan, Patrick Bassal, Diane Moug, Patrick Bassal, Sena Kendir, Jonathan Bray*

GEER teams (Phase 1, 2, and 3) performed several levels of reconnaissance concerning ground damage from liquefaction and lateral spreading. This included initial documentation immediately after the events, follow-up assessment of the spatial extent and coverage, and detailed deformation measurements in site-specific areas for foundation settlement and lateral spreads. The towns that were the primary focus of the investigations were; Gölbaşı, İskenderun, Dörtöy, Demirköprü, Türkođlu, although liquefaction related ground failures were observed in other towns as well. There was also liquefaction related reconnaissance on settlement induced flooding, bridge foundation failure, and transportation corridor damage.

### 4.1 Gölbaşı, Adıyaman

The town of Gölbaşı is located along a lake that was formed as a pull-apart basin due to a left-step of the EAF. The town is divided by Atatürk Boulevard passing through the town center, parallel to the Gölbaşı lake orientation. Figure 4.1 shows the areas in and around Gölbaşı inspected by GEER Teams.

#### 4.1.1 Regional and Site Observations - Gölbaşı, Adıyaman

Ground failure was significant at the inspected areas. Significant amounts of liquefaction-induced soil ejecta (with an apparent presence of fine-grained soils), lateral spreading, and differential settlements in several buildings were documented in many locations at the lakeside. Similar surface manifestations were also observed by Gölbaşı Lake. Structural damage was moderate to severe in the areas affected by liquefaction, and manifestation of liquefaction was not apparent in the other part of the town ( on visits approximately one month after the mainshock). Figures 4.2 and 4.3 illustrate ground failure manifestations with evidence of liquefaction-induced ejecta of what seems to be silty/clayey sands; samples were collected for testing at METU so key characteristics such as the particle size distribution and plasticity index can be assessed. In addition, cracking near buildings and vertical settlements on free field conditions (i.e., away from infrastructure) were also apparent.

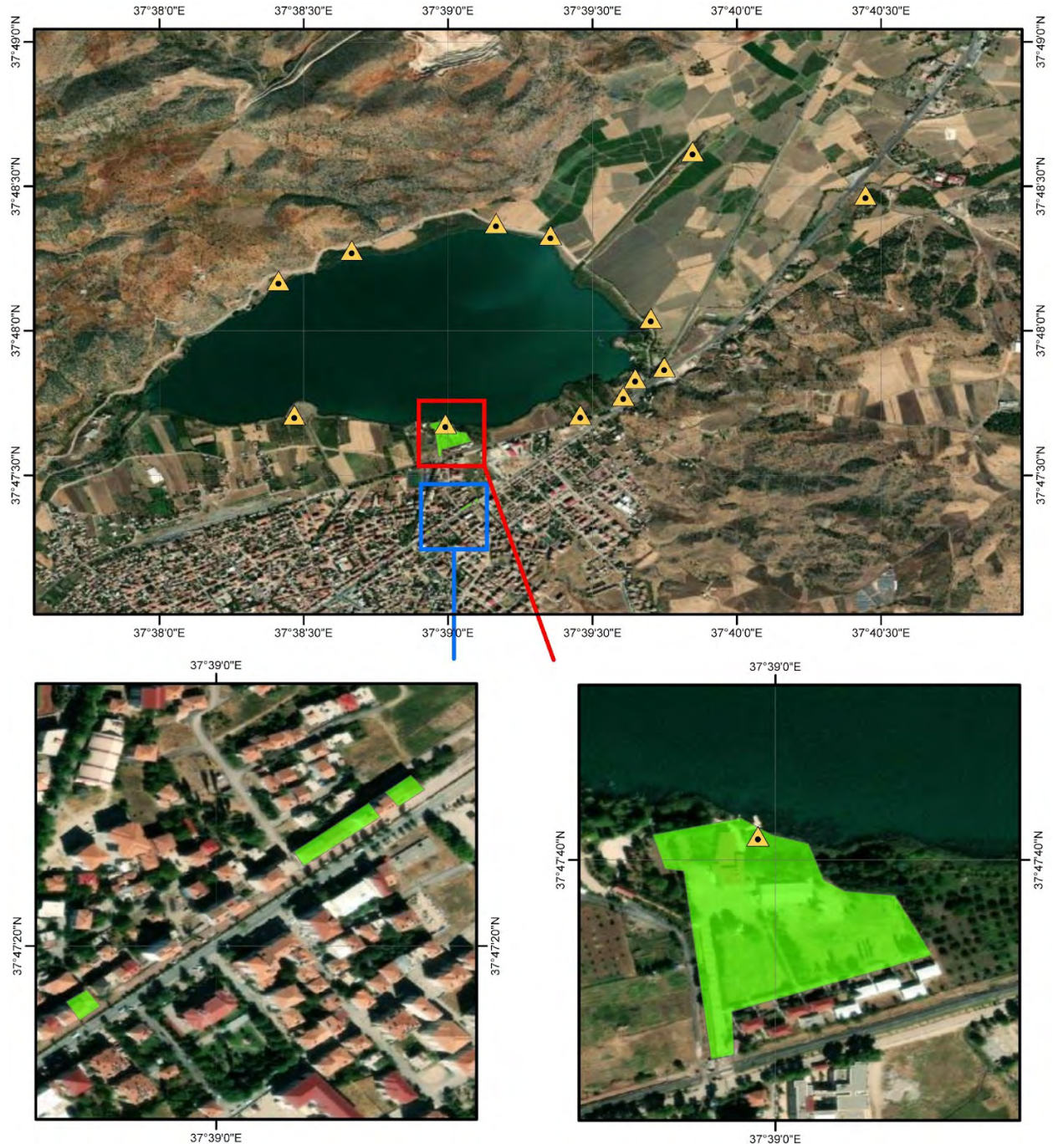


**Figure 4.1.** Gölbaşı areas inspected by GEER Teams. Top: General locations, triangles indicate areas with lateral spreading, squares indicate areas with inspected buildings. Bottom left: buildings inspected in the Golbaşı area. Bottom right: lateral spreading near the Golbaşı lake with drone images.



**Figure 4.2.** Liquefaction-induced ejecta in Adiyaman Gölbaşı region. Samples collected for laboratory testing (37.779003 N, 37.626491 E).



**Figure 4.3.** Liquefaction-induced cracks and fractures Gölbaşı (37.780058 N, 37.628457 E).

Figure 4.4 illustrates the conditions before and after the Kahramanmaraş earthquake sequence for a lateral spread near the Gölbaşı lake area based on Google Earth images from September 2022 and March 2023. Figure 4.5 shows images captured with a drone, illustrating the general and localized patterns of the lateral spreading. Figure 4.6 shows areas within the lateral spreading footprint inspected by the GEER ground team . The damage patterns are complex with significant cracking and displacements in the horizontal and vertical offsets. In addition, there is an apparent presence of ejecta through the cracks in the lateral spreading area.



**Figure 4.4** Aerial view of the lateral spreading area. Top: Google Earth Image on 9/2022. Bottom: Google Earth image on 3/2023. Referential Coordinates: 37.79° (Lat), 37.65 (Lon)

The horizontal deformations increase towards the lake with cumulative displacements estimated in the order of 2m based on local measurements. These measurements will be complemented with the future post-processing of the collected drone information. The two buildings in Figure 4.4 settled, which may have been influenced by the lateral spreading and localized soil-structure interaction effects. Settlements for the building on the East side of Figure 4.4 were estimated in the order of 50 cm. Measurements were not conducted in the other building due to access difficulties.



**Figure 4.5.** Drone images collected on the lateral spreading area on Feb 28, 2023. Top: General lateral spreading features. Bottom: localized features. Referential Coordinates: 37.79° (Lat), 37.65 (Lon)

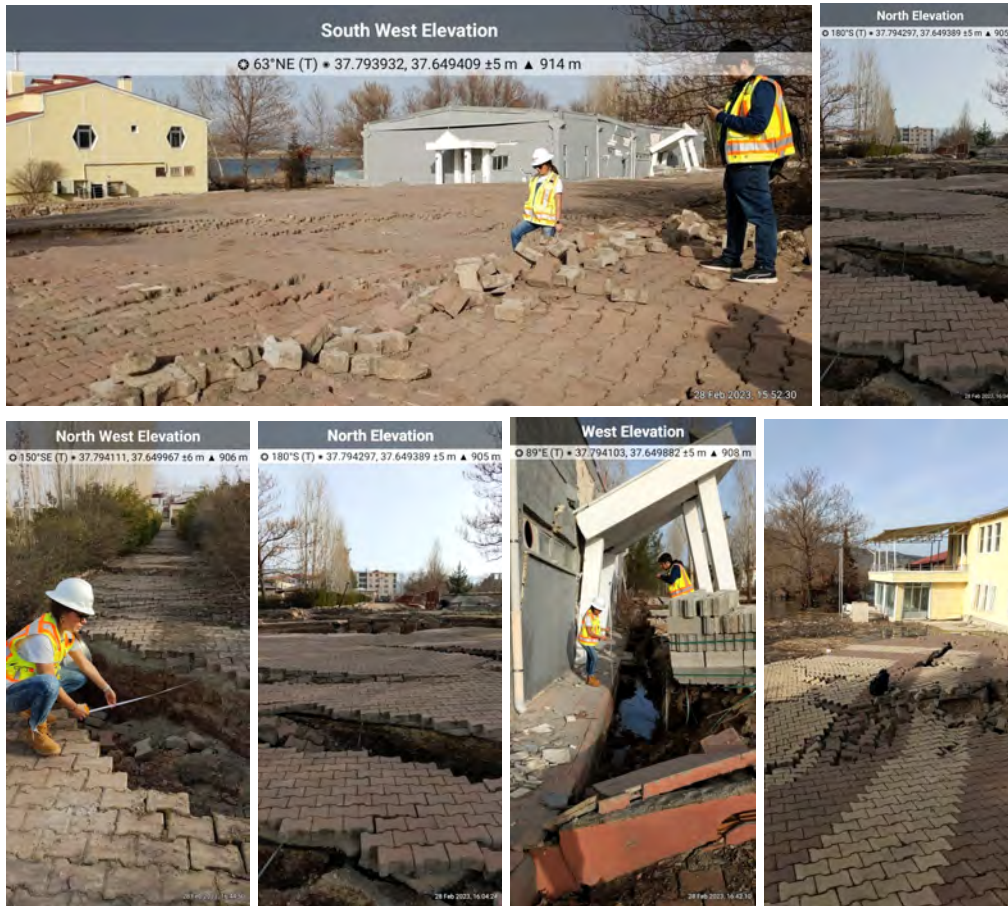


**Figure 4.6** Localized lateral spreading patterns. Photos taken on February 28, 2023.

Figures 4.7 -4.8 illustrate representative liquefaction-induced damage patterns in buildings at Gölbaşı. Figure 4.1 shows the general location of these buildings and the coordinates in the photos show specific locations. The patterns are complex, but the presence of ejecta is apparent and there is significant cracking. Specific descriptions are on the figure captions, but in general the observations can be grouped in four categories: (1) buildings with differential settlement (e.g., Fig. 4.7a,b), (2) buildings with uniform settlements (e.g., Fig. 4.8), (3) buildings with differential settlements and tilting (e.g., Fig. 4.7 c,d,e), and (4) few buildings with a significant tilt and only supported by near buildings (e.g., 4.7f)

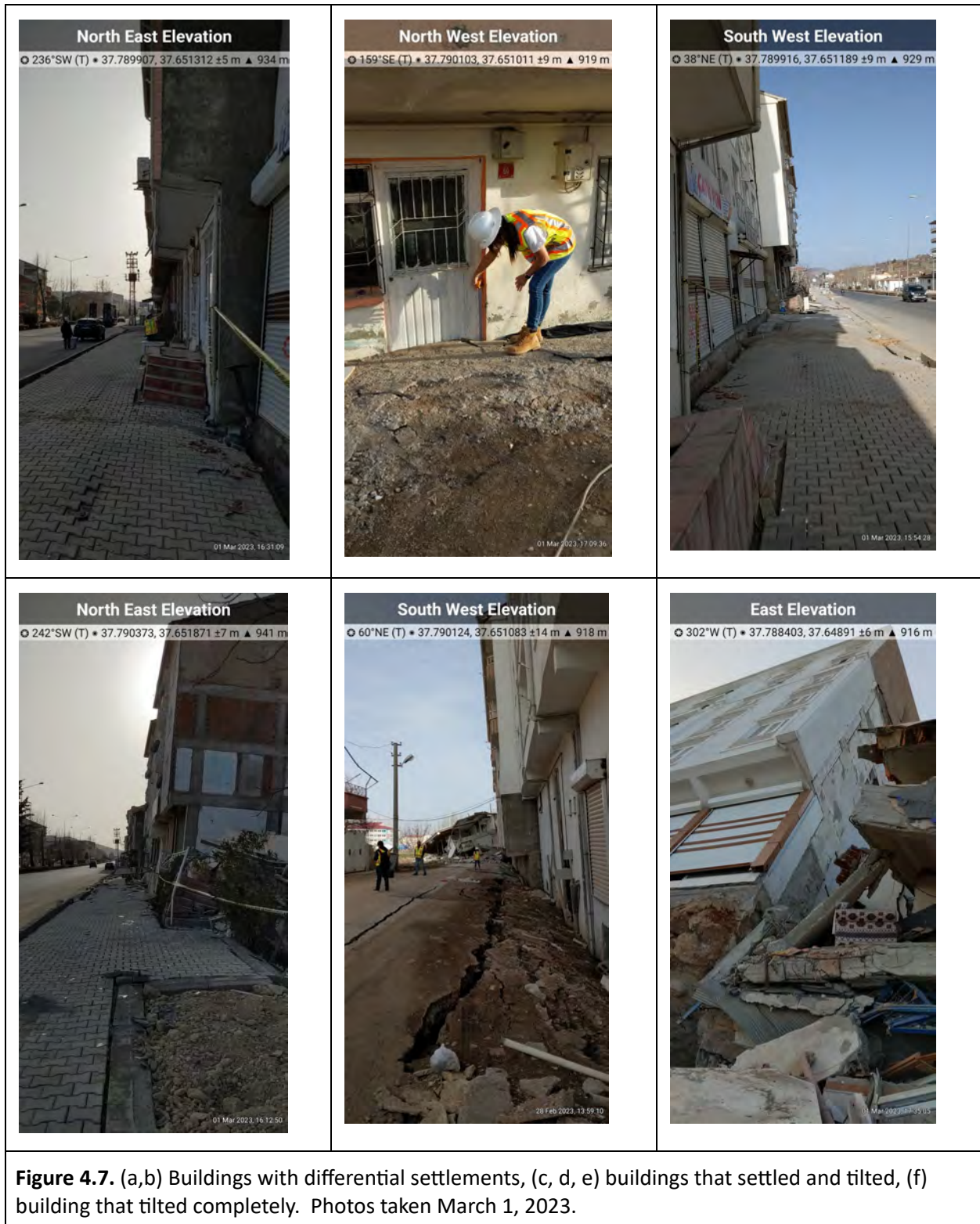






**Figure 4.8.** Buildings with uniform settlements in the Gölbaşı area (37.78686 N, 37.63738 E).

In general the inspected buildings showed significant damage, with a ground failure index mostly in the GF2 and GF3 category based on the index defined by Bray and Stewart (2000; Table 3.8) and used after the 1999 Kocaeli earthquake. Details of the ground failure indexes assigned to the inspected buildings in addition to other information of relevance (e.g., estimated settlements) are presented in Figures 4.9-4.11.



**Figure 4.9.** Top left: coordinates -37.78994, 37.65102, no tilt, vertical Settlement 20 cm, GF3, D1. Top right: coordinates -37.79000, 37.65115, no tilt, vertical settlement 30cm, GF3,D0. Bottom left: coordinates- 37.79003, 37.65122, no tilt, settlement 99 cm, GF3, D1. Bottom right: coordinates- 37.78978, 37.65076, 1 degree tilt, 10 cm settlement, D0, GF2.



**Figure 4.10.** Top left: coordinates -37.78981, 37.65089, no tilt, vertical Settlement 12 cm, GF2, D0. Top right: coordinates -37.78966, 37.65089, no tilt, vertical settlement 30cm, GF3,D1. Bottom left: coordinates- 37.78969, 37.65099, no tilt, settlement 18 cm, GF2, D0. Bottom right: coordinates- 37.78976, 37.65113, no tilt, 10 cm settlement, GF2, D0.



**Figure 4.11.** Top left: coordinates -37.78984, 37.65125, no tilt, vertical Settlement 20 cm, GF2, D1. Top right: coordinates -37.78996, 37.65139, 5° tilt, vertical settlement 28cm, GF3,D0. Bottom left: coordinates- 37.79014, 37.65161, 3° tilt, settlement 23 cm, GF3, D1.

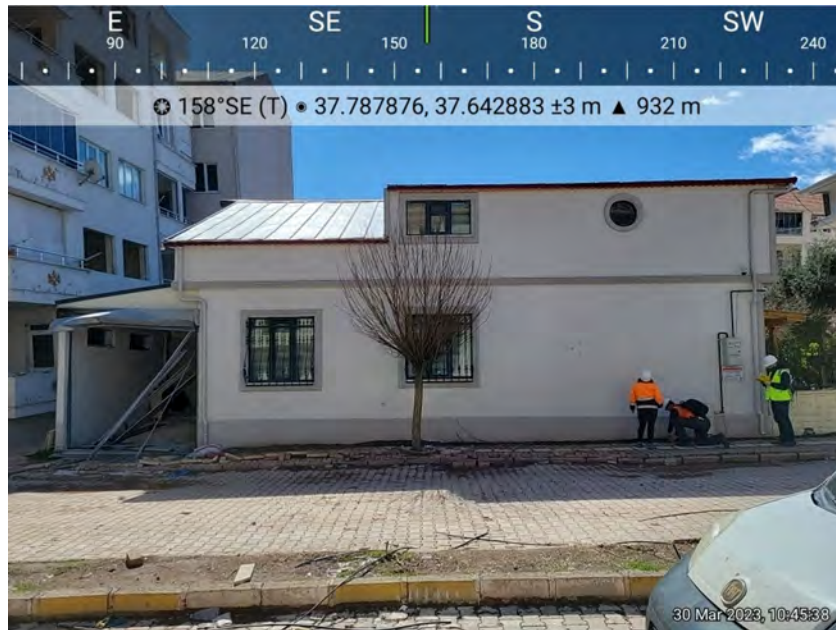
#### **4.1.2 Building Tilt and Settlement - Gölbaşı, Adıyaman**

The GEER Phase 3 Team documented building settlements in Gölbaşı on March 30 2023. Nine individual buildings were documented, as well as two apartment complex groups. Observations from two adjacent individual buildings and one apartment complex group is included herein. Additional observations will be written into the next version of the report.

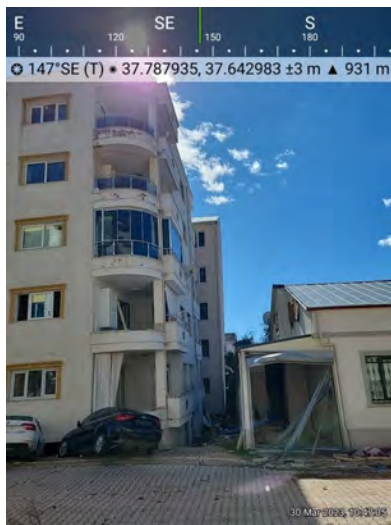
##### **(a) Two 2-story residential buildings on Zübeyde Hanım Caddesi**

Two adjacent two-story residential buildings were surveyed to document the differences in performance. A two-story plaster and cinder single residential building is located on the southeast corner of Zübeyde Hanım Caddesi and Gazi Caddesi (37.787737N, 37.642873E). The second building is a two-story multi-residential building with a partial basement located on the northeast corner of Zübeyde Hanım Caddesi and 52. Sk (37.787559N, 37.642979E). These buildings are documented herein due to the contrasts in their performance. Ejecta was documented in the yard between the two buildings and two soil samples were obtained. These buildings are described in further detail below.

Negligible settlement was observed at the two-story single-residential building (37.787737N, 37.642873E). The building is a 10.32 m north-to-south and 13.4 m east-to-west with an additional 2 m wide garage on the east side (Figure 4.12a). The building is approximately 5.6 m high. The structure appears to be cinder block and plaster construction with no apparent basement. Although there was negligible settlement documented, there was damage to the structure that appeared to be due to ground deformation at the structure to the east. Figure 4.12b shows the notable settlement at the east-adjacent structure. An approximately 10-cm crack was observed on the south side of the building near the connection between the house and the garage; additionally, a 1 degree tilt towards the house was measured on the east wall of the garage.



(a)



(b)



(c)

**Figure 4.12.** 2-story cinder block and plaster construction residential building in Gölbaşı with no discernable settlement: (a) (37.787876N, 37.642883E) street view of the building with attached garage showing disturbance in the adjacent sidewalk and road, (b) (37.787935N, 37.642983E) settlement at adjacent 5-story building and its effect on the attached garage, (c) (37.787712N, 37.643074E) crack that opened on the south side of the house due to displacement of the garage. Photographs taken on March 30, 2023.

Significant settlement was observed beneath the two-story building with a partial basement as shown in Figures 4.13a-c. The building was measured to be 9.9 m north-to-south and 12.2 m east-to-west with an approximate height of 7 m. Settlement at the front door building entrance at the southwest corner was measured to be over 1.1 m. Ponded water was present along the south side of the building. The east perimeter of the building settled about 20 cm more than the west perimeter of the building, inducing some tilt. The building owner told our team that the building was originally constructed without a basement, but it was later added.



**Figure 4.13.** Settled two-story residential building with a partial basement in Gölbaşı: (a) view of building from southwest corner (N37.787388°, E37.642918°), (b) collapsed deck over partial basement along north wall (N37.787781°, E37.642868°), (c) front door entrance at southwest corner with over 1.1 m of measured settlement (N37.787494°, E37.643019°). Photographs taken on March 30, 2023.

**(b) Two 5-story apartment buildings on 511 Street**

Two adjacent five-story apartment buildings on 511 street in Gölbaşı were observed to document their differences in performance (Figure 4.13a). Both apartment buildings are nearly identical in appearance, with the exception that the south building (N37.789046°, E37.642642°) has a one-story basement and the north building (N37.789318°, E37.642494°) has no basement. The structures were newly constructed within the last 4 years, and are composed of a reinforced concrete frame with masonry infilled walls. They are located just within 700 m of the Gölbaşı Lake to the North, and are adjacent to a channelized creek just across 511 street at the south.

Both buildings appeared structurally sound, but had shown obvious signs of settlement (typ. greater than 10 cm) around their perimeter. Settlement and ground cracks were observed around the south building (with a basement). The owners allowed access into the building's basement, which was observed to have some ponded water along its southern wall (Figure 4.14c). Although the owners mentioned that water often puddles in the basement due to the lack of a sump pump, the water may also indicate some tilt towards the south. Traces of soil (i.e., possible ejecta) and minor cracking of the concrete floor was also observed near structural columns within the basement. The north building showed significant settlement and separation from the adjacent ground at its southeast corner (Figure 4.13c). Extensional cracking observed along the north and south wall of the building (parallel to the lakeshore) totaled about 45 cm, which approximately matched the accumulated cracking along a nearby concrete wall (perpendicular to the lakeshore) (Figure 4.14d). Lidar scans were performed for these apartment complexes; the data are being processed and will be included in the next version of the report.





## 4.2 İskenderun, Hatay

İskenderun is the second most populated district of Hatay, located west of the Amanos Mountains along the eastern shore of the Gulf of İskenderun. İskenderun has approximately 152 km of coastline and hosts the second biggest port of Türkiye, the Port of İskenderun. The modern center of the district is built on the alluvial plain on the flanks of the Amanos Mountains by the sea shore. This city center was developed in a generally low lying area and the Çay region was referred to as “the swamp” by locals. The city experienced significant growth in the 1950s and 1960s which resulted in an increase in population and urbanization to this alluvial plain.

### 4.2.1 Regional and Site Observations - İskenderun, Hatay

İskenderun was one of the most impacted districts of Hatay after the 2023 earthquakes. In the areas close to the flanks of the Amanos Mountains the observed damage was mainly structural. In the neighborhoods that are closer to the shore the observed damages were mainly geotechnical dominated by liquefaction induced settlement and lateral spreading, though several major buildings collapsed without evidence of ground failure. Figure 4.15 shows the areas visited between February 26 and March 5 where liquefaction-induced damage was observed.

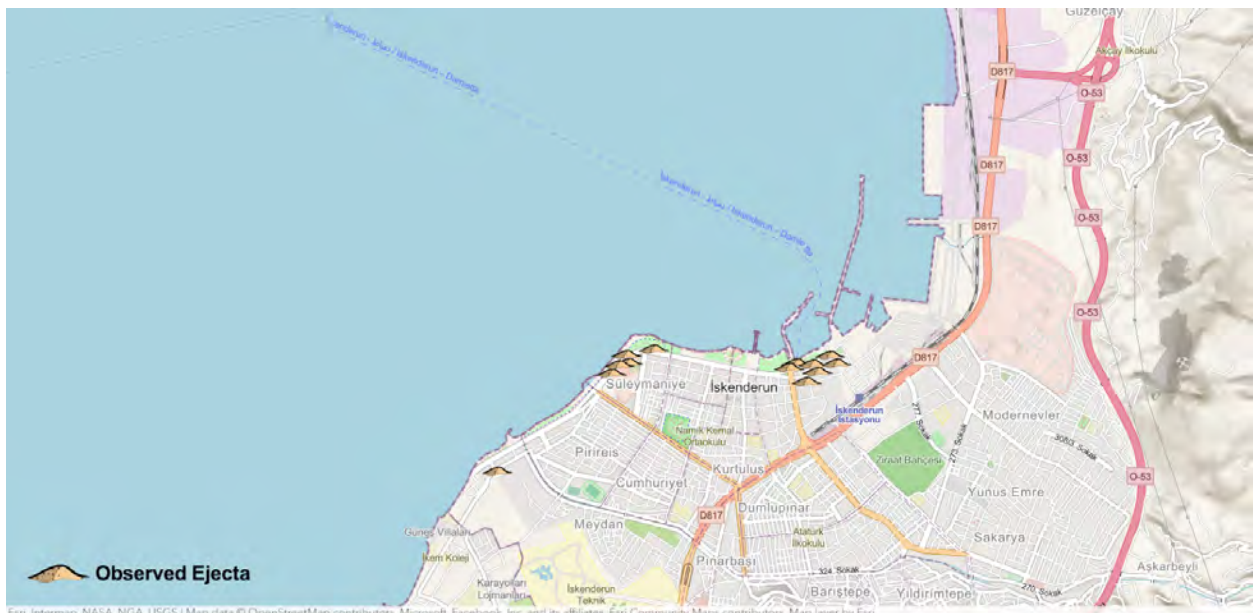


**Figure 4.15.** Areas visited between February 26 and March 5 (Phase 2) where liquefaction induced hazards were observed.

The Atatürk Boulevard, which runs along the coastline, was buried with sand ejecta (up to 30 cm, according to locals) in several stretches of the road following the first mainshock (M7.8). The pictures taken by the locals that were shared with our team show a significant amount of sand ejecta that covered the Atatürk Boulevard on its northern end in the Çay District (Figure 4.16).



**Figure 4.16** Liquefaction induced sand ejecta that inundated portions of Atatürk Boulevard after the Mw7.8 mainshock photographed by a local in the area prior to the second main shock.



**Figure 4.17.** Liquefaction ejecta observed along the waterfront park along Atatürk Boulevard. (36.59431, 36.16419)

While significant amounts of ejecta covered Atatürk Boulevard, and the parking lots and grass areas along the waterfront in the Çay District, there were no indications of sand boils or ejecta along the waterfront park to the south of the Çay District. Based on discussions with the locals, the majority of the asphalt road was covered in ejecta; however, there were no sand ejecta observed along the waterfront grass areas immediately next to the Atatürk Boulevard (Figure 4.18) . The waterfront park was built by filling up the shoreline in the 1980s. The fill material in

the park areas seemed to be mainly composed of clayey soils which may have acted as a nonliquefiable crust that minimized ejecta. This needs to be verified with subsurface investigations.

Some ejecta were observed at isolated spots along the waterfront (Figure 4.19). However, the ejecta observed along the boardwalk of the waterfront park is composed of terracotta sand with fine gravel, unlike the liquefaction-induced ejecta observed along Atatürk Boulevard and other locations. Cracks along the waterfront park were also observed, these cracks run roughly parallel to the coastline, indicating potential lateral spreading. Observed cracks were as wide as 16.5 cm. Some large cobbles observed along the boardwalk indicated potential sea overflow. The ground around the amphitheater that is located in the waterfront showed signs of ~23 cm vertical and ~33 cm horizontal displacement (Figure 4.20).



**Figure 4.18** Despite Atatürk Boulevard being covered by ejecta after the earthquakes, no ejecta was observed in the grass areas of the neighboring waterfront park. Coordinates: 36.59431, 36.16426.

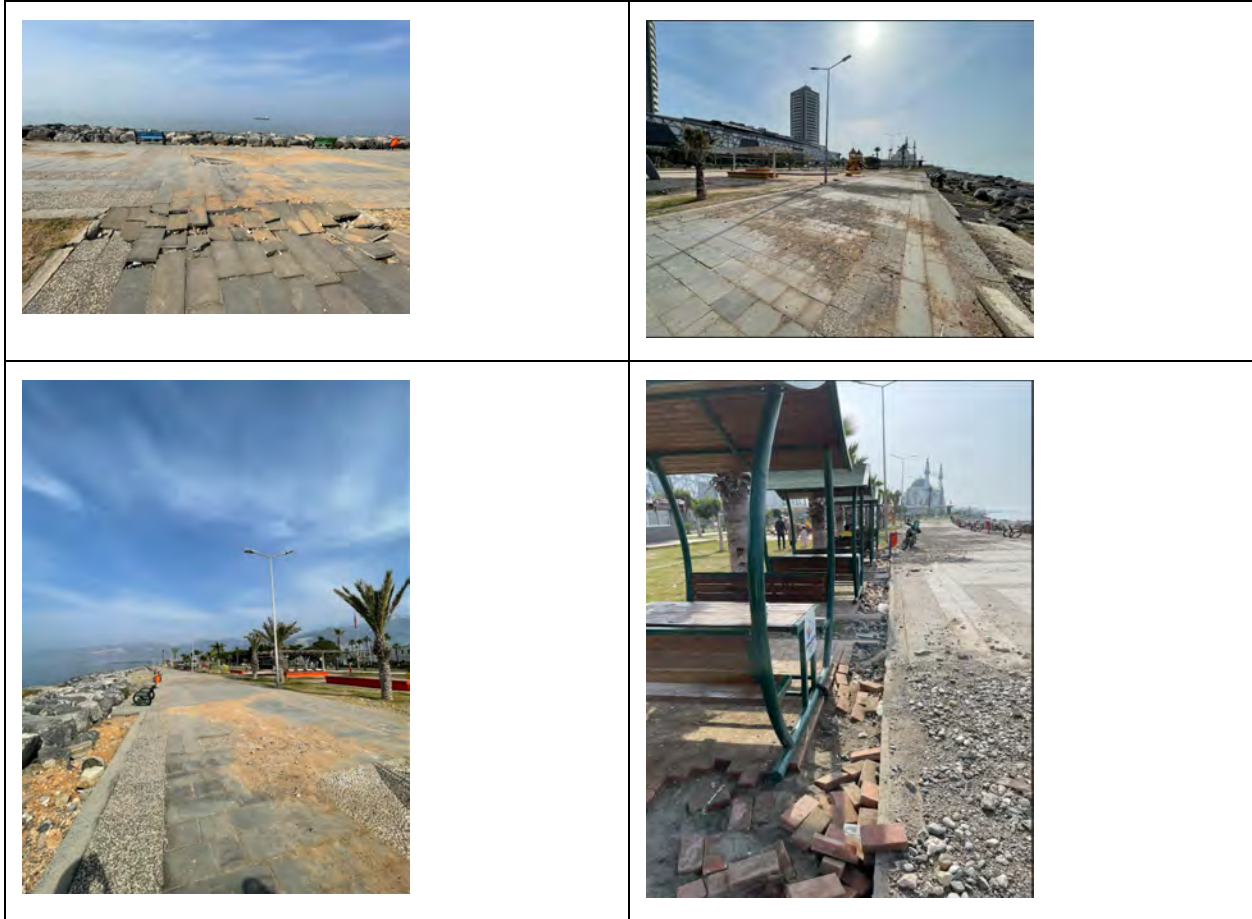


**Figure 4.19.** Observed cracks and base course ejecta along the waterfront boardwalk. (March 2, 2023; 36.59456N, 36.16024E)



**Figure 4.20.** Lateral and vertical displacement at the amphitheater located on the waterfront boardwalk. (March 2, 2023; 36.59573N, 36.16206E)

The northern end of the Atatürk Boulevard around Çay neighborhood was built with 4 to 5 story residential buildings. A majority of these buildings did not appear to suffer significant structural damage but instead experienced significant damage due to liquefaction induced ground failure. The measured building settlements in this area were as much as 60 cm with respect to the free field (Figure 4.21).







**Figure 4.21.** (5 images in all) Some four- to five-story buildings located to the northern end of the Atatürk Boulevard near Çay neighborhood experienced liquefaction induced settlement over 60 cm in some locations. Some of the buildings that included a basement experienced less liquefaction-induced settlement but the basement levels were flooded.

Surface manifestations of liquefaction in terms of sand ejecta were documented both in the free field and around the buildings that settled after the earthquakes. Figure 4.22 shows spots of sand ejecta in İskenderun, Hatay. Liquefaction-induced building settlements (Figure 4.23) were estimated as 35-50 cm throughout the Çay, Piri Reis, Savaş, and Süleymaniye districts. After the earthquake, the coastal line with a 200-300 m wide area remained under the water for a while

apparently because of liquefaction effects based on discussions with the locals. Evidence of surface manifestations are significant, and the thickness of the ejecta reaches up to 25 cm at some locations.



**Figure 4.22.** Liquefaction-induced ejecta in Iskenderun, Hatay (36.812645 N, 36.181357 E)

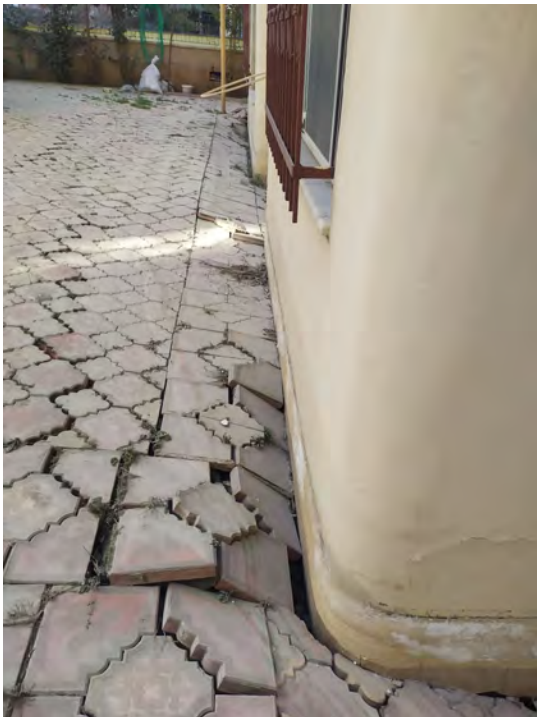


**Figure 4.23:** Liquefaction-induced building settlements in Iskenderun, Hatay (36.589045 N, 36.176512 E).

The area located south of İskenderun Harbor on Atatürk Boulevard was exposed to significant liquefaction. The soil ejecta thickness varies between 10-25 cm (Figure 4.24), and eyewitnesses stated that the soil boils continued two days after the earthquakes at recreational areas and along the coastal road. There were liquefaction-induced lateral spreading cracks in places that measured on the order of 25-35 cm on average (Figure 4.25). The pump house, which is being used for draining the excessive water, was tilted almost 50 cm toward the sea but still functioning.



**Figure 4.24:** Liquefaction-induced ejecta in Atatürk Boulevard (36.591661 N, 36.175382 E).



**Figure 4.25:** Examples of liquefaction-induced lateral spreading at Atatürk Boulevard (36.59147 N, 36.174378 E).

The İskenderun Harbor is located on Atatürk Boulevard, where there was evidence of liquefaction-induced lateral spreading after the earthquakes. The lateral spreading varied between 50-100 cm on the dock (Figure 4.26). According to the eyewitnesses, the docks were found directly on the sand layer, and the sand ejected due to ground shaking and continued for more than one day. They stated that the whole port settled 80-100 cm (Figure 4.26), and boulders on the breakwater spread 3-15 meters away from its original position (Figure 4.26).





**Figure 4.26:** (6 images in all) Lateral spreading and settlements at Iskenderun Harbor (36.59308 N, 36.175733 E)

Soil ejecta was widely observed in the Iskenderun port area (Figure 4.27). The thickness of soil ejection was roughly 10 cm locally. Additionally, gravel ejection was observed (Figure 4.27 right). A total of 25-50 cm lateral spreading was observed due to liquefaction. The port was not functioning due to damage and misalignment of the cranes during the earthquake.



**Figure 4.27:** Sand boils, cracks and gravel ejecta due to seismic soil liquefaction in a private port in Iskenderun (36.603545 N, 36.19225 E).

#### 4.2.2 Detailed Lateral Spreading Measurements - İskenderun, Hatay

GEER Team Phase 3 obtained detailed measurements of lateral ground displacements (i.e., lateral spreading) over a total of seven transects perpendicular to the İskenderun shoreline. Four of the transects labeled as LS-1 to LS-4 were taken directly from the waterfront and are documented herein. Three other transects labeled as LS-5 to LS-7 were taken in the Çay District near buildings with noticeable settlement, and are detailed later in this report.

The lateral spreading transects herein were measured by taking the distance from a set datum (e.g., inside of waterfront seawall) to all observed cracks along that line. The width of all crack openings were measured and accumulated along each transect, in a manner similar to the methodology of Robinson et al. (2010) used in the 2010 Darfield earthquake in Christchurch, New Zealand. The transect locations were chosen to typically coincide with long stretches of concrete blocks and pavement, where crack openings were easier to identify (e.g., not obscured by vegetation) and relatively unaffected by water action from the floods that occurred since the earthquake events.

The measurements were taken on March 28 and April 1 of 2023. A rainstorm occurred on March 29 that caused extensive flooding, inundating several city streets over 200 m from the waterfront. Notable differences along the shoreline are presented herein, before and after this rainstorm event.

A map depicting the transect locations of LS-1 to LS-4 is presented in Figure 4.28 below. Figures 4.29 to 4.32 depict photos of each lateral spreading transect. Figure 4.33 depicts the accumulated measured lateral displacement along each transect from the shoreline.

LS-2 was taken along the side of the Doğan restaurant 1-story patio building. LS-3 was taken about 10 m away to understand whether LS-2 was influenced by the structural performance of the patio. Also, accumulated cracking along the base of the patio building wall and extending guardrail wall approximately matched adjacent ground cracking at LS-2 (about 30 cm of cracking was measured over a distance of about 19 m along the walls).

LS-4 was measured twice on March 28 and April 1. It was observed that the seawall rubble was about 1 m higher and the reinforced concrete parapet wall behind the rubble was much more heavily damaged during our visit on April 1. Construction equipment wheel tracks were also observed along the waterfront in this area. It is believed that additional rubble was manually placed as a temporary protection against future storms. Our measurements indicate that lateral displacements increased by about 7 cm over the intervening period. Despite potential uncertainties in our measurements, this may have been caused by movement or vibrations from heavy machinery used to place the rubble, scour and movement of surficial features (e.g.,



concrete pavement blocks) during the March 29 storm, or delayed or residual lateral spreading since the earthquake.



**Fig 4.28.** Map of measured lateral spread locations (LS-1 to -4) extending from the seawall in Iskenderun, Hatay Province, Türkiye (Google Earth® image dated February 16, 2023, centered near N36.5928°, E36.1632°).



(a)



(b)



(c)



(d)

**Fig 4.29.** Photos of lateral spread LS-1 taken March 28, 2023: (a) observed 0.5 to 0.8 m reduction in height of rubble mound seawall at start of LS-1 relative to infilled area of Nihal Atakaş Camii mosque (N36.59356°, E36.15827°), (b) pavement tile separation near shorefront (N36.59333°, E36.15809°), (c) pavement crack extending along southwest bound portion of Atatürk Blvd (N36.59299°, E36.15882°), (d) separation between curb and bike lane (N36.59340°, E36.15866°).



**Fig 4.30.** Photos of lateral spread LS-2 taken April 1, 2023: (a) seawall at start of LS-2 (N36.59367°, E36.167191°), (b) sunken park bench and spreading along eastern wall of Doğan restaurant patio (N36.59367°, E36.167191°), (c) cracks near column at southeast corner of patio (N36.593392°, E36.167236°), (d) cracking along back of patio (N36.59345°, E36.16712°).



(a)



(b)

**Fig 4.31.** Photos of lateral spread LS-3 (10 m east of LS-2) taken April 1, 2023: (a) seawall at start of LS-3 (N 36.593433°, E36.166759°), (b) walkway at end of LS-3 (N36.593105°, E36.167324°).



(a)



(b)

**Fig 4.32.** Photos of lateral spread LS-4 along tiled concrete walkway: (a) on March 28, 2023 (N36.59300°, E36.16870°), (b) on April 1, 2023 (N36.59300°, E36.16870°). Notice damage to seawall and higher rubble mound in more recent photo, presumably caused by additional rubble placement in the intervening time between photos.

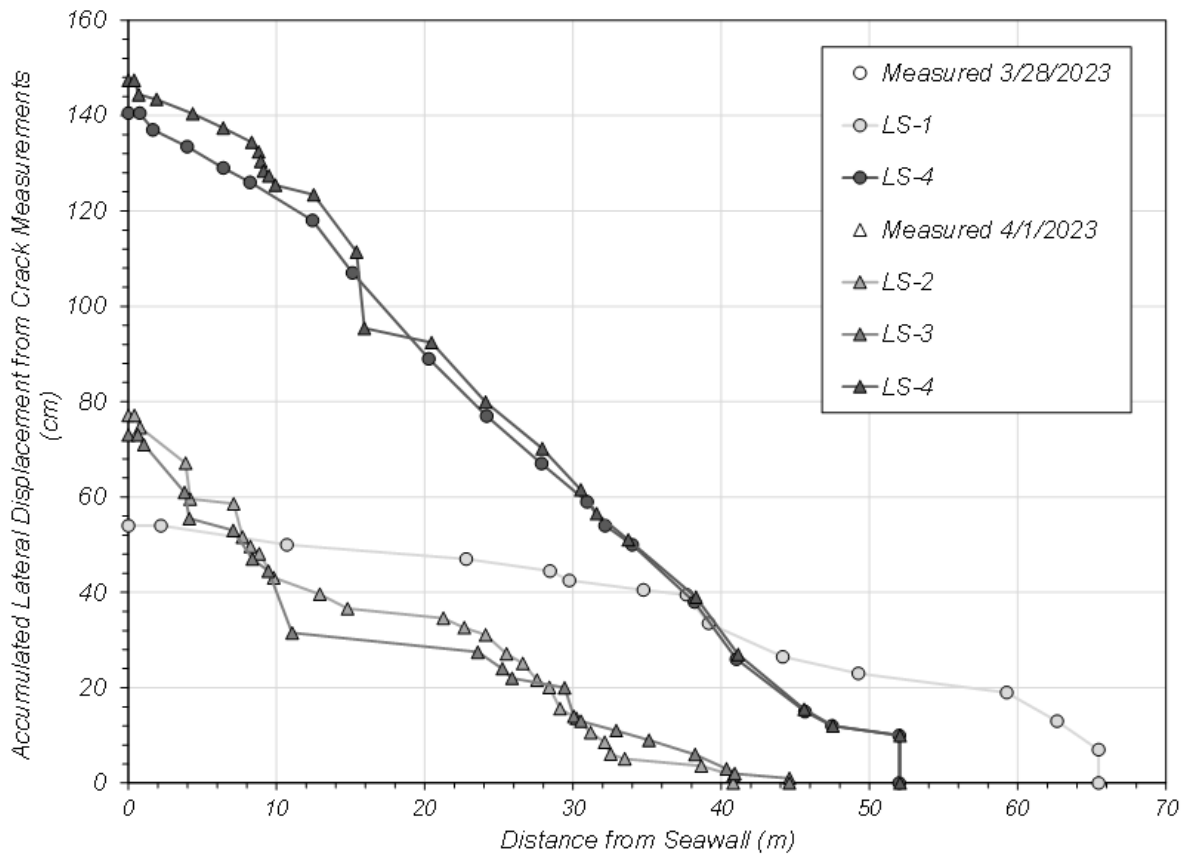


**Fig 4.33.** Accumulated lateral displacements as measured from crack opening widths along LS-1 to -4 relative to distance from the seawall in Iskenderun.

#### 4.2.3 Lateral Ground Displacements near Çay District Mid-Rise Buildings - İskenderun, Hatay

Lateral ground displacements were measured by GEER Team 3 along three transects near Çay district buildings in İskenderun from March 28 to April 1, 2023. The purpose of these measurements was to check the total local ground displacement relative to adjacent buildings that were also observed to settle (i.e., the buildings described in Section 4.5.1). These measurements can help indicate whether the cracks observed adjacent to the buildings primarily occurred due to vertical building movements (i.e., settlement-induced ground extension) or global lateral movements (i.e., lateral spreading as observed along the İskenderun shoreline and described in section 4.2.1 of this report). The transects, labeled as LS-5 to -7, are mapped in Figure 4.34. Measurements were taken following a similar procedure as described in section 4.2.1.



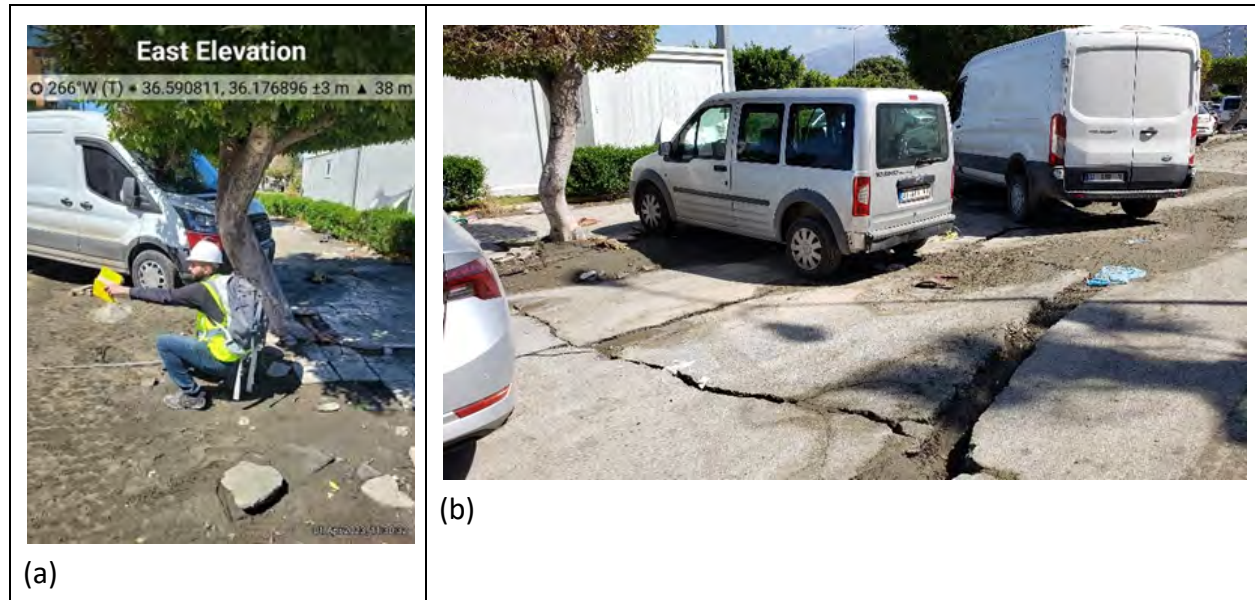
**Fig 4.34.** Map of measured lateral spread locations (LS-5 to -7) extending from Atatürk Boulevard in the Çay district of İskenderun, Hatay Province, Türkiye (Google Earth® image dated February 16, 2023, centered near N36.5906°, E36.1784°).

As indicated in the map, transects LS-5 to -7 did not extend to the shorefront. This was due to the GEER team’s inability to access the boat dock, and the difficulty of deducing cracks within the adjacent grassy park that may have been obscured following recent floods. However, significant spreading likely occurred shoreward of the measured transects, as evidenced by preserved sand boils observed in the grassy park and extensional cracking observed along the perimeter of the boat dock as shown in Figure 4.35. The documented cracks were visible along the paved ground in the vicinity of the buildings of interest.



**Figure 4.35.** Sand boils and lateral spreading near boat dock in Cay district of Iskenderun, Hatay Province, Türkiye (N36.591476°, E36.178898°).

Figures 4.36 to 4.38 depict photos along each lateral spreading transect. Figures 4.36a-e depict measurements along LS-5, which begins at the sidewalk near the park along the north side of Atatürk Blvd. A separated block of about 2-m-wide and >30-m-long was observed along Atatürk Blvd, exhibiting a minor down-drop vertical offset of about 5 cm and bounded by 10-12 cm and 18-20 cm wide lateral extension cracks (Fig 4.36b). Additional minor cracking was observed southward along LS-5, including a 5 cm crack aligned with the front edge of a nearby building foundation at the south side of Atatürk Blvd.







Figures 4.37a-d depict measurements along LS-6, which begins at the south side of Atatürk Blvd and runs between two rows of buildings parallel to Atatürk Blvd. The adjacent buildings had settled and measurements of settlement are discussed in Section 4.6 of this report. Observed ground cracking was typically minor directly adjacent to the buildings, but became more pronounced in the alley/backside area between the two rows of buildings. Measurements taken along a lot boundary wall in this area (Figures 4.37b-c) depicted extension cracks totaling over 17 cm in width over an 8 m segment (>2% extensional strain). The building at the south of LS-6 (No. 24 Kaan Ela) was built over deep foundations, but the failure of adjacent fill had created a void along the foundation perimeter (Figure 4.37d). Shore parallel cracks were not observed in this area but may have been accommodated by the void.



**Figure 4.37.** Photos of lateral spread LS-6 taken March 28 and 29, 2023: (a) start of LS-6 at south sidewalk along Atatürk Blvd in front of building Belli Apartment #18A (N36.590652°, E36.177784°), (b) cracking along wall behind buildings (N36.590435°, E36.177746°), (c) cracking along wall behind buildings (N36.590478°, E36.177905°), (d) end of LS-6 along the side of building Kaan Ela #24 (N36.590458°, E36.17794°).

Figures 4.38a-b depict measurements along LS-7, which begins at the south side of Atatürk Blvd and runs along the east edge of the “four buildings” case study site of Section 4.6.1.3. Observed ground cracking was typically minor directly adjacent to the northeast corner building (No. 28). The east side of this building was an empty lot being used for holding post-earthquake debris. Cracking along LS-7 became more pronounced in the alley/backside area of the buildings, where the hogsback deformation bulge was observed (Figure 4.38b).

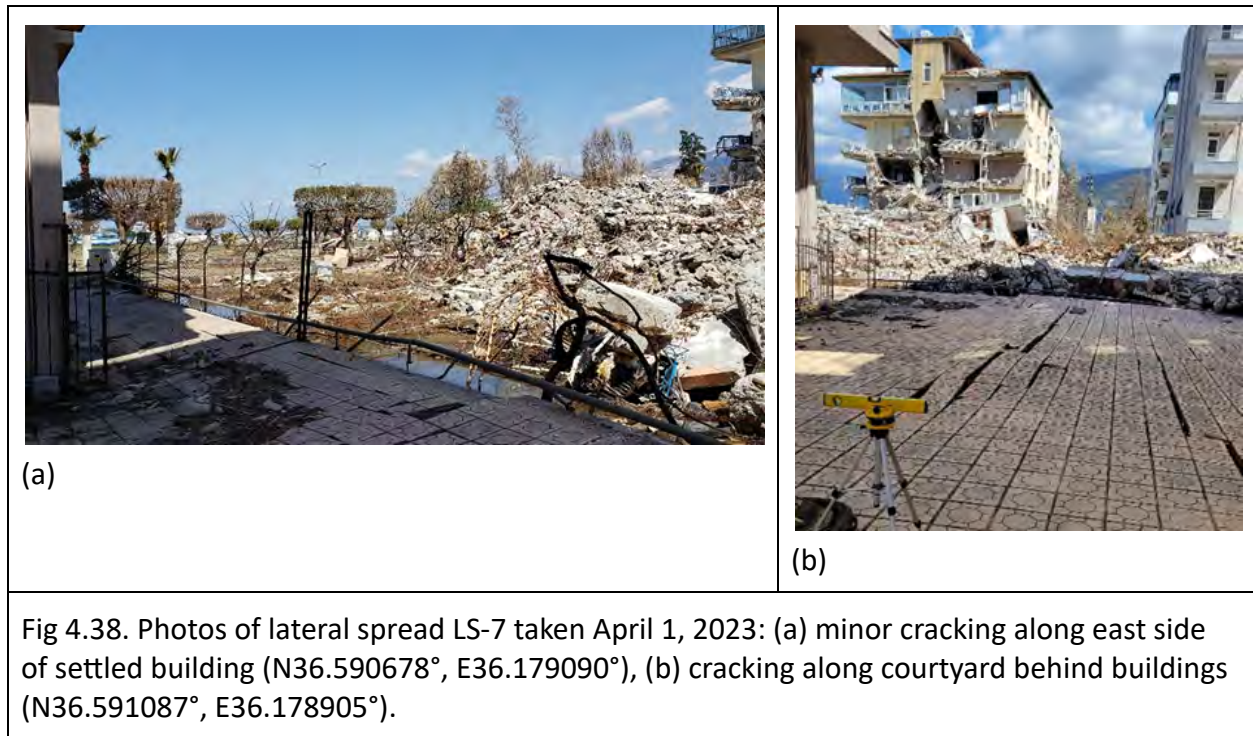


Figure 4.38 depicts the accumulated measured lateral displacement along each transect relative to their distance from the shorefront. This allows for a consistent comparison between transects, relative to potentially global shoreward lateral spreading displacements. As previously discussed, the boat dock and park north of the transects herein experienced extensive cracking as well, but were not easily documented. LS-5 depicts the extensive displacements observed along Atatürk Blvd, between about 70 to 90 m away from the shorefront at the edge of the boat dock for this transect. All transects also depict a higher rate of displacements in the alley behind the two rows of buildings, about 120 to 140 m from the shoreline for all transects. A reduction in the rate of observed cracking is visible in the areas along the building foundations (i.e., typ. 90 to 120 m, and over 140 m from the shorefront). Cracking was not observed along Bahçeli Sahil Evler Street to the south of the buildings. While this data suggests an influence of building foundations on the propagation of ground cracks, it remains unclear whether the extensive network of cracks observed in the building alleys was primarily caused by global seaward lateral spreading, building settlement, or a combination of both effects.

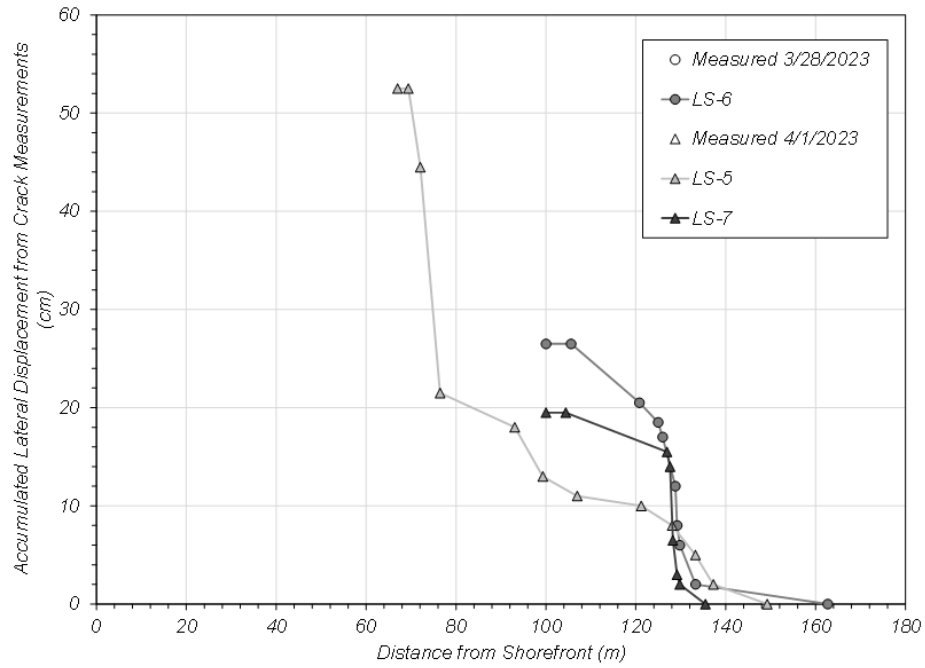


Fig 4.39. Accumulated lateral displacements as measured from crack widths along LS-5 to -7 relative to distance from the approximate shorefront of the Çay district in İskenderun.

#### **4.2.4 Post-earthquake flooding - İskenderun, Hatay**

Residents of İskenderun reported regular flooding in the near-shore areas, including the Çay district, following the 6-February earthquakes. These reports from residents were consistent with observations from the Phase 3 team that many owners were pumping water from their basements in the Çay district. The owner of No. 28 Bahçeli Sahil Evler Caddesi, Ahmet Palalıoğlu, explained that he was sealing off the basement windows to his apartment building due to the regular flooding. Additionally, standing water was seen along the edges of buildings along Ataturk Boulevard between 41. Sk. and Ziya Gokalp Cadiz (approximately 36.591562N and 36.170615 E) on March 28th. The Phase 1 team collected reports that there was a broken water main in İskenderun. Although the more frequent flooding since the earthquake is not currently attributable to liquefaction ground settlement over a large area of İskenderun, it is a possible explanation combined with damage to shoreline and water distribution infrastructure.

The GEER Phase 3 team observed notable flooding that took place on March 29th 2023 (Figure 4.40); on this day there was heavy rainfall and strong winds in the İskenderun area. The flooding was observed from the Cay district and southeast along Ataturk Boulevard and the shoreline to past Mithatpaşa Cadiz. The photos show that there was flooding at least two roads in from the shoreline, including past Mareşal Fevzi Çakmak Caddesi (Figure 4.40a), and past Bahçeli Sahil Evler Caddesi (Figure 4.40b) in the Cay district. The flooding on April 1st was observed by the team to advance from the shoreline. The team returned to İskenderun and Çay on April 1, 2023 when flooding had largely subsided, however there was significant standing water remaining. Drone footage taken on April 1 2023 with observations of standing water in the Çay district is shown in Figure 4.41.



(a)

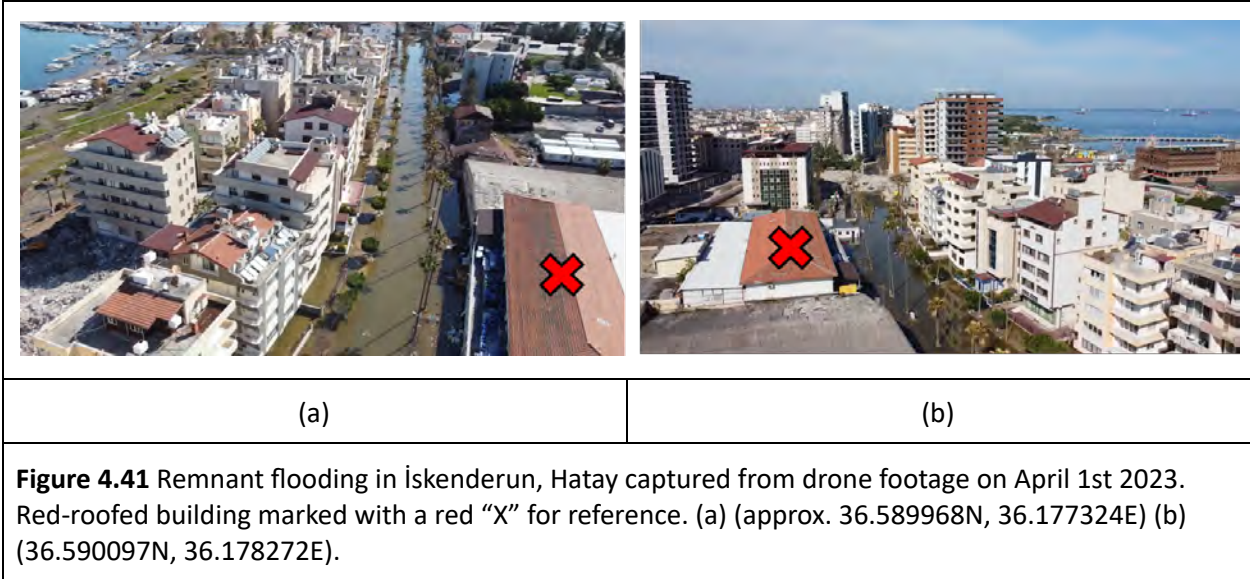


(b)



(c)

**Figure 4.40** Flooding in İskenderun, Hatay: (a) (36.591183N, 36.169776E) flooding in a commercial district (b) (36.5910217N, 36.1791387E) flooding in the Çay district, (c) (36.592232N, 36.168659E) flooding of Atatürk Boulevard, near a commercial district. Photos taken on March 29<sup>th</sup> 2023.



#### 4.2.5 U-box D817 wall underpass flooding and performance - İskenderun, Hatay

Post-earthquake flooding was observed in the D817 underpass on Google Earth images from February 8 2023 (Figure 4.42). The underpass is approximately 7.5 m deep (measured with a laser distance tool) from the surface of the road-level at the intersection of İsmet İnönü Caddesi and D817 (36.582926N 36.168968E). The GEER Phase 3 team observed negligible damage (i.e., absence of tilting or cracking in retaining walls, deformation or cracks in road pavement) to the underpass structure on March 28th 2023 (Figure 4.43a). Some damage to the surface road-level sidewalks was observed (Figure 4.43b). Local taxicab drivers reported that the underpass flooded with about 1 m of water and a significant amount of sand soon after the earthquake. The approximate elevation of the surface road at the İsmet İnönü Caddesi and D817 intersection is 10.5 m to 11 m above sea level (GPS elevation), therefore the elevation of the underpass roadways is approximately 2.5 m to 3 m above sea level at this location. On March 28th 2023 some seepage was observed at the retaining wall joints and stormwater drains (Figure 4.43c). The Phase 3 team observed no flooding in the underpass on March 29th when major flooding occurred in the near-shore areas of İskenderun.



**Figure 4.42.** Image of u-box underpass in İskenderun, Hatay from Google Earth on 8-February-2023, showing flood water in the underpass.





#### 4.2.6 Building Settlement and Tilting- İskenderun, Hatay

The GEER Phase 3 Team documented building settlements in İskenderun on March 27, 28, 29 and April 1, 2023. The Phase 3 team survey included a range of building settlements from less than 10 cm of settlement to greater than 40 cm of settlement, and differential settlements. Interactions of building settlements and ground deformations at groups of buildings were also observed. The GEER Phase 3 team observed 19 buildings in İskenderun, of which there were 3 building groups where interactions between buildings were observed and documented. Lidar scans were performed at some of the surveyed buildings. The buildings surveyed in the Çay district are shown in Figure 4.44 along with the approximate location of lidar scans. This report includes a subset of the surveyed buildings; observations at all surveyed buildings and the lidar data will be included in a forthcoming version of the report.

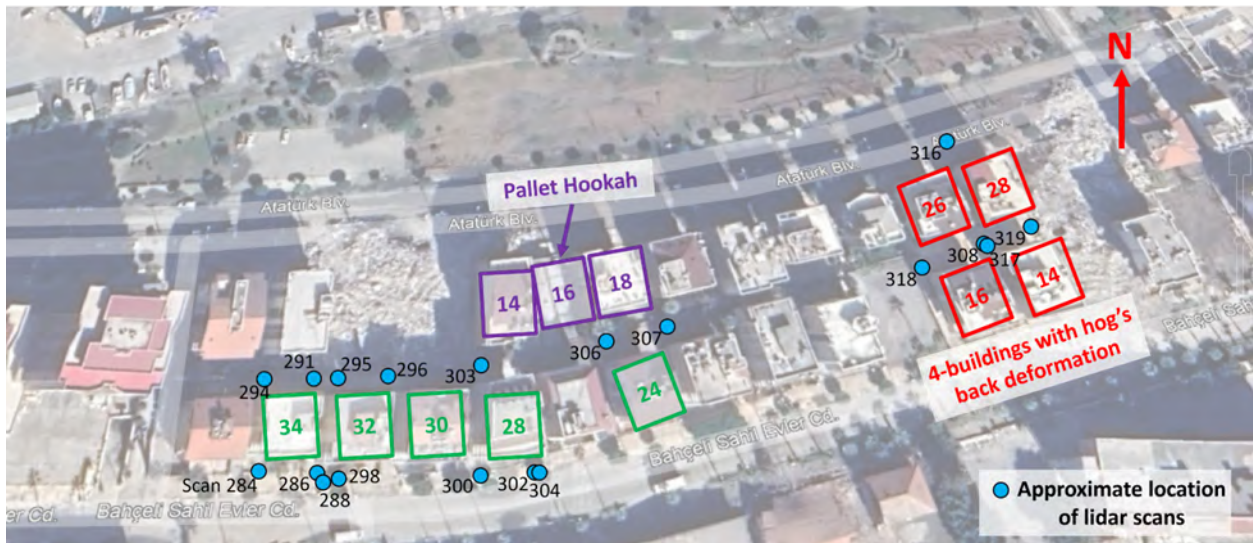


**Figure 4.44.** Location of the surveyed buildings by the Phase 3 team in the Çay district of İskenderun along with approximate locations of lidar scans. Approximate location of the middle of the figure is 36.590595N, 36.177981E).

##### (a) No. 34 Ersoz, Bahçeli Sahil Evler Caddesi

The residential apartment building No. 34 Ersoz located on Bahçeli Sahil Evler Cadiz (36.59018N, 36.17715E) was surveyed by the Phase 3 team on 27-March-2023. The street-view of the building is shown in Figure 4.45a. Settlement was measured at the four corners of the building (Figure 4.45b). The measured settlements are 35 cm, 44 cm, 23 cm, and 14 cm for the NE, SE, SW, and NW corners, respectively. There was minimal damage to the structure observed from the exterior. There was no apparent basement for the building. On the east side of the building, there is access to a sub-ground level electrical panel. An elevator is also present on the east side of the building. The estimated distance from ground level to the slab was 0.94 m based on

access to the electrical panel room. Lidar scans were performed at this location; the data are being processed and will be included in the next version of the report.



(a)



(b)

**Figure 4.45** İskenderun, Hatay. (a) (36.590233N, 36.177248E) building surveyed at No. 34 Bahçeli Sahil Evler Caddesi, (b) (36.590341N, 36.176822E) measurement performed on NE building corner and showing ground deformation. Photo (a) taken on 1-April-2023; photo (b) taken on 27-March-2023.

**(b) No. 16 Kazım Karabekir Caddesi, Pallet Hookah**

Liquefaction settlement interactions between buildings were observed for a group of three buildings in the Çay district. The group of three buildings, shown in Figure 4.46a, were two 5-story buildings on either side of a steel-framed single story restaurant called “Pallet Hookah” (36.590605N, 36.177820E). Settlement from the two 5-story buildings affected a “hog’s back” pattern of deformation between the two buildings, which appeared to cause deformations on either side of Pallet Hookah building and small settlements in the middle. The hog’s back deformation of Pallet Hookah is apparent in Figure 4.47b by the split in the sign located to the left of the “H”. Additionally, tension cracks in the floor running between the front and back of the building were observed. Negligible damage was observed from the exterior of the residential buildings. The orientation of the buildings is such that the fronts are facing approximately north. The building to the east of Pallet Hookah settled about 40 cm relative to Pallet Hookah, based on measurements at three corners of the building. The building to the west of Pallet Hookah settled approximately 51 cm relative to Pallet Hookah, based on one measurement at the front of the building (limited access prevented more measurements from being obtained).



(a)



(b)

**Figure 4.47** Iskenderun, Hatay. (36.5907337N, 36.177843E) Photos showing liquefaction settlement building interactions. The Pallet Hookah building underwent relatively little settlement relative to the two adjacent buildings. Settlement from the two 5-story buildings resulted in a “hog’s back” type of ground deformation that resulted in differential ground deformations across Pallet Hookah. Photos taken on 28-March-2023.

**(c) Four buildings in Çay, İskenderun, Hatay: No. 26 and 28 Atatürk Boulevard, No. 14 and 16 Bahçeli Sahil Evler Caddesi.**

A group of four buildings was surveyed in the Çay district to document building settlements and the effect on ground deformations around the buildings. The four surveyed buildings were No. 26 Atatürk Boulevard (36.590763N, 36.178930E), No. 28 Atatürk Boulevard (36.590803N, 36.179113E), No. 16 Bahçeli Sahil Evler Caddesi, (36.590519N, 36.179021E), and No. 14 Bahçeli Sahil Evler Caddesi, (36.590562N, 36.179196E). Figures 4.48a,b show the rear courtyard of the four buildings and the ground deformation induced between them. A hog’s back deformation was evident based on the mounding ground shape and east-west tension cracks in the courtyard tile. Additionally, on March 29th 2023, flooding in the Çay district impacted all of the four buildings but did not inundate the courtyard. The No. 28 and No. 14 were similar construction buildings 6-stories tall. No. 26 and No. 16 were similar construction and 6-stories with a half 7th-story.

The settlements for each building were estimated from (i) lidar scans on March 29 and April 1 2023, (ii) a laser-level survey on April 1 2023, and (iii) flood water depths on March 29 2023. The difference of ground levels relative to the reference ground level in the middle of the hog’s back deformation is shown in Figure 4.49, along with measured dimensions for the building group. If neither laser-level nor lidar scan estimates were available, the settlement was estimated from measured floodwater depths relative to a lidar-scan based value for the building. Settlements were largest at No. 16 (average 72 cm) and No. 26 (average 60 cm), and smallest at No. 14 (42

cm) and No. 28 (33 cm). Note that these estimated settlements do not account for initial surface grades.



(a)



(b)



(c)

**Figure 4.48** A group of four 6 and 7 story buildings in the Çay district. The photos show “hog’s back” ground deformations in the rear courtyard between the four buildings. (a) (36.590728N, 36.179267E) rear of south buildings, (b) (36.590733N, 36.179261E) rear of north buildings, (c) (36.590642N, 36.178817E) all buildings. All photos captured on March 29th 2023.

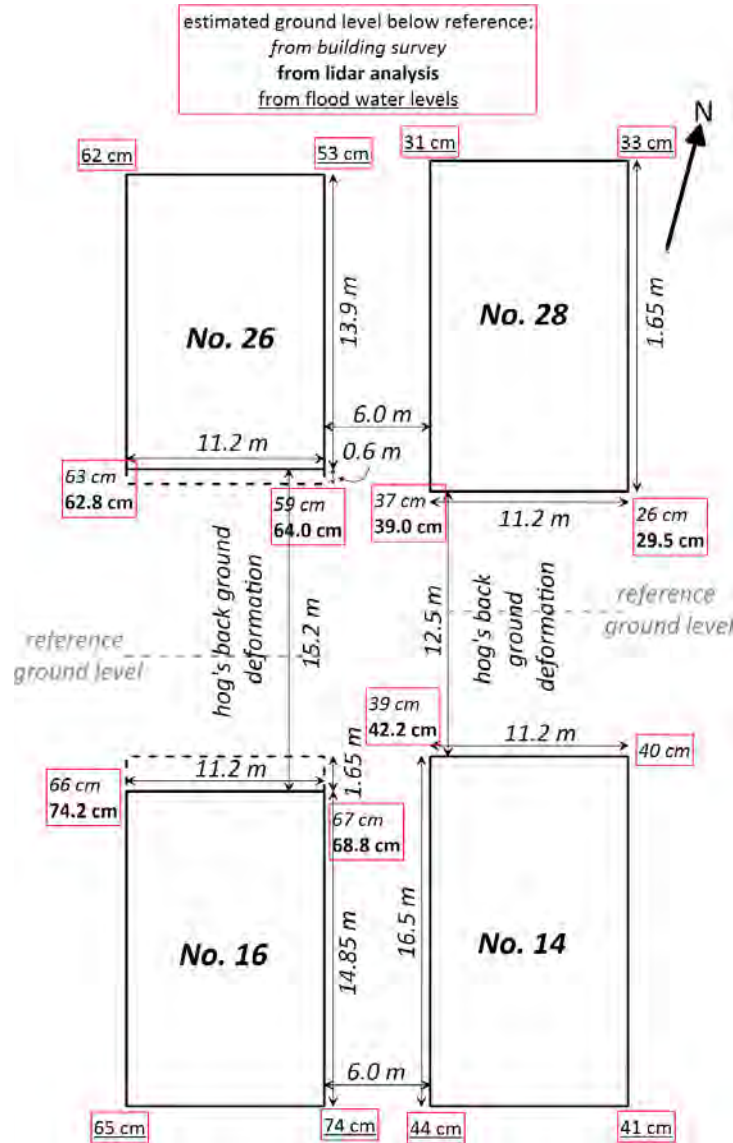


**Figure 4.49** Estimated settlements at the group of four buildings; settlements are relative to the northeast corner of No. 14 which appeared to have the lowest settlement. The settlements were measured on March 29th 2023 during flooding in Iskenderun. Relative settlements were estimated from depth of water at each building corner.

**(c) No. 33 Mareşal Fevzi Çakmak Caddesi**

The GEER Phase 3 surveyed settlement at a building that underwent less than 10 cm of settlement on 28-March-2023 (No. 33 Mareşal Fevzi Çakmak Caddesi), in an area where larger settlements were observed. The 5-story residential row building has first floor commercial use and faces northeast (Figure 4.50). The adjacent lot northwest of the building is empty; southeast of the building is a building in contact with the surveyed building. Deformation of the

sidewalk adjacent to No. 33 indicates that liquefaction settlement took place (Figure 4.50b). Surveys of settlement from the sidewalk to the northwest edge, center and northeast edge measured settlements of 5 cm, 7 cm, and 6 cm, respectively, indicating a slight sag in the center of the building. Figure 4.50c shows the laser-level survey at the center of the building. The front of the building (northeast edge) was measured as 26.55 m in width. The length of the building is approximately 19 m (estimated on Google Earth from the northwest edge). The building is approximately 16.1 m in height. The building owner reported that there is no basement. No exterior damage was observed.



(a)



(b)



(c)

**Figure 4.50** Çay district in İskenderun, Hatay (36.5925941N, 36.166185E) building with small settlement: (a) view of building facing west (280°), (b) (36.5925824N, 36.1661118E) deformed sidewalk, (c) (36.592725N, 36.1660907E) laser-level survey to the center of the building (dashed green line added where laser-level indicator is). Photos taken on March 28<sup>th</sup> 2023.

### 4.3 Dörtyol, Hatay

Figure 4.51 shows the locations visited in the Dörtyol area along the Mediterranean coastline, including a tangerine orchard, the fisherman's wharf, and the Öğmeiş apartment complex. A large network of lateral spread cracks were observed that intersected with a tangerine orchard. The prevailing topography in the area was a mild slope toward the coastline. Figure 4.52 shows the locations along the crack network that we visited. We first observed a large crack on the south side of the road across from the orchard (Figure 4.53a, 36.817203, 36.182253). Moist soil was observed in the crack at a depth of approximately 50 cm. The cracks continued northwest into the orchard. The owners of the orchard provided access to their property where we observed many cracks with widths on the order of about 10 cm to 3 m, with depths on the order of about 1 - 1.5 m. Several cracks were accompanied by liquefaction ejecta, including the first crack immediately on the north side of the road which measured 10.5m long and 2.5m wide (e.g., Figure 4.53b, 36.817305, 36.182039). Prior to our arrival, the owners had repaired a crack in their gravel road which previously had a 1-m vertical offset. Ejecta throughout the orchard appeared to have a noticeable amount of fines. Sand boils were often found within several meters of the cracks, including one that measured 5m x 5.6m x 20cm deep (Figure 4.54, 36.818331, 36.181038), which appeared to contain sand with silt. The orchard owners said the groundwater is approximately 5-7 m deep.

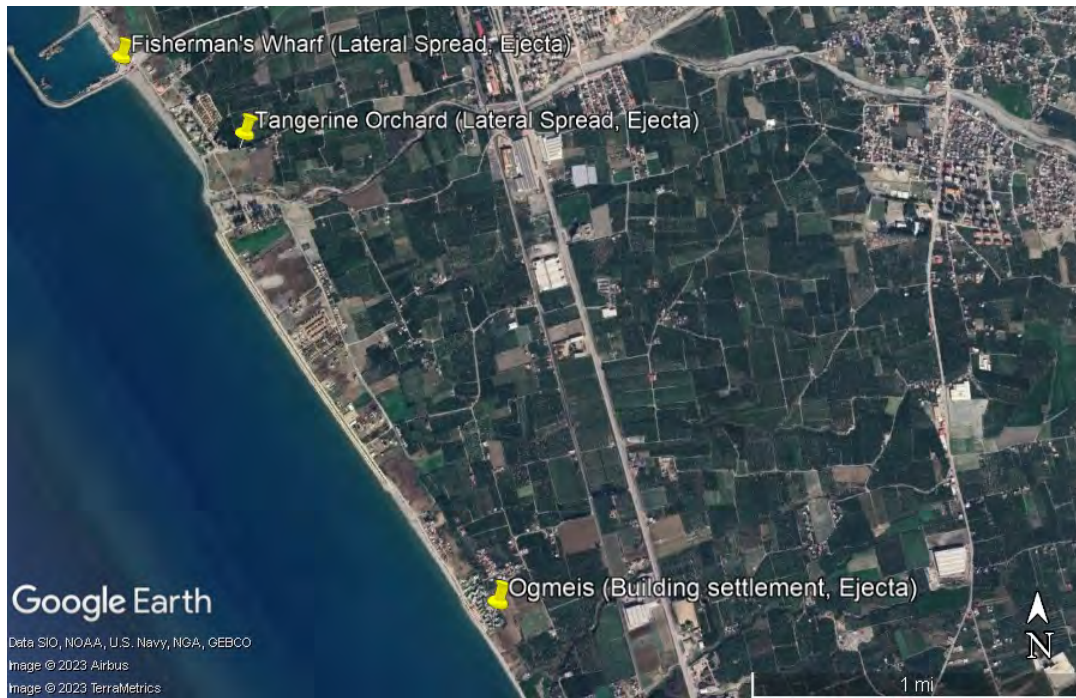
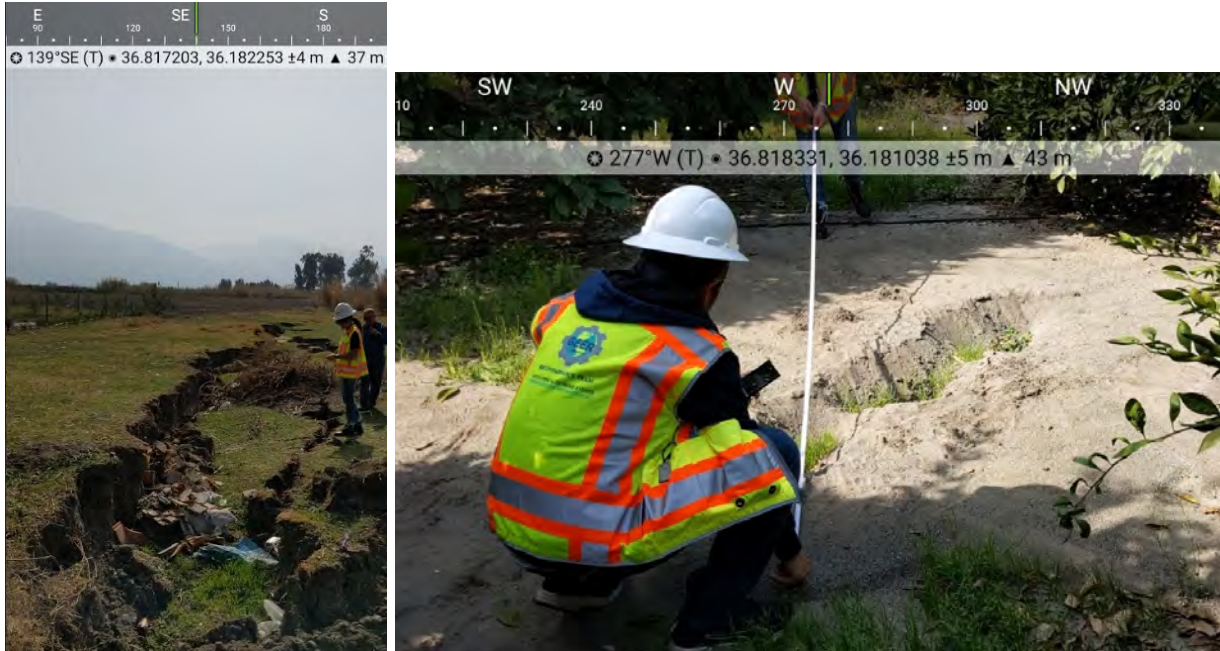


Figure 4.51. Overview of locations visited in Dörtyol.





**Figure 4.52.** Overview of locations visited along the network of cracks that intersected the tangerine orchard.



**Figure 4.53.** a) large crack on the south side of the road across from the orchard (36.817203, 36.182253); b) crack immediately on the north side of the road which measured 10.5m long and 2.5m wide (36.817305, 36.182039). Photos taken March 3, 2023.

Multiple GEER teams visited the Fisherman's Wharf .In several spots, sand boiling and lateral spreading were observed. On the dock, lateral spreading was reported, the extent of which was measured with reference to the displacements of the concrete panel blocks. Besides, the vertical displacements and deformations were documented due to the compression and spreading of the material beneath the dock. Locally, the settlements reached up to 75 cm, and the total lateral movement was measured at 70-80 cm. Figure 4.54 shows where the GEER Team 2 measured displacements at each concrete joint. Figure 4.55 provides images from GEER Team 2 during measurements and Figure 4.56 contains images of damage around the wharf from the GEER advanced team (Phase 1).



**Figure 4.54.** Locations at Fisherman’s Wharf where GEER Team 2 measured displacements.

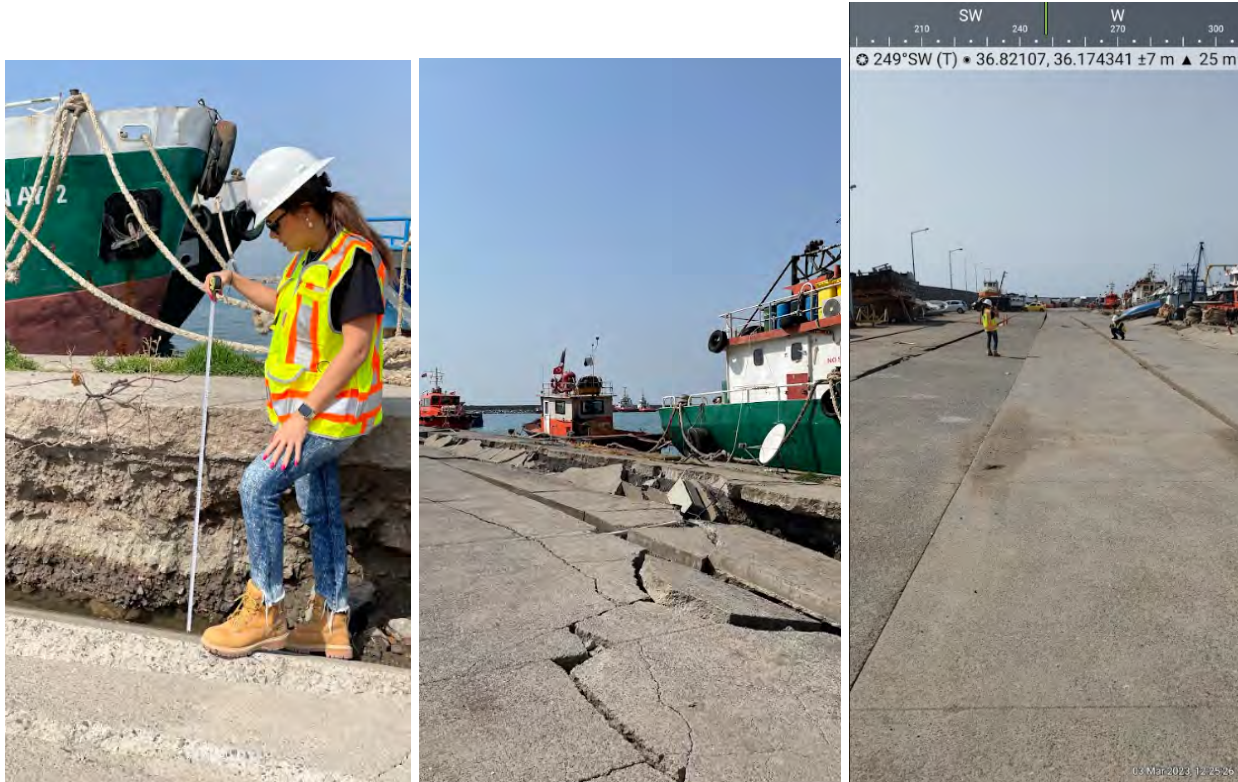


**Figure 4.55.** Images of damage taken along the Fisherman’s Wharf during GEER Team 2 reconnaissance. Photos taken March 3, 2023 (36.820771 N, 36.173860 E)



**Figure 4.56:** Liquefaction-induced lateral spreading and surface manifestation of liquefaction at Fisherman's Wharf, Dörtyol-Hatay (36.820771 N, 36.173860 E)

The southernmost point in Dörtüol that we visited was the Öğmeiř apartment complex (36.7958, 36.1979). Staff at the complex told us the buildings were 40-45 years old. Several experienced settlement and some had additional damage (cracking, e.g. Figure 4.57). Generally, buildings with a basement seemed to have less damage and settlement compared to the buildings constructed on grade. One building with a partial basement had a garage opening that was compressed and pushed the door out of alignment. Throughout the courtyard area, sand on the paved surface appeared to be sand boils along cracks in the concrete and along joints between slabs. The staff also said some buried irrigation pipes for landscaping burst as a result of the earthquake damage.



**Figure 4.57.** Building damage in the Öğmeiř neighborhood related to settlement. Photo taken March 3, 2023 (Coordinates: 36.79628, 36.19710).

#### **4.4 Demirköprü, Hatay**

A bridge across the Orontes River on highway D420 near the town of Demirköprü was severely damaged from liquefaction and possible lateral spreading of the river bank (Figure 4.58 and 4.59). The bridge was one of two bridges set side-by-side for opposing traffic. The other bridge did not fail and was being used when we visited.



**Figure 4.58.** Bridge failure across the Orontes River in Demirköprü, Hatay Province on Highway D420.



**Figure 4.59.** Abutment rotation and collapse of bridge across the Orontes river, Demirköprü, Hatay Province on Highway D420.

Immediately south and downstream of the failed bridge in Demirköprü lies a barren plowed field with numerous areas of liquefaction. Several sand blows and linear fissures with sand ejecta were present within the field (Figures 4.60, 4.61, and 4.62). Sand blows typically aligned linearly, presumably along extensional cracking/fracturing likely resulting from lateral spreading along the nearby Orontes River, south of Demirköprü, Hatay Province (Figure 4.63).



**Figure 4.60.** Barren plowed field along the Orontes River, south of Demirköprü, Hatay Province containing numerous liquefaction features.

## Reyhanli Hatay

☉ 271°W (T) ● 36°14'35"N, 36°21'36"E ±26ft ▲ 290ft



**Figure 4.61.** Large sand blows dispensing several cubic meters of clean fine sand along the Orontes River, south of Demirköprü, Hatay Province.





**Figure 4.62.** Sand blows typically aligned linearly, presumably along extensional cracking/fracturing likely resulting from lateral spreading along the nearby Orontes River, south of Demirköprü, Hatay Province.

## Antakya Cilvegozu Yolu Hatay Merkez Hatay

🌐 174°S (T) 🌍 36°14'45"N, 36°21'23"E ±13ft ▲ 306ft



**Figure 4.63.** Lateral spreading along the Orontes River, south of Demirköprü, Hatay Province.

### **4.5 Türkoğlu, Kahramanmaraş**

An isolated bridge near Kilılı (Figure 4.64, 37.4123, 36.9066) performed well and was still in service on the date we visited it (March 4, 2023). The bridge was built relatively recently (according to Google Street View, it was nearing completion in November 2022). Horizontal offsets were measured along the centerline at each joint on the bridge. The maximum offset at the abutment on the NW end of the bridge was 15 cm, whereas all other offsets were 0-5 cm.

The Türkoğlu Lojistik Merkezi is a continuously paved area over 1 km long and over 200 m wide with no structures except the entrance building. It serves as a storage and loading/unloading area for many trains that enter the area. A security guard showed us several locations throughout the paved area with large cracks in the pavement that were several meters long, as well as locations with gravelly and sandy ejecta, particularly near cracks and joints between slabs (e.g., Figure 4.65, 37.372, 36.861). The security guard informed us that there are plans to

set up shipping containers within the Lojistik grounds to provide shelter for displaced people in the region.

Outside the perimeter wall of the Lojistik, a large pipe section acting as a culvert under the road was damaged and some possible ejecta with high fines was visible near the depression in the ground (37.3752, 36.8676). It is difficult to determine whether the damage was caused by liquefaction or could have been related to some other mechanism. Further down the road (37.370574, 36.869232) there was significant damage to a 5.7 m-long section of road and caused a horizontal offset of 3.2 m (e.g., Figure 4.66). This displacement appeared to be coincident with fault cracks on both shoulders of the road.



**Figure 4.64.** Isolated bridge near Kılılı (37.4123, 36.9066) with good performance. Photos taken March 4, 2023.

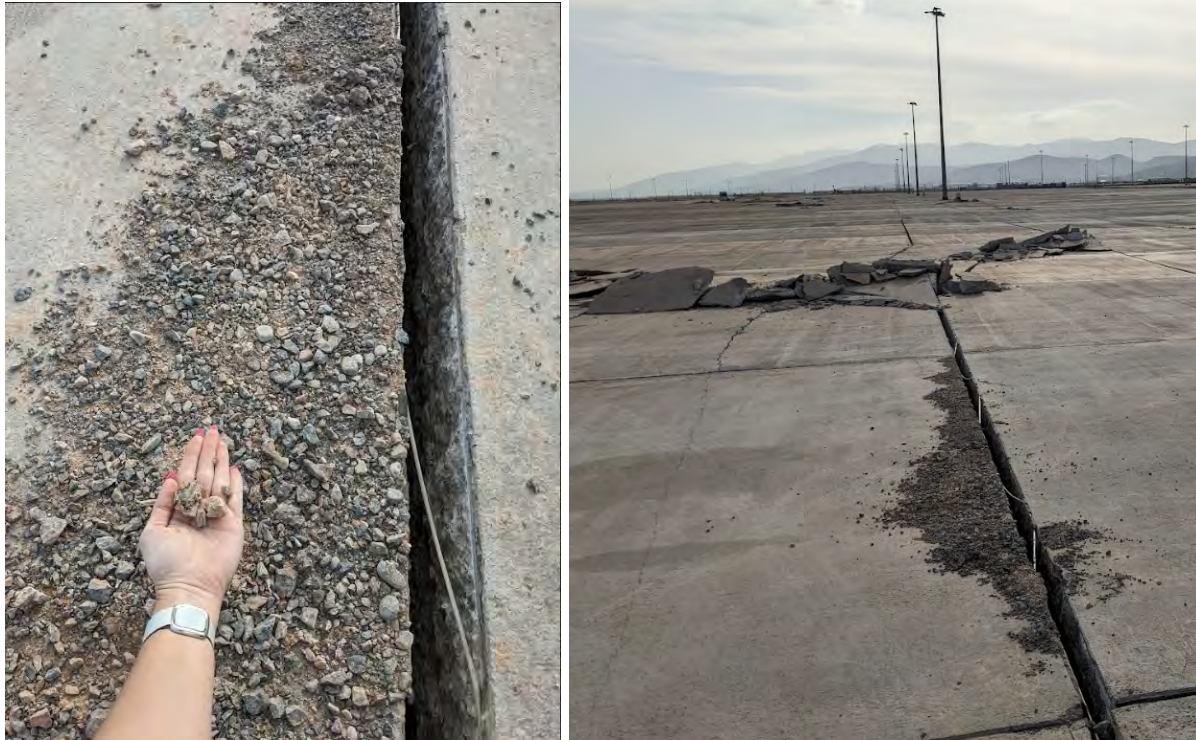


**Figure 4.65.** Observations of ground cracks and gravelly ejecta in the Lojistik area south of Türkoğlu (37.372, 36.861). Photos taken March 4, 2023.



**Figure 4.66.** a) Observed damage to a 5.7 m-long section of road with a horizontal offset of 3.2 m (37.370574, 36.869232); b) possible ejecta with high fines near a culvert south of Lojistik (37.3752, 36.8676). Photos taken March 4, 2023.

## 4.6 Antakya, Hatay - Bridge Damage

GEER Team 3 observed five vehicular bridges in the Antakya, Hatay Province region on March 31, 2023. The purpose of the GEER team visit was to observe and document earthquake-induced damages, including zones of compression and extension along the bridge deck and superstructure, structural damage (e.g., cracks, spalling) at the bridge piers and pile caps, structural damages at the abutments, and soil and retaining wall failures near the abutments. Three of the bridges crossed the Orontes river and are labeled herein as the D817, Utku Acun Cadiz, and Bekir Karabacak Koprusu bridges, based on the supported highway or roadway. The other two bridges crossed the Karasu River and are labeled herein as the Hatay Hospital and Hatay Stadium bridges, based on nearby major facilities. All bridges are mapped in Figure 4.67.



**Figure 4.67.** Map of observed bridges in Antakya, Hatay Province, Türkiye (Google Earth<sup>®</sup> image dated February 14, 2023, centered near N36.2401°, E36.1882°).

### 4.6.1 D817 Bridge crossing the Orontes River

The D817 Bridge crossing the Orontes River (N36.248721°, E36.199764°) was open to regular traffic at the time of the GEER Team 3 investigation on March 31, 2022. Observations of structural damage of the bridge abutments, piers, and deck, as well as slope failures near the bridge, are depicted in Figures 4.68 to 4.70.



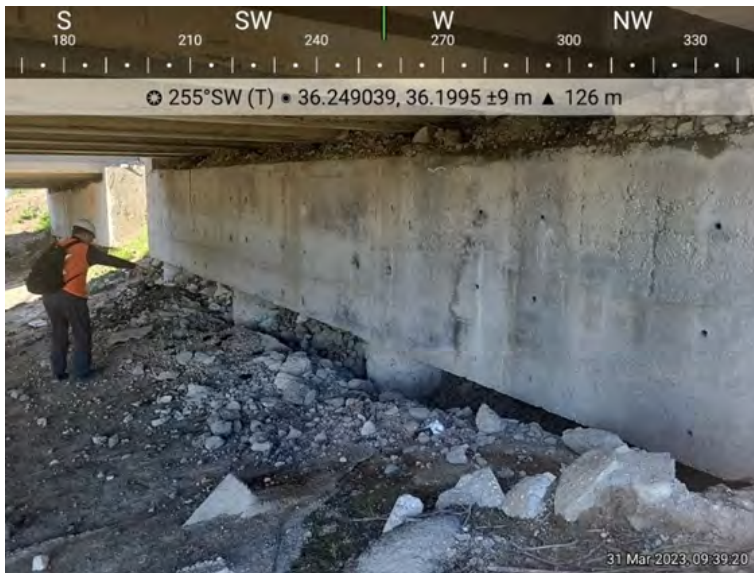
**Figure 4.68.** Drone image of D817 Bridge crossing the Orontes River from the south end of bridge (N36.248220°, E36.199871°).



(a)



(b)



(c)



(d)

**Figure 4.69.** D817 Bridge damage: (a) compressional damage at the end of southeast-bound bridge deck (N36.248300°, E36.200089°), (b) flexural-extensional cracking at the end of northwest-bound bridge deck (N36.249112°, E36.199416°), (c) concrete spalling of shear keys (?) at the northwest abutment shafts (N36.249039°, E36.199500°), (d) shear failure spalling at the top of a concrete pile near the northwest abutment shaft near pile near the northwest abutment below southwest-bound bridge (N36.248944°, E36.199294°).



**Figure 4.70.** Local slope failures along northwest bank near the D817 Bridge: (a) southwest side of bridge with 30 to 40 cm lateral movement and 50 to 60 cm vertical movement (N36.248709°, E36.199016°), (b) northeast side of bridge (N36.249590°, E36.200036°).

#### 4.6.2 Utku Acun Cadiz Bridge crossing the Orontes River

The Utku Acun Cadiz Bridge (N36.232885°, E36.185190°) crossing the Orontes River was open to regular traffic at the time of the GEER Team 3 investigation on March 31, 2022. Observations of structural damage of the bridge abutments, piers, and deck, as well as slope failures near the bridge, are depicted in Figures 4.71 to 4.72.





**Figure 4.71.** The Utku Acun Cadiz Bridge crossing the Orontes River, as viewed from southeast corner of bridge (N36.232597°, E36.185509°).

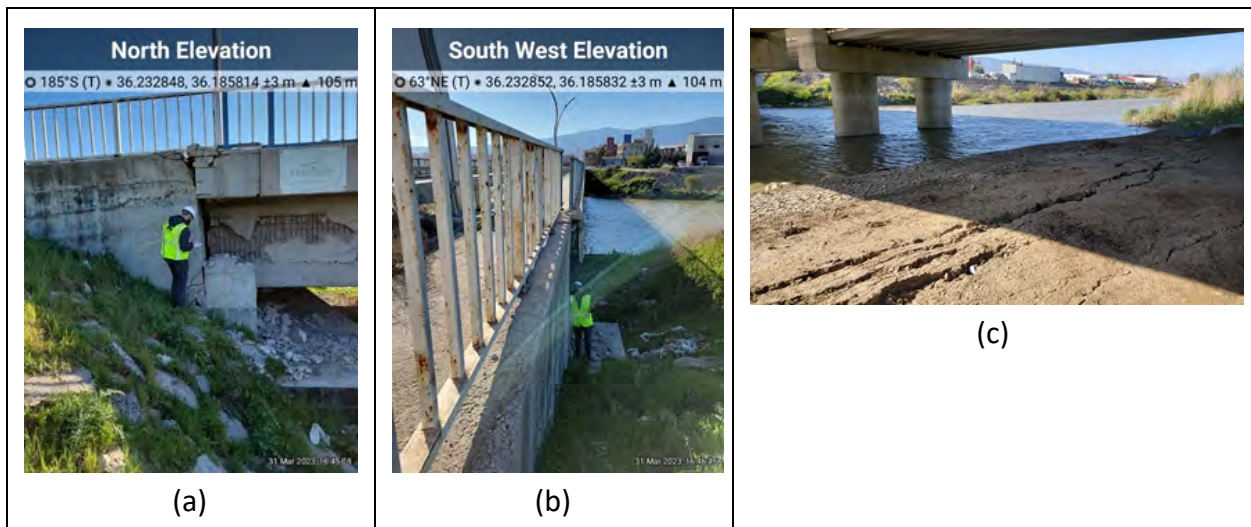


**Figure 4.72.** Damage at east abutment of Utku Acun Cadiz Bridge: (a) north side of abutment tilting 1° to 2° back (eastward), with a separation gap of over 12 cm near the deck (N36.232848°, E36.185814°), (b) west-bound deck shifted about 17 cm to the north over east abutment (N36.232852°, E36.185832°), (c) ground cracks below east abutment (N36.232674°, E36.185562°).

#### 4.6.3 Bekir Karabacak Koprusu Bridge crossing the Orontes River

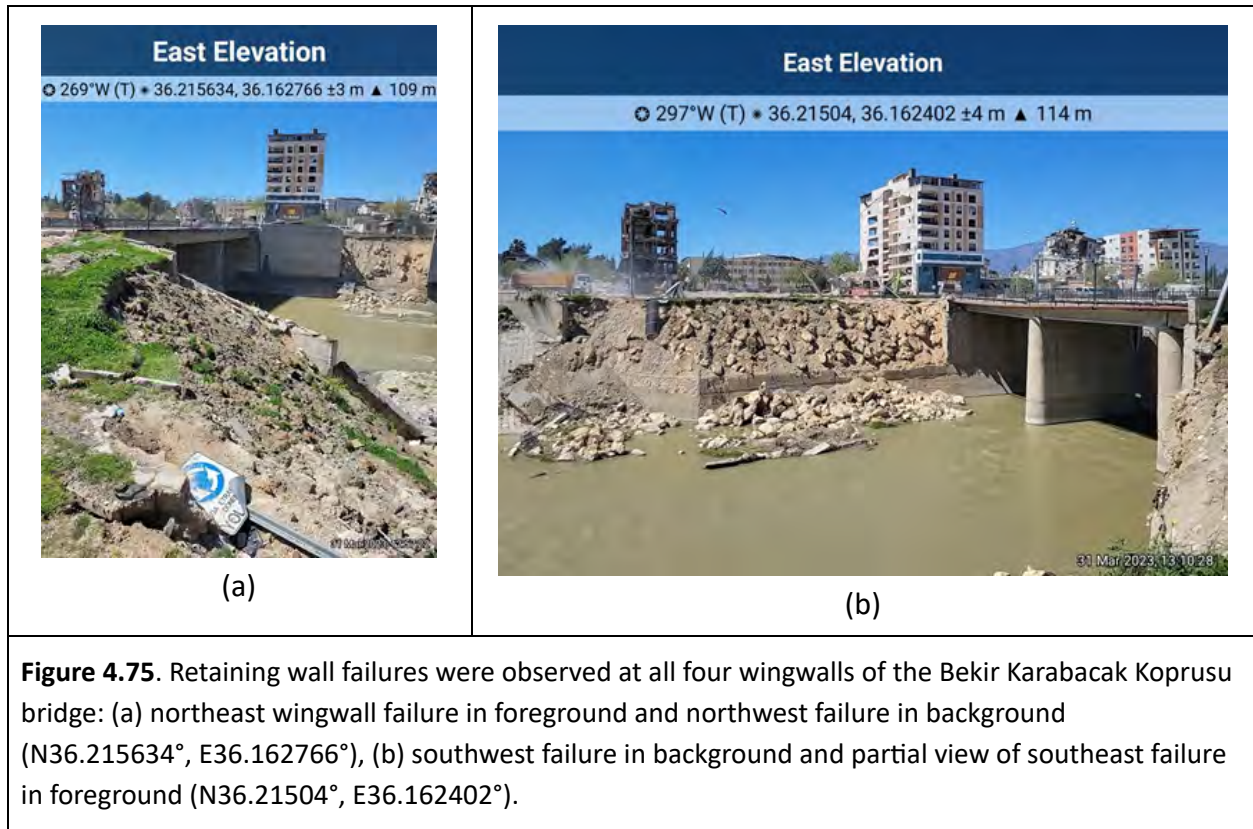
Only the west bound segment of the Utku Acun Cadiz Bridge crossing the Orontes River (N36.215483°, E36.162144°) was open to traffic at the time of the GEER Team 3 investigation on March 31, 2022. Observations of structural damage of the bridge abutments, piers, and deck, as well as retaining wall failures of the wingwalls adjacent to the bridge abutments, are depicted in Figures 4.73 to 4.75.



**Figure 4.73.** The Bekir Karabacak Koprusu Bridge crossing the Orontes River, as viewed from near a retaining wall failure at the northwest wingwall of the bridge (N36.216033°, E36.16187°).



**Figure 4.74.** Movement measured along east-bound Bekir Karabacak Koprusu bridge deck: (a) deck is 37 cm higher than adjacent roadway overlying east abutment (N36.215338°, E36.162435°), (b) pavement buckling and dislocations indicate over 40 cm measured horizontally of compression (N36.215566°, E36.161873°).



#### 4.6.4 Hatay “Stadium” Bridge crossing the Karasu River

The bridge near the Hatay Stadium crossing the Karasu river (N36.254522°, E36.203283°) was closed to regular traffic at the time of the GEER Team 3 investigation on March 31, 2022. However, limited access was allowed for personnel associated with the temporary settlement at the stadium. Observations of structural damage of the bridge abutments, piers, and deck, as well as slope failures near the bridge, are depicted in Figures 4.76 to 4.80.



**Figure 4.76.** Hatay Stadium Bridge crossing the Karasu River from the east end of bridge: (a) east-bound bridge (N36.25472°, E36.203879°), (b) west-bound bridge (N36.255039°, E36.204092°).

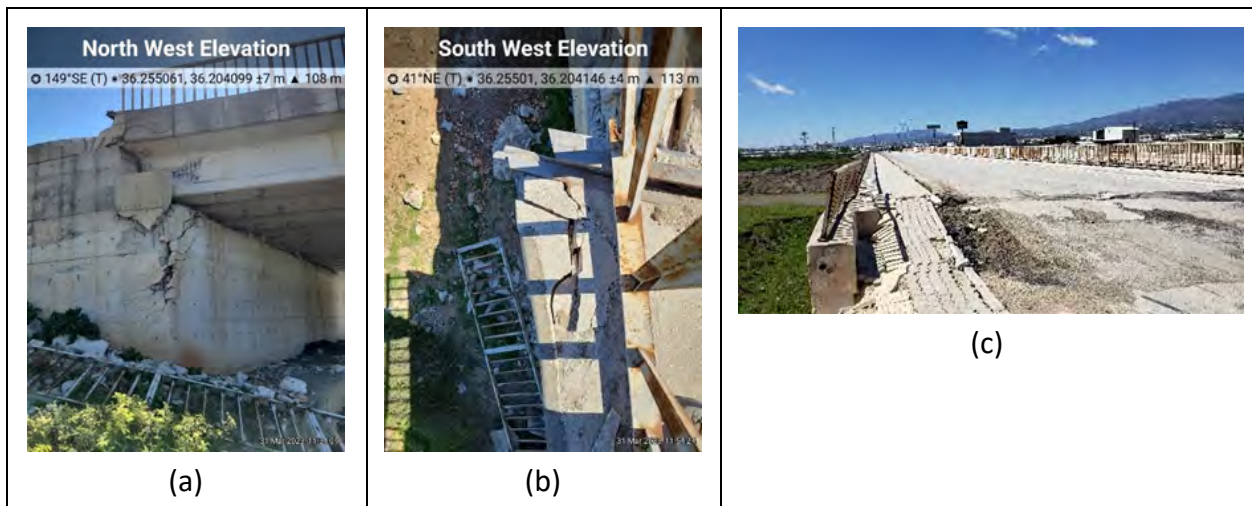


**Figure 4.77.** Damage at east abutment of Hatay Stadium Bridge: (a) cracking and spalling on the beams and abutment at north edge of deck support (N36.255061°, E36.204099°), (b) right-lateral offset at north edge of deck (N36.25501°, E36.204146°), (c) pavement damage and misalignment of deck at south end of abutment (N36.254772°, E36.204323°).

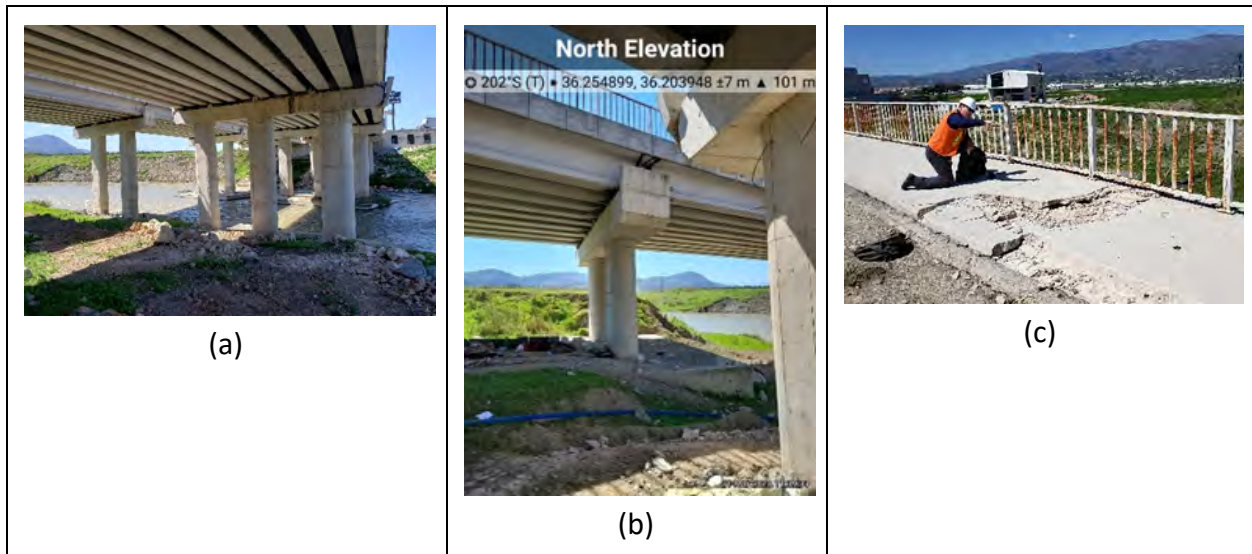


**Figure 4.78.** Damage at eastern-most bent of Hatay Stadium Bridge: (a) cracking at substructure deck supports (N36.254879°, E36.203865°), (b) pile caps are undamaged (N36.254899°, E36.203948°), (c) concrete spalling of pavement extends across west-bound bridge (N36.254791°, E36.203671°).

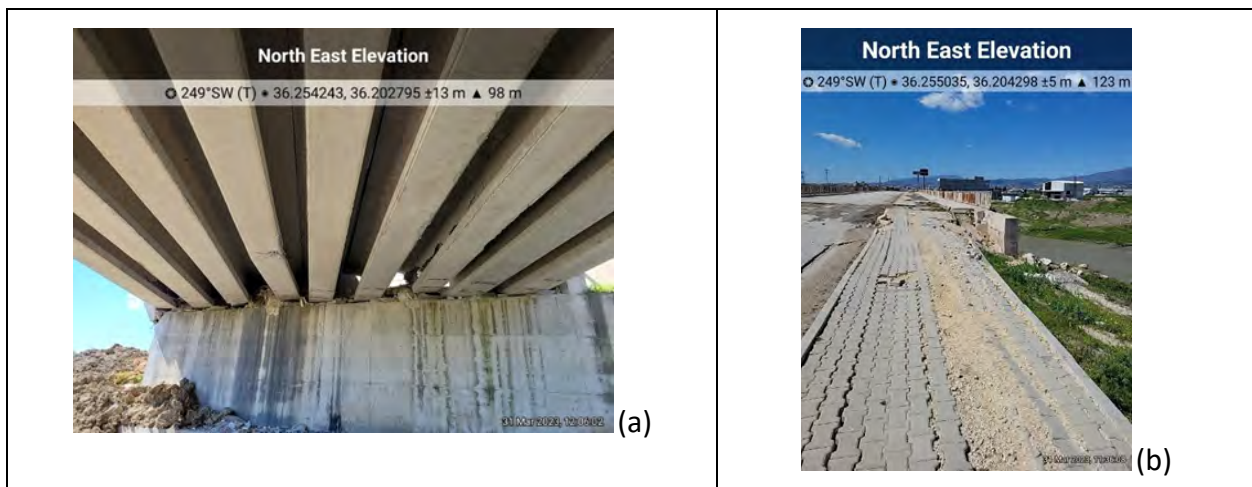


**Figure 4.79.** Damage at west abutment and superstructure of Hatay Stadium Bridge: (a) spalling and out-of-plane flexural failure of one of the beams bending of east-bound deck support (N36.254243°, E36.202795°), (b) pavement damage and misalignment of deck at north end of abutment (N36.255035°, E36.204298°).



**Figure 4.80.** Local slope failures near Hatay Stadium Bridge: (a) slumping beneath west end of bridge (N36.254215°, E36.20285°), (b) translational stability failure on east bank and rotational failure affecting transmission lines on west bank of Karasu river (N36.253994°, E36.202873°).

#### 4.6.5 Hatay “Hospital” Bridge crossing the Karasu River

The main bridge near the Hatay Devlet Hastanesi (hospital) crossing the Karasu river (N36.272610°, E36.207843°) was open to traffic and appeared structurally sound during a quick drive-by observation by GEER. However, local soil slumping failures (Figure 4.81) were observed along the east bank adjacent to the bridge. The three eastern-most deck spans of an older bridge just south of the main bridge had collapsed. While the collapsed bridge appears redundant, Google earth imagery suggests it was in use for vehicular traffic at least until July 2022.



**Figure 4.81.** Local slumping failure and collapse of old bridge deck along the East bank to the South (background of photo) of the main Hatay Devlet Hospital Bridge (foreground of photo) (N36.27264°, E36.208344°).

## 5.0 Performance of Buildings

*Halil Sezen, Bora Gencturk, Rupa Garai, Parth Gudhka, Morgan Griffith, Mike Mieler*

### 5.1 Introduction

This chapter documents the observations and provides preliminary analysis of the data collected of the damage caused to the buildings by the earthquake sequence that struck Türkiye on February 6, 2023.

The shakemap PGA contours for the **M** 7.8 Kahramanmaraş Earthquake are shown in Figure 5.1 with a maximum peak ground acceleration (PGA) recorded as  $1.057g^1$  and the shakemap PGA contours for the **M** 7.7 Elbistan Earthquake are shown in Figure 5.2 with a maximum recorded PGA of  $0.77g^2$ .

The field observations of the EERI Buildings Team were consistent with the sustained damage and consistent to locations that experienced large PGA values as the highest proportion of the heavily damaged or collapsed buildings were seen in and around Hatay, Kahramanmaraş, Malatya and Adiyaman provinces.

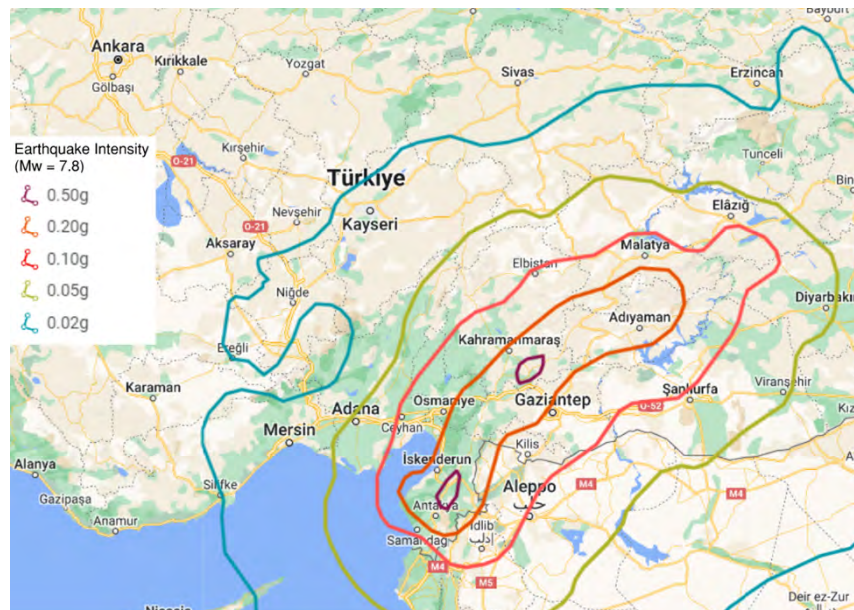


**Figure 5.1.** USGS shakemap PGA contours for the Mw 7.8 Pazarçık-Kahramanmaraş Earthquake.

<sup>1</sup> USGS, 2023 - <https://earthquake.usgs.gov/earthquakes/eventpage/us6000jllz/executive>

<sup>2</sup> USGS, 2023 - <https://earthquake.usgs.gov/earthquakes/eventpage/us6000jlqa/executive>



**Figure 5.2.** USGS shakemap PGA contours for the Mw 7.7 Elbistan-Kahramanmaraş Earthquake

Table 5.1 shows the distribution of the buildings in the earthquake affected provinces per occupancy classification. Table 5.2 shows the percentage of households by construction year of residence for the provinces in the earthquake affected regions in comparison to Türkiye as a whole. The buildings built post 2001 in this region are slightly more than those at the national average, while the buildings built prior to 2000 are less than the national average. More than 37% households in the affected regions are residing in houses built prior to 2000.



**Table 5.1.** Number of Buildings per occupancy use in the provinces affected by the earthquakes, Ministry of Interior (MAKS), Türkiye<sup>3</sup>

Province	Residential	Commercial	Public	Other	Total
Adana	404,502	29,920	8,916	7,779	451,117
Adiyaman	107,242	5,765	4,370	3,119	120,496
Diyarbakir	199,138	11,412	11,964	3,165	225,679
Elazig	106,569	7,221	2,872	7,051	123,713
Gaziantep	269,212	22,829	5,480	8,162	305,683
Hatay	357,467	33,511	10,382	5,489	406,849
Kahramanmaras	219,351	12,358	6,879	4,565	243,153
Kilis	33,399	1,526	1,651	736	37,312
Malatya	159,896	8,370	6,670	4,051	178,987
Osmaniye	128,163	9,428	3,105	2,384	143,080
Sanliurfa	347,902	18,847	11,790	4,089	382,628
<b>Total</b>	<b>2,332,841 (89.0%)</b>	<b>161,187 (6.2%)</b>	<b>74,079 (2.8%)</b>	<b>50,590 (1.9%)</b>	<b>2,618,697 (100.0%)</b>

<sup>3</sup> 2023 Kahramanmaraş Hatay Depremleri Raporu, Türkiye Cumhuriyeti Cumhurbaşkanlığı, Strateji ve Bütçe Başkanlığı, March 2023

**Table 5.2.** Percentage of Households by Construction Year of Residence (2021), Ministry of Interior (MAKS), Türkiye<sup>4</sup>

Province	Pre 1980	1981-2000	Post 2001	Unknown
Adana	13.0	34.8	38.7	13.5
Adiyaman	8.7	23.6	52.3	15.4
Diyarbakir	6.5	26.6	58.1	8.8
Elazig	10.0	23.6	52.8	13.6
Gaziantep	6.6	25.9	51.6	15.9
Hatay	13.5	32.6	50.0	3.9
Malatya	11.7	26.9	58.1	3.3
Kahramanmaras	11.2	21.7	52.3	14.9
Kilis	14.0	28.1	48.4	9.5
Osmaniye	10.5	25.7	46.5	17.3
Sanliurfa	5.5	18.5	61.0	14.9
<b>Affected Provinces Average</b>	<b>10.0</b>	<b>27.6</b>	<b>51.1</b>	<b>11.3</b>
<b>Türkiye</b>	<b>12.6</b>	<b>30.9</b>	<b>47.4</b>	<b>9.1</b>

<sup>4</sup> 2023 Kahramanmaraş Hatay Depremleri Raporu, Türkiye Cumhuriyeti Cumhurbaşkanlığı, Strateji ve Bütçe Başkanlığı, March 2023

As of March 6, 2023, an assessment of the damage caused by the earthquake has been conducted on 1,712,182 buildings across 11 provinces by the Ministry of Environment, Urbanization and Climate Change (ÇŞİDB) – Türkiye. Table 5.3 shows that 35,355 buildings collapsed, while 17,491 buildings require immediate demolition. Additionally, 179,786 buildings have been classified as heavily damaged, 40,228 as moderately damaged, and 431,421 as slightly damaged. Notably, among the buildings that were destroyed or severely damaged, there were not only residential structures but also historically and culturally significant buildings, as well as schools, administrative buildings, hospitals, and hotels.

**Table 5.3.** Number of buildings per various damage levels (6 March 2023), ÇŞİDB<sup>5</sup>

<b>Level of Damage</b>	<b>Number of Buildings</b>
No damage	860,006
Light damage	431,421
Moderate damage	40,228
Heavy damage	179,786
Collapse/Partial collapse	35,355
Urgent need of demolition	17,491
Could not detect	147,895
<b>Total</b>	<b>1,712,182</b>

<sup>5</sup> 2023 Kahramanmaraş Hatay Depremleri Raporu, Türkiye Cumhuriyeti Cumhurbaşkanlığı, Strateji ve Bütçe Başkanlığı, March 2023

As part of the reconnaissance efforts following the Kahramanmaraş earthquake sequence, the EERI Buildings Team visited the population centers that were most affected by the earthquakes including İskenderun, Samandağı, Kırıkhan, Antakya, Adana, Osmaniye, Kahramanmaraş, Gaziantep, Adıyaman, Gölbasi, Malatya, Hassa, İslahiye and Nurdağı, covering a total distance of 3200 km in 6 days while collecting data in the field (Figure 5.3). The team focused on understanding the overall structural performance of buildings, including correlation with peak ground acceleration at nearby ground motion recording stations. In addition to residential building performance, the team also documented and categorized the response of industrial facilities, commercial buildings, school buildings, and religious and historical structures.

The preliminary observations and findings from the data collected are presented in the following sections.

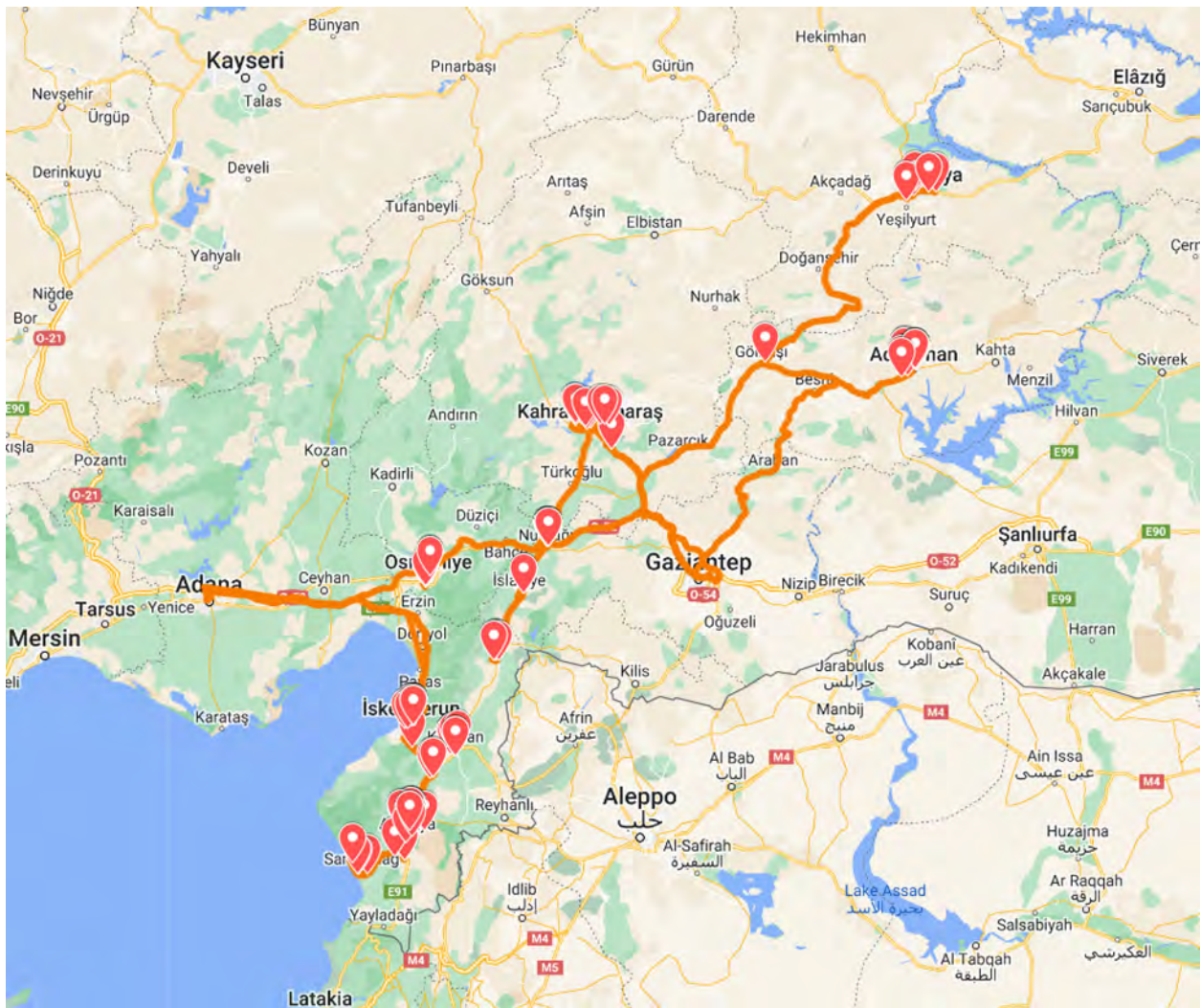


**Figure 5.3.** Map showing the route of EERI Buildings team in the field with the locations of the observed buildings.

## **5.2 Breadth and Depth of Observations**

In addition to the general observations made in various cities and towns, the EERI Buildings Team assessed 126 sites with one or more buildings. The total number of buildings from all the sites was 167. In some cases, a site included several (up to 37) virtually identical buildings, which showed similar damage patterns. These buildings within a complex were evaluated based on the most heavily damaged one, assuming that the variation in the other buildings is due to inherent randomness of the earthquake motions and response of non-ductile buildings.

The building occupancy distribution is shown in Figure 5.4. About 73% (91 out of 126) of the buildings/sites visited were residential construction. In addition, the EERI Buildings Team visited schools/universities, industrial facilities, hospitals, historical buildings (mosques and churches, among others), one government building (a courthouse in Hassa) and some commercial buildings. The lateral force resisting systems of the buildings visited are shown in Figure 5.5. For being the typical construction type, most buildings were reinforced concrete (RC) with a combination of shear walls and moment frames as the lateral load resisting system. Some of the buildings (mostly 1-5 stories) were RC moment frames. In addition, some tunnel form shear wall construction was encountered in residential buildings. The team visited one RC core shear wall building with a steel gravity frame, some steel moment frame buildings, and two precast concrete industrial facilities. The historical buildings visited were mostly unreinforced masonry (URM).

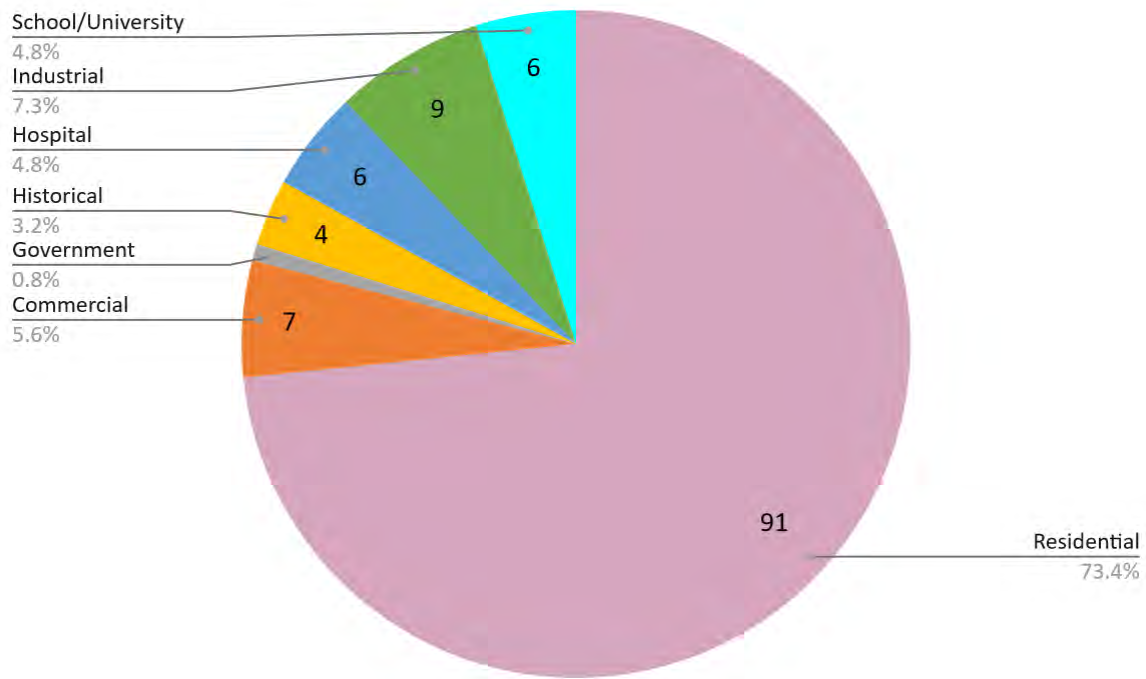


**Figure 5.4.** Occupancy type distribution of buildings visited by the buildings team.

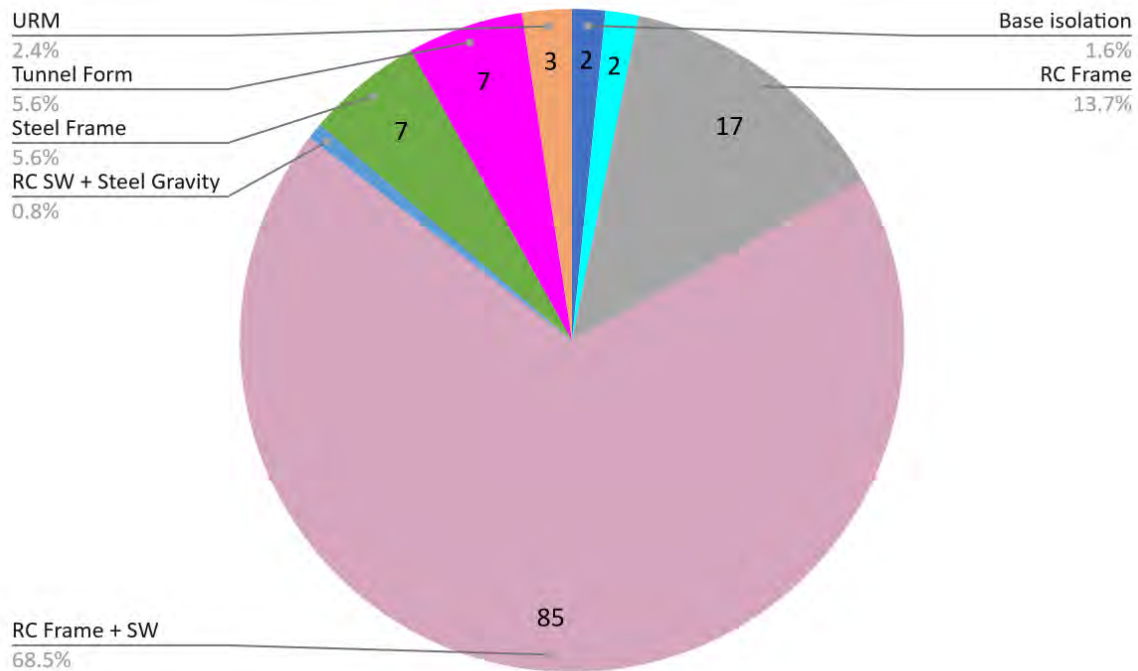


**Figure 5.5.** Lateral force resisting systems of the buildings visited by the EERI Buildings Team (RC: reinforced concrete, SW: shear wall).

The PGA and PGV values are calculated at the sites that were visited by the EERI Buildings Team as respectively shown in Figure and Figure 5.7. These PGA and PGV values are the maximums of PGAs and PGVs from the three major earthquakes in the earthquake sequence, specifically, Kahramanmaraş (**M** 7.8), Elbistan (**M** 7.7) and Defne (Hatay) (**M** 6.3) earthquakes. As seen in these figures, the PGA was between 0.2 g and 0.7 g for most buildings. A smaller number of buildings experienced PGAs lower than 0.2 g. The maximum PGV values were mostly from 20 cm/s to 110 cm/s.

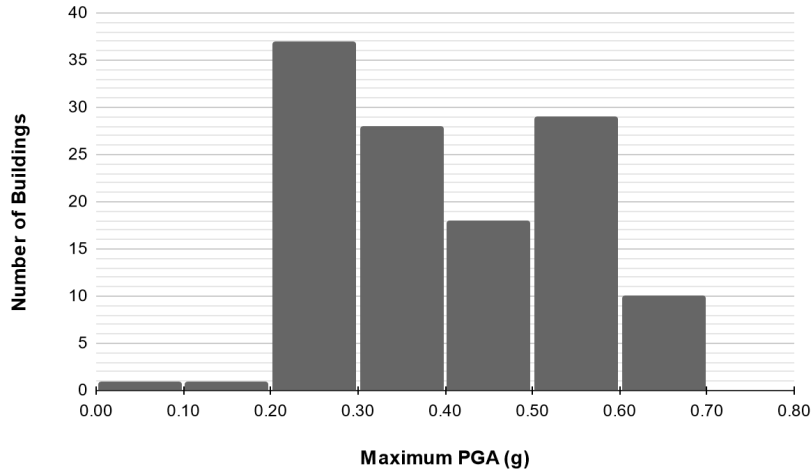


**Figure 5.6.** Distribution of the maximum PGA at the visited sites from the three earthquake sequence:  $M_w$  7.8 Kahramanmaraş,  $M_w$  7.7 Elbistan and  $M_w$  6.3 Defne earthquakes.

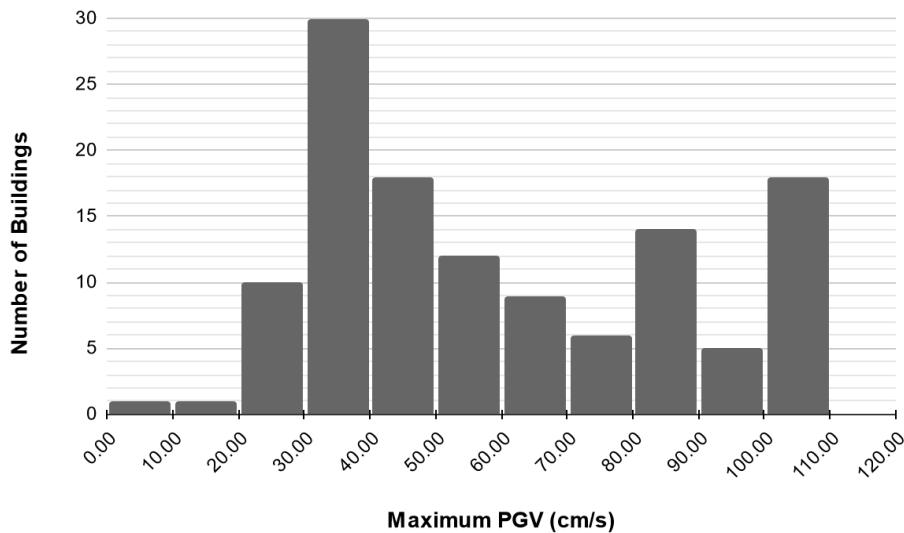


**Figure 5.7.** Distribution of the maximum PGV at the sites visited from the three earthquake sequence: **M** 7.8 Kahramanmaraş, **M** 7.7 Elbistan and **M** 6.3 Defne earthquakes.

The EERI Buildings Team mostly focused on modern construction (built after 2000) as those are more likely to incorporate lessons learned in previous earthquake and provide an opportunity to identify possible further improvements to design criteria, and on buildings that did not collapse as those offer a greater opportunity to understand the spatial distribution and progression of damage within the building. In the remainder of this chapter, the data and evaluations presented are only for residential buildings. This choice is made for a consistent evaluation of these buildings in terms of observed damage as they were (with three exceptions) either RC moment frames or RC shear wall and moment frame combinations. These buildings visited by the EERI Buildings Team are representative of the performance of buildings in the earthquake region constructed according to modern building codes. The distribution of the buildings in terms of the number of stories is shown in Figure 5.8. As seen in the figure, most buildings were in the 6-10 story range, which is very typical of the region. The team did not encounter any building with more than 20 stories.

The distribution of buildings in terms of damage class as determined by the EERI Buildings Team is shown in Figure 5.9. It is seen that most of the buildings visited were in the heavy damage category followed by those with moderate damage. Some partial collapse cases were also observed in some very recently constructed buildings. The team used repairability as a performance objective to distinguish between moderate and heavy damage with those in the latter category more than likely requiring demolition. In some cases, moderate damage was observed but serious design and construction deficiencies such as poor confinement, insufficient lap splicing, and poor detailing or lack of shear reinforcement were observed. These buildings were categorized as heavy damage (58%) as they will most likely be demolished due to these deficiencies. Only a very small fraction of the buildings visited showed light or no damage. It is noted here that the building database was biased towards damaged buildings; however, the team also visited some randomly selected buildings in every town with no prior knowledge of the damage status.



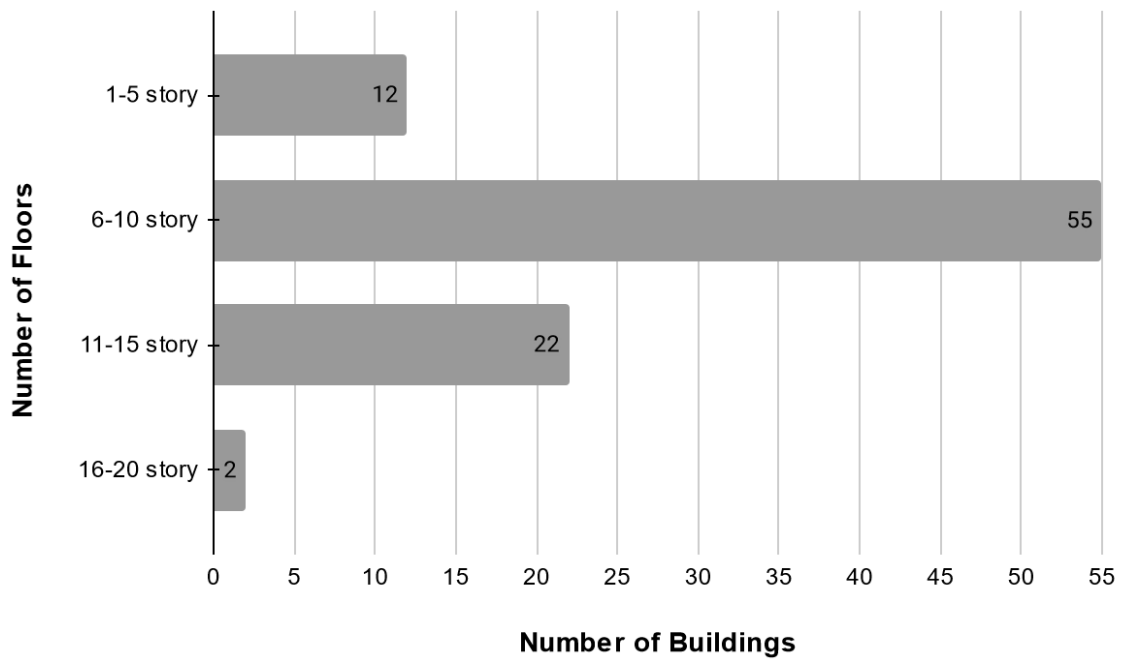


**Figure 5.8.** Distribution of the residential buildings visited by the buildings team in terms of the number of floors.

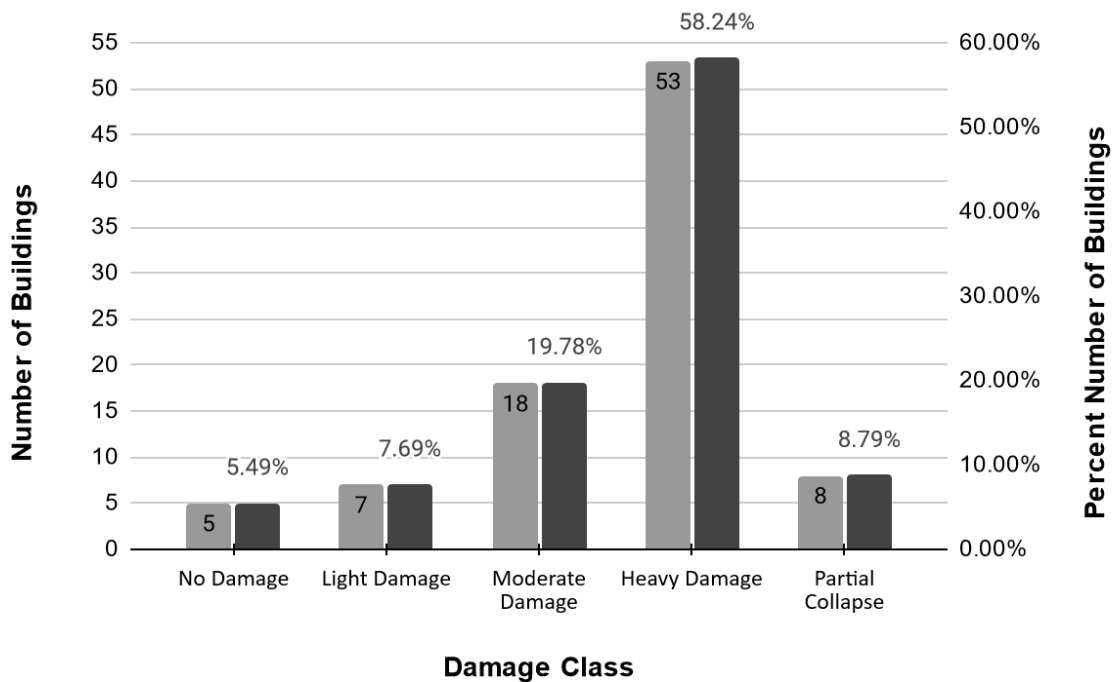


**Figure 5.9.** Distribution of the residential buildings visited by the buildings team in terms of damage class.

The percentages of the damage types observed in the residential buildings visited by the team are shown in Figure 5.10. It is noted here again that the total number of buildings used to calculate the percentages here was 91. Despite being mostly modern construction, it is seen that diagonal shear cracking of concrete elements was still prevalent. These cracks were observed in the beams, coupling beams, columns, and shear walls. Rebar buckling was the most commonly observed damage. This is a clear indication of insufficient transverse reinforcement. The team observed that several of the rebar buckling cases occurred in the plastic hinge regions of beams, again, indicating lack of stirrups, which prevented these beams from developing ductile plastic hinges. Some rebar ruptures were observed but much less frequently. This was partly a result of the fact that large strain demands could not be adequately transferred to the longitudinal reinforcement in the column and wall bases in most cases due to inadequate bar development length. Concrete crushing was observed mostly in column and wall bases on one or both sides as the compression side changes during load reversals. Most often, the compression failure of the concrete occurred in the concrete cover and within a few inches of the longitudinal rebar, again, indicating lack of ductility. Plastic hinging was observed in only 37% of the buildings and in most cases, the plastic hinges did not develop properly (either light damage or non-ductile heavy damage with rebar buckling). Despite beam plastic hinges being the desired mode of energy dissipation in special RC moment resisting frames, plastic hinges in the beams were observed only 22% of the time.

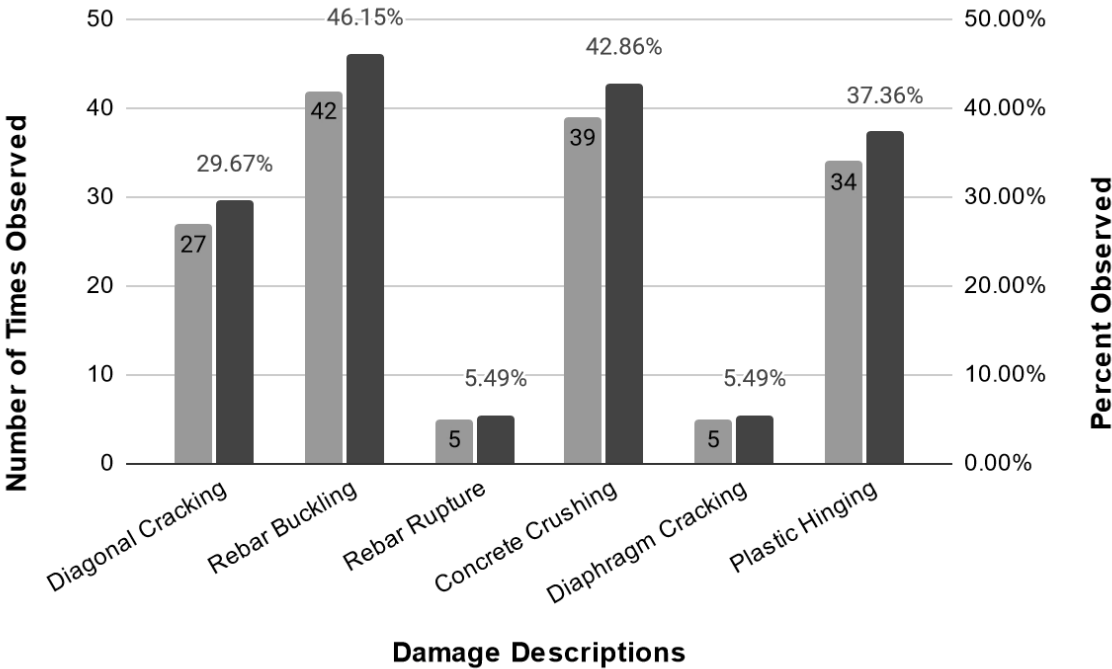


Figure 5.10. Types of damage observed in the residential buildings visited by the EERI Buildings team.

## 5.3 System Level Building Performance

### 5.3.1 Shear Wall and Beam-Column Frame System

As mentioned in Section 5.2, the affected cities visited by the EERI Buildings Team primarily had residential buildings, which typically had shear wall piers and frame systems. The shear wall piers were located within the partition walls of the residential units and commonly were not equally distributed in the two orthogonal directions, making one direction inherently weaker than the other direction. The longitudinal directions of shear wall piers were commonly perpendicular to the street to allow for as much front glass windows or open space as possible in the shops in the first story of the multi-story buildings. The shear wall piers and the columns were framed with moment frame beams or coupling beams. These coupling beams were not deep and did not have diagonal reinforcement.

It was observed that the vertical elements including shear walls and columns did not have adequate transverse steel for confinement and shear resistance and the rebar lap splices in the hinge zones were exposed with the concrete spalling off during the earthquake. Shear failure and unsymmetrical axial deformation at the bottom of the columns and in the beam-columns joints resulted in the excessive residual lateral drift and in some cases total collapse of the structure (Figures 5.11 through 5.13).



**Figure 5.11.** RC shear wall frame system building under construction, Antakya (plan on the left; floor plate on the right)



**Figure 5.12.** RC shear wall frame system building under construction, Antakya (yielding in beams and shear walls on the left; collapsed structure on the right)



**Figure 5.13:** Residual lateral drift in a RC shear wall frame structure, Antakya, Hatay Province.

### 5.3.2 Tunnel Form Shear Wall System

Residential buildings built by the government used tunnel form construction with the main lateral force resisting system consisting of reinforced concrete shear walls. This tunnel form construction allows for walls and slabs to be cast simultaneously in one cycle combining the benefits of speed, quality and accuracy. The specifics of reinforcement detailing for this type of construction as compared to the typical residential buildings that had heavy damage and suffered collapse were unknown to the EERI Buildings Team. However, at least in Hatay and Kırıkhan, detailing of steel reinforcement in these buildings appear to meet the requirements for ordinary shear walls in ACI 318-19. It was observed that these buildings behaved rather well in the seismic event. An example from Kırıkhan with the fault rupture located on the building corner is shown in Figures 5.14 and 5.15. One reason for the good performance of these buildings is the large number of shear walls, which offered a high level of redundancy for load redistribution.

In some unique cases, single localized short wall failure was noted, which was clearly a design issue.

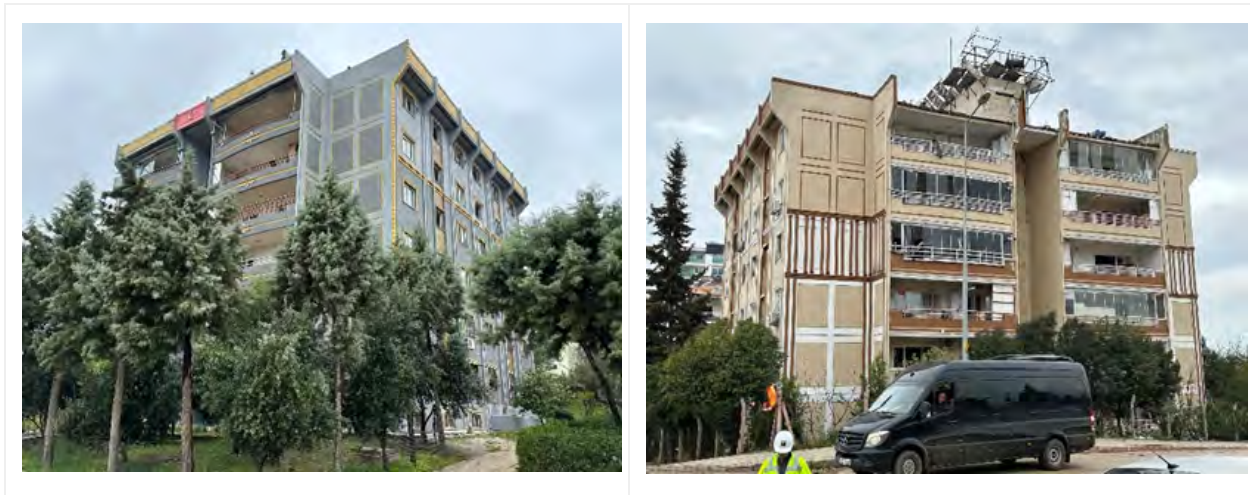


**Figure 5.14.** Structures with tunnel-form construction for government buildings, Kırıkhan



**Figure 5.15:** Localized short column effect induced by partial failure of masonry infill walls.

### **5.3.3 Steel Framed System**

The primary construction material used for residential construction was reinforced concrete. However, some steel framed structures were encountered for residential construction in İskenderun and Antakya. A set of three buildings utilizing steel construction in İskenderun remained undamaged (Figure 5.16). However, our understanding was that due to the high cost of the construction, the owners and contractors were out of business and the buildings were essentially vacant during the earthquake. In another instance, a steel framed building had minimal damage on exterior walls but no apparent structural damage.



**Figure 5.16.** RC core with steel gravity framing (tower photo at the top, framing and steel connection photos at the bottom)

We also observed three similar steel buildings in Hatay, which experienced very high intensity of shaking. All three buildings had a combined basement level for parking. One of the three buildings had moderate damage, the majority of which was concentrated in the infill walls. The other two buildings had a partial collapse. In the building shown in Figure 5.17, the perimeter column was supported by the basement wall, but it appeared that there was a shear anchorage failure leading to the column slipping off the basement wall. The perimeter beams developed a catenary action, however, the vertical movement at the failed column was significant enough to result in a partial collapse.



**Figure 5.17.** Steel-framed structure with failure at the base of the steel columns

### **5.3.4 Vertical Irregularities**

In multi-story buildings, the extended leasable/occupiable space at levels above the ground floor was common. In order to maximize the floor area, it is common in Türkiye for designers to use a greater area in the floors above than in the ground floor by adding cantilevers or overhangs (Figure 5.18). In certain instances, the lateral and gravity loads at the diaphragm level above the ground floor are transferred to the shear walls which form the primary lateral system of the building. An example of this is shown in Figures 5.18 and 5.19. The lateral and gravity loads on the multi-story shear walls were transferred through a cantilever beam with inadequate strength and stiffness, resulting in heavy damage of the façade and the non-structural elements in the primary structure. In this structure located in Antakya, significant damage was observed in the cantilever beams, perimeter columns and shear walls, and also in the adjacent link beams.





**Figure 5.18.** Structures with cantilevers/overhangs at floors above the ground level



**Figure 5.19.** Significant structural damage to cantilever beams and coupling beams

### **5.3.5 Pounding Effects**

A common problem in the affected cities was the proximity and inadequate seismic gaps between buildings. Particularly in Kırıkhan and Adıyaman, it was noted that there were a number of buildings with varying heights (5-12 stories) with inadequate separation (roughly only a couple of inches) between them (Figure 5.20). And in some cases, it was found that these inadequate separations were utilized to locate pipes and other utilities to service the building. With the slabs of these buildings not being in the same horizontal plane, the pounding became more detrimental, in some cases resulting in partial collapse of the structure.

In Antakya, pounding was more prevalent. There were several instances observed, where the neighboring buildings had collapsed or had severe lateral impact into a structure that had seen limited distress or damage on its own. Figure 5.21 shows a structure that had three buildings, which were on the left, back and front, collapsed into it. It was difficult to understand if the structure could have experienced any damage if not have been impacted by three structures on its sides, in lieu of partial collapse in the current condition.



**Figure 5.20.** Insufficient separation in seismic joints between buildings



**Figure 5.21.** Structure impacted by neighboring buildings (pounding effect)

### 5.3.6 Settlement and Overturning due to Liquefaction

Settlement and overturning due to liquefaction were observed by the EERI team primarily in two cities, i.e., İskenderun and Gölbaşı. Further information on the liquefaction and foundation performance is provided in Chapter 4. In İskenderun, traces of liquefaction were observed in a region with alluvial soils in the valley close to the Mediterranean Sea. Some structures collapsed in the region. However, among the structures that were still standing, a uniform settlement up to a maximum of 18 inches (450 mm) was observed, including structures that were 5 to 6 stories tall. The paved areas between the buildings did not experience settlements and had a noticeable bulge as shown in Figure 5.22.

In Gölbaşı, there appeared to be a strip of land with liquefiable soil, resulting in one side of the buildings settling relative to the other. This variable settlement even resulted in overturning of the buildings in a few instances and tilting of buildings in most instances.



**Figure 5.22.** Overturning and tilting of structures due to liquefaction, İskenderun



**Figure 5.23.** Permanent tilt in the structure due to liquefaction.



**Figure 5.24.** Settlement in the structure due to liquefaction.

## **5.4 Structural Performance of Reinforced Concrete Components**

### **5.4.1 Floor Slabs and Asmolen**

The floor system called “asmolen” in Turkish is commonly used in the earthquake affected regions. In this floor system, the voids between the joists are filled with bricks or lightweight

masonry blocks to improve insulation and to reduce the cost of labor and materials (Figure 5.25). Additionally, a flat slab appearance is achieved inside the apartments, which is considered more aesthetically pleasing with no beams visible. The thickness of the asmlen slab including embedded beams and joists is uniform and varies between 8 in. (200 mm) and 13 in. (330 mm). It was observed that, in general, both asmlen slabs and conventional concrete slabs with beams appeared to be very strong and rigid making it very difficult to achieve strong column-weak beam behavior in RC buildings, and most of the deformation demands were concentrated in the columns. As a result, damage or failure of these floor slabs were very rare (Figure 5.26). Usually, such damage is a result of partial collapse or major damage occurred in the building's vertical load carrying system including columns and/or shear walls. Damage in the building with asmlen slab shown in Figure 5.26 was a result of impact from the collapsed neighboring buildings.



**Figure 5.25:** Filler-joist floor systems (asmolen) with different filler blocks including bricks or hollow masonry blocks.



**Figure 5.26.** Large deformations in filler-joist (asmolen) floor system.

#### **5.4.2 Beams in Buildings with Shear Walls and Beam-Column Frames**

Overall, the EERI Buildings Team observed less damage in beams than in columns or shear walls. Although the beams generally appeared to be stronger and suffered less damage, there were many examples of damage near the beam ends. This type of observed damage typically corresponds to initiation of plastic hinge mechanism. In some cases, the beams reached their full plastic hinge capacity and concrete crushed at the beam ends (Figure 5.27). In most cases, the beams could not develop an efficient plastic hinge due to lack of sufficient transverse reinforcement to support the longitudinal reinforcement. This resulted in premature buckling of the longitudinal bars, spalling of the concrete cover, and lack of energy dissipation in the plastic hinge. Figure 5.28 shows diagonal or shear cracks in a well-reinforced beam in a collapsed building.



**Figure 5.27.** Plastic hinges at beam ends.



**Figure 5.28.** Uniformly distributed well-detailed transverse steel in a shear damaged beam in a collapsed building.

### 5.4.3 Coupling Beams and Deep Beams

Shorter beams were commonly used in buildings especially around stairwells, elevator shafts and near or above entrances or other openings. In many cases, diagonal or shear cracks developed in short beams between columns or in coupling beams linking the shear walls. As shown in Figure 5.29, diagonal cracks occurred in many coupling beams above door openings in the lower five stories of a 13-story building in Kahramanmaraş. This is consistent with the larger shear force demand expected in the lower stories. The EERI Buildings Team did not observe X-shaped or diagonal reinforcement in these coupling beams. The tunnel-form building in Figure 5.29 had only shear walls and did not have any columns. In some buildings, concrete crushed, and damage was distributed along a significant portion of the beam length (Figure 5.30).



**Figure 5.29.** Diagonal cracks in beams connecting shear walls in a building constructed using tunnel forms .



**Figure 5.30.** Damage distribution along the shorter beam including diagonal cracking.

#### 5.4.4 Beam-Column Joints and Column-Foundation Joints

The EERI Buildings Team did not observe any transverse steel inside the column-foundation or beam-column joint regions. Based on observations in the field, it can be concluded that the damage inside the joints was probably not one of the major causes of collapse in buildings, but they potentially aggravated the damage progression once the damage started near the ends of the columns. Figure 5.31 shows the exposed joint region of a column, which was damaged during the partial collapse of the building. Longitudinal bars buckled mainly due to lack of transverse steel in the joint region as well as opening of column ties at the top of the column in the first story.



**Figure 5.31:** Column joint region with no transverse steel, which is exposed after the right side of the building collapsed.



### 5.4.5 Columns

The EERI Buildings Team rarely observed ductile steel reinforcement details that are required in columns in special moment-resisting frame systems. One reason for this may be that such ductile buildings performed very well and no steel bars were exposed during the earthquake. Our observations are based on the detailing of steel bars that were typically exposed due to concrete cover spalling off or other damage. Figure 5.32 shows a well-detailed column with relatively closely-spaced transverse steel with overlapping hoops and 135-degree end hooks but concrete appeared not to have adequate strength. This column experienced uniformly distributed cracking along its length. Buckling of the longitudinal bars between the transverse steel is an indication of the relative effectiveness of the overlapping column ties in supporting the longitudinal bars in the transverse direction under large seismic demands.

In the region affected by the earthquake, the majority of the column reinforcement details were similar to those specified in ACI 318-19 for ordinary frames, e.g., lack of cross ties or overlapping hoops, wide column tie spacing, 90-degree hooks at the ends of ties, insufficient transverse steel to confine concrete or support longitudinal bars, and lap splices near or at the bottom of the columns. Typically, the columns had a rectangular cross section with a length equal to two to four times the width. Failure of one such column about its weak-axis bending direction can be seen in Figure 5.33. Out of hundreds of column failures observed by the EERI Buildings Team, Figure 5.34 shows one example of the typical damage associated with poor seismic detailing. This column had lap splices cut approximately 2 ft (600 mm) above its bottom. The column ties had 90-degree end hooks and did not include overlapping hoops or cross ties.

The most common occurrence of short column damage and failure was due to presence of partial infill walls on either side of the column or due to failure of the upper half of full-height infill walls. Figure 5.35 shows the short column effect and damage due to partial infill walls.



**Figure 5.32.** Column with overlapping ties experienced uniform cracking along its length.



**Figure 5.33:** Column failure in the weak-axis direction.



**Figure 5.34:** Failure of a column with lap splices near the bottom and insufficient transverse steel.



**Figure 5.35.** Short column effect and damage due to partial height infill walls.

#### 5.4.6 Shear Walls

The EERI Buildings Team observed the effective contribution of shear walls to lateral resistance of a range of buildings including combined shear wall and beam-column frame systems, and complete shear wall systems constructed using tunnel forms (Section 5.3.2). Short lap splices were commonly used near the bottom of the shear walls. Lap splices at the bottom of the first story columns and shear walls can be seen in Figure 5.36, which shows the completed foundation of a school building under construction in the central region of Kırıkhan.

In general, it was observed that the increased amount and number of shear walls in a given building led to better structural performance and overall less damage. In many cases the

presence of shear walls, even if they were very limited in number and size, prevented the collapse of buildings. For example, in the building shown in Figure 5.37, the U-shaped shear walls on the perimeter of the stairwell (or concrete core shear wall confining stairwell) prevented the collapse of the building after loss of multiple columns in the first story of that building. Similarly, in many buildings as in Figure 5.32, the shear walls in the first or lower stories were heavily damaged. The observed level of damage, e.g., diagonal cracking or concrete crushing as in Figure 5.33, decreased with increasing height. In other words, consistent with the expected lower seismic shear force demand in the upper floors of the building, typically there was limited or no damage in the shear walls in the upper floors or near the roof.

Tunnel form or complete shear wall buildings were mostly constructed by government as well as by some private contractors. The EERI Buildings Team observed some limited damage in these residential shear wall buildings in Kırıkhan and Antakya, while no damage was observed elsewhere, e.g., in Hassa. This is mainly because of the presence of abundant redundancy in the lateral and vertical load carrying system (see Section 5.3.2). As a result, the damage was typically concentrated in the most critical locations of shear walls and did not spread within the building. Figure 5.34 shows concrete crushing and transverse and longitudinal rebar rupture near the end of the shear wall where normally the axial stress is the largest due to combination of axial loads and bending moments.



**Figure 5.36.** Short lap splices above the foundation at the bottom of first columns and story shear walls in a building under construction.

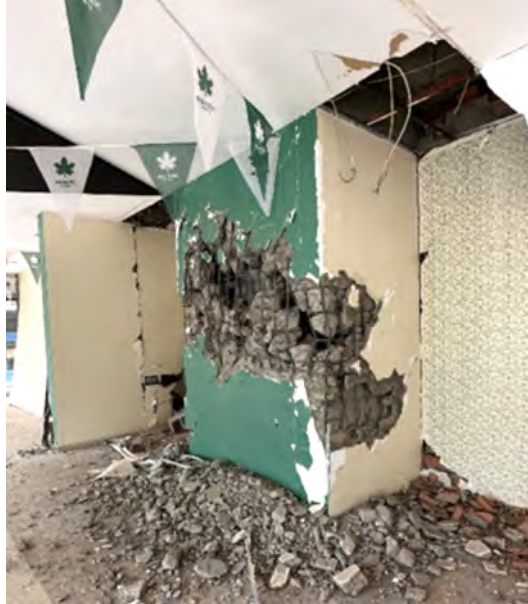


**Figure 5.37:** Damage in both orthogonal directions of a U-shaped RC shear wall.



**Figure 5.38.** Damaged shear walls in the lower stories of a building.



**Figure 5.39.** Damage in the first story of a tunnel-form shear wall building.

#### **5.4.7 Foundations**

The EERI Buildings Reconnaissance Team observed almost no structural damage or performance issues with the foundations themselves. However, in locations where liquefaction or soil failures occurred, many undamaged buildings sunk into soil, tilted as a rigid body or experienced permanent uniform drift (see Section 4.5). In general, there was very limited or no structural damage in many of these buildings due to direct effect of soil failures or settlement. It can be concluded that, overall, reinforced concrete shallow foundations including isolated footings and mat foundations (as structural components themselves) performed very well even in locations where liquefaction and soil failures were widespread such as in Golbasi (see Section 5.3.6) or in the neighborhoods of Iskenderun near the port (see Section 4.2.5).

### **5.5 Historical Buildings**

While reinforced concrete buildings dominate the building stock of recent decades in the earthquake-affected cities, many older buildings and buildings in more rural areas consist of URM, and to a lesser degree, wood construction. The performance of these buildings was generally consistent with the well-documented behavior of such buildings during past earthquakes around the world: URM buildings in areas of strong shaking often exhibited significant structural damage or collapse. This section highlights the behavior of these buildings through several examples.

The EERI Buildings Team documented several older unreinforced masonry buildings along the east bank of the Orontes River in Antakya. Similar to other neighborhoods in downtown Antakya, many buildings in this area collapsed or partially collapsed, and there was significant

damage to many of the remaining buildings. A three-story, URM building housing the Antik Beyazit Hotel experienced collapse of many of the exterior walls, resulting in the partial collapse of the wood-framed roof structure (Figures 5.40-5.42). According to information provided by travel websites (<https://www.booking.com/hotel/tr/antik-beyazit.html>), the building was constructed as a private residence in the early 1900s. The remaining wall piers along the front of the building exhibited diagonal cracking patterns characteristic of URM wall performance in earthquakes. The second story of the neighboring building, also constructed of URM, collapsed onto the first story (Figure 5.43). The EERI Buildings Team did not access the interior of either building due to the precarious nature of the remaining structures. The load path redundancy provided by multiple interior walls is believed to be a factor in preventing complete collapse of these buildings.

Larger commercial URM buildings in this area of Antakya exhibited similar damage patterns, e.g., (Figures 5.44-5.46). The second story of a multi-tenant commercial building collapsed onto the first story. It appeared that the arched structure of the first story provided stability and prevented it from collapsing as well. The construction date of this building is unknown to the EERI Buildings Team, but it is located adjacent to the historic Greek Orthodox Church, which also sustained significant structural damage. Debris from collapsed buildings in this area revealed a variety of masonry types, including stone and adobe brick (Figure 5.47).



**Figure 5.40.** Building housing the Antik Beyazit Hotel prior to the earthquake (source: Google Maps).



**Figure 5.41.** Damage to the unreinforced masonry building housing the Antik Beyazit Hotel.

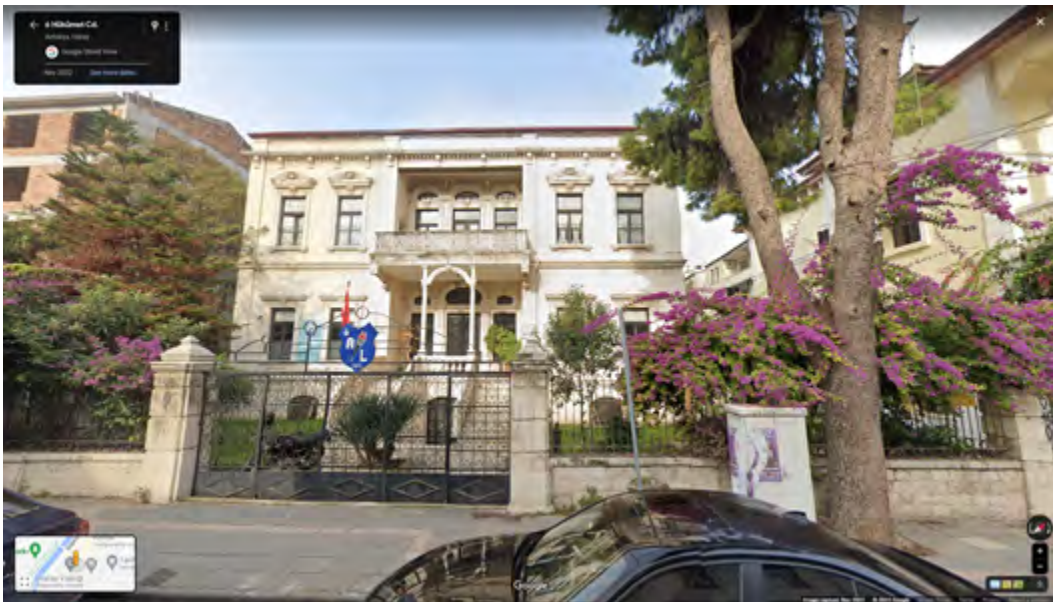


**Figure 5.42.** Building next door to the Antik Beyazit Hotel prior to the earthquake (source: Google Maps).





Figure 5.43. Collapse of the second story at a neighboring building.



Figure 5.44. Multi-tenant commercial building prior to the earthquake (source: Google Maps).



**Figure 5.45.** Collapse of the second story onto the first story at a multi-tenant commercial building.



**Figure 5.46.** Arched structure of the first story.



**Figure 5.47.** Adobe brick masonry debris of a collapsed two-story building.

## **5.6 Other Structures**

The EERI Buildings Team documented conditions at a number of religious, educational, healthcare and public buildings. These buildings exhibited a wide variety of structural systems and the earthquake damage patterns ranged from non-structural damage to partial collapse. Some trends in building performance among this somewhat disparate group of buildings are summarized in the following subsections.

### **5.6.1 Base Isolated Buildings**

The Team documented conditions at three base isolated hospital buildings: one under construction in Kahramanmaraş (Figure 5.48), and two in service in Malatya (Figures 5.49 and 5.51). All three buildings are reinforced concrete frame structures with friction pendulum type isolators. In all three cases, no structural damage to the hospital buildings was observed by the EERI Buildings Team or reported by hospital staff, despite significant structural damage to many nearby structures. Minor residual displacement was measured by the EERI Buildings Team at the isolators, up to approximately two inches in Kahramanmaraş. Because the hospital at Kahramanmaraş was under construction at the time of the earthquake, the keeper bolts used to hold the isolators in place had not been removed, leading to deformation of the keeper bolts and the associated connections on the sides of the isolators. The team members observed rust

and displacement (off-centered) in the isolators at Battalgazi hospital in Malatya (Figure 5.49). There was localized cracking of masonry infill walls at the hospitals in Malatya.



**Figure 5.48.** Base isolated hospital building under construction in Kahramanmaraş.



**Figure 5.49.** Base isolated hospital in service in Malatya.



**Figure 5.50.** Residual displacement of friction pendulum type isolator in Kahramanmaraş. Note that the keeper bolts had not yet been removed and were deformed by the isolator motion.

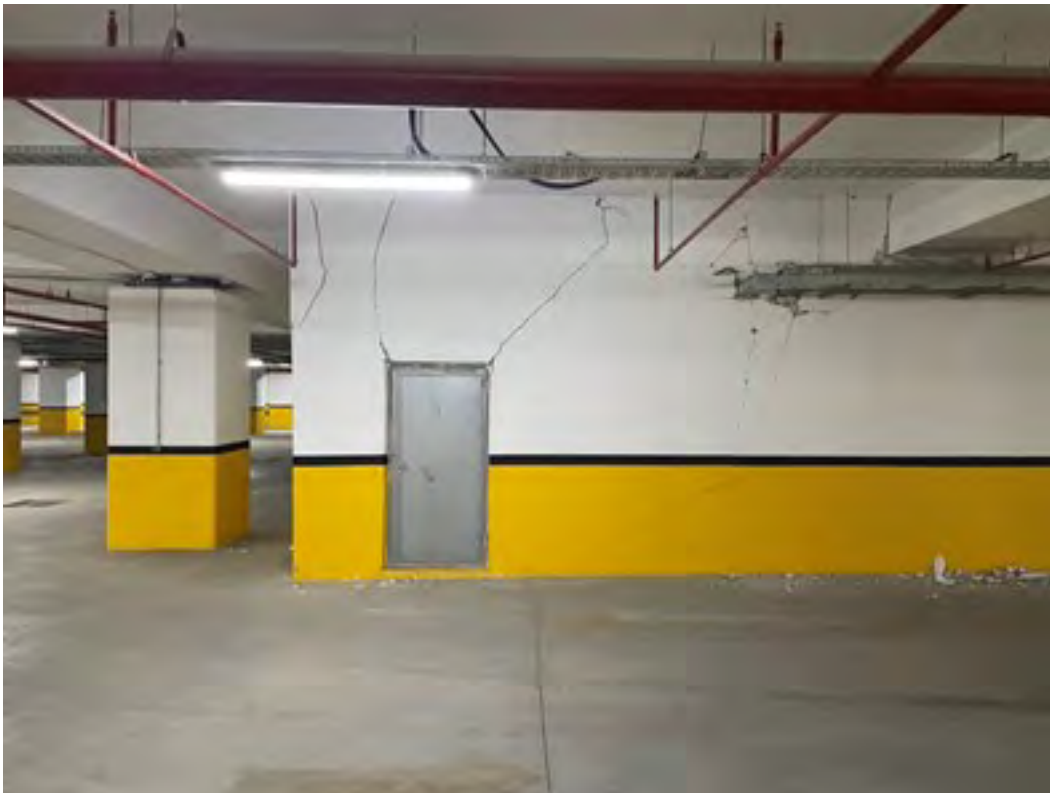


**Figure 5.51.** Cracking of masonry infill wall in Malatya.

### 5.6.2 School, Library and Courthouse Buildings

Multiple school, library and courthouse buildings documented by the EERI Buildings Team consist of low- and mid-rise reinforced concrete frame buildings (Figures 5.52-5.55). While typically older, these buildings generally performed well in comparison to high-rise reinforced concrete buildings as discussed above. The lack of a soft/weak story at ground level is believed to be a contributing factor to the better performance of many of these buildings. Many of these buildings also benefited from redundant load paths provided by multiple interior walls.

The EERI Buildings Team documented conditions at the Iskenderun Technical University, where buildings generally performed well structurally. However, portions of the site experienced liquefaction, resulting in differential building settlement (Figure 5.56). In addition, sky bridges between buildings sustained damage at the connections between the bridges and the buildings, resulting in the collapse of one sky bridge (Figure 5.57). The lack of ability of these connections to accommodate relative movement between bridge and building is believed to be the primary contributing factor to this damage. Based on publicly available aerial photographs, the primarily two- and three-story buildings of the campus were constructed between 2007 and 2011.



**Figure 5.47.** School building in Samandağ.



**Figure 5.53.** Library building in Nurdağı.



**Figure 5.54.** Courthouse building in Hassa.



**Figure 5.55.** Damage to exterior walls of Hasa courthouse.





**Figure 5.56.** Evidence of liquefaction adjacent to a building of Iskenderun Technical University. Perhaps fittingly, the photographed area is used as an outdoor laboratory for the University's geotechnical engineering department.



**Figure 5.57.** Collapse of a sky bridge at Iskenderun Technical University.

### 5.6.3 Religious Buildings

Mosques and churches documented by the EERI Buildings Team were typically URM or RC, depending on their age. They often included large open rooms and decorative features such as minarets and domes. Many of these structures experienced damage associated with collapse or partial collapse of the large open spaces and decorative features. For example, the Odabaşı Camii mosque, located just north of downtown Antakya, sustained collapse of the central dome and the four minarets (Figures 5.58-5.59). While the construction date of the RC building is currently unknown to the EERI Building Team, the debris revealed relatively modern (deformed) reinforcing bars; however, there appeared to be a general lack of adequate detailing of the members relative to modern reinforcing bar layout. Similar damage was observed to the URM Yeni Cami mosque in Malatya, which was reportedly reconstructed in 1913 (Figure 5.60).



**Figure 5.53.** Damage to the Odabaşı Camii mosque north of downtown Antakya.



**Figure 5.59.** Interior of Odabaşı Camii mosque with collapsed dome.



**Figure 5.60.** Damage to Yeni Cami mosque in Malatya.

#### **5.6.4 Industrial Buildings**

The EERI Buildings Team documented several industrial buildings, particularly in and around Kırıkhan, just north of Antakya. These buildings were mainly steel frame or precast concrete construction (Figures 5.61-5.62). Despite the poor performance of many nearby mid- to

high-rise RC buildings, the steel frame industrial buildings in this area generally performed well. While the age of these buildings is unknown to the EERI Buildings Team, many of them appeared to have been constructed recently. Damage to these steel frame industrial buildings was primarily limited to infill walls (Figure 5.61).

Precast concrete industrial buildings in this same area performed poorly. In particular, connections between precast columns and girders failed, resulting in collapse of the roof structures (Figures 5.62-5.63). The precast connections typically consisted of short dowels between adjacent members, which likely provided little resistance to relative movement between the members. Because of the open warehouse configurations of these buildings, there was no redundancy in the roof support structure. Debris was in the process of being removed from the site of two such buildings at the time of the EERI Buildings Team's reconnaissance in the area.



**Figure 5.61.** Good performance of steel frame industrial structure in Kırıkhan. Note the damage to the infill wall on the left side of the photograph.



**Figure 5.62.** Remnants of precast concrete industrial building in Kırıkhan. The photograph was taken by the owner prior to the cleanup of debris.



**Figure 5.63.** Precast connection at failed girder of Kırıkhan industrial building shown above.

## **5.7 Non-Structural Components or Contents**

While the focus of the EERI Buildings Team was on documenting the structural performance of buildings, whenever possible, the team also observed the performance of nonstructural elements, as described in the following subsections.

### **5.7.1 Façades**

One of the most common façade types observed by the field team (especially in residential buildings) was masonry infill walls covered with insulation and a waterproof membrane, often with windows framed into the infill walls. Typically, infill walls are constructed using lightweight masonry units, hollow clay bricks, or a combination of both, as shown in Figure 5.59. When a building drifts in response to an earthquake, the infill walls can crack and, if the displacements are large enough, the walls can crumble and fall out, either onto the street below or into the building. In less intense shaking, the insulation and waterproof membrane can delaminate from the building and fall to the ground below. Both these failure modes pose a significant risk to life safety and can impede functional recovery. Figures 5.65 through 5.69 show the different types of damage observed to masonry infill façades.



**Figure 5.64.** Lightweight masonry units and hollow clay bricks are commonly used as infill wall materials.

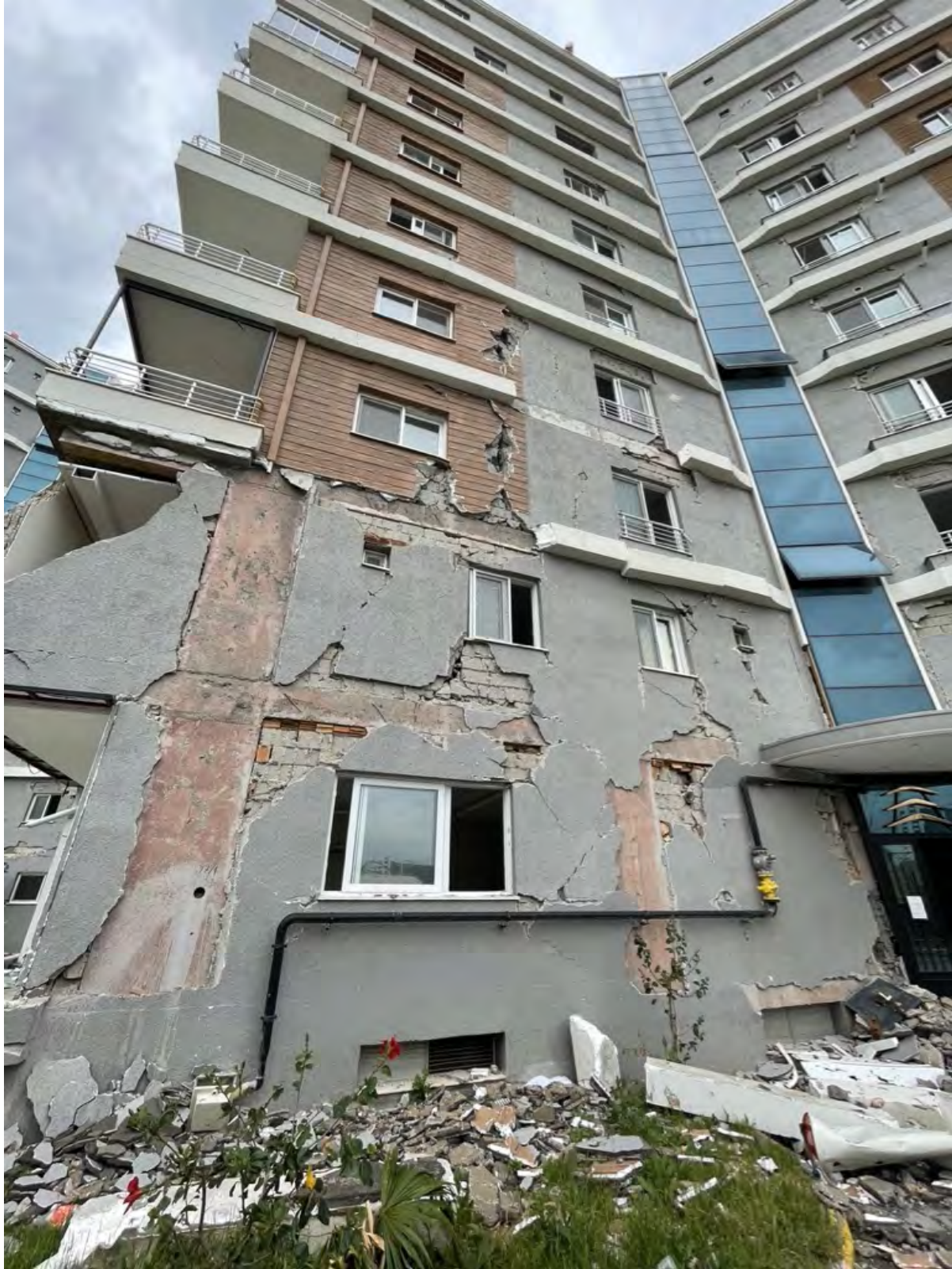


**Figure 5.65.** Cracking of infill wall facade with delamination of insulation and waterproof membrane in residential building near İskenderun.





Figure 5.66. Shear cracking in infill partitions at ground floor of residential building in Malatya.

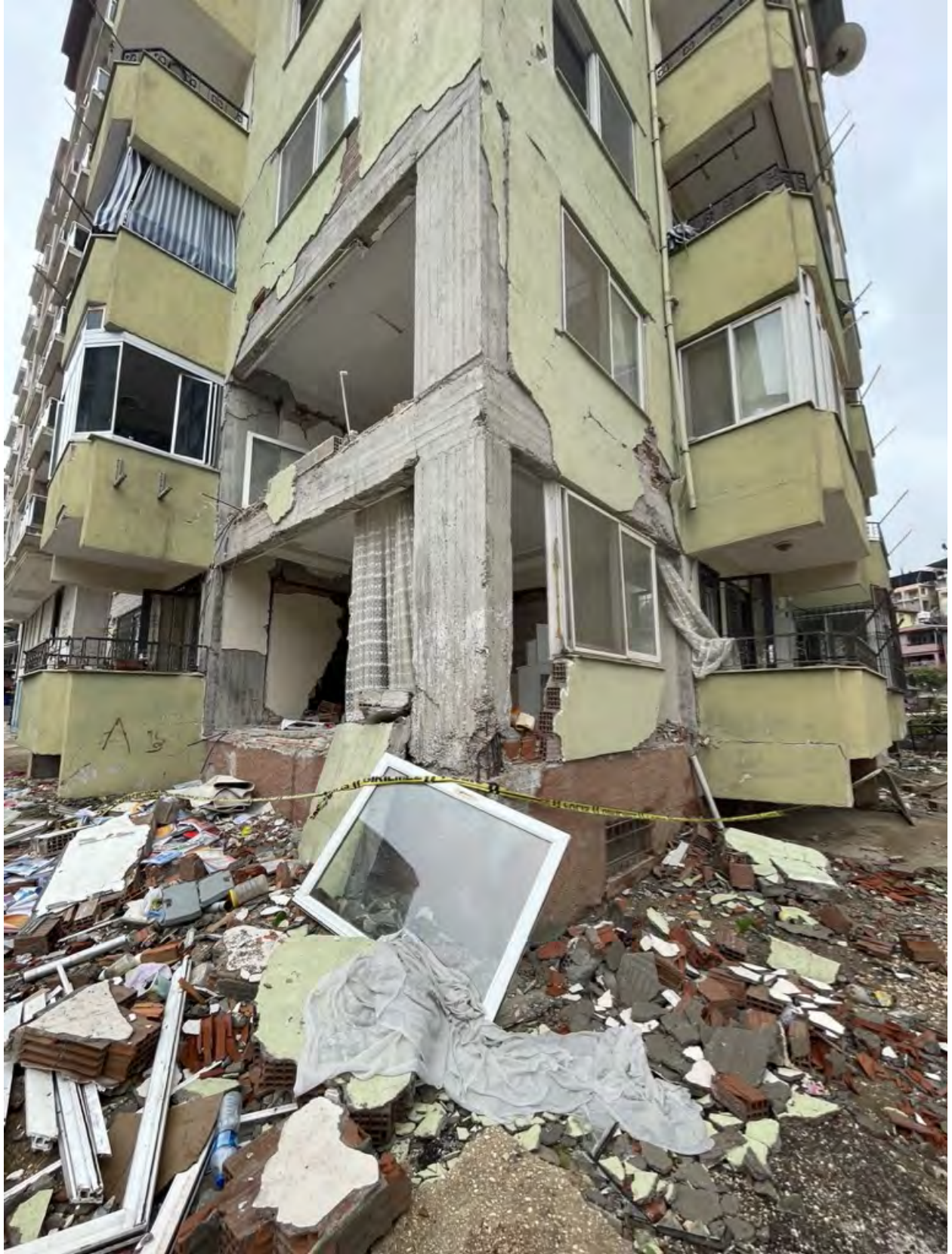


**Figure 5.67.** Failure of masonry infill wall at lower floors of a residential building in Kırıkhan.



**Figure 5.68.** Infill facade damage up the height of a residential tower in İskenderun.



**Figure 5.69.** Failure of infill facade at a hospital near Kırıkhan that damaged an ambulance and the power feed to the building.

Storefront glazing was frequently observed in the ground floors of commercial and mixed use buildings. This type of facade consists of glass panels set in metal frames, which often completely fill the space between structural members like columns or walls. Storefront glazing was also vulnerable to damage and failure, especially in the presence of more significant structural drift and damage. Figures 5.65 through 5.68 show some of the damage patterns observed to storefront glazing.



**Figure 5.70.** Damage to individual glass panels in storefront glazing facade in commercial building in Iskenderun.



**Figure 5.71.** Damage to metal frame and glass panels in storefront glazing facade in mixed use building near Antakya.



**Figure 5.72.** Global buckling of metal frame of storefront glazing at ground floor of mixed use building in Iskenderun.



**Figure 5.73.** Failure of metal frame in storefront glazing due to structural damage in columns of a mixed use building near Adiyaman.

### 5.7.2 Interior partitions

Masonry infill walls are frequently used as interior partitions across all building types in Turkey, especially concrete frame and wall buildings. They exhibit similar failure patterns as exterior infill walls and also pose a risk to life safety and can impede functional recovery, as shown in Figures 5.74 through 5.76. Sometimes electrical conduit and water pipes were embedded in the infill walls, resulting in damage that could impact the functionality of the building.



**Figure 5.74.** Failure of infill partition in a residential building near Malatya.





**Figure 5.75.** Infill partition damage in a residential building near Adiyaman.

Steel frame partitions with drywall sheathing were also observed, though these types of interior partitions were not common. The photo below shows fallout of drywall panels and buckling of the steel partition frame in a commercial building in Kahramanmaraş.



**Figure 5.76.** Damage to steel frame partitions with drywall sheathing in commercial building in Kahramanmaraş.

### **5.7.3 Rooftop equipment and structures**

Rooftop equipment such as solar water heaters are common throughout Türkiye. These heaters typically feature a solar panel and water tank supported on a metal frame anchored to the roof. Due to the weight of the water tank, collapse of these solar heaters was frequently observed, sometimes resulting in them falling to the ground (Figures 5.77 and 5.78). The team also observed damage to and failure of rooftop penthouses and appendages, including collapse of wood-framed roof structures with heavy clay tiles (Figure 5.79).



**Figure 5.77.** Varying levels of damage to rooftop solar water heaters in a residential building near Kırıkhan.



**Figure 5.78.** Failure of rooftop solar water heaters in Antakya.



**Figure 5.79.** Collapse of wood-frame gable roof structure in a school building in Antakya.

#### **5.7.4 Ceilings**

Damage to suspended ceilings was observed in some non-residential buildings, including fallout of individual acoustic tiles, pull out of the metal frame at the perimeter, and loss of vertical support of part or all of the suspended ceiling frame, as shown in Figures 5.80 through 5.84. Many of the observed suspended ceiling systems lacked seismic restraints. Damage to ceilings pose a significant life safety risk and can impact the functionality of the building.



**Figure 5.80.** Fallen ceiling tiles and HVAC ducts near a hospital entrance in Kırıkhan.



**Figure 5.81.** Failure of perimeter metal framing of suspended ceiling in mixed use building in Hassa.



**Figure 5.83.** Loss of gravity support of suspended ceiling in commercial building in Kahramanmaraş.



**Figure 5.84.** Loss of gravity support of suspended ceiling in residential building in Adiyaman.

### **5.7.5 Building contents**

Damage to important building contents, including toppling of computers and shelves, was observed throughout the earthquake impacted region (see Figures 5.85 and 5.86). In addition, bolted edges of the square metal plates of a water tank were torn off in a school building in Kahramanmaraş (Figure 5.87). Building contents typically lacked seismic restraint, though brackets were observed anchoring a large bookshelf to the wall of a school in Kahramanmaraş (Figure 5.88).



**Figure 5.85.** Toppling of large storage shelf in a hospital room in Kırıkhan (along with damage to masonry infill walls and suspended ceilings).



**Figure 5.86.** Toppling of computers and books from bookshelves in a library in Nurdağı.





Figure 5.87. Damage to water tank in a school in Kahramanmaraş.



**Figure 5.88.** Example of a large bookshelf with seismic restraints (side and top) in a school building in Kahramanmaraş.

### **5.7.6 Stairs**

Stairs are critical to ensure safe egress from a building after an earthquake. Because they span between floors, stairs are vulnerable to damage induced by the differential movement between the floors if they are not properly detailed. The EERI Buildings Team recorded several instances of significant damage to concrete cast-in-place stairwells in residential buildings, as shown in Figures 5.89 and 5.90. In some instances, the infill walls adjacent to the stairwells collapsed onto the stairs, further hampering safe egress.



**Figure 5.89.** Structural damage to a stairwell in a residential buildings in Adiyaman (including debris from failed masonry infill wall)



**Figure 5.90.** Structural damage to a stairwell in a residential buildings in Malatya (including debris from failed masonry infill wall)

## 6.0 Hospitals

*Gordon Wray, Ali Sumer, Onder Akinci, Ricardo Henocho, Bret Lizundia, Maryann Phipps, Ali Roufegarinejad, Dr. Volkan Kara, Yuksel Tonguc*

In the weeks following the 2023 Kahramanmaraş Earthquake Sequence, EERI assembled a team of structural engineers with hospital and seismic isolation expertise to assess the performance and recovery of hospitals in the affected region. A medical doctor and a structural engineer from Türkiye joined the team. The team met in Ankara for a meeting at AFAD headquarters before traveling to Adana, which served as the home base for five days of field reconnaissance in the provinces of Kahramanmaraş, Hatay, Osmaniye, Gaziantep, and Adana. In addition to structural engineering observations, the team was interested in whether the hospitals continued to provide service to the community in the days and weeks after the event. If service was interrupted, the team sought to understand the reasons why and how those lessons can be applied to high-seismic areas of the United States and California. All photos within this chapter were taken by the EERI Hospitals team unless noted otherwise.

Within the earthquake affected area of Türkiye, there are approximately 14 million people, 116 hospitals, and 24,000 beds, resulting in 17 beds per 10,000 residents. The breakdown by province is shown in Table 6.1. These numbers are similar to those in California with 18.7 beds per 10,000 population in 2021.<sup>6</sup> Hospital damage and post-earthquake response within Syria was not part of the team's objective and therefore is not covered in this report.

### 6.1 *Breadth and Depth of Observations*

Over the span of five days (March 14-18, 2023) the EERI Hospitals team observed 28 hospital buildings. Additional hospital data were collected by the EERI Buildings team (3) and Degenkolb Engineers (6) within a similar timeframe. The sampling of buildings included old and new; large and small; and government, private, and university hospitals. Six buildings were seismically-isolated; the rest were fixed-base. The diverse sampling was intended to be representative of the hospitals in the affected area. See Figure 6.1 for a map of the hospitals visited overlaid with the PGA contours from the earthquake sequence. See Table 6.2 for a summary of the hospitals visited and PGA and PGV data (consistent with the ground motions from Chapter 3 of this report. See Figure 6.2 for histograms depicting the Operational Status by PGA and Year of Construction.

---

<sup>6</sup> <https://www.kff.org/other/state-indicator/beds-by-ownership/>

**Table 6.1.** Population and Hospital Data by Province in earthquake affected area

Province	Population*	# of Hospitals	Hospital Bed Capacity**	# of Beds per 10,000
Hatay	1,686,043	12	2,847	17
Kahramanmaraş	1,177,436	10	1,934	16
Adiyaman	635,169	10	1,184	19
Osmaniye	559,405	5	735	13
Malatya	812,580	12	1,733	21
Gaziantep	2,154,051	12	3,060	14
Adana	2,274,106	14	4,345	19
Diyarbakır	1,804,880	18	2,703	15
Elazığ	591,497	8	1,690	29
Kilis	147,919	2	635	43
Şanlıurfa	2,170,110	13	2,987	14
Region Total	14,013,196	116	23,853	17

\*Source: Address Based Population Registration System, 2022

\*\* Source: Türkiye Earthquakes Recovery And Reconstruction Assessment Report Strategy and Budget Office (SBO) of the Presidency of the Republic of Türkiye, Ministry of Health  
Number of Hospitals includes Ministry of Health, University and Private Hospital data.

The depth of observations depended on level of access and extent of damage. While staff encountered at some facilities provided in-depth interviews and allowed full interior access, others were protective of their information or were closed. Table 6.2 includes information on survey level where Level 1 indicates exterior only access, Level 2 indicates access to interior and exterior, and Level 3 includes interview with hospital staff. Most of the “Exterior-Only” Level 1 observations were a result of the hospital being closed.





**Table 6.2.** Hospital data collected by EERI Hospitals Team, Building sTeam, and Degenkolb Engineers

Hospital Name	# of Beds <sup>4</sup>	Survey Level <sup>2</sup>	PGA (g)	PGV (cm/s)	Year of Const.	Struct. Damage	Nonst. Damage	Operational Status <sup>4,5</sup> (6 Weeks)	Comments
<a href="#">Pazarcık Government Hospital</a> <sup>3</sup>	125	3	1.50	103	2020	None	Moderate	Partial	Nonstructural repairs in progress
<a href="#">Private Eastern Mediterranean Hospital</a>	93	1	1.00	104	1997	Unknown	Moderate	Closed	
<a href="#">Defne Private Hospital</a>	245	1	0.98	132	2008	Moderate	Severe	Closed	Egress Stairs collapsed
<a href="#">Mosaic IVF Center, Antakya</a>	n/a	1	0.89	88	2004	Unknown	Unknown	Closed	
<a href="#">İslahiye Government Hospital</a>	n/a	1	0.83	134	2013	None	Minor	Closed	
<a href="#">Hassa Government Hospital - Old</a>	50	2	0.75	205	1992	Minor	Severe	Closed	Wood roof damage
<a href="#">Hassa Government Hospital - New</a>	50	1	0.75	204	2023	None	Minor	Open	
<a href="#">Hatay Government Hospital</a>	250	1	0.67	100	2013	Unknown	Unknown	Partial	
<a href="#">Kırıkhan Government Hospital</a>	210	1	0.59	67	2016	Unknown	Unknown	Partial	
<a href="#">Türkoğlu Dr. Kemal Beyazıt Government Hospital</a>	100	3	0.57	103	2018	Minor	Severe	Closed	
<a href="#">Nurdağı Government Hospital</a>	25	3	0.55	86	2016	None	Severe	Closed	
<a href="#">Necip Fazıl City Hospital - Under Construction</a> <sup>1</sup>	n/a	1	0.54	104	2023	None	None	n/a	Isolators were locked during construction. Locks broke
<a href="#">Necip Fazıl City Hospital</a>	1000	1	0.53	105	2012	Minor	Minor	Open	
<a href="#">Belen Government Hospital</a>	10	3	0.44	61	2023	None	Minor	Open	Under construction at the time of the earthquake. Construction was expedited later
<a href="#">Markasi Private Hospital</a>	85	3	0.37	61	2015	None	Minor	Open	
<a href="#">Hatay Education and Research Hospital</a>	150	1	0.37	228	2001	Collapse	Collapse	Closed	
<a href="#">Sular Academy Hospital</a>	300	1	0.35	56	2021	Unknown	Unknown	Open	
<a href="#">Sular Vatan Private Hospital</a>	n/a	1	0.34	51	2008	Unknown	Severe	Closed	
<a href="#">Megapark Private Hospital</a>	n/a	1	0.34	50	2007	Minor	Severe	Closed	
<a href="#">Palmiye Private Hospital</a>	132	3	0.29	52	2008	None	Minor	Closed	Voluntarily closed
<a href="#">Gelişim Private Hospital</a>	206	3	0.28	54	2005	None	Minor	Open	

<a href="#">İskenderun Government Hospital</a>	670	2	0.28	55	2011	None	Minor	Partial	
<a href="#">İskenderun Government Hospital - 1968</a>	n/a	1	0.28	65	1968	Collapse	Collapse	Closed	
<a href="#">İskenderun Government Hospital - 2005</a>	600	1	0.28	65	2005	Unknown	Moderate	Closed	
<a href="#">İskenderun Government Hospital - 2020</a>	n/a	1	0.28	65	2020	None	Minor	Closed	
<a href="#">Elbistan Government Hospital</a>	450	2	0.24	54	2017	None	Minor	Open	
<a href="#">Dörtyol Government Hospital<sup>1</sup></a>	250	2	0.24	53	2022	None	None	Open	Ceiling, partition damage
<a href="#">Malatya Women's Maternity Hospital<sup>1</sup></a>	350	2	0.23	71	2017	None	Minor	Open	Ceiling, sprinkler, partition damage
<a href="#">Malatya Training and Research Hospital</a>	1055	2	0.23	68	2013	None	Minor	Open	Ceiling, sprinkler, partition damage
<a href="#">Erzin Government Hospital</a>	50	1	0.21	39	1994	None	Minor	Closed	
<a href="#">Dr. Ersin Arslan Training and Research Hospital</a>	154	1	0.21	37	1962	Minor	Minor	Closed	1 column damaged
<a href="#">Battalgazi State Hospital<sup>1</sup></a>	300	2	0.20	55	2022	None	Minor	Open	Ceiling, partition damage
<a href="#">Osmaniye Government Hospital - Base Isolated<sup>1</sup></a>	600	2	0.17	34	2023	None	None	Open	
<a href="#">Osmaniye Government Hospital</a>	n/a	1	0.16	32	2015	Unknown	Unknown	Partial	
<a href="#">Adana University Hospital</a>	1000	1	0.07	41	1972	None	unknown	Closed	
<a href="#">Adana Government Hospital<sup>1</sup></a>	1550	2	0.06	35	2017	None	Minor	Open	Minor damage to partition walls at isolation plane

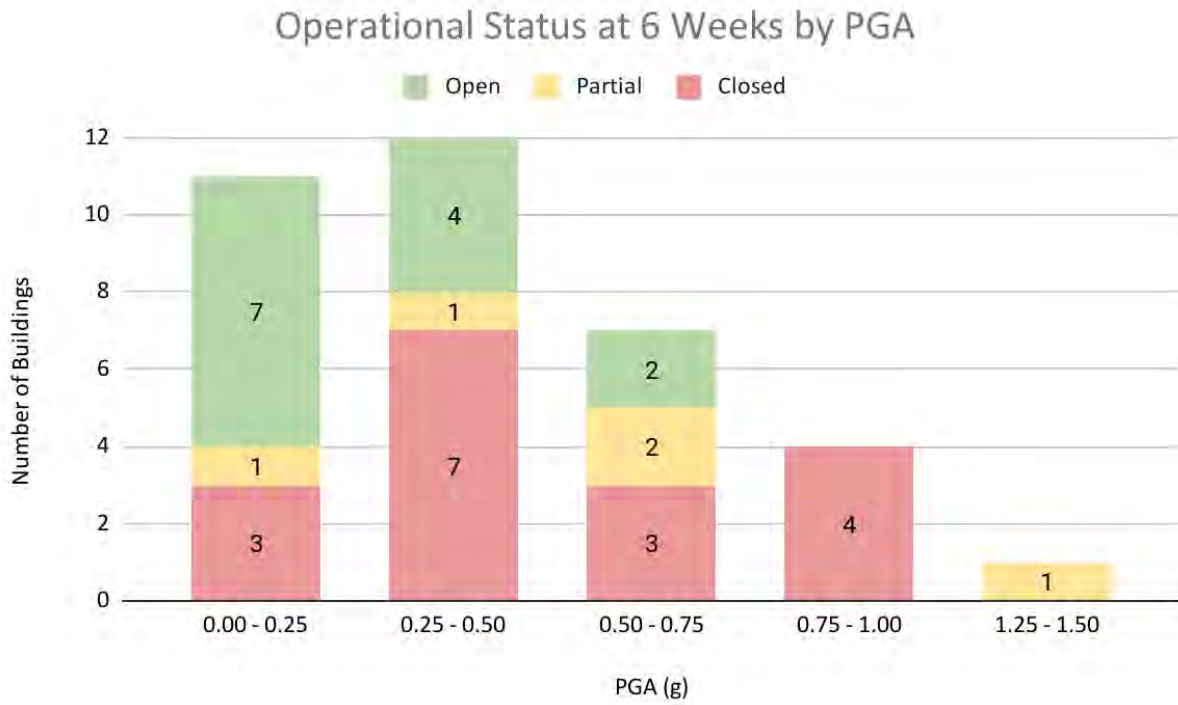
<sup>1</sup> Seismically-Isolated Building (also shaded gray)

<sup>2</sup> Survey Level 1 = Exterior-only, Survey Level 2 = Interior + Exterior, Survey Level 3 = Interview with Staff

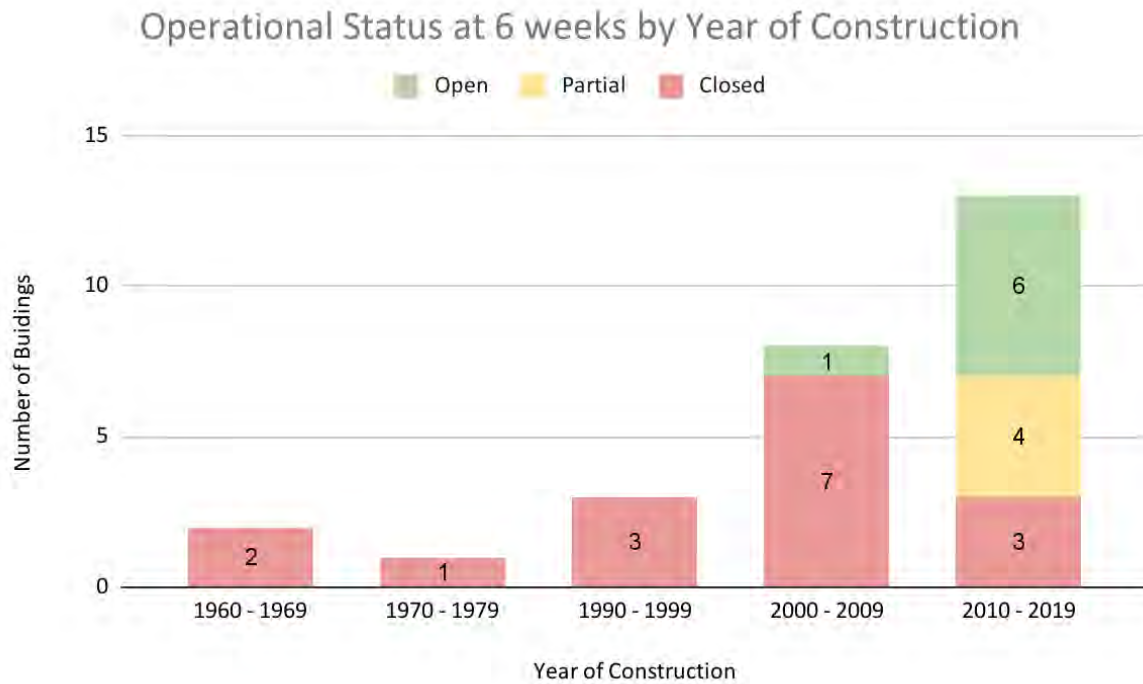
<sup>3</sup> Pazarçık Government Hospital is located 3km from nearest station TK4614 which recorded a RotD50 PGA of ~2.2g during the M7.8 event. This acceleration is significantly higher than other nearby stations with PGAs less than 1.0g, leading the EERI hospital team to question its accuracy.

<sup>4</sup> n/a = not available

<sup>5</sup> Hospitals operating from tents, not utilizing interior space, are marked as "Closed"



(a)



(b)

Figure 6.2. Charts representing data from Table 6.2

## 6.2 Structural Performance

The observed hospitals ranged from one to ten stories in height, with many three or four stories. They included both fixed base and seismically isolated structures. The lateral force-resisting systems were primarily reinforced concrete shear wall (RCSW) and reinforced concrete moment frames (RCMF), both with masonry interior partitions and perimeter masonry infills. Concrete shear walls were often found at stair cores. The gravity load-carrying systems observed include flat plate, waffle, and one-way joists with hollow clay tile left-in-place forms between the joists. Foundations include mats, spread footings under columns, strip footings under walls, and deep foundations such as piles in some cases. Seismic joints were common between wings and generally more prevalent than typically seen in the United States. A typical hospital floor plan is shown in Figure 6.3.

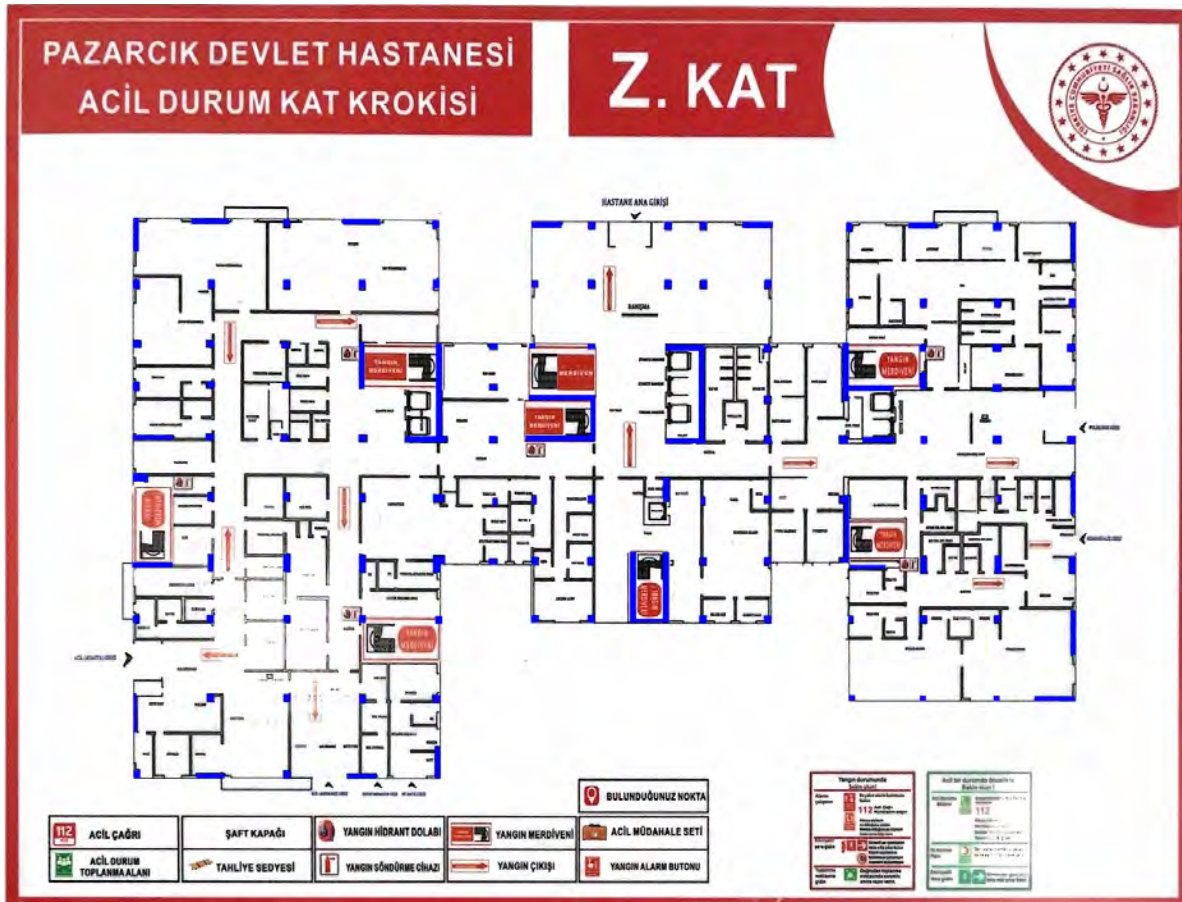


Figure 6.3. Pazarcık Government Hospital Floor Plan. Blue lines indicate concrete shear walls.

The following types of structural damage were observed. Examples follow with more detail.

- Shear walls: Diagonal tension cracking and horizontal cracks at construction joints where the wall meets the floor slab were observed in stair shear wall cores.
- Masonry Infills: Stiff, relatively heavy masonry infill at exterior walls and at interior partition lines were installed tight to the concrete columns and beams without gaps, participated in resisting load, and had light to severe cracking and spalling, with many instances of out-of-plane failure ranging from small pieces to entire panels. In some shear wall stair cores, the side with the door was infilled, and the other sides were concrete, and the masonry infills were more heavily damaged than the concrete.
- Columns and beams: Limited damage was observed in the buildings the team could visit. The quality of exposed concrete varied, with noticeable rock pockets visible in beams and columns, particularly in older buildings.
- Concrete stairs: Slip joints were not observed. Stairs resisted loads, and they failed in some cases, hindering or preventing egress. There were examples where the stair runs had nearly fully disengaged and were hanging vertically from rebar.
- Foundations: Some rocking on shallow foundations appeared to be observed in some buildings. Settlement (up to about 15 cm) of the soil and supported hardscape around the perimeter of a pile supported hospital was seen.

Of the hospital buildings observed that were constructed within the last 20 years, we observed little evidence of structural damage in fixed-based concrete structural systems. Using the terminology of ASCE/SEI 41-17, these buildings provided Damage-Control (or better) structural performance despite exposure to PGA greater than 1.0g in locations. The vintage of the buildings suggest they were designed to the 2007 Turkish Building Code which incorporated lessons learned from the 1999 Kocaeli and Düzce Earthquakes. Neither structural drawings nor calculations were available to confirm the basis of design.



**Figure 6.4.** Pazarcik Government Hospital,  $PGA = 1.50g$ ,  $PGV = 103 \text{ cm/sec}$ . This hospital (125 beds), completed in 2022 had no significant structural damage observed or reported but suffered considerable nonstructural damage, which led to evacuation. Outpatient type urgent care services were provided Day 0 (immediately after the earthquake). Most patients were transferred to other hospitals. Clinics were consolidated on the first floor on Day 10. The rest of the hospital was closed and underwent removal and replacement of most finishes prior to reopening (in progress Week 6).



**Figure 6.5.** Nurdağı Government Hospital as observed on March 17, 2023.  $PGA = 0.55g$ ,  $PGV = 86 \text{ cm/s}$ . This small local hospital (25 beds) was only one year old at the time of the earthquake. It suffered widespread nonstructural damage, but only limited structural damage. It was immediately evacuated and closed. An emergency tent hospital was set up on the premises to serve the community.

Hospitals in Türkiye are designed with an Importance Factor of 1.5, similarly to practice in the United States. The strength and stiffness provided by the concrete shear walls served to limit damage to the gravity frame elements, preventing collapse. Hospital buildings constructed after 2000 benefited from the availability of ready-mix concrete, which improved the quality of the material relative to site-mixed. Government hospitals are constructed and administered by the Ministry of Health. This attention to plan review and site inspection resulted in better structural performance relative to typical commercial or residential buildings.

Older buildings in regions of intense shaking did collapse. The team observed the 1968 Building at İskenderun Government Hospital and the Additional Service Building at Hatay Education and Research Hospital in Antakya. Both of these buildings had already been demolished at the time of the visit, so no direct observations could be made about the reasons for their collapse.



**Figure 6.6.** İskenderun Government Hospital as observed on March 15, 2023 (photos on right) , PGA = 0.28g, PGV = 55cm/s, This hospital contained multiple buildings constructed between 1968 and 2020. The 1968 building collapsed, the 2005 suffered extensive nonstructural damage and could not be occupied. All patients were relocated to the floor of the 2020 steel building before being transferred to other facilities.

Most buildings use unreinforced masonry (URM) as partition and exterior infill walls. These stiff materials include hollow clay tile (HCT), lightweight cellular hollow concrete block, and autoclaved aerated concrete (AAC). The AAC walls were the most typical in recently built hospitals. They are solid, ranging in thickness from 10 cm (4 in.) to 20 cm (8 in.). Gypsum wallboard on metal stud partitions were observed, but it was not common. The masonry infill walls were typically placed up tight to surrounding concrete columns and beams, without any observed seismic gap. Out-of-plane restraints at the top and sides were not observed. These infill walls increase the initial stiffness and strength of the building but are typically the first

elements to experience damage due to their low deformation capacity. Damage initiates as diagonal shear cracks and progresses to out-of-plane failures under strong shaking. In a hospital building in Hatay, diagonal compression struts in the masonry were observed to have induced shear cracking in the adjacent concrete columns. Heavy damage to masonry partitions and infills is a safety hazard to occupants. In addition, visible cracks and dislodged masonry have a psychological impact on occupants, creating fear and, in some cases, an unwillingness to reoccupy.



**Figure 6.7.** Masonry partition wall damage at Türkoğlu Dr. Kemal Beyazit Government Hospital as observed on March 13, 2023, PGA = 0.57g, PGV = 103 cm/s.





**Figure 6.8.** Exterior masonry infill wall damage at Megapark Private Hospital as observed on March 13, 2023, PGA = 0.34g, PGV = 51cm/s.

Stairs are typically not designed to be part of the primary structural system of buildings. However, when they are rigidly connected to the structure, they can act as diagonal struts that attract seismic loads. Stairs were formed from cast-in-place concrete, poured up to their surrounding walls. Stairs contained within C-shaped concrete shear wall cores performed well, while those adjacent to unreinforced masonry performed poorly (Figure 6.9). The consequence of improperly detailed stairs can be catastrophic, especially when these elements are the primary means of egress from a building following a seismic event (Figure 6.10).



**Figure 6.9** Egress stair adjacent to masonry wall at Türkoğlu Dr. Kemal Beyazit Government Hospital as observed on March 13, 2023.



**Figure 6.10** Collapsed egress stair Defne Private Hospital, Antakya, Hatay as observed on March 18, 2023. PGA = 0.98g, PGV = 132 cm/s.

### 6.2.1 Foundations

Members of GEER Team 3 (Patrick Bassal, Diane Moug, Jonathan Bray, and Sena Kendir) visited the Hatay Government Hospital in the Antakya, Hatay Province region to observe its geotechnical performance. The hospital was closed due to structural damage and the parking lot was being used as a temporary shelter ground for earthquake survivors at the time of GEER visit on March 31, 2023.

The free-field soils had settled relative to the hospital building throughout its perimeter, exceeding 40 cm in some areas (Figure 6.11a-b). The hospital and surrounding parking lot and facilities appear to be built over recently placed fill, due to their higher elevation than the surrounding river valley. The building elevation remained stable, indicating differential settlement occurred. Pipelines and utilities connected to the building were damaged as a result of this settlement.



(a)



(b)

**Figure 6.11.** Free-field soil settlement around the Hatay Government Hospital as observed on March 31, 2023: (a) near emergency entrance at west side of building , (b) settlement of over 40 cm at perimeter of southwest wing of main hospital building. Photos by GEER team.

Similar soil settlement was observed at Pazarçık Government Hospital in the province of Kahramanmaraş, where the free-field soils settled relative to the hospital foundation (Figure 6.12). At this site, the hospital was confirmed to be founded on piles. No reports of damage to pipes or underground utilities were reported



**Figure 6.12** Free-field soil settlement at Pazarçık Government Hospital in Kahramanmaraş as observed on March 17, 2023.

### **6.3 Non-Structural Performance**

Nonstructural components include cladding, partitions, ceilings, mechanical/electrical equipment, utility distribution systems, medical equipment, and other furnishings. Collectively, nonstructural components make up a significantly greater percentage of building cost than the cost of the structure, especially in hospitals (Taghavi and Miranda, 2003). Failure of these systems often occurs before failure of the structure, rendering the building unusable even when the structure is undamaged. The team observed that most hospital closures were attributed to the poor performance of nonstructural systems.

The structural engineering of these systems is an often-overlooked aspect of overall building design in many parts of the world. The 2018 Turkish Building Seismic Code includes a short chapter on the design of nonbuilding structures and the anchorage of mechanical and electrical equipment. Prior to adoption of the 2018 Code, the engineering design of these systems was not emphasized. Even with the inclusion of nonstructural provisions in the 2018 code, these services are generally not provided by the Engineer of Record for the building.

Exterior wall systems are constructed of unreinforced masonry infill (of different types) between concrete beams and columns. These infills are subject to cracking in-plane and failure out-of-plane resulting in life-safety hazards both inside and outside the buildings. See Figure 6.6 for an example of hollow-clay tile failure at a building exterior wall. Use of heavy stone panels as cladding systems are vulnerable to failure since their connection is made to lightweight masonry walls. Anchors are poorly developed and subject to pull-out. Lightweight cladding systems, such as metal panels, performed better.

As described in Section 6.2, interior masonry partitions add significant lateral stiffness to the building, attracting seismic load. Their weak construction is subject to cracking at low levels of lateral deformation. Typically story drift ratios in the order of only 0.002 or 0.003 are enough to initiate damage in masonry infill walls (Chiozzi and Miranda, 2017). Masonry walls can fail dramatically as shown in Figure 6.7, but more common are widespread cracks in masonry and plaster that can affect nearly all vertical surfaces in the building making the building appear to be more damaged than an engineer would report. Prevalence of cracks in walls degrades the confidence of the building's safety from hospital staff and patients and is among the primary reasons buildings and floors were closed. Six weeks after the earthquake, repair crews were busy patching cracks in walls on levels that had been evacuated and not used since the earthquake.



**Figure 6.13** Interior partition damage and ceiling repair.

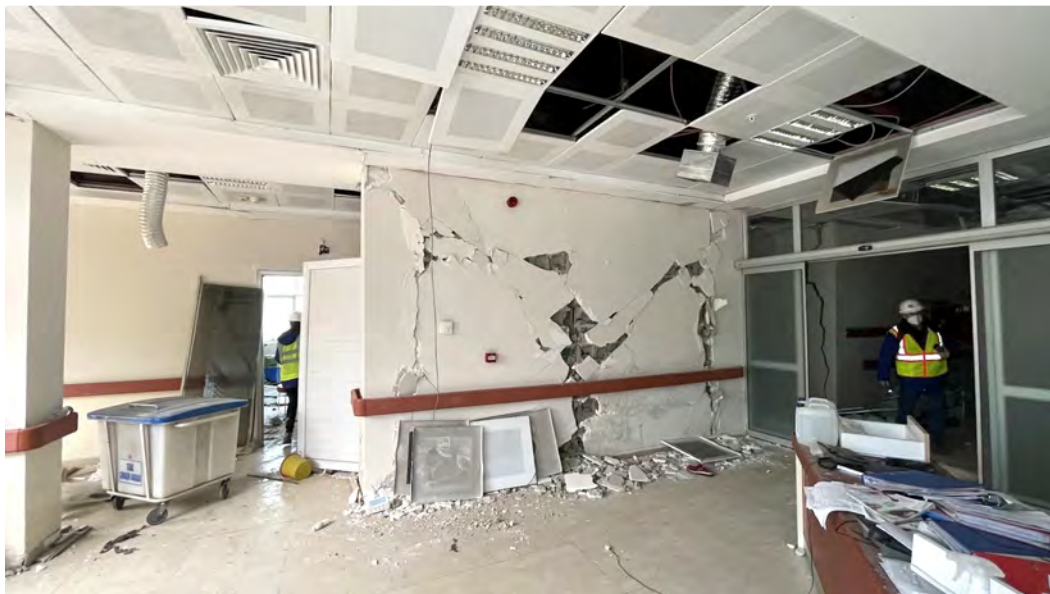


**Figure 6.14** Interior partition and ceiling damage.

Ceiling construction in Turkish hospitals is often a system of panels (metal and acoustic tile) on suspended T-shaped runners, similar to acoustic tile ceilings in the United States. The suspended ceilings in Türkiye did not have diagonal wires or compression struts as required by standards governing ceiling installations subject to high seismic demands. The ceiling failures observed included metal panels falling from the grid and the grid itself falling from the supporting slab. Like the partition walls, repairs were being made to the ceiling systems where areas were being readied for re-occupancy.

Equipment within buildings was not anchored as required by US codes (ASCE 7/SEI, Chapter 13); however, larger equipment generally remained in position, smaller equipment had varying performance. Several unanchored emergency generators, chillers, and other large units at-grade experienced intense shaking without displacing at the base (Figure 6.15). Even unanchored roof-mounted units showed very little evidence of displacement. The equipment, however, was not always functional, even if it did not shift position. Non-functioning emergency generators were the first reason cited for closure of at least one hospital, while other hospitals praised their emergency generators as the reason their limited outpatient services were able to remain in service. High aspect ratio equipment and tanks were found toppled when improperly anchored, see Figure 6.16.



**Figure 6.15.** Unanchored generator (left) and unanchored chiller (right) in Iskenderun, Hatay province.



**Figure 6.16.** Toppled tanks in [Nurdağı Government Hospital](#).

Overhead utility distribution systems such as piping, ductwork, conduits, and fire sprinklers were not seismically braced. Of the hospitals that were in the process of returning to full service, some cited water leaks as a consequence of the earthquake, however this was not independently verified. In many areas, water service from the city was disrupted immediately following the earthquake, but in the following days and weeks, city water mains were restored and the piping systems in hospitals were partially repaired.

Large medical equipment also typically did not appear to be anchored to the structure, but similarly did not show evidence of sliding. Imaging equipment was observed to be in the original position, but took time to resume service due to a need for recalibration and limited availability of technicians. One hospital described that an In-vitro Fertilization (IVF) incubator fell to the ground and broke, which caused the department to be closed despite little other damage. Lead times on replacing these essential pieces of equipment are reported as several months.



**Figure 6.17** CT Scanner required recalibration in Pazarcık, Kahramanmaraş province.

Interior furnishings and building contents were either unanchored or insufficiently anchored, resulting in toppled cabinets, shelving units, and storage areas. In some locations, cabinets had been anchored to the lightweight masonry partitions with plastic drywall anchors, which were insufficient for the seismic loads. Where shelving units were adequately anchored, the contents of shelves were spilled on the floor resulting in a mess but not a life-safety hazard of falling units.





Figure 6.18. Cabinet failure at Nurdağı Government Hospital.

#### **6.4 Seismically-Isolated Building Performance**

Türkiye is considered a leader in adoption of seismic isolation for hospitals with over 65 isolated hospitals as of 2021 with more under construction<sup>7</sup>. Eleven of these buildings are located in the affected area of southern Türkiye. The 1999 Kocaeli and Düzce Earthquakes damaged 12 hospital buildings beyond repair<sup>8</sup> which prompted the Ministry of Health in 2013 to enforce that “Hospital Buildings, located in Seismic Zones 1 and 2 with a number of capacity over 100 beds should be constructed with seismic-isolation”.<sup>9</sup> Additionally, the Ministry of Health has provided guidelines for isolation design, which are similar to those of ASCE/SEI 7.

---

<sup>7</sup> B. Sadan (2023)

<sup>8</sup> M. Erdik (2001)

<sup>9</sup> M. Erdik et al. (2018)

The EERI Hospitals team observed four seismically-isolated hospitals in the cities of Adana, Osmaniye, and Dörtyol, the EERI Buildings Team observed hospitals in Malatya and Türkoğlu, and the Degenkolb team observed a building in Malatya. All were operational following the earthquakes and were accepting transfers from hospitals that were not able to provide service. General observations were that the isolator displacements were small relative to the capacity of the bearings. A preliminary nonlinear response history analysis (NLRHA) was conducted by the EERI Hospital team to validate the observed displacement of the isolators under M7.8 earthquake motion. The analysis was based on the best estimates of isolator material and geometric properties as well as the building mass. Station TK 8003, located just steps away from the seismically-isolated Osmaniye Government Hospital, was used for the analysis. The initial results showed that the displacements observed at the Osmaniye Government Hospital were roughly consistent with the expected values based on the isolator properties and input motions. However, further studies are needed to evaluate the observed displacements of all seismically isolated hospitals in the earthquake-affected regions of Türkiye and determine if they are in line with the expected values, taking into account the bearing properties and recorded motions.

**Table 6.3.** Seismically-isolated hospitals observed by EERI Hospital and Building teams

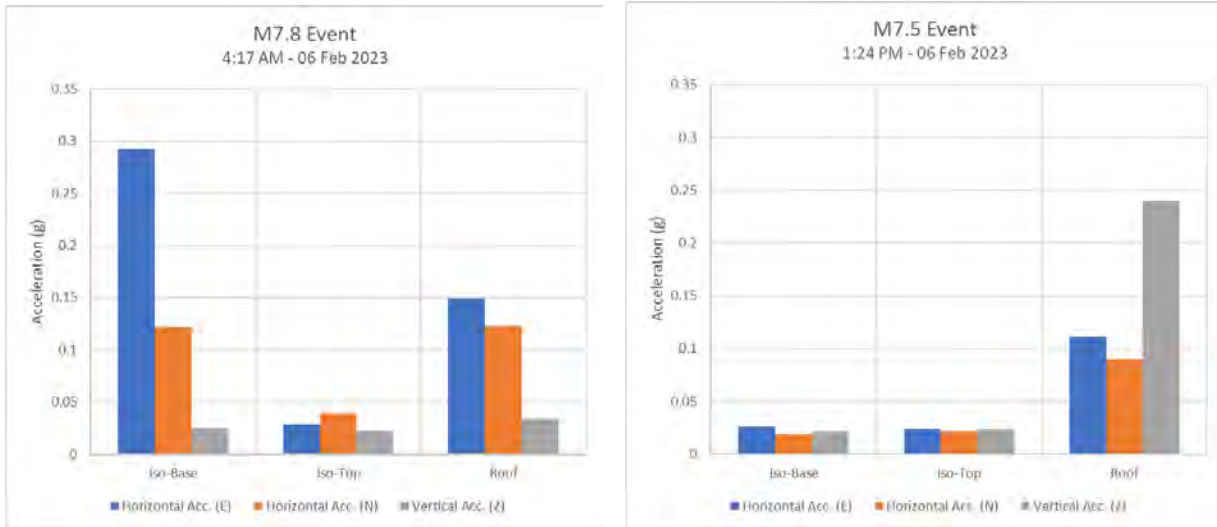
Site	Bearing Type and Manufacturer	PGA (g)	Sa @ 1.0 s (g)	Observed Isolator Displacement
<a href="#">Adana Government Hospital</a>	Triple Friction Pendulum - EPS	0.06	0.17	3 cm
<a href="#">Dörtyol Government Hospital</a>	Double Friction Pendulum - TIS	0.24	0.45	7.5 cm
<a href="#">Osmaniye Government Hospital</a>	Double Friction Pendulum - TIS	0.17	0.27	5-7 cm - system constrained by infilled moat
<a href="#">Malatya Women's Maternity Hospital</a>	Double Friction Pendulum - TIS	0.23	0.51	4 cm - The retaining walls appear to have restricted isolator movement, resulting in minimal observed isolator displacement.
<a href="#">Battalgazi State Hospital</a>	Double Friction Pendulum - TIS	0.19	0.31	17 cm (9 cm residual displacement, reported to be reducing over time and aftershocks)
<a href="#">Necip Fazıl City Hospital - Under Construction</a>	Double Friction Pendulum - TIS	0.52	0.66	This is a hospital under construction. 18 cm- Isolators were locked during construction. Locks broke

Adana Government Hospital is one of the world's largest base-isolated buildings with nine independent towers on a common isolated podium supported by 1,512 Triple Friction Pendulum isolators supplied by Earthquake Protection Systems. The isolation plane is located at the top of the columns within the below-grade parking garage level. The building is instrumented and recorded free-field accelerations on the order of 0.1g. For the M7.8 event on 06 Feb 2023, the accelerations just above the isolators were recorded as 0.03g, and 0.13g was at the highest roof level, demonstrating that the isolation system was effective at reducing the acceleration input to the building.

For the **M7.7** event on Feb 06, 2023 at 1:24 PM, the maximum recorded PGA at the base of friction pendulum isolators was approximately 0.03g. The accelerations recorded at the floor right above the isolation plane were also nearly 0.03g. This indicates that the isolators did not slide or, if it did, due to the low ground acceleration, the building was only minimally moved. The highest point of the roof had accelerations of 0.11g, which are still considered low. Overall, the hospital functioned as a seismically isolated hospital during the larger **M7.8** event that was closer to the site, thereby reducing ground motion accelerations. However, during the smaller **M7.7** event with the epicenter farther from the site, the hospital acted as a fixed-based hospital. Adana was outside the area of the strongest shaking with accelerations lower than the design level earthquake.



(a)



(b)

(c)

**Figure 6.19** a. Isolators in the parking level of Adana Government Hospital as observed on March 16, 2023; Recorded Accelerations in the Hospital, b. M7.8 Event, c. M7.5 Event.

Dörtyol Government Hospital completed construction in 2022 on 341 double friction pendulum isolators with 40 cm displacement capacity. Inspection of the dishes indicated that the inner slider moved about 3 cm on the bottom dish and 4.5 cm on the top dish for a total displacement of 7.5 cm. No damage was observed in the building, at the isolation plane, or at the moat.

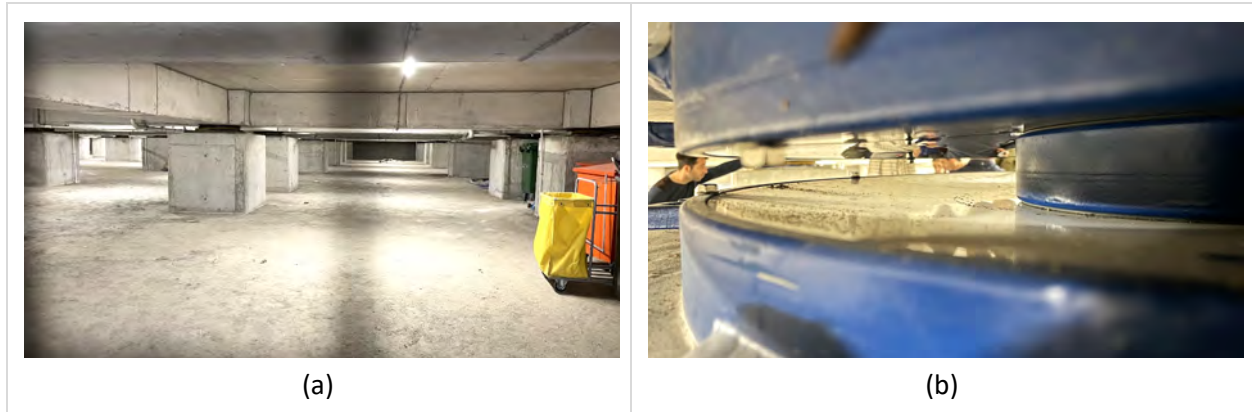


**Figure 6.19** Isolators at Dörtyol Government Hospital as observed on March 16, 2023.

Osmaniye Government Hospital is a newly constructed building, not yet open to the public at the time of visit. This 600-bed facility sustained 0.24g accelerations in the earthquakes and moved about 7 cm as recorded on scratch plates in the corners of the basement. This team observed that the perimeter moat was infilled mainly with pumice stone gravel, a type of volcanic rock, severely constraining the ability of the building to reach larger isolated displacements.



**Figure 6.20** Osmaniye Government Hospital as observed on March 16, 2023: (a) building exterior, (b) isolation system scratch plate, (c) moat with soil backfill, (d) Utilities crossing isolation plane.

At the Adana City Hospital, concrete sidewalks crossed over the moat gap as shown in Figure 6.21.



**Figure 6.21** Concrete sidewalk crossing the moat gap at Adana City Hospital as observed on March 16, 2023.

Poor detailing at the isolation plane may impede full building displacement and result in damage to the nonstructural systems. The infilled moat at Osmaniye Government Hospital was the most egregious example of a detail that limits the protection otherwise offered by seismic isolation, but other details may result in damage to utilities. The example in Figure 6.22 shows a steel water pipe with a fully-extended braided-hose connection across the isolation plane. This connection provides a limited amount of displacement capacity in both the axial and transverse directions in small events, but is likely to break the pipe when it tries to extend further in moderate or larger events. Figure 6.23 shows partitions below the isolation plane without a gap sufficient to accommodate the movement.



**Figure 6.22.** Utilities crossing isolation plane as observed at the Adana City Hospital on March 16, 2023.

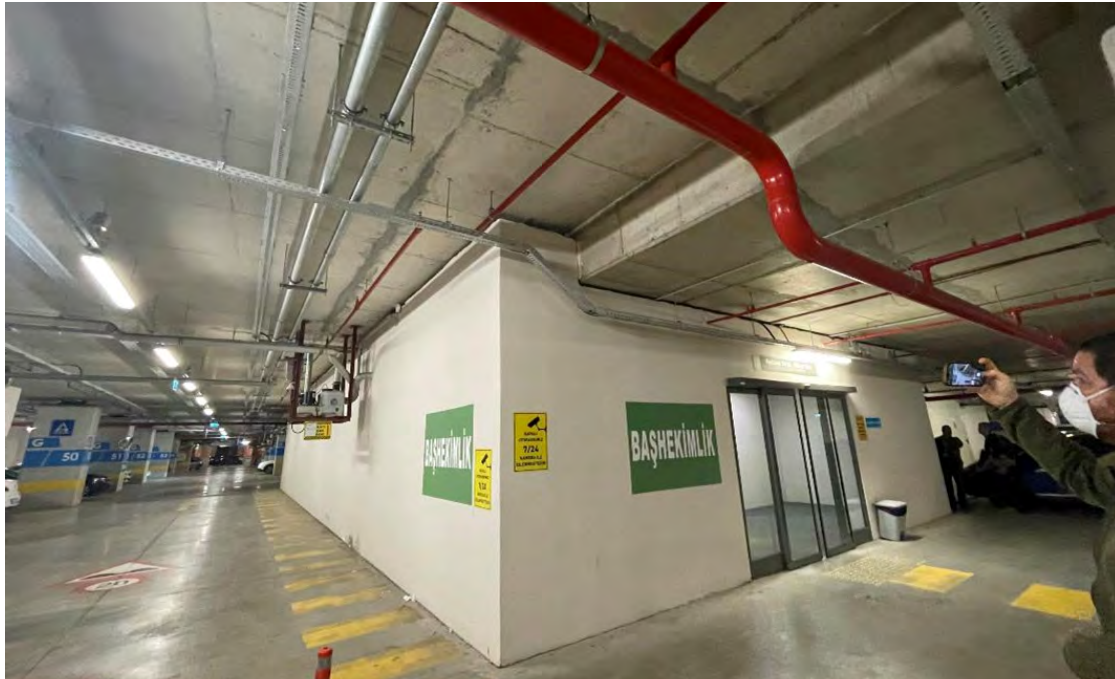


**Figure 6.23** During the Hospital’s team visit to Adana City Hospital on March 16, 2023, it was observed that there was insufficient clearance for partitions to accommodate isolator displacement. The plane of isolation is located at the top of basement columns, just beneath the ceiling, and partition walls will move with the slab-on-grade below the plane of isolation. To address this issue, the partitions need to be separated with the full isolator displacement where they abut the concrete beams that move with the superstructure above the plane of isolation. Additionally, the red sprinkler piping is supported from the concrete superstructure above the plane of isolation, but it penetrates through the partitions without any oversize holes to allow for isolator movement.

## **6.5 Post-earthquake Operation and Return to Function**

Post-earthquake operation and functional recovery of hospitals rely on a complicated network of structural, architectural, mechanical, medical outcomes layered with human decisions. In the minutes following an earthquake, hospital management needs to decide whether patients and staff can remain in the building or if evacuation is necessary, knowing that the act of moving patients puts lives at risk. Hospital post earthquake operations require increased capacity for trauma indications with the need for surgical interventions.

Confirming structural safety of the building is the first priority, which allows patients and staff to shelter-in-place even in the absence of power, gas or water. Minutes after the earthquake, structural engineers and building officials are not on site, therefore hospital management typically makes decisions based on what they can see with the emotion of having just



experienced the terrifying event. Often, they reported seeing widespread cracks in plaster and masonry partitions which appear like the structure is compromised. Out of caution and a lack of confidence in the structure, many buildings with partitions and other nonstructural damage were either fully evacuated or moved to the emergency department on the ground floor level. A timely assessment by an engineer or building official is critical to assessing the vulnerability of the building to likely aftershocks.

Hospital's emergency department cannot function as intended if services in other parts of the hospital are compromised. Emergency departments often ended up being evacuated, and downgraded to an outpatient urgent care type services, which are typically set up outside of the hospitals via tents. The timing of this urgent care setup has not been documented.

Continuity of electrical service to the building is the next step towards recovery. Emergency generators are the critical component to allow a building to remain functional. Hospitals with functional generators were able to maintain a percentage of their operations. Batteries of some medical devices (mechanical ventilators) were able to provide service for a short period of time. Hospitals without functional generators and intact electrical distribution systems could not provide service to patients.

Water service is the next critical utility and the continuity of this service is outside the control of the hospital since water is provided by the city. Water is the major component of washing and cleaning of reusable medical instruments. If onsite water supplies are not maintained, then restoring water service from the city is a critical element in the functional recovery of hospitals in the days following an earthquake.

Gas service is another critical utility for heating. The cold winter days, at the time of the earthquake, lack of heating further hindered the functionality of the hospitals. When electricity became available, electric space heaters were used in some rooms. Although the main gas lines were repaired quickly in Hatay and some parts of Kahramanmaraş, gas service was still not available due to many compromised gas lines. In some areas gas may not be the source of heating. In these cases alternative heat sources have the same importance.

The availability of local staff is a resource with potential scarcity after an earthquake. Staff and their families are potential victims of the earthquake along with the patients, especially in hardest hit areas. In Iskenderun, the team learned that multiple doctors, nurses, and support staff died, and others left the region in the days and weeks following the earthquakes, resulting in a shortage of available staff to serve patients. Surviving personnel voluntarily rushed towards their hospitals and worked to aid others, but providing human resources in the affected area

requires a comprehensive planning. Additionally, shortages of critical supplies such as material for casts and thread for sutures were reported, limiting the ability of otherwise functioning hospitals to provide emergency services. The timing of external support (deployment of Emergency Medical Teams to the area) should be confirmed from the authority of disaster management.

## **6.6 Key Observations**

The team's observations of Turkish hospitals following the February 2023 Kahranmanmaş earthquakes can be organized into four groups: (1) pre-earthquake planning and design, (2) immediate post-earthquake hospital functionality in the first 15 minutes after the event, (3) the first 24 hours after the event, and (4) up to six weeks after the event (when the team visited).

### **6.6.1 Pre-Disaster Planning and Design**

- Structural systems of hospital buildings constructed since 2000 using improved codes following the 1999 Kocaeli and Düzce Earthquakes generally performed well even in areas of very intense shaking.
- Nonstructural systems, particularly unreinforced masonry wall partitions and exterior infill walls, unanchored equipment, and unbraced ceilings were not designed for earthquakes and performed poorly. Damage to these systems was a primary contributor to immediate closure of the hospitals. Lengthy repair times impeded the return to full function.
- Seismically-isolated hospitals typically performed relatively well. Türkiye should be commended for its widespread adoption of seismic-isolation technology to protect large, new hospitals.
- Hospitals with on-site wells and/or water storage tanks were able to use them when city water was shut off or failed.
- Türkiye has a network of 5,000 trained medical professionals, organized into teams, with equipment and trucks, who quickly arrived at damaged hospitals. Tents at the hospital sites were set up in varying time frames. Teams were part of a network that the Ministry of Health had developed of volunteer medical professionals with equipment and vehicles called the National Medical Rescue Team (UMKE). They were typically what the World Health Organization characterizes as a Type 1 Fixed field hospital that has outside tents for initial and field triage, basic resuscitation and stabilization, basic nursing care, initial wound care, superficial burns, basic fracture management, medication, and out-patient transfer.
- AFAD has a vast network of seismic stations throughout the country. The instrumentation data are centralized and accessible through a government website.

### 6.6.2 Immediate Post-Earthquake Hospital Functionality (First 15 Minutes)

- The first 15 minutes are critical to make decisions on whether to evacuate the hospital. Decisions to evacuate are made quickly and cannot be reversed easily when set in motion.

### 6.6.3 Immediate Post-Earthquake Hospital Functionality (First 24 Hours)

- Resilience for hospitals was observed to be complicated and fragile.
  - General: Resilience was initially all about nonstructural damage, until shaking intensity was large enough to cause significant structural damage. The strength of structural systems served to protect the buildings. When demand exceeded the strength capacity, failures were severe (not ductile).
  - Fear: Cracks in partitions made patients and staff afraid to stay or return.
  - Redundancy: One lost incubator shut down an in-vitro fertilization (IVF) ward.
  - Resources: Running out of surgical suture thread shut down an entire surgery.
  - Staff: Local medical professionals and their families are victims too; significant staffing shortages occurred in some hospitals.
  - Lack of patient recording system due to equipment failure, a significant patient surge, and staff shortage lead to undocumented patient care and transfer in the first few days.
- Emergency generators were critical to continued operations.
- Hospitals with on-site wells used them when city water was lost or shut off.
- Elevator restart had to wait for technicians to arrive, even when the elevator was not actually damaged.
- Trained structural safety assessors were not available in the first few days for some hospitals, and there was concern about the length of time administrators needed to wait until an assessment could occur. Timely, appropriate (not too conservative) safety assessments matter greatly.
- The lack of timely evaluations and safety assessments caused some hospitals to evacuate, which may have been unnecessary in some cases. Transferring patients to other facilities due to structural damage, nonstructural damage, or “cautious” evacuations overwhelmed surrounding hospitals. Many patients did not survive the transfer.
- Ambulance and logistics systems are critical to managing patient transport to appropriate facilities.

#### **6.6.4 Post-Earthquake Restoration of Services (First Six Weeks)**

- Field medical response teams started to function relatively quickly in the earthquake affected area (within hours in several places and days in others). They used the parking lots of many damaged hospitals.
- Many international emergency medical teams were also in the field in the next 3-4 days.
- Transfers were made between the regional hospital network.

### **6.7 *Parallels to California Hospital Seismic Compliance***

Recommendations based on the observations of Section 6.6 are provided in Section 6.8. This section relates the field observations to ongoing hospital seismic compliance activities in California, as California is the geographic area of practice for many of the EERI hospital team members. Many of the deficiencies identified in Turkish hospital construction are being proactively addressed by legislation in California where hospital construction is under the jurisdiction of the state agency called the Department of Healthcare Access and Information (HCAI), formerly called the Office of Statewide Health Planning and Development (OSHPD). HCAI has been proactive in addressing seismic vulnerabilities of older hospital buildings across the state since the late 1990s.

Hospital design and construction in California have been under the jurisdiction of the state since 1973 with the passage of the Alfred E. Alquist Hospital Seismic Safety Act. This legislation established a statewide seismic safety building standards program (OSHPD) following the M6.6 Sylmar earthquake in 1971 that significantly damaged the newly constructed Olive View Hospital. In the 1994 Northridge Earthquake, hospitals constructed under the Seismic Safety Act fared well, but several constructed prior to the act suffered damage. In 1994, California passed Senate Bill 1953 to establish regulations for hospitals constructed prior to 1973, requiring them to be evaluated or retrofitted to modern code seismic standards by 2030.

This program required all of the nearly 3282 hospital buildings (across 414 general acute care facilities) to be seismically evaluated to meet structural and nonstructural targets. Buildings were assigned a Structural Performance Category (SPC) and Nonstructural Performance Category (NPC) of 1-5 (1 is the worst, 5 is the best rating). Priority was placed on identifying and retrofitting (or removing) the most vulnerable buildings first. The remaining building stock has expectations of providing at least Life-Safety performance (SPC 2 or better) until the year 2030, and functional performance beyond 2030 . The seismic performance of post-2000 buildings in Türkiye was consistent with the structural requirements of SPC 2 or better.

In addition to the primary structure, classification of SPC 2 requires mitigation of certain nonstructural items, such as falling hazards, including unreinforced masonry partitions and hollow clay tile, cladding systems, masonry veneer, parapets, and canopies that could block means of egress. The presence of these hazards would preclude most Turkish hospital buildings from achieving SPC 2 under California code. The evidence of the closure of the hospitals due to these failures reinforces the need for these requirements in the building code.

Early program milestones required that the emergency systems of all buildings meet current code standards, resulting in retrofits to communications equipment, emergency generators, bulk medical gas, fire alarms, and emergency lighting and signage. Achieving this milestone in California classifies the building as NPC 2. Observations of Turkish hospitals highlighted the importance of functional emergency generators and safe, well defined egress. Buildings with generators were able to remain partially functional, those without did not.

As of April 2023, a majority of the pre-1973 buildings in California are classified as SPC 2 and NPC 2; they are thus noncompliant by the 2030 standards. These buildings are life-safe and have emergency systems in place, but may not provide service after a large earthquake. Work to achieve seismic compliance of older hospital buildings will continue until 2030 as older buildings are retrofitted or replaced with buildings that meet new code seismic standards.

Similar to the Uniform Building Code (and California Building Code), Turkish building codes continue to evolve with new knowledge of seismic behavior. The evolution of both codes are often informed by major earthquakes. Turkish building code seismic provisions in Türkiye were enacted in 1940 and revised in 1944, 1949, 1953, 1961, 1968, 1975, 1998, 2007 and 2018. 2007 and 2018 edition (effective 1/1/2019) have many parallels with United States building seismic standards.

Both Türkiye and California governments identified that hospitals are essential for disaster recovery. California improved the building code and required that older buildings comply. Türkiye improved the building code and required that new hospitals are seismically-isolated to provide the highest level of protection against earthquake damage. Both are headed down the path of improved performance for hospitals and could learn from each other on how best to achieve the goals of operational performance after the big one.

## **6.8 Preliminary Recommendations**

The team's primary goal was to understand whether hospitals continued to provide service to the community in the days and weeks after the event. If service was interrupted, the team

sought to understand the reasons why and how those lessons can be applied to high seismic areas.

The following summary provides preliminary recommendations related to post-earthquake hospital recovery. Recommendations for improved resiliency are organized into the same groups used on Section 6.6 for observations: (1) pre-earthquake planning and design, (2) immediate post-earthquake hospital functionality in the first 15 minutes after the event, (3) the first 24 hours after the event, and (4) up to six weeks after the event (when the team visited). At this stage, the recommendations are preliminary and are intended to be general for high seismic regions. They are not organized by target audience (such as engineers or policy makers) or location (such as California, the U.S., or other countries). Recommendations for long-term recovery are also not directly included.

A final section provides recommendations for future information gathering needs.

#### **6.8.1 Pre-Earthquake Planning and Design**

- Develop a viable hospital disaster plan and have staff regularly practice executing it.
- Develop strategies for providing rapid post-earthquake safety evaluations consistent with the requirements of the authority having jurisdiction. This might include agreements with private consultants, building occupancy resumption programs, and strong motion instrumentation and other technologies. Include strategies for different time frames (such as the first 15 minutes, first days, and first weeks after the event).
- Provide for substantial emergency generator capacity and redundancy where possible. Test generators regularly. Redundancy means having more generators (not just one large generator). Encourage the application of new technologies for power supply and redundancy, including microgrids, battery backups, fuel cells, and/or photovoltaic cells.
- Make provisions for supplemental water. Hospitals in Türkiye with on-site wells and/or water storage tanks were able to use them when city water was shut off or failed.
  - Construct wells on hospital property where possible and integrate them into the plumbing network.
  - Provide supplemental storage tanks.
  - Install quick connect systems for easy connection to water trucks.
- Provide for redundancy in critical medical equipment. Position them in the building so that they are easy to evacuate if needed (intensive care units would be placed on the ground floor, so there would be no need for elevators for immobile patients). Blood banking and embryo banking units are other examples.
- Provide enhanced capacity of key supplies.
- Limit use of brittle finishes such as adhered stone veneer.

- Limit extensive nonstructural damage by providing engineered and plan-reviewed anchorage and bracing of nonstructural components detailed to accommodate the expected level of movement.
- Prepare for elevator shut down by establishing contracts in advance, and explore developing procedures for in-house restart.
- Train reserve medical teams and supervisors and supply them with equipment and trucks to set up field hospitals near damaged hospitals.
- Encourage low damage design strategies for hospitals, such as seismic isolation.
- Instrument buildings with strong motion sensors and other measurement devices to aid in post-earthquake safety evaluation decision making.
- Encourage policies and training that foster ingenuity, nimbleness, and creativity of administrators and staff in responding to the earthquake. Develop support networks and contacts that can be engaged for assistance following the event.
- Identify items that are specific to the hospital recovery needs, and focus planning efforts on protecting them and providing backup systems for them.
- Investigate development of methods for reducing partition damage.

#### **6.8.2 Immediate Post-Earthquake Hospital Functionality (First 15 Minutes)**

- The first 15 minutes are essential to decisions on whether to evacuate a hospital. Decisions to evacuate are made quickly and cannot be reversed easily when set in motion. Shutting down the building and stopping service totally could prevent vital medical assistance to some victims near the area.
- Implement the hospital disaster plan.
- Have on-call experienced structural engineers, preferably those familiar with the facility, available by phone/video link for consultation on post-earthquake safety assessments immediately after the event.
- Have staff trained in the hospital disaster plan in every shift (night and weekend). As a backup, when trained staff are not available, develop a short checklist of key items that can be used by other hospital staff, such as medical team members, to help them make important decisions.
- Develop guidance on whether and how to “drop cover hold-on” in hospitals.
- Develop guidance on hospital staff priorities for exiting quickly vs. helping patients who are not mobile. Irregular evacuations can cause fatal risks to patients. This is acknowledged to pose difficult choices and challenges.
- If evacuation is chosen, select an area (near or away from the hospital building according to the damage status) to set up temporary field hospitals and begin preparing to move appropriate functions.

- Develop effective communication with the crisis center and other potential help providers (GSM, phone, internet) give feedback, get help and data, and make decisions together.

### **6.8.3 Immediate Post-Earthquake Hospital Functionality (First 24 Hours)**

- Trained structural evaluators were not available for some hospitals, and there was concern about the length of time administrators needed to wait until an assessment could occur. Timely, appropriate (not too conservative) safety assessments matter greatly. Utilize trained structural engineering professionals for post-earthquake safety evaluation, preferably with knowledge of the hospital from before the event.
- Keep the staff informed about the evaluation process and status.
- Structural evaluators should not conservatively “over tag.” Shutting down a hospital cannot be easily undone.
- Consolidate supplies and resources in safe areas. Focus on needs of medical priorities and ones that can be managed.
- Create a time and space for tired staff to relax and check on their families and homes.
- Be ready to revise the hospital’s function according to the new needs.
- Collaborate with field medical response teams.

### **6.8.4 Post-Earthquake Restoration of Services (First Six Weeks)**

- Repair nonstructural wall cracks quickly, to assuage staff and patient concerns. Cracks in partitions make patients and staff afraid to stay or return. Provide clear official declarations about the safety of the building and the hospital functions.
- If the hospital no longer functions, move equipment that can still function to new safer locations for reuse elsewhere. Some medical devices may need calibration so do not use any device before approval.
- Functioning elevators are critical for the relocation of equipment.
- Link post-earthquake safety evaluations to GIS based public facing websites, so assessment and occupancy limitations are accessible.
- All healthcare workers (including managers and supervisors) are victims, and they have the potential to suffer from post-traumatic stress disorders (PTSD). Provide protective and treating psychosocial service. Reschedule working hours and share responsibilities.
- Get help from professionals outside the earthquake area to run medical functions (medical managers, doctors, nurses).
- Post evaluation placards on buildings, easily visible by the public, such as recommended in the ATC-20 process.



### 6.8.5 Future Information Gathering Needs

The EERI team was able to collect substantial information during the visit and after return. However, there is much more to learn. The following recommendations highlight important areas where further information gathering is recommended.

- Expand the data collection effort to additional hospitals beyond those reported here.
- Obtain detailed performance information about recently constructed hospitals that were evacuated, and the team was unable to gain access to.
- Obtain clear information on post-earthquake safety evaluation procedures used for hospitals.
- Obtain more information about damage to MEP distribution systems, including water leaks.
- Publish information on strong motion recordings in seismically isolated hospitals together with reliable estimates of movement across the plane of isolation as well as in the superstructure.
- Publish structural framing plans for hospitals to permit detailed analysis and study of the effects of ground shaking on buildings from different eras of the building code.

## 7.0 Performance of Lifelines

*Riccardo Cappa, Ezra Jampole, Brad Wham, Jeffrey Hunt, Robert Kraus, Brent Chancellor, Menzer Pehlivan, Onder Akinci, Burcu Guldur, Merve Bayraktar, Ahmet Citipitioglu, Selcuk Toprak, Engin Nacaroglu, Muhammet Ceyaln, Altug Bayram*

### 7.1 Introduction

Lifelines are essential facilities and structures that provide basic needs to communities. Their continued operability after natural disasters such as earthquakes are key to the efficacy of emergency response, to the continued occupancy of buildings, to the distribution of energy, and to the timely repair and rebuilding of cities and communities. Lifelines include a wide range of buildings, systems, and equipment, including:

- Transportation (bridges, viaducts, tunnels, roads, rail, etc.)
- Energy (coal and gas plants, hydroelectric dams, electrical substations and transmission and distribution networks, Liquefied Petroleum Gas infrastructure, etc.)
- Ports
- Airports
- University campuses and schools
- Water and wastewater plants, pipe network, and pumping stations
- Industrial facilities (e.g., silos, steel mills, asphalt plants)
- Hospitals

Approximately five weeks after the February 6 earthquakes occurred in Türkiye, a multidisciplinary team (“Lifelines Team”), consisting of engineers from companies and universities, in partnership with EERI, traveled to Türkiye to study the impacts of the earthquakes on lifeline facilities and structures. The Lifelines Team conducted field reconnaissance between March 17-23, 2023. The Lifelines Team was split between two to three vans each day, to cover most of the larger area impacted by the February 6 earthquakes. The vans drove a combined distance of more than 3,000 miles, which is roughly the drive between San Francisco and Boston. Figure 7.1 shows the 160+ sites visited by the Lifelines Team during the field reconnaissance. This chapter summarizes the Lifeline Team reconnaissance activities and provides an overall summary of observations for selected lifelines (Transportation, Energy, and Water and Wastewater Systems, and University Facilities). A full report documenting the Lifelines Team’s observations made during their reconnaissance trip together with preliminary conclusions and recommendations for further studies will be published later this year.

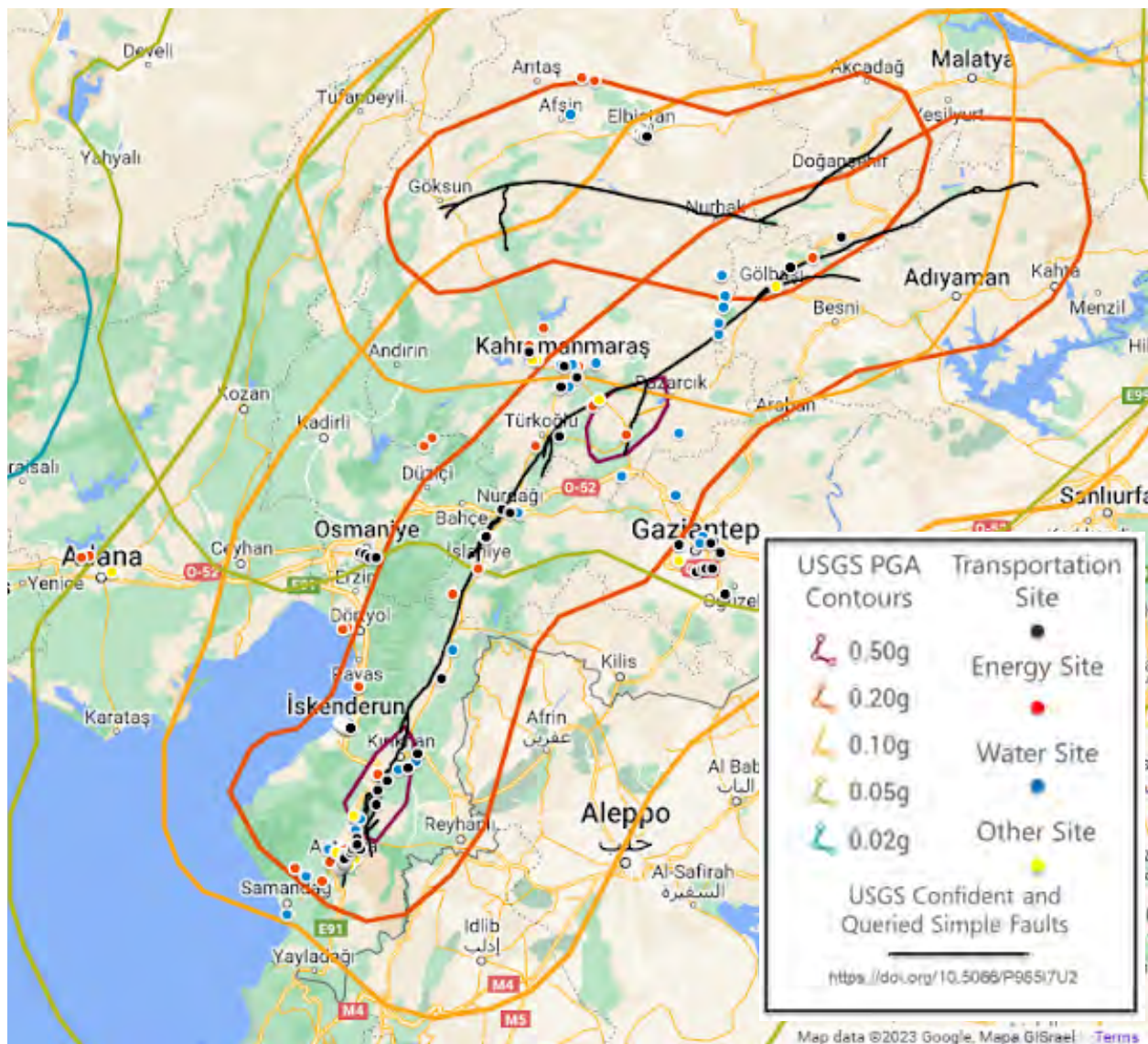


**Figure 7.1.** Location of sites visited by the EERI Lifelines Team

## 7.2 Data Collection Methods

The Lifelines Team undertook a rigorous mapping of the performance of lifelines across the affected regions in Türkiye, resulting in invaluable documentation of their performance to improve our current understanding of the seismic vulnerabilities in these facilities and structures.

The Lifelines Team’s technical objectives for this reconnaissance effort included:

- Conduct a high-level lifelines damage assessment and performance review
- Perform data collection on facilities and structures across different areas of the affected regions, in order to evaluate and correlate the observed damages with earthquake shaking intensity and possible site-specific issues
- Document damage and response for a diverse group of lifelines
- Assess both damaged and undamaged lifeline facilities and structures
- Identify opportunities to improve existing seismic standards and engineering practices
- Identify opportunities for future research studies

The Lifelines Team’s data collection methods included:

- Phone calls with local university professors and the Disaster and Emergency Management Presidency of Türkiye (AFAD) representatives to facilitate site access;
- Interviews with local facility operators and managers, and with municipality officials to understand the post-earthquake performance of their assets and the impact on society;
- Documentation of the condition of the equipment, facilities, and structures with photographs, videos, and measurements;
- Review of existing damage reports compiled by the utility operators, plant managers, and other authorities after the earthquake;
- GPS data tracking of the team tours across the visited region; and
- Dashcam video recordings of selected areas as the team traversed the visited motion region.

The data collected by the Lifelines Team will be archived online for public use on free databases such as DesignSafe and SiteEye.

Appendix A lists the preliminary ground motions estimated at the sites visited by the Lifelines Team for three earthquakes. The ground motion estimates include PGA, PGV, and Sa(1 sec). These ground motions were developed following the procedure discussed in Section 3 of this report. The ground motions in Appendix A represent Rot50 values. They were computed by interpolating the available recordings in the area and estimating the local Vs30 profile based on ground slope. These ground motions are considered approximate and are currently being refined using geology-based Vs30 profiles. Despite being approximate, they provide useful insights on the expected ground motions experienced at the visited sites. In the following sections, the site ID listed in Appendix A is provided to link the sites with their corresponding coordinates (latitude and longitude) and estimated local ground motions.

## **7.3 Transportation Systems**

### **7.3.1 Bridges/Viaducts**

The EERI Lifelines Team observed 66 bridge/viaduct sites that contained 98 bridges/viaducts subjected to PGAs up to 1.37g (Appendix A). Hereafter, we generally refer to viaducts as bridges. Thirty-five sites had one individual bridge, 30 sites had two bridges (e.g., one bridge for each direction of traffic), and one site had three bridges. The locations of the bridge sites were selected to study the effect of varying ground motion intensities on the response of the bridges and to investigate different damage states for a variety of types of bridge construction and configurations. The locations of the bridge sites visited are shown in Figure 7.2 overlaid on the USGS PGA contour maps for the **M7.8**<sup>10</sup> and **M7.7**<sup>11</sup> earthquakes. In Figure 7.2, the USGS confident and queried simple faults (Reitman et al. 2023) are shown with a black line.

---

<sup>10</sup> USGS,2023 - <https://earthquake.usgs.gov/earthquakes/eventpage/us6000jllz/executive>

<sup>11</sup> USGS, 2023 - <https://earthquake.usgs.gov/earthquakes/eventpage/us6000jlqa/executive>

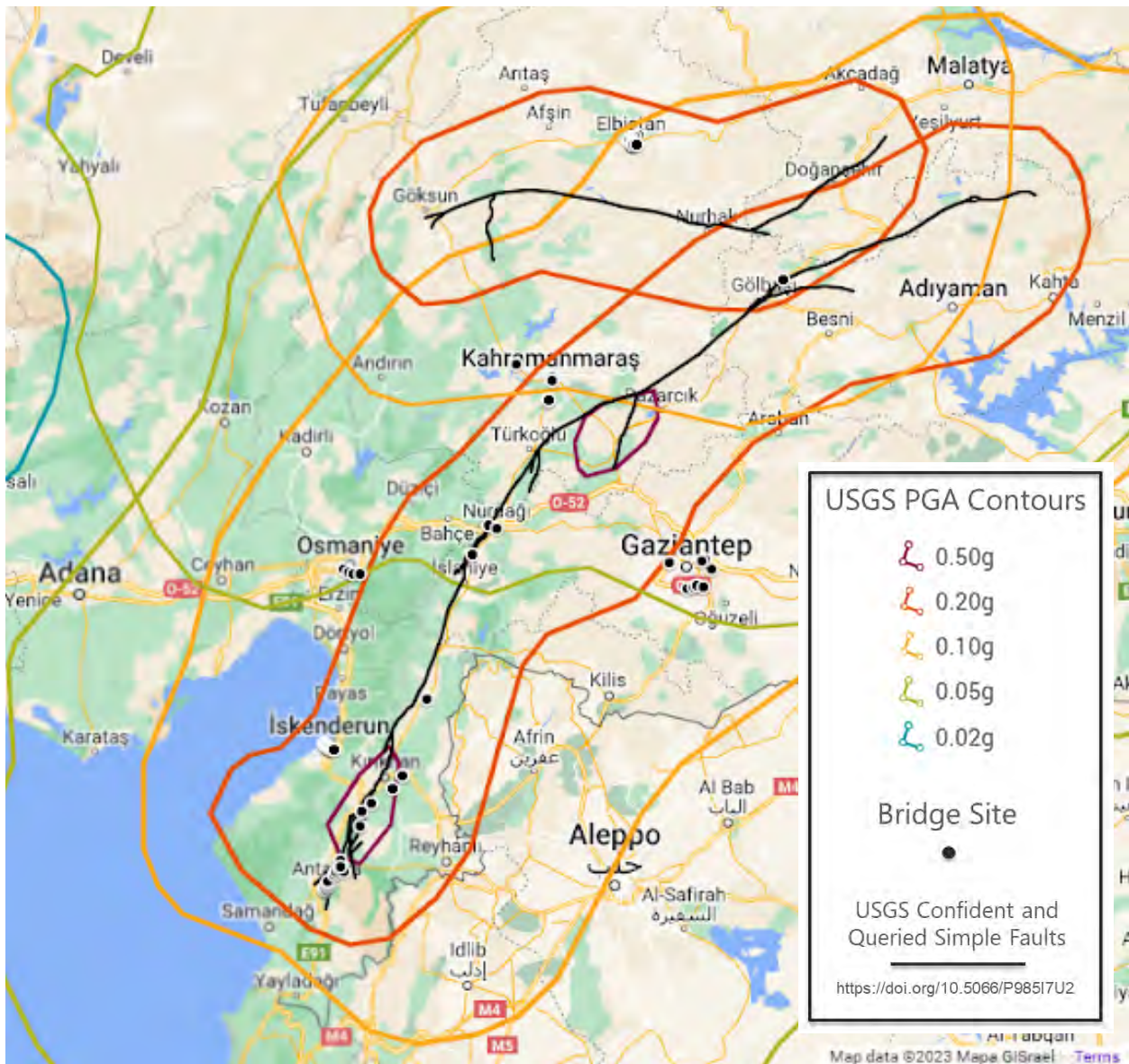


Figure 7.2. Location of visited bridge sites.

Common bridge conditions and damage types observed by the Lifelines Team include the following:

- Damage to bridge components due to incomplete or inadequate load paths from the bridge deck to the bent caps and abutments. There were several conditions that caused and/or contributed to this distress:
  - Absence of diaphragms or elements between girders to provide lateral stability at bent caps and/or supports

- o Undersized or an insufficient number of shear keys between girders at the supports to transfer lateral loads in the transverse direction
- Longitudinal movement between the girders and the bent caps/abutments, resulting in “walking out” of thick elastomeric bearing pads
- Damage to bridges caused by foundation and geotechnical issues
  - o Abutment settlements
  - o Embankment failures/lateral spreading at abutments
  - o Failure of retaining walls in the wings of abutments
  - o Leaning and residual drift of bridge piers and abutments in both the longitudinal and transverse directions

The EERI Lifelines Team observed two collapsed bridges, 8 bridges with severe damage, 13 bridges with moderate damage, and 75 bridges with light damage or no damage. The severely damaged bridges were either non-operational, had significantly reduced load-carrying capacity due to damage to individual elements, or had significant residual displacement of bridge piers and abutments. Moderately damaged bridges were primarily characterized by longitudinal cracking of the web at the ends of precast concrete bridge girders, damage to shear keys between girders at the supports, and abutment sidewall failures. Examples of typical damage conditions are shown in Figure 7.3-7.7.



**Figure 7.3.** Severely damaged concrete bridge girders resulting in reduced load carrying capacity, (ID No. 33 in Appendix A).

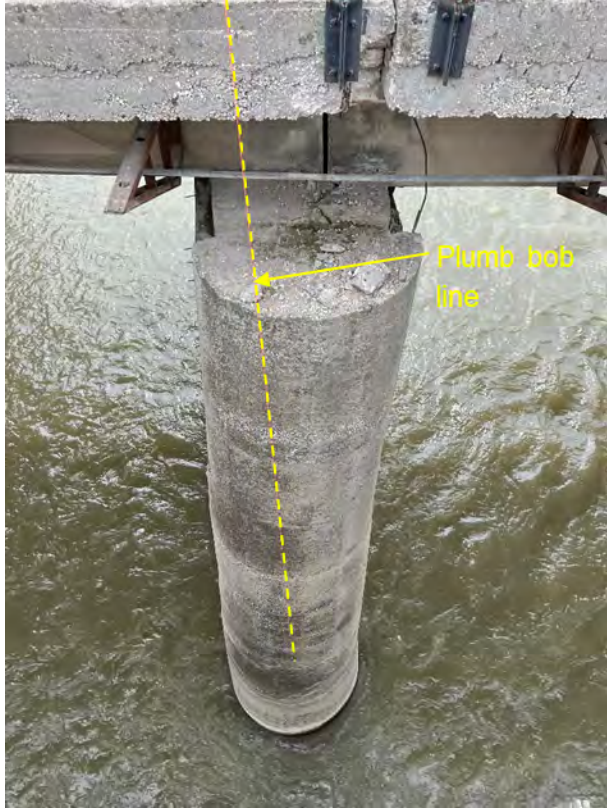


**Figure 7.4.** Significant residual displacement of pier (left) and abutment settlement (right), (ID No. 16 in Appendix A).



**Figure 7.5.** Dislodged (left) and ejected (right, ID No. 33 in Appendix A) elastomeric bearing pads.





**Figure 7.6.** Longitudinal cracking at end of precast concrete girders.



**Figure 7.7.** Damage to lateral support wings at bents (left) and to shear keys (right).

### 7.3.2 Tunnels

Prior to visiting Türkiye, the Lifelines Team heard reports that, generally, tunnels performed well in the earthquake sequence. There were reports of one tunnel, the Erkenek tunnel, being closed due to damage. Therefore, members of the EERI Lifelines Team visited this tunnel to observe and document the damage.

The Erkenek tunnel is located at a latitude of 37.9236 and longitude of 37.8773 on the D850 highway in the Maltaya province. This tunnel is on a major highway connecting the Eastern Anatolian region with the Mediterranean region. The tunnel was constructed between 2011 and 2017. This tunnel consists of two newer bores and an older offset bore. This older bore is no longer in service or was used as a service roadway prior to the earthquake sequence. The D850 highway has two lanes of traffic in each direction at the tunnel location. Each of the newer tunnel bores contains two lanes of traffic.

When the Lifelines Team visited the Erkenek tunnel (ID No. 84 in Appendix A) on March 20, 2023, both bores of the tunnel had been reopened to traffic. As the Lifelines Team passed through the south bore, they observed damage to the tunnel, which included failure and collapse of portions of the inner tunnel liner and longitudinal cracking of the outer tunnel casing. Photographs of damage to the south bore of the tunnel are shown in Figure 7.8. The Lifelines Team observed similar types of damage to the north bore of the tunnel.

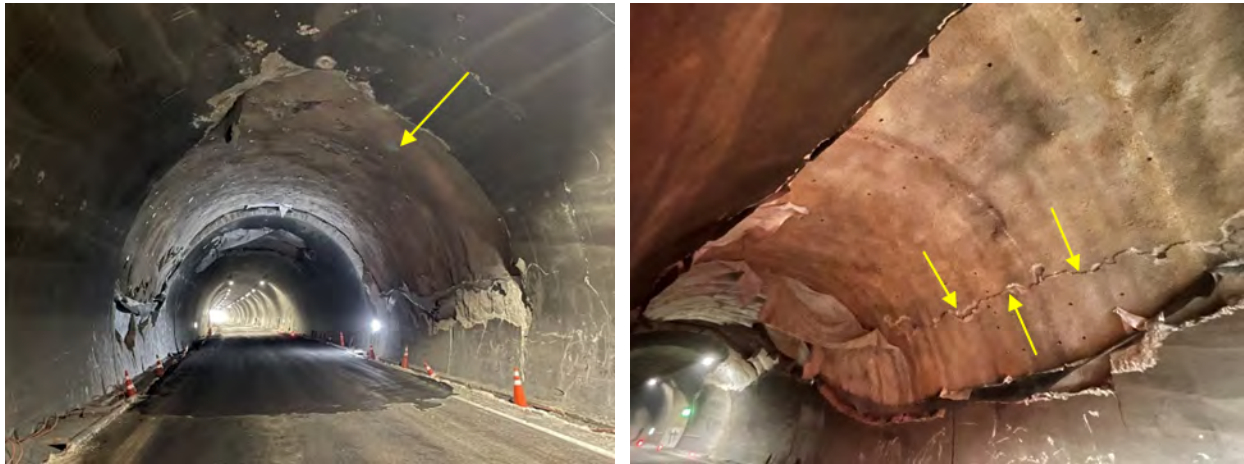


**Figure 7.8.** Collapse tunnel liner (left) and longitudinal crack in the outer tunnel casing (right) observed in the south bore (ID No. 84 in Appendix A).

### 7.3.3 Roadways

While traversing between other lifeline sites, we observed some damage to roadways. This damage was primarily due to geotechnical issues such as embankment failure and lateral spreading of roadways next to rivers and locations where the road crossed the fault rupture (i.e., when crossing the surface fault rupture). Examples of roadway damage are shown in Figures 7.9 and Figure 7.10. Some roadways in mountainous areas were temporarily blocked by rockfalls and landslides.

In areas with heavy damage to buildings (e.g., Antakya), roadways had been blocked by building collapses and debris, requiring them to be cleared, or for makeshift new vehicle paths to develop adjacent to the old road (Figure 7.10).



**Figure 7.9.** Embankment and roadway failure near a dam located (left, ID No. 83 in Appendix A) and near a bridge (right, ID No. 45 in Appendix A).



**Figure 7.10.** Embankment and roadway failure in Antakya (left, ID No. 19 in Appendix A), makeshift road around collapse debris in Antakya (right, near ID 20 in Appendix A).

### 7.3.4 Airports

Lifelines Team members visited the Gaziantep and Kahramanmaraş airports. We did not visit the Hatay airport but relied on reports from contacts in Türkiye who relayed reports of the damage suffered at this airport. During our visits, we met with authorities at the airports to gather information about the performance of these airports during and after the earthquake sequence.

The Gaziantep airport (ID No. 95 in Appendix A) did not sustain significant damage and remained operational after the earthquake sequence. The terminal that is used for most flights in and out of Gaziantep was designed according to the 2018 Turkish earthquake code and was constructed beginning around 2021. Handover of the terminal from the construction company to the owner/operator was still ongoing at the time of the earthquake sequence. According to

personnel we interviewed and our own visual observations, damage to the airport was primarily limited to minor nonstructural damage to ceiling finishes and drywall and movement at expansion joints. A few ceiling fixtures were also displaced or popped loose. There was no damage reported to the baggage handling system; the system reportedly remained fully operational after the earthquake sequence. No structural damage was reported in the new terminal. We did not visit any of the older terminals or the control tower at the airport.

The Kahramanmaraş airport terminal (ID No. 105 in Appendix A) was constructed in 2019. We reviewed some of the exterior façade and entrance structure but were not able to tour and observe much of the airport terminal. The structure for the main terminal space and atrium over the departures ticketing area appeared to be a structural steel L-portal space truss. We observed some cracks in drywall finishes and cracked glass in the entrance doors. We also observed evidence of slip in some steel structure bolted connections. We met with airport personnel to ask them about the performance of the airport during the earthquake sequence. Based on their reports the airport was non-operational for two days after the earthquake sequence and re-opened the third day. There was non-structural damage throughout the airport. Suspended ceilings and non-mounted television monitors fell and there were major leaks from the sprinkler piping. The basement and baggage area were flooded by these water leaks. It reportedly took six to seven days to refurbish and repair the ceiling system. External power to the airport was cut off for about 20 days and during this time the airport operated on backup generators. According to airport personnel, the airport was used as an emergency evacuation shelter in the days immediately after the earthquake sequence with approximately 1,000 people sheltering in the airport.

The Lifelines Team did not visit the Hatay airport (ID Nos. 43 in Appendix A), but rather relied upon reports from contacts in Türkiye who took part in the emergency repairs. Based on these reports there was significant damage to the runway at the airport. The runway pavement buckled, and several sections of the runway were no longer level. The buckled runway section was removed and patched along with several other sections of the runway shortly after the earthquake to allow supply planes to use the airport. There was no major damage to the terminal structural system and facade. The terminal structure was constructed using tubular columns supporting a steel tubular truss roof structure. There was settlement adjacent to the terminal which caused damage and disruption to mechanical, electrical, and plumbing infrastructure. A glass covered steel canopy at the entrance of the terminal collapsed, closing the main access to the terminal building. This collapse was apparently due to lack of a proper lateral structural system. Figures 7.11 through 7.13 show examples of the observed damage.



Figure 7.11. Condition of Hatay airport runway after earthquake sequence (left) and after repairs (right)



Figure 7.12. Repair work to the Hatay airport runway



Figure 7.13. Collapsed canopy at entrance to Hatay Airport

**7.4 Energy Systems**

**7.4.1 Coal and Gas Power Plants**

Figure 7.14 shows eight power plants (coal and gas fueled) located in the region of the M7.8 and M7.7 earthquakes. We visited three of the largest coal plants located in the Iskenderun and Elbistan areas within the 0.2 PGA contours (highlighted in yellow in Figure 7.14), which were the

most heavily affected sites. The plant in İskenderun (Figure 7.15) commenced operation in 2019. The Afsin-Elbistan Plants A and B (Figures 7.16 and 7.17) are both 1300 MW and were commenced in the late 1980's and early 2000's, respectively. Appendix A lists the ground motions estimated at these sites (ID Nos. 73, 146, and 160).

One of the two units in the İskenderun plant was up and running at the time of our visits. The operator indicated this unit (Unit 2) was offline at the time of the earthquake and sustained less damage than the other unit that was online (Unit 1). Unit 2 was restarted about 30 days after the mainshock. About 5% of the full load (~20-30 MW) are needed for blackstart (i.e., to autonomously restart generation after a grid blackout). Grid power was available after a week. Unit 1 was offline when we visited the site in mid-March due to a previously scheduled outage.

Damage at the İskenderun plant was minor and included the following:

- Broken bushings atop a large step-up transformer (Figure 7.18a). Another large, unanchored yard transformer moved 10 cm but was otherwise undamaged (Figure 7.18b);
- Glass fiber Reinforced Plastic (GRP) seawater circulation pipes with joint displacements exceeding their design tolerances and resulting minor water leaks;
- In the 80 m tall boiler structure, there were signs of the main steam line swinging and hitting adjacent steel frame members. Some hangers and shock absorbers were bent;
- The Unit 1 large vertical gas channel booster intake (gas chamber) moved 60 cm horizontally and hit the steel structure, causing minor cracks in the columns;
- Some minor distresses were noticed at connection between conveyor belts and supporting coal crushing structure;
- About 2-4 cm of settlement was observed all around the turbine building foundation. This and other important structures are on 800 mm diameter deep soil mixing columns extending 30-45 m vertically;
- Some valve actuators in both turbines were inoperable and were replaced;
- One PC control cabinet with circuit breakers caught fire following the **M7.7** earthquake and was replaced;
- One elevator in the power house went out of rail and was inoperable following the second shock, but was quickly fixed and is now operating without issues;
- Fallen ceiling tiles atop control board and operators in the control room;

All the eight units at the other two plants in Elbistan (Plants A and B) were still offline at the time of our visit. These two plants have an identical configuration (~4x330 MW) but are of different vintage (built 20 years apart). At the time of our visit, the newer of the two plants

(Plant B) was experiencing issues with water leaks in the boiler system, which was left unmanned after the mainshock and was exposed to water freezing temperatures. The other plant appears to have received less damage but was facing a shortage of skilled workers, which was slowing down the completion of all the necessary visual inspection and system testing efforts. Both plants were expecting their recovery operations to take a few months to complete. Additional insights may be collected at these sites in the future once the units are restarted and testing has been completed. Our tour was limited to selected structures and locations. Damage identified so far by the operators at both plants includes:

- Minor vertical crack on a few base columns of the concrete cooling tower;
- Half dozen tall insulators broke their ceramic part or their connection to the supporting steel frame (e.g., Figure 7.19);
- One step-up transformer suffered a couple of bushing breaks. Another large step-up transformer suffered an oil leak from 6 inch pipe connection due to a failed gasket (Figure 7.20). No fire was reported. The gasket was replaced and the connection tightened up to put the transformer back into service;
- In the boiler building there was evidence of pipe banging against adjacent steel frames and supports, and some hangers were bent or broke their connections;
- The Plant B operator reported most of the damage was observed at elevations above 40 m from the ground. We could not access those floors;
- One of the powerhouse elevators was crushed by its balancing concrete block. The operator is investigating the root cause of failure;
- A 6 inch vertical settlement was noticed at the ground floor of the powerhouse over a 10x200 ft area (Figure 7.21). None of the electrical and mechanical components installed on or near this area appear to be damaged;





Figure 7.14. Map of coal and gas plants visited (indicated with yellow markers) and not visited (indicated in purple markers) overlaid on peak ground acceleration contours from USGS (footnotes 5 and 6).



Figure 7.15. Iskenderun plant Unit 2 boiler structure.



Figure 7.16. Afşin-Elbistan coal plant A.



**Figure 7.17.** Afşin-Elbistan coal plant B.



**Figure 7.18.** İskenderun plant a) example of transformer that sustained broken bushing and b) unanchored transformer that moved 10 cm laterally



**Figure 7.19.** Afşin-Elbistan coal plant B switchyard equipment.



Figure 7.20. Afşin-Elbistan coal plant B transformer with oil leak at flange.



Figure 7.21. Afşin-Elbistan coal plant B – settlement observed in the powerhouse.

**7.4.2 Hydroelectric Dams**

There are several hydroelectric dams in the affected region (pins in Figure 7.22) spanning power generating capacities from 54 MW to 2400 MW. The Lifelines Team visited five dams

(highlighted in yellow in Figure 7.22) that do not have blackstart capability and were subjected to PGAs of up to 0.46g (ID Nos. 40, 44, 83, 134, and 137 in Appendix A). The overall performance of these hydroelectric dams was very good. All the units were up and running once they received power back from the grid, which took 3 to 6 days depending on the location. At these sites there were no significant cracks or deformations indicating gross dam instability. Observed damage was limited to minor lateral spreading at the crest of the dam and rockfall onto property and roadways from adjacent slopes. For example, at the Kılavuzlu dam, the clay-core dam was intact but some minor lateral spreading was observed at the crest of the dam along the roadway at the top of the dam (Figure 7.23).

At the nearby Menzelet dam, the clay-core of the dam was also undamaged. The roadways to the dam were blocked after the earthquake by rockfall from adjacent slopes, requiring equipment to clear the roads. Some adjacent retaining wall structures had been damaged by rockfall (Figure 7.24).

One 5 MW river dam (Alabalık) suffered some river bank slope stability issues and dam structure cracks (e.g., Figure 7.25).

Some minor vertical tilting (~1 cm over 200 m) was observed at the concrete arch 510 MW Berke Dam, which commenced operations in 1999.

No damage was recorded at the 2x1.65 MW Karaçay Dam, which stores 35 million m<sup>3</sup> of drinking water for the Hatay region and was completed in 2019, but the operator reported that the access road had been cluttered by rockfalls and slope failures.

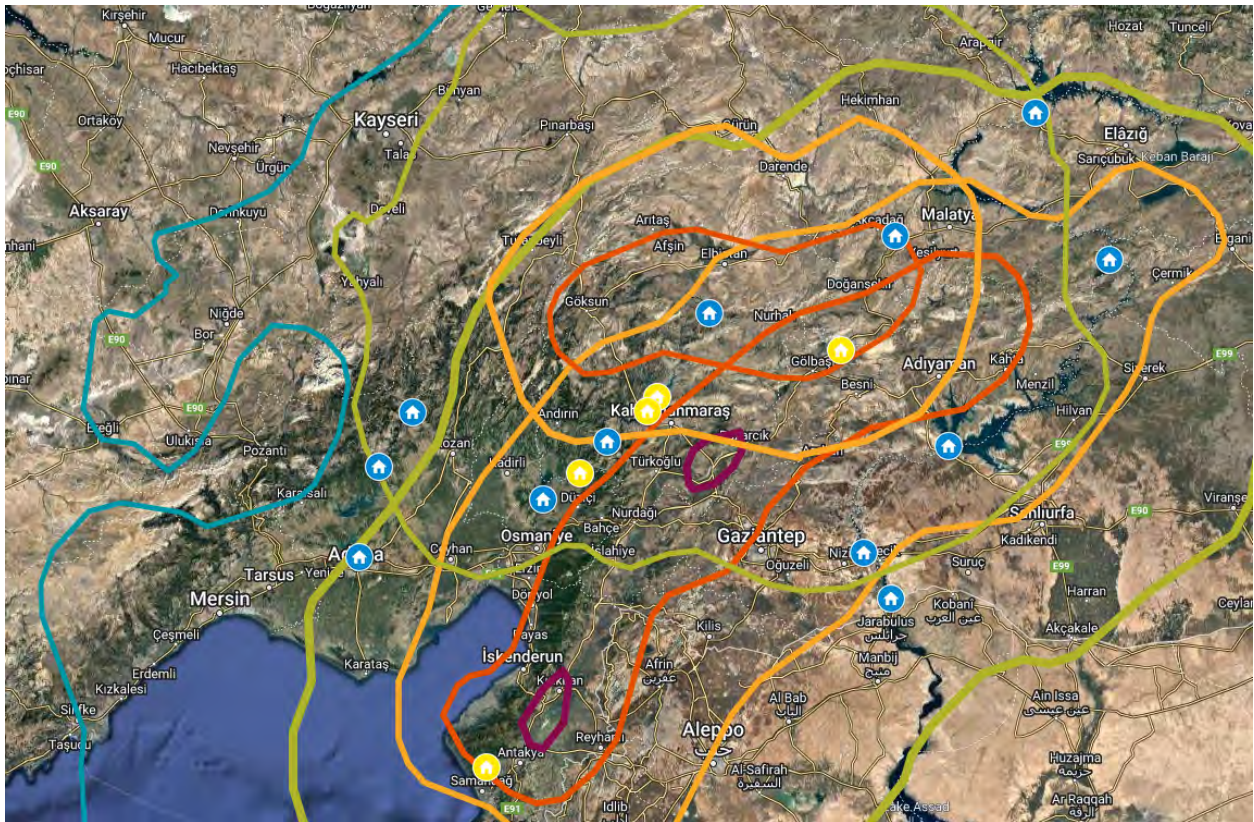


**Figure 7.22.** Map of hydroelectric dams visited (indicated with yellow markers) and not visited (indicated in blue markers) overlaid the USGS PGA contour maps for M7.8 and M7.7 earthquakes.



**Figure 7.23.** Lateral spreading of dam crest at Kilavuzlu dam.



Figure 7.24. Example of rockfall at Menzelet dam.



Figure 7.25. River bank failures at Alabalik dam.

**7.4.3 Electrical Substations**

The Lifelines Team visited more than twenty distribution and transmission substations operated by Toroslar and TEIAS/TOROS and Enerjisa, which were subjected to PGAs ranging 0.06-1.37g (ID Nos. 2, 5, 9, 41, 46, 55, 101, 110-116, 138-142, and 165 in Appendix A). For a subset of those sites, mainly located in the Hatay and Gaziantep region and Adana downtown, the Lifelines Team was provided onsite tours of the condition of substation buildings and equipment. Substation buildings typically were double height concrete frames, with masonry infill and concrete beams at the mid-height of the columns. Transmission and distribution lines to the substations were a combination of overhead and underground, with older areas typically having overhead lines. Damage to the substation buildings typically included masonry infills falling onto



equipment, cracks in beam-column panel zones, and nearby structures falling on the substation buildings. Several substation buildings collapsed. Figure 7.26 shows the range of damage to substations buildings in Antakya. Figure 7.27 shows sample impact damage to one substation in Adana resulting from collapse of an adjacent multi-story residential building.

Substation equipment performed generally well, unless it was struck by debris or poorly anchored. For example, the mechanical and electrical equipment within the Adana substation in Figure 7.27 survived the high frequency impact loads without issues. The Lifelines Team visited another substation in Kapicam (south of Kahramanmaraş) located less than 1,000 ft from the surface fault rupture (Figure 7.28). Ground records suggest the site PGA exceeded 0.6g. The fault at this location moved 10 ft laterally. The substation operator reported one transmission tower just outside the fence moved 9 ft with respect to the substation, but was able to accommodate the differential displacement. The only notable seismic effect was an unanchored transformer that toppled and spilled oil but did not catch fire.



**Figure 7.26.** Example of range of damage to substation buildings in Antakya.

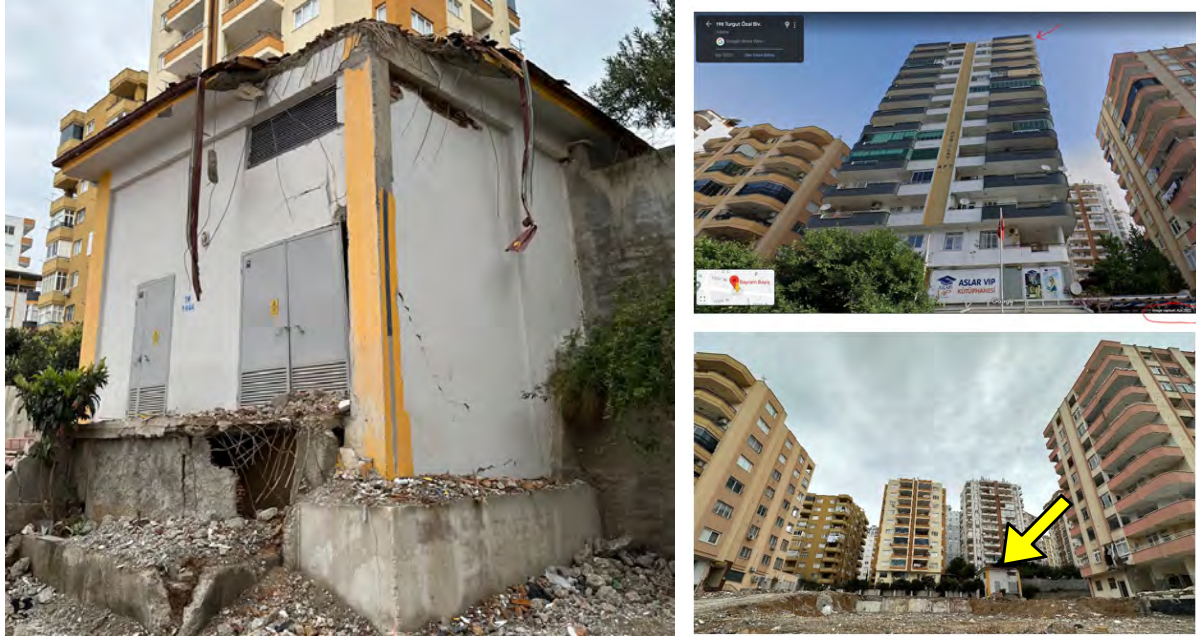


**Figure 7.27.** Example of substation in Adana struck by the collapse of an adjacent multi-story building (ID No. 2 in Appendix A).



**Figure 7.28.** Kapiçam substation nearby surface fault rupture (ID No. 165 in Appendix A).

#### 7.4.4 Transmission and Distribution Overhead Systems

With the exception of one collapsed high voltage transmission tower and some damage to smaller trussed transmission poles, the EERI Lifelines Team did not observe significant damage to electrical transmission systems. The collapsed high voltage tower failed because a landslide moved two legs of the four-leg tower approximately 12 feet out of position, while the remaining two legs were not displaced by the landslide. Figure 7.29 shows the collapsed transmission tower and the surrounding conditions. It is noteworthy that adjacent lattice towers, which were not affected by the landslide but would have been subjected to similar inertial forces, appear to have been undamaged. The Lifelines Team observed one tower mere feet from a 10 ft fault offset that was undamaged.



**Figure 7.29.** Collapsed transmission tower (ID No. 39 in Appendix A).

Distribution structures were only occasionally damaged directly by inertial forces, however, in Antakya, they were often damaged by collateral effects such as debris from buildings falling directly on them or on their attaching conductors (Figure 7.30). In several instances, hollow, precast-concrete distribution poles failed approximately five to eight feet above ground level from what appeared to be inertial forces (Figure c). In the few failed poles documented closely, these poles were only lightly reinforced with small-diameter wire reinforcing that had lost a majority of its cross sectional area due to corrosion. There were typically only limited visual indications of this deterioration that would have been visible at the exterior surfaces of the poles (e.g., limited corrosion byproduct/staining) prior to the earthquake.

Failures of distribution poles at the soil-structure interface were observed at a number of locations in Antakya. These poles, often of similar hollow, precast-concrete construction, were directly embedded an unknown depth in soil and experienced significant rotations at their base, on the order of 20 degrees or more. A rock fall also damaged a series of concrete distribution

poles, while simultaneously blocking a road outside of Islahiye. This required replacement with wood poles, with workers accessing the site by helicopter (Figure 7.31).



**Figure 7.30.** Distribution overhead structures damaged by debris (Antakya).



**Figure 7.31.** Rockfall damaged concrete distribution poles, replacement wood poles (near ID 141).

#### **7.4.5 Energy Transmission and Distribution Facilities**

Several large diameter energy transmission pipelines carrying oil and gas from the Middle East to Europe are routed through the impacted region.

Officially, eighteen major damages of natural gas main transmission lines were reported by BOTAŞ, the company responsible for these systems in Türkiye. The damages left Gaziantep, Hatay, Kahramanmaraş and Adıyaman without natural gas following the event. Officials reported that, as of 11 Feb. 2023, repairs to the major damages, including steel pipelines, were complete and additional work was needed in the cities to return service to residents.

News and social media reported significant explosions/fires in the region immediately following the earthquakes. Satellite imagery supports speculation that these fires were associated with

energy pipeline damage. Despite repeated attempts, the Lifelines Team was not able to meet with representatives with knowledge of the situation nor visit related facilities.

#### **7.4.6 LPG Storage and Distribution Facilities**

LPG is used extensively in Türkiye for cooking, heating, and powering cars. The Lifelines Team visited three LPG terminals in the İskenderun Bay (Milangaz, Aygaz, and Rubis) and three LPG bottling and storing plants in Antakya, Türkoğlu, and Kahramanmaraş (Figure 7.32). According to the preliminary ground motion estimates, these facilities were subjected to PGAs of up to 0.64g (ID Nos. 1, 82, 96, 98, 143, and 144 in Appendix A).

The LPG terminals generally performed very well. The three terminals combined have more than 20 large circular gas storage tanks and spheres built between 1980's and 2010's. Damage to these tanks was limited to a buckled (bent) steel brace and minor cosmetic cracks in the supporting concrete columns. One liquid fuel tank suffered some damage to its floating roof and spilled 6.5 tons of fuel that did not catch fire (the operator reported that the rainy conditions at the site that day contributed to prevent ignition). Some small leaks were noticed in the steel gas intake lines running into the sea, which were resolved by tightening the pipe flanges. The main seismic effect noted along the İskenderun coast was lateral spreading towards the sea, which extended for at least 10 km parallel to the coast. At one of the terminals, the westward displacement was about 50 cm and resulted in separation of the boundary walls (Figure 7.33). None of the equipment at this site was significantly damaged by the lateral spread.

Operations at the Hasgaz bottling facility west of Antakya were halted after the precast structure housing the production line collapsed (Figure 7.34). The structure joints appear to be weak and have insufficient strength to support the lateral earthquake loads. The columns opened outward resulting in the collapse of the girders. No fire or explosion was reported as a result of the girder collapse atop bottling equipment and gas bottles. The structure's foundation performed well, and the operator is planning to build a new structure atop it.

The Lifelines Team also visited an LPG storage facility in Kahramanmaraş, and an LPG production facility near Türkoğlu. These facilities are reportedly two of the main producers of gases for hospitals and food production facilities in the region. At the storage facility in Kahramanmaraş, numerous gas bottles were overturned (Figure 7.35), and several unanchored vertical cylindrical tanks toppled (Figure 7.36) or moved laterally (Figure 7.37). The overturned bottles were all empty or closed and did not release gas as a result of overturning.

The production facility in Türkoğlu was built in 2017 in an industrial park. The owner reported that the facility was designed for higher earthquake standards than required by code, increasing

construction costs by 30%, however, it was the only facility over more than twenty facilities in the industrial park that was operational after the earthquake. Typical conditions included storage tanks rocking, broken anchors, and a generator that fell off its rails (Figure 7.38). Additionally, a new administration building, which had not yet been occupied, experienced nonstructural damage.



**Figure 7.32.** Map of LPG storage and distribution facilities visited overlaid atop USGS PGA contour maps for M7.8 and M7.7 earthquakes.



**Figure 7.33.** Lateral spread causing separation in the boundary walls at one of the LPG terminals due to lateral spreading.



**Figure 7.34.** Collapse of precast production building at the Hasgaz plant west of Antakya.



**Figure 7.35.** Overturned gas bottles at LPG storage facility in Kahramanmaraş (ID 143 in Appendix A).



**Figure 7.36.** Overturned of an unanchored vertical tank at LPG storage facility in Kahramanmaraş (ID 143 in Appendix A).





**Figure 7.37.** 45 metric-ton unanchored vertical tank moved 90 cm laterally at LPG storage facility in Kahramanmaraş (ID 143 in Appendix A).



**Figure 7.38.** Deformed anchors and damaged generator at LPG production facility in Turkoglu (ID 144 in Appendix A).

#### 7.4.7 Petrol Stations

While in transit to various sites in Hatay, the Lifelines Team observed that the vast majority of the petrol stations appeared to be operational and relatively undamaged (e.g., Figure 7.39). At a few locations, the petrol station was the only structure standing. The stations typically consisted of pump stations covered by a canopy structure with an adjacent one-story accessory/store building. There were only a handful of observed collapses of the canopy structures along the

Lifelines Teams' route of travel. The adjacent one-story accessory/store building was more often severely damaged, however, the pumps appeared operational (e.g., Figure 7.40). We did not stop at these stations to verify the structural performance of the canopy structures and adjacent building and to collect detailed notes on the equipment performance. Our observations are mainly based on what we could see from the road as we were driving. Additional insights were provided by operators and managers of the LPG sites we visited in the region. They reported that about 15% of the 230+ petrol stations in the Hatay region were inoperable following the earthquake sequence due to floating tanks and toppled unanchored equipment.



**Figure 7.39.** Example of petrol station in Antakya without evident structural damage.



**Figure 7.40.** Example of petrol station in Antakya with standing canopy structure and heavily damaged one-story accessory building.

#### **7.4.8 Wind Turbines**

The Lifelines Team did not review the performance of wind turbines in detail. However, conversations with the locals and preliminary field observations suggest the wind towers had no observable damage and were operable following the earthquake sequence (e.g., Figure 7.41).



**Figure 7.41.** Example of wind turbines located west of Antakya.

### **7.5 *Water and Wastewater Systems***

Damage to water and wastewater systems varied from significant to minor across the impacted region. In the last 20 years, many local (city level) water utilities have been consolidated into larger province level utilities. Three of these province level water utilities were visited and reported herein, followed by specific performance of water infrastructure systems, namely water towers, water treatment, and wastewater treatment facilities. The water system related sites are shown blue in Figure 7.42.

Across all water utilities, significant sacrifices were made to restore services to customers as quickly as possible. The lives of many staff members were lost in the earthquake. One of the greatest challenges in the aftermath of the earthquakes was staff shortages. The tremendous efforts are acknowledged and appreciated by residents across the region.

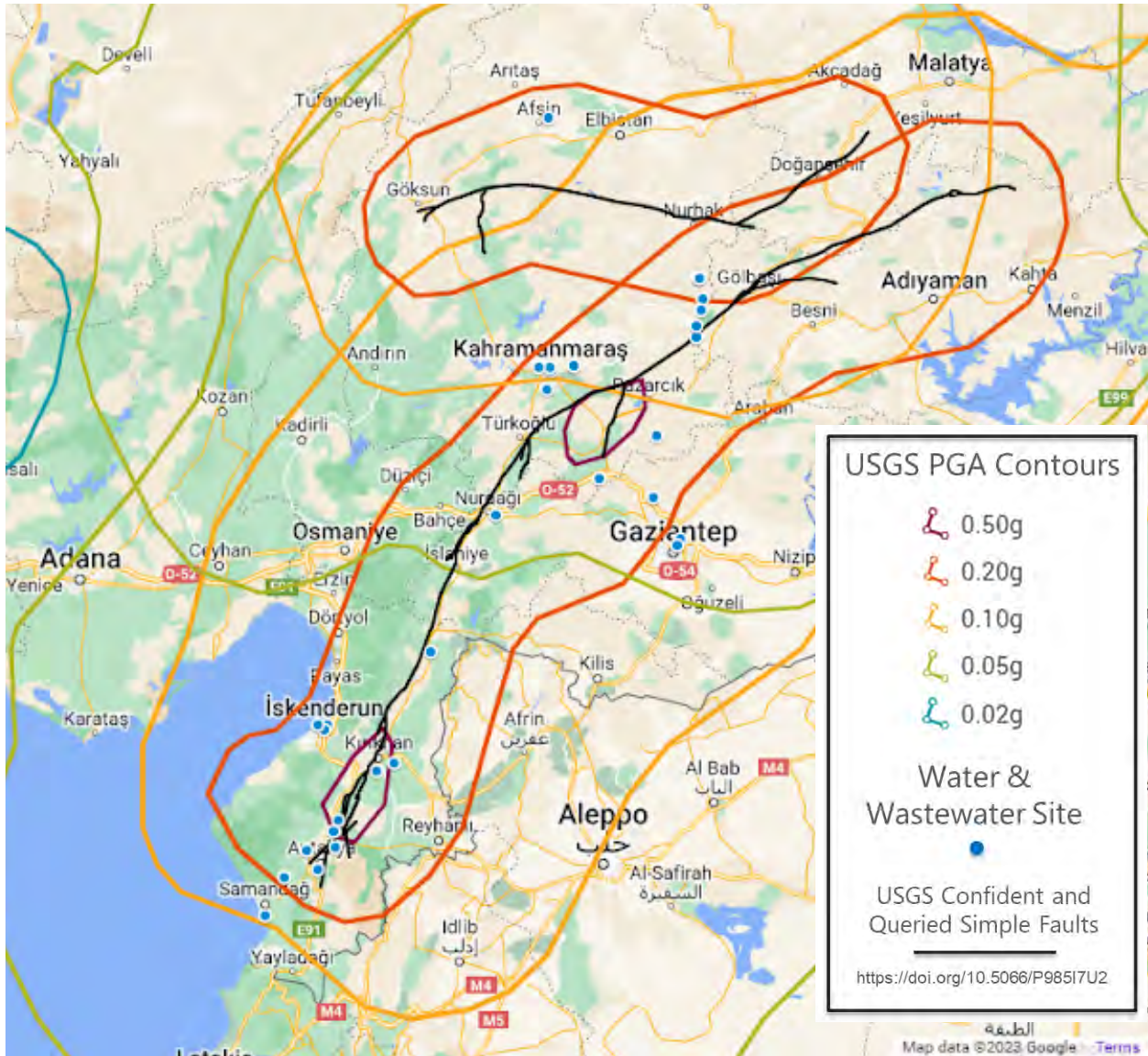


Figure 7.42. Water and wastewater facilities visited by the EERI Lifelines Team

**7.5.1 Water Utilities, Transmission, and Distribution Systems**

**(a) Kahramanmaraş Water and Sewerage Administration (KASKİ)**

KASKİ was incorporated in 2016 and serves the province of Kahramanmaraş, including the centrally located city of Kahramanmaraş and surrounding cities/towns. KASKİ serves a population of approximately 1.17 million people (2020 data). Water sources that serve Kahramanmaraş (city) include:

- Ayvalı Dam, approximately 20km west of the city (Ø1400mm steel pipe)

- Karasu Hatti (50 km) spring to the west of the city (Ø1200mm pipeline constructed in 2002).
- 3 well fields to the south of the city

Other primary infrastructure includes: 1 water treatment plant; 34 water tanks/storage structures; and 9 pump stations.

The distribution systems consist of 3200 km of water distribution pipeline (1800-2000km within Maraş) and approximately 1500km of wastewater pipelines. Within Kahramanmaraş the water system consists of polyethylene (PE) (50%), asbestos cement (AC) (15%), polyvinyl chloride (PVC) (15%) and cast/ductile iron (CI/DI) pipe (approximate values). For newer installations in general, Ø300mm diameter and less is PE, Ø300-700mm is ductile iron, and Ø700mm and greater are steel. The composition of pipe materials in the surrounding towns/cities differs widely based on historic preferences before the 2016 incorporation.

On 20 March 2023 KASKİ reported conducting approximately 5000 repairs to water infrastructure, equating to an average of 120 repairs/day. All pipe systems experienced some damage. Much of the damage was associated with pullout of unrestrained joints. While generally performing well, some localized ballooning of older HDPE pipe was reported with the speculative causes being either long-term degradation from pressure or acute damage due to earthquake impacts. Utilities reported difficulty in rapidly repairing HDPE and are now requiring periodic testing of all pipe materials for new installation across their system. Several locations of ongoing pipe repairs were visited and documented. Sinkholes, surface water manifestation, and infiltration into adjacent structures continue to occur across the region; indications of further needed repairs to the distribution system.

Another reported challenge was associated with pipe locating. KASKİ has GIS maps of more recent pipeline installations (a practice becoming more common for utilities in the US). However, due to the large fault offsets in the region (approximately 5m, see surface fault rupture section of this report) corrections to their GIS coordinate system are now necessary to provide accurate locations for buried infrastructure.

The water treatment plant experienced moderate damage and was able to continue providing water during the aftermath. However, residents at the west side of Maraş (higher elevation), reported no water service for 3 days following the event. After 3 days discolored/muddy water began running from taps. As of late March, the water was clear but highly chlorinated and residents (sample size of 4) did not feel comfortable drinking. Little information was available on

wastewater treatment plants or the wastewater distribution system and follow up work is highly encouraged.

**(b) Gaziantep Water and Sewer Authority (GASKİ)**

Located at the intersection of the Mediterranean and Southeastern Anatolia, Gaziantep is one of the most important cities in Türkiye and the 6th most populous city. As of 2022, it has a population of 2,154,051. Gaziantep city center drinking and potable water is supplied from Düzbağ, Kartalkaya, and Mizmilli sources.

The water distribution network in Gaziantep city center consists of 90% ductile pipes. Prestressed concrete pipes, PE, and fiberglass pipes are also included in the system. After the February 6 earthquake sequence, water interruption was experienced in the city center due to damages to water intake structures, energy transmission lines and transmission lines. On February 8, repairs to Kartalkaya pumping station were completed. Water started to be supplied to the city gradually. As of February 8, Mizmilli water source was also commissioned and allowed to be used only as domestic water. As of February 21, it was allowed to be used as drinking and potable water. As of March 5, water was supplied to the entire city.

Düzbağ transmission line is a pumped system consisting of 5 pumps (1 spare). Drinking water transferred from the regulators to the loading pond with a capacity of 6750 m<sup>3</sup> by 4 pumps is transferred to the distribution network with Ø1200 mm, Ø1800 mm and Ø2600 mm steel pipes. There are 15 line valves, 44 discharge valves and 55 suction cups along the line. Due to the February 6 earthquake sequence, 3 suction valves and 3 relief valves located 5 km from the tunnel were damaged. In addition, the support mechanisms of the 3.52 km long Ø2600 steel pipe in the tunnel were damaged due to movement in the direction of the pipe. After the earthquake, the pipe was cut from the part of the pipe inside the tunnel and the pipe was translated by a total of 30 cm in two directions with the help of hydraulics. This translation allowed the support points of the pipe to return to their pre-earthquake position. In addition, structural damages occurred in the tunnel structure due to fault movement.

Mizmilli transmission line consists of 42 km long Ø1200 steel pipe. Mizmilli is groundwater sourced and water supply is provided from 30 wells with an average depth of 120 m. The groundwater level in each well is around 25-30 m. The pumping system supplies water to the 20,000 m<sup>3</sup> tank in 4 stages with 5 pumps (1 spare). The pumping station suffered structural damage due to the February 6 earthquake sequence. To prevent damage to the pumps and to continue the water supply, controlled demolition was carried out and the pumps were temporarily protected by corrugated steel buildings (Figure 7.43).

Between 6 February and 24 April, 18,847 damages occurred in Gaziantep city center, 24,541 damages in İslahiye, 23,035 damages in Nurdağı and 7591 damages in Araban, Yavuzeli Nizip Karkamış, Oğuzeli in drinking water and sewage pipelines. In total, 80,560 damages occurred and were repaired. The GASKİ team, which activated the drinking water in a short time after the earthquake despite the terrain conditions and quickly repaired the breakdowns in the days after the earthquake, made great sacrifices. Unfortunately, 8 GASKİ staff members lost their lives due to the earthquake.



**Figure 7.43.** Mizmilli pump station (ID No. 79 in Appendix A). Building removed around pumps housed in protective structures.

**(c) Hatay Water and Sewerage Administration (HATSU)**

The province of Hatay, located at the southwest of the heavily impacted region, is provided water and wastewater services by Hatay Water and Sewerage Administration (HATSU), servicing a population of over 1.6 million according to 2019 data. Six of the fifteen districts that HATSU serves experienced significant infrastructure damage, including Antakya, İskenderun, and Kırıkhan. Operations of all 15 districts were heavily impacted due to fluctuations in population in the aftermath of the event, exacerbated in part by population growth associated with emigration from Syria predating this event, and associated increases in demand for drinking water.

For 20 days following the 6 February earthquake sequence, potable water was supplied to the region via trucks and distributed water tanks. As water service returned to the primary pipelines of the distribution system, the main lines were tapped with approximately 400 wells throughout the region to provide water to residents living in surviving structures and to many living in tents and containers outside of the temporary tent and container cities. A combination of building damage (uninhabitable) and water service line damage made service to buildings in most communities infeasible and resulted in this practice to provide a most basic level of service.

As of 19 March 2023, water was being supplied to most of the distribution system, however, the entire region was under a boil-water notice due to treatment quality concerns. One system within HATSU (İskenderun, a seaside city with significant levels of liquefaction) reported supplying 2-3 times the normal volume of water to overcome leaks and breaks throughout their distribution network. Inability to provide water pressure because of these breaks meant difficulty in delivering water to units located at the fourth or higher floors of taller buildings in İskenderun, especially during peak demand times. While the performance improved during lower demand times (i.e., the middle of night) for these higher floor units. It is expected that the significant number of uninhabitable buildings in İskenderun (collapsed or damaged) and the associated level of population emigration from the region would reduce service demand on the system. That the service demand had increased significantly points to water distribution performance concerns and likely widespread damage throughout the drinking water (and wastewater) system that has not yet been resolved.

The Hatay region is supplied water via three primary transmission pipelines. Repairs to these pipelines were prioritized immediately following the event to provide bulk water supply. Preliminary details of transmission pipelines and repairs include:

- 19 km of predominantly cast iron pipe, older construction, 20 repairs
- 19 km long of ductile iron pipeline, constructed in 2000's, 2 repairs
- 26 km long of ductile iron pipeline, newest construction, 4 repairs

The distribution system is composed of a variety of pipe types, including ductile iron, plastic, concrete, and steel. İskenderun reported damage to the water distribution system as predominantly pullout of unrestrained joints. Specific details of damages and associated repairs were unavailable and further study is suggested to correlate ground movement characteristics with system performance. Many damages remained difficult to access due to collapsed buildings or other impeding factors.



Despite challenges to physical infrastructure, HATSU reported the greatest challenge immediately following the event was related to personnel. Of the 2,540 HATSU staff, managers struggled to find 200 employees who were able to support operations during the days after the main event. Condolences are extended to the 34 HATSU staff members that lost their lives.

### 7.5.2 Water Towers

Several reinforced concrete water towers were observed throughout Hatay, especially in Antakya and İskenderun, all of which appeared quite similar in their construction. These towers typically consist of six inclined, rectangular columns. Between four and five levels of horizontal ring-beams interconnect these columns at equal vertical spacings along their height and at their connection to the reinforced-concrete water tank at their top. Damage was focused around beam-column joints and typically increased in severity with height as the plan dimensions of the towers narrowed. Damage modes ranged from column cover spalling adjacent to joints to varying degrees of joint failure where little to no transverse column or joint reinforcement was visible. Residual drifts were observed at some towers, and in at least one case this drift was quite significant and estimated to be on the order of several percent.

In İçada, Hatay, the water tower was leaning precariously over several houses, with residents anxious for its removal. Transverse reinforcement appears to be absent around longitudinal column reinforcing in some locations where column cover spalling had occurred, including at and adjacent to beam-to-column joints as depicted in Figure 7.44. Smooth reinforcing bars (i.e., reinforcing lacking mechanical deformations) were typical for both longitudinal and transverse reinforcing at this tower where exposed.



**Figure 7.44.** Water tower in İçada, Hatay, with significant residual drift and beam-column joint failures, several at joints with no transverse column/joint reinforcement visible (ID No. 100 in Appendix A).

A similar water tower in Antakya, Hatay, (Figure 7.45) exhibited less obvious residual drift, though still visually perceptible. The columns in this instance were partially outboard of the ring beams, and damage was primarily limited to the concrete columns adjacent to the beam-column joints where concrete cover spalling was extensive. Column cover spalling was typically centered above ring beams, and lap splicing of longitudinal reinforcing was visible immediately above the uppermost ring beam where spalling was most severe. Transverse reinforcement spacing visible in these areas is approximately  $\frac{1}{2}$  of the smaller column gross dimension. Previously painted areas of the column indicate potential concrete consolidation issues and / or limited concrete cover over reinforcing likely affected these elements prior to the earthquake.



**Figure 7.45.** Water tower in Antakya with lesser residual drift and extensive cover spalling of concrete columns above upper ring beam levels (ID No. 109 in Appendix A).

### 7.5.3 Water Treatment Plants

Three water treatment plants were visited by the Lifelines Team, in addition to interviews with water system managers of KASKİ, GASKİ, and HATSU as described above.

The water treatment plant in Karaçay, Hatay, (ID No. 37 in Appendix A) was subjected to PGAs of 0.42g and 0.65g during the **M7.8** and **M6.3** earthquakes. The plant was operational at the time of our visit but experienced damage to several buildings and hydraulic structures that were significantly impacting their operation. Some treatment structures proved particularly susceptible to minor seismic settlements. Additionally, non-structural components posed unique and considerable risks following the earthquake. The plant is situated on a hillside site below a hydropower reservoir and above the community being served.

Limited structural damage was observed to the two-story administrative building at the plant constructed of concrete frames, floor slabs, and roof slab with unreinforced masonry wall infill. One of the largest buildings on the site had a space truss roof framing system with hollow structural section truss members and a metal-deck or other light-weight roof sheathing (Figure 7.46a). Despite indications that this space truss system may have been designed without consideration of seismic forces (e.g., no enlargement of chord members positioned as cross-ties, anchorage of trusses to walls/columns that appeared non-ductile), the light-weight approach performed well with only cracking or concrete breakout damage at a small number of truss-to-wall corbel connections (Figure 7.46b). At smaller buildings, collapse of infill masonry partitions impacted operations as will be discussed in nonstructural components, below.



**Figure 7.46.** (a) Interior overview of light-weight, space truss roof framing system within sedimentation-tank building. Truss is uniform with no enlargement of cross-tie chord members. (b) Concrete breakout damage at anchorage of roof space truss node to corbel at the exterior concrete wall. Anchorage damage beyond minor cracking was observed in very few locations.

Free-field settlement immediately adjacent to the sedimentation tank building was estimated to be approximately 5 cm (Figure 7.47), though in other areas of the facility settlements on the order of 20 cm were observed. Sedimentation tanks in this building consisted of parallel flow channels constructed of concrete curbs performing as weirs atop a bottom slab. These weir-based systems were highly sensitive to even the smaller differential settlements observed near this building, with a significant proportion of the weirs either becoming entirely stagnant or rapidly flowing streams due to relative elevation increases or decreases, respectively (Figure 7.48). In still other locations, the curbs forming these sedimentation channels had translated atop the slab due to inertial forces and allowed large flows to bypass the sedimentation process entirely (Figure 7.49). Ultimately, the use of a central inflow channel with unregulated gravity flow to this network of sedimentation channels meant that localized damage or settlement to even a small number of channels led to significant negative impacts on the operation and efficacy of the entire sedimentation process.



**Figure 7.47.** Measurement of estimated settlements of approximately 5 cm adjacent to sedimentation process building (background)



**Figure 7.48.** Sedimentation channel weirs rendered ineffective due to differential seismic settlements. Arrow indicates area of rapid flow (more settlement) with adjacent channels nearly stagnant (less settlement).



**Figure 7.49.** Displacement of concrete curbs under inertial forces caused sedimentation channels to leak and be bypassed entirely (arrows indicate displacement of curbs from original position)

Elsewhere in the facility, as was also observed at some wastewater treatment plants, seismic settlements appear to have led to as-yet unquantified damages to below-ground piping at the facility. While investigation of these conditions had not yet begun, below-ground utility tunnels in the treatment plant showed signs of water infiltration in a few places (Figure 7.50).



**Figure 7.50.** Observed water infiltration in below-ground utility tunnels believed by facility operators to be potentially an indication of damage and leaks in below-ground piping infrastructure.

Similar to other lifeline facilities and buildings, the impact of unreinforced masonry (URM) wall infill collapses were considerable and impeded posts-earthquake recovery and operation. In the unique context of a water treatment plant, this damage also posed a considerable secondary hazard to the plants' occupants and the nearby community. At the time of the earthquake, the Karacay treatment process used gaseous chlorine rather than liquid. The chlorine gas was stored in large (approximately 200 cm long by 80 cm diameter) pressurized canisters connected to a small-diameter pipe network. The earthquake sequence caused a partial collapse of an URM infill wall (Figure 7.51) that fortunately did not compromise the toxic gas containment boundary. The water district had reportedly switched to liquid chlorine for treatment throughout their facilities shortly after the earthquake once this containment risk became apparent. Masonry infill fallout and / or non-structural equipment anchorage deficiencies also impacted the backup generator area and other non-structural equipment and controls, similarly to that observed at many other lifeline structures.

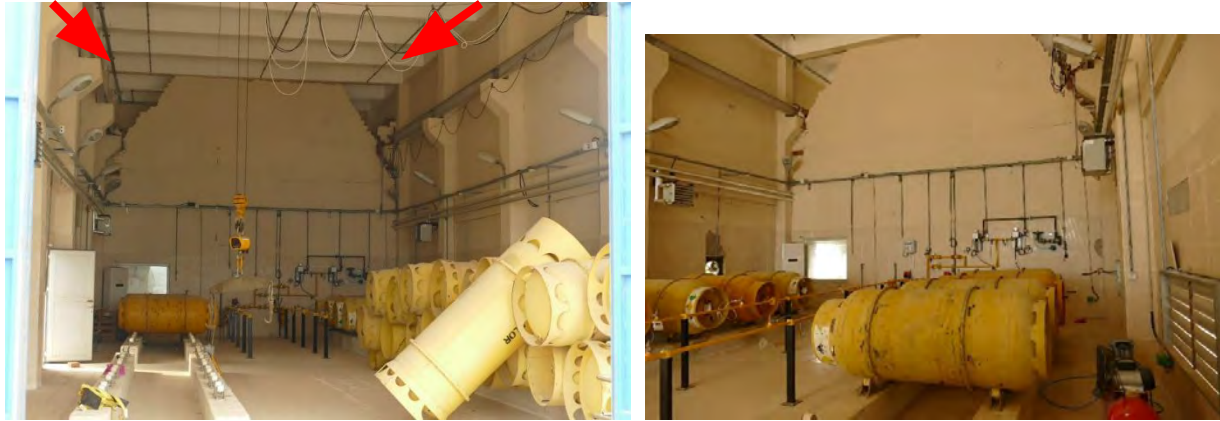


**Figure 7.51.** Large, pressurized chlorine gas canisters and associated piping for the treatment process remain below a partially collapsed URM wall approximately 8 m tall (arrow).

#### **7.5.4 Wastewater Treatment Plants**

The Lifelines Team documented conditions at nine wastewater treatment plants, six of which were distributed throughout Hatay and many were constructed within the last 10 years as well as one older facility in Antakya (ID Nos. 30, 31, 34, 35, 59, 90, 91, 119, and 167 in Appendix A). These sites were subjected to PGAs up to 0.72g.

Various levels of damage were experienced by HATSU's 16 wastewater treatment plants. As of 19 March 2023, 10 of 16 were operational. Five remained inoperable due to damages discussed below, three of which were observed during our reconnaissance. While not accessed by the EERI Lifelines Team, one relatively small plant in Antakya reportedly experienced complete collapse due to subsidence on the order of 90 cm together with the living complex it was a part of. Facilities were generally dependent on generators or other temporary power sources following the event, and power was reportedly still not available in many areas of the region as of the time of our visit.

Many wastewater treatment plants were relatively similar in construction, consisting of reinforced concrete tanks, digesters, and equipment supports with associated smaller, concrete-frame buildings with masonry-infill exterior and interior walls. Treatment facilities were generally located at lower elevations within the alluvial valley to allow for gravity flow to the facilities. Foundations for tanks and other hydraulic structures ranged from shallow mats to partially embedded approximately four meters below the adjacent ground surface. Ground improvement was implemented in at least one of the three visited plants during the construction of due to soft soil conditions, the significant loads imposed and a recognized liquefaction hazard at many of the sites.

Damage to wastewater treatment plants in Hatay generally consisted of structural damage to hydraulic structures, ground settlement induced damage to structures and to adjacent below-ground piping, and damage to nonstructural components that were generally unanchored or inadequately anchored. Structural damage and below-ground damage observed was anticipated to take considerably longer to repair and return the plants to operation than other performance shortcomings at these few facilities not yet operational.

Structural damage to hydraulic structures was generally limited to those walls not designed for hydrostatic loads, and most commonly to the dividing walls within aeration tanks. These aeration tanks are generally obround in shape, with one or more interior walls extending most of their length without direct connection to the exterior containment walls (Figures 7.52). The interior walls typically supported elevated air-system piping as well as slabs for personnel access at their tops. The dividing walls are accessed by elevated concrete bridges to the exterior walls of the tanks, commonly located near the ends of the walls. Where observable, the reinforcing in these dividing walls, typically 40cm thick, was relatively little. While braced in effect at their tops by the elevated walk bridges to the stronger exterior walls on each side, collapsed portions of interior walls were commonly isolated from wall portions with such bracing by pour joints with no reinforcing across them (Figure 7.53). In one facility, walk bridges near each end of the dividing wall extended to opposing exterior walls of the tank promoting a torsional response of the wall as the bridges progressively failed in tension due to reinforcing pullout (Figure 7.54). In either failure type, the dividing walls were unable to perform as cantilevers from the base of the tanks once isolated and collapsed into the tanks, precluding operation of the facilities until repairs can be made. Structural damage to intake structures and other smaller components were noted at some facilities.





**Figure 7.52.** Collapsed central dividing wall (between arrows) and damaged piping now submerged within aeration tank (Kırıkhan, Hatay) (ID No. 30 in Appendix A).



**Figure 7.53.** Concrete pour joint (arrow) dividing collapsed portion of interior wall (now below water surface) from surviving portion of dividing wall with stiffening walk bridges; no reinforcing provided across joint (Kırıkhan, Hatay) (ID No. 30 in Appendix A).



**Figure 7.54.** Partially collapsed dividing wall (arrow) where stiffening walk bridges existed only on one opposing side at each end of wall. Configuration promoted a torsional response of the dividing wall as bridges pulled out from the dividing wall in tension (Serinyol, Hatay) (ID No. 31 in Appendix A).

Geotechnical factors also contributed to the damage observed at several facilities, with damage from seismically-induced settlements leading to below-ground piping damage and damage to some tanks. At Narlıca Wastewater Treatment facility (ID No.34 in Appendix A), ground improvement using jet grouting under the structures during construction was made. At this facility, seismically induced free-field settlements adjacent to tanks and other structures ranged from approximately 4 to 15 cm and liquefaction ejecta was observed in the free-field adjacent to the structures (Figure 7.55). In other visited facilities, where no ground improvement was implemented, measure seismically-induced settlement as large as 25 cm (Figure 7.56). Voiding beneath slabs as much as 10 cm were observed. These settlements lead to below ground damage and leaks for the interconnecting piping in these plants. At one facility, below-ground pipe leaks subsequently led to flooding in interior basement areas housing pumps integral to the treatment process, illustrating the potential of cascading damage and impeding factors at these complex facilities. At the same facility, below-ground leakage of digester tanks had occurred and investigation or repair efforts had understandably not yet begun.



**Figure 7.55.** Free-field liquefaction ejecta observed at Narlıca Wastewater treatment facility (Narlıca, Hatay) (ID No. 34 in Appendix A).



**Figure 7.56.** Free-field settlements of approximately 16 cm adjacent to tanks structures led to damage and leaks in below-ground piping (Serinyol, Hatay) (ID No. 31 in Appendix A).

Nonstructural component damage further complicated or prevented the continued operation of a number of facilities as well. Inadequate bracing and / or anchorage of piping led to damaged supports and displaced or damaged piping in several facilities (Figure 7.57). Electrical components, control panels, and other pumps and equipment were often unanchored at their

bases or to adjacent walls. Some of these components appeared to have survived overturning with limited damage while others were rendered inoperable during the earthquake. For example, a 625 kW generator at Serinyol Treatment Plant was unanchored to its slab and slid approximately 35 cm toward the north (Figure 7.58). Despite self-contained fuel tanks and flexible electrical and exhaust connections, the cooling system contacted the building exterior leading to an oil leak that prevented generator operation during the subsequent multi-day power outage. In Narlica Treatment facility, shaking displaced filter media / membranes from within a treatment tank (Figure 7.59), and these membranes were reportedly irrevocably damaged once they had been exposed to air for an extended period of time.



**Figure 7.57.** (a) Displaced large-diameter vertical pipes with fractured strap bracing (arrows). (b) Fractured vertical, plastic pipes (arrows) with long unbraced lengths (Narlica, Hatay) (ID No. 34 in Appendix A).

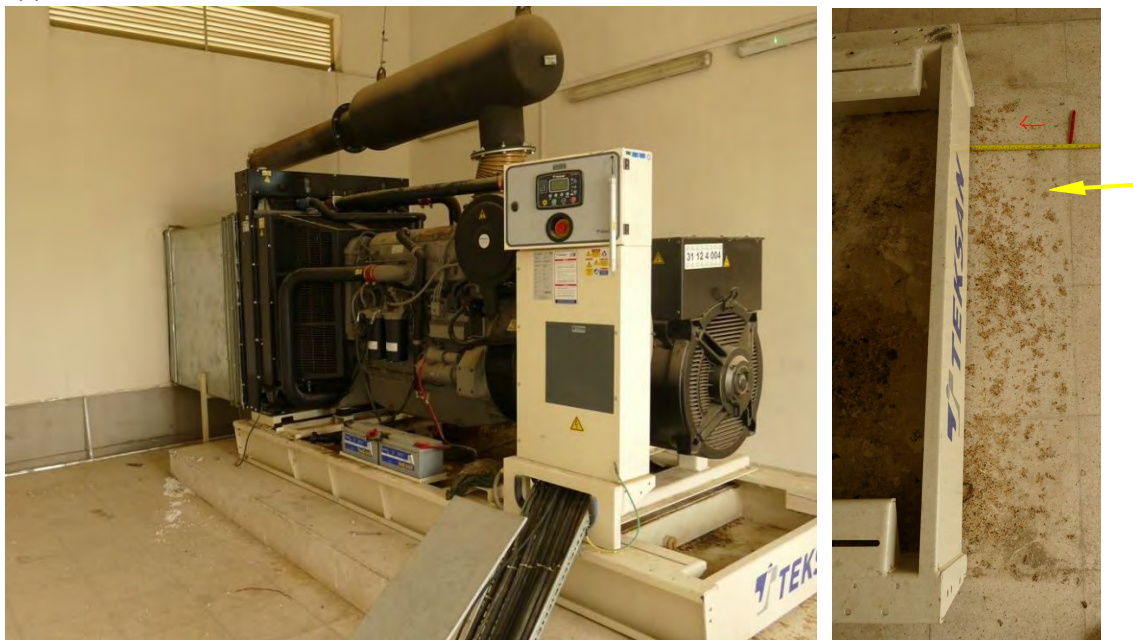


**Figure 7.58.** 265 kW Generator was unanchored and displaced approximately 30 cm to the north (figure left). Electrical and exhaust connections were flexible, but cooling structure impact led to oil leak (Serinyol, Hatay) (ID No. 31 in Appendix A).

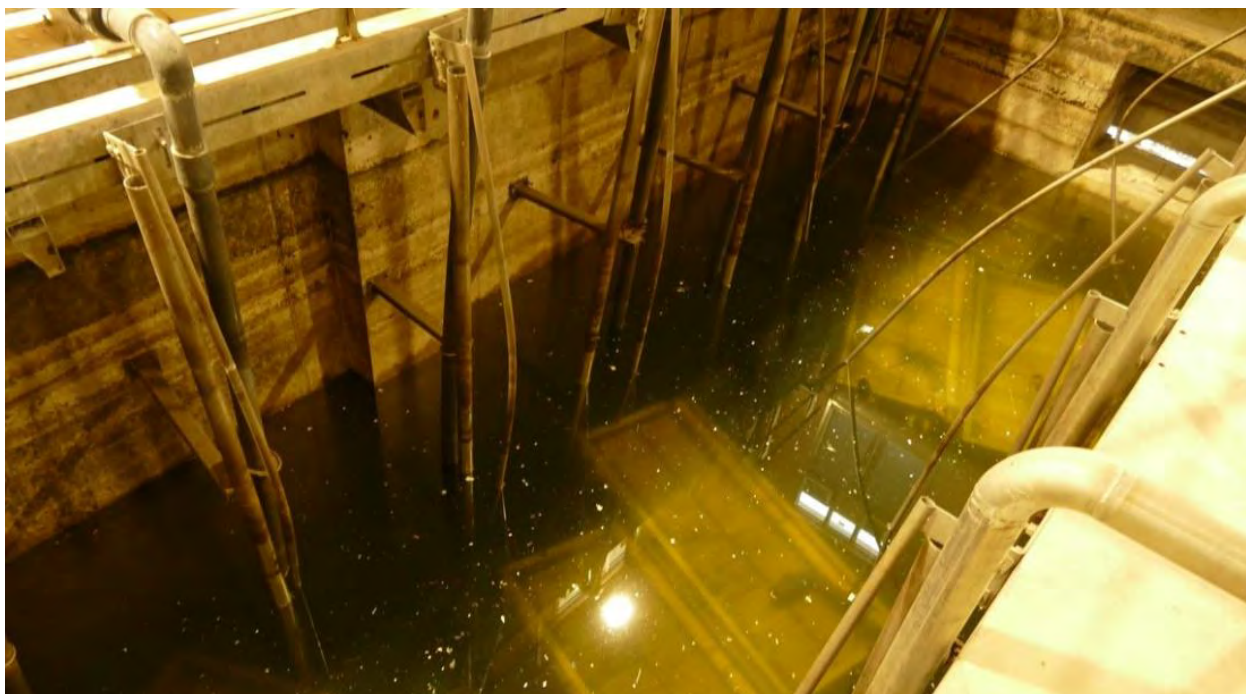


**Figure 7.59.** Filter media / membranes floating in treatment tank after shaking free from their attachments at the Narlica Plant. Membranes reportedly damaged in other tanks where they were exposed to air for long periods. (ID No. 34 in Appendix A).

## **7.6 University Facilities**

In addition to serving as learning and research centers, university campuses provide important functions for surrounding communities as they typically contain self-sufficient utility systems, food/cafeteria halls, and dormitories. University campuses in the affected region were often used as sites for emergency shelters for housing displaced residents. The Lifeline Team visited three university campuses, located in Hatay, Gaziantep, and Kahramanmaraş. These sites were subjected to PGAs of about 0.17-0.71g.

### **7.6.1 Mustafa Kemal University (MKU) in Hatay**

The MKU campus was founded in 1992 and hosts 25,000 students. The university hospital offers medical services to students and academic and administrative staff. The hospital comprises various polyclinics, fully equipped clinical laboratories, radiological examination rooms, and an emergency service.

The Lifelines Team met with faculty members and emergency response managers at MKU to discuss the performance of the campus buildings and structures. The hospital and main campus structures had relatively modest damage and were operable following the **M7.8** and **M7.7**

shocks but were closed to the public after the **M6.3** shock inflicted additional damage. Preliminary site ground motion estimates are 0.71g, 0.02g, and 0.34g for the **M7.8**, **M7.7**, and **M6.3**, respectively (ID No. 29 in Appendix A). The campus is located less than 1 km from the fault on a gently sloped hill.

The Lifelines Team was allowed to inspect a subset of the buildings on campus, while the hospital was not accessible. In general, the campus buildings performed very well considering the earthquake sequence, with some isolated cases of damage, e.g.:

- Masonry infill wall cracks and separations in a substation building supporting the campus electric grid (Figure 7.60). This distress was limited to the partition walls with no observed structural damage. No damage was observed to equipment housed in this substation building. We did not visit the larger substation supporting the hospital, but the operator indicated it was undamaged, and both substations were reportedly operable once offside power was restored.
- The Agricultural Sciences Building had no obvious structural damage based on the limited review we performed, however, the building suffered extensive damage to masonry infill walls and roof parapets (Figure 7.61). Some mechanical equipment was still wall-supported despite the extensive cracks in the infill (7.62). Several mechanical and electrical components were found to have displaced and toppled without causing cascading damage (e.g., Figure 7.63).
- Fallen ceiling tiles and ceiling light gratings were observed at multiple locations, including the hospital hallway, which was visible from outside (Figure 7.64).

We also documented two undamaged transformers without horizontal and vertical restraints between the supporting steel frame and the wheel rails that did not show signs of significant displacements (Figure 7.65). The lack of movement of these transformers and the good performance of structures and equipment onsite suggests the local motion might have been damped by geologic features.



**Figure 7.60.** Infill damage at local substation



**Figure 7.61.** Example of masonry infill damage at the Agricultural Science building.



Figure 7.62. Example of equipment surviving masonry infill damage at the Agricultural Science building



Figure 7.63. Example of displaced and toppled equipment at the Agricultural Science building.





**Figure 7.64.** Example of fallen ceiling tiles and light gratings at the MKU hospital hallway.



**Figure 7.65.** Example of transformers without vertical restraints that were undamaged

## 7.6.2 Gaziantep University

The EERI Lifelines Team visited Gaziantep University on March 21, 2023. The site was subjected to an estimated PGA of 0.22g (ID No. 99 in Appendix A).

We met with Prof. Dr. Mustafa Özakça who shared with us some of the history of the campus and toured us through several campus buildings. Gaziantep University was founded in 1973 and has buildings of different ages and types of construction. Some of the older buildings on campus

were constructed with significant amounts of concrete shear wall relative to the floor area. Buildings constructed in later years reportedly did not have as much wall area and shifted to more of a concrete frame like building.

Overall, there was little earthquake damage to campus buildings. The Lifelines Team observed some infill wall cracking in the canteen building (Figure 7.66) and some infill cracking and cracking in structural elements of the library building. In the library, most book stacks were located on the 4<sup>th</sup> elevated level. Reportedly, most of the books came off the bookshelves during the earthquake sequence. There was some minor concrete spalling on the underside of a central stair at the entrance of the library. Steel post shores were installed under this stair as a precautionary measure (Figure 7.66). At the time of our visit the library had not been reopened to students, even though the cracking we observed in structural elements appeared to be relatively minor. The natural gas service at the campus was reportedly cut off for two or three days after the earthquake sequence to check for damage, but no damage was found.



**Figure 7.66.** Cracking of infill wall in canteen (left) and spalling of underside of stair and steel shoring post in library (right).

### 7.6.3 Kahramanmaraş Sütçü İmam University (KSU)

The EERI Lifelines Team visited KSU campus on March 21, 2023. The site was subjected to an estimated PGA of 0.17g (ID No. 107 in Appendix A).

We met with Prof. Dr. Mehmet Metin Köse who shared with us some of the history of the campus and toured us through the campus engineering buildings and the physical plant. Afterwards the Lifelines Team also separately toured the medical hospital/clinic associated with the university.

The engineering buildings on the campus were constructed around 2008 to 2010. Dr. Köse reported that the campus buildings performed well. Our observations of visited buildings were consistent with this report as we observed very little cracking of finishes. The university campus had water and electricity service right after the earthquake sequence. At the time we visited the campus the entire campus had been converted to be used as emergency housing and shelter.

The hospital/clinic also performed well structurally. We observed some cracking at the interface of infill walls and structural elements (Figure 7.67), some tile damage near expansion joints (Figure 7.67) and cracked glazing in automatic doors (Figure 7.68). Additionally, we observed a failure of a small roof structure at one corner of the hospital (Figure 7.68). Much of the hospital/clinic also appeared to have been converted to temporary housing.



**Figure 7.67.** Cracking at joint between infill wall and column (left) and cracking of tiles at expansion joint (right)



**Figure 7.68.** Cracking of glazing in automatic sliding door (left) and damage to hospital/clinic rooftop structure (right)

Appendix A to Chapter 7 - GROUND MOTIONS AT SITES VISITED BY THE LIFELINES TEAM

Site Information					M7.8			M7.5			M6.3		
ID	Site Category	Site Name (Facility or Structure)	Lat. (+)	Long. (+)	PGA (g)	PGV (cm/s)	Sa (1 s) (g)	PGA (g)	PGV (cm/s)	Sa (1 s) (g)	PGA (g)	PGV (cm/s)	Sa (1 s) (g)
1	LPG, Terminal	LPG Rubis	36.8546	36.1727	0.22	42	0.41	0.05	16	0.09	0.06	5	0.03
2	Substation	TEIAS Distribution Substation No. 1 – TR 1844	37.0495	35.2748	0.06	30	0.15	0.04	35	0.14	0.02	2	0.01
3	Bridge	Sevgi Parkı	36.1897	36.1514	0.70	99	1.24	0.02	11	0.07	0.97	99	0.64
4	Bridge	D420	36.1922	36.1517	0.70	100	1.26	0.03	12	0.07	0.98	101	0.66
5	Substation	TEIAS Distribution Substation No. 2 – TR 1440	37.0490	35.2817	0.07	36	0.19	0.04	42	0.17	0.02	2	0.02
6	Bridge	Mehmet Yeloğu Köprüsü	36.1953	36.1565	0.50	63	0.72	0.02	7	0.04	0.83	70	0.41
7	Water	WW Pump, near port	36.5907	36.1759	0.23	44	0.30	0.02	11	0.04	0.06	4	0.03
8	Bridge	Atatürk Parkı Pedestrian Bridge	36.1969	36.1569	0.60	91	1.20	0.02	11	0.07	0.97	101	0.68
9	Substation	TEIAS Distribution Substation No. 3 – TR 1892	37.0479	35.2555	0.07	32	0.16	0.04	38	0.15	0.02	2	0.02
10	Water	İskenderun Water Distribution System Manager	36.5758	36.1682	0.27	50	0.37	0.03	12	0.05	0.08	4	0.04
11	Bridge	Asi Sokak Pedestrian Bridge	36.2001	36.1591	0.58	90	1.23	0.02	11	0.07	0.97	102	0.70
12	Bridge	Ata Köprüsü Bridge	36.2024	36.1610	0.57	89	1.26	0.02	11	0.08	0.97	103	0.72

Site Information					M7.8			M7.5			M6.3		
ID	Site Category	Site Name (Facility or Structure)	Lat. (+)	Long. (+)	PGA (g)	PGV (cm/s)	Sa (1 s) (g)	PGA (g)	PGV (cm/s)	Sa (1 s) (g)	PGA (g)	PGV (cm/s)	Sa (1 s) (g)
13	Bridge	Mustafa Rasih	36.2043	36.1616	0.57	89	1.27	0.02	11	0.07	0.97	102	0.72
14	Bridge	Semih Azmi	36.2066	36.1618	0.58	95	1.35	0.02	11	0.08	0.98	102	0.74
15	Bridge	Yavuz Sultan Selim	36.2100	36.1619	0.59	110	1.51	0.02	12	0.08	0.99	104	0.78
16	Bridge	Bekir Karabacak	36.2154	36.1621	0.61	137	1.81	0.03	13	0.09	1.01	110	0.89
17	Gen.	meet with Parl. Rep.	36.2288	36.1335	1.01	95	0.79	0.02	11	0.06	1.47	94	0.79
18	Industrial Facility	Cesan Asphalt Plant	36.9705	35.6471	0.09	25	0.16	0.04	21	0.09	0.03	2	0.02
19	Road	Embankment Failure	36.2207	36.1638	0.63	125	1.74	0.03	13	0.09	1.00	116	1.02
20	Bridge	Bridge	36.2329	36.1851	0.57	96	1.68	0.03	11	0.09	0.76	120	1.11
21	Industrial Facility	Industrial district east of Adana	36.9756	35.6031	0.08	21	0.11	0.04	18	0.07	0.02	2	0.01
22	Water	Meet with Antakya Water Director	36.2401	36.1051	0.86	91	0.64	0.02	9	0.05	1.23	82	0.53
23	Bridge	Bridge	36.2414	36.1914	0.56	97	1.66	0.03	12	0.10	0.68	111	0.99
24	Gen.	Firefighter station	37.0073	35.3615	0.06	35	0.13	0.04	32	0.11	0.03	2	0.02
25	Gen.	meet with Istanbul head of emergency extreme event facility	36.2288	36.1335	1.01	95	0.79	0.02	11	0.06	1.47	93	0.79
26	Bridge	Cevre Yolu	36.2487	36.1997	0.55	96	1.57	0.03	13	0.10	0.59	97	0.77
27	Bridge	Hatay Devlet	36.2724	36.2078	0.62	101	1.39	0.03	12	0.09	0.49	73	0.48
28	Gen.	drive through damaged Antakya	36.2063	36.1598	0.60	100	1.37	0.02	11	0.08	0.99	103	0.74
29	University	Mustafa Kemal University Campus and Hospital	36.3307	36.1956	0.71	74	0.63	0.02	6	0.03	0.34	28	0.16

Site Information					M7.8			M7.5			M6.3		
ID	Site Category	Site Name (Facility or Structure)	Lat. (+)	Long. (+)	PGA (g)	PGV (cm/s)	Sa (1 s) (g)	PGA (g)	PGV (cm/s)	Sa (1 s) (g)	PGA (g)	PGV (cm/s)	Sa (1 s) (g)
30	Water, WWTP	Kırıkhan WWTP	36.4598	36.3496	0.60	97	0.87	0.03	17	0.07	0.14	12	0.13
31	Water, WWTP	Serinyol WWTP	36.3228	36.2148	0.72	104	1.10	0.03	12	0.07	0.43	48	0.32
32	Bridge	Bridge	36.2404	36.2146	0.61	79	1.14	0.02	7	0.04	0.48	61	0.37
33	Bridge	Bridge by Hatay Stadium	36.2546	36.2034	0.61	101	1.55	0.03	12	0.09	0.56	87	0.63
34	Water, WWTP	Narlıca Atıksu Arıtma WWTP	36.2504	36.2081	0.57	97	1.54	0.03	13	0.10	0.54	87	0.63
35	Water, WWTP	Samandağı Wastewater Treatment Plant	36.0586	35.9637	0.21	73	0.48	0.02	12	0.06	0.36	37	0.48
36	Gen.	Debris Disposal Site	36.2113	36.1984	0.47	56	0.87	0.02	7	0.04	0.59	68	0.42
37	Water, TP	Karaçay WTP (HATSU KARAÇAY İÇMESUYU ARITMA TESİSİ)	36.1638	36.0287	0.42	83	0.57	0.02	9	0.04	0.65	61	0.36
38	Gen.	Antakya Castle - Aerial Views of Valley	36.1951	36.1773	0.35	39	0.52	0.01	5	0.03	0.62	56	0.32
39	Transmission Tower	Failed Transmission Tower	36.1492	36.0836	0.49	78	0.60	0.02	8	0.04	0.69	60	0.34
40	Dam	DSİ Büyük Karaçay Dam	36.1869	35.9888	0.31	56	0.31	0.01	6	0.02	0.46	38	0.19
41	Substation	Hatay 380 kV TEIAS Substation	36.2051	36.1140	1.10	109	0.99	0.02	10	0.06	1.15	91	0.57
42	Gen.	drive through damaged Antakya	36.2007	36.1569	0.62	96	1.28	0.02	11	0.07	0.99	103	0.71
43	Airport	Hatay Airport	36.3646	36.2727	0.70	73	0.61	0.02	7	0.03	0.22	16	0.10
44	Dam	Berke Barajı	37.3726	36.4616	0.14	17	0.10	0.06	11	0.05	0.01	1	0.00
45	Bridge	Bridge	36.4037	36.2795	0.64	99	0.93	0.03	15	0.07	0.25	22	0.18

Site Information					M7.8			M7.5			M6.3		
ID	Site Category	Site Name (Facility or Structure)	Lat. (+)	Long. (+)	PGA (g)	PGV (cm/s)	Sa (1 s) (g)	PGA (g)	PGV (cm/s)	Sa (1 s) (g)	PGA (g)	PGV (cm/s)	Sa (1 s) (g)
46	Substation	Berke Dam Substation	37.3539	36.4357	0.17	21	0.13	0.07	14	0.07	0.01	1	0.01
47	Bridge	Bridge	36.4298	36.3083	0.64	100	0.91	0.03	15	0.06	0.18	15	0.13
48	Bridge	Kırıkhan Yolu	36.4655	36.3799	0.55	88	0.79	0.03	18	0.07	0.13	11	0.12
49	Water, storage	Leaning water tower	36.4833	36.4064	0.47	83	0.74	0.03	21	0.09	0.12	11	0.13
50	Gen.	Rockfalls and spreads, walls, train tracks	37.1032	36.6464	1.35	119	1.05	0.05	11	0.06	0.03	2	0.02
51	Bridge	Bridge	36.5048	36.4121	0.48	91	0.79	0.03	20	0.09	0.11	10	0.11
52	Bridge	Highway bridge	37.1014	36.6525	1.37	120	1.06	0.05	11	0.06	0.03	2	0.02
53	Road/Culvert	Highway D360 Culvert	37.3790	36.9004	0.51	110	0.82	0.09	19	0.08	0.02	3	0.02
54	Recording Station	TK 2708	37.0993	36.6484	1.47	122	1.07	0.05	11	0.06	0.04	2	0.02
55	Substation	TEIAS Fevzipaşa 154 kV Substation	37.1025	36.6565	1.38	135	1.24	0.05	13	0.07	0.03	3	0.03
56	Bridge	Cengiz Topel	36.5898	36.1500	0.22	39	0.27	0.02	10	0.04	0.05	5	0.05
57	Bridge	Yaşar Doğu	36.5891	36.1502	0.22	39	0.27	0.02	10	0.04	0.05	5	0.05
58	Bridge	Bridge	36.5855	36.1523	0.26	62	0.50	0.04	21	0.10	0.08	10	0.11
59	Water, WWTP	Nurdağı WWTP	37.1690	36.7589	0.62	108	1.25	0.06	14	0.07	0.02	3	0.02
60	Bridge	505 Sokak	36.5830	36.1578	0.27	63	0.52	0.04	21	0.10	0.09	9	0.10
61	Bridge	Bridge	36.5798	36.1635	0.28	60	0.47	0.03	17	0.08	0.09	7	0.06
62	Bridge	Sadık Ahmet	36.5783	36.1650	0.26	50	0.36	0.03	12	0.05	0.08	5	0.04
63	Bridge	Pınar Başı	36.5765	36.1672	0.27	50	0.36	0.03	12	0.05	0.08	4	0.04
64	Bridge	Süleyman Şah	36.5756	36.1732	0.26	46	0.33	0.02	11	0.04	0.08	4	0.03
65	Bridge	Bridge	36.5748	36.1801	0.26	49	0.35	0.02	11	0.05	0.09	5	0.04



Site Information					M7.8			M7.5			M6.3		
ID	Site Category	Site Name (Facility or Structure)	Lat. (+)	Long. (+)	PGA (g)	PGV (cm/s)	Sa (1 s) (g)	PGA (g)	PGV (cm/s)	Sa (1 s) (g)	PGA (g)	PGV (cm/s)	Sa (1 s) (g)
66	Bridge	Midyat	36.5753	36.1818	0.27	49	0.35	0.02	11	0.05	0.09	5	0.04
67	Industrial Facility	Osmaniye Industrial District	37.0157	36.1038	0.15	24	0.18	0.05	14	0.08	0.03	3	0.01
68	Water, Utility	Gaski Water	37.0842	37.3871	0.20	27	0.22	0.08	33	0.18	0.01	1	0.01
69	Bridge	Musa Şahin	37.0598	36.2184	0.18	33	0.27	0.06	21	0.14	0.04	4	0.03
70	Bridge	Atatürk	37.0546	36.2318	0.18	33	0.27	0.06	20	0.13	0.04	4	0.03
71	Bridge	Dereobası	37.0485	36.2493	0.17	29	0.23	0.05	16	0.10	0.04	4	0.02
72	Bridge	Zorkun	37.0479	36.2693	0.16	25	0.19	0.05	13	0.08	0.03	3	0.02
73	Coal Plant	İskenderun Coal Plant	36.6914	36.2091	0.26	55	0.40	0.03	14	0.06	0.06	3	0.02
74	Bridge	Aksu	37.5105	36.9051	0.34	75	0.70	0.09	24	0.15	0.03	4	0.04
75	Bridge	Bridge	37.5145	36.9059	0.36	71	0.63	0.08	19	0.11	0.02	3	0.03
76	Bridge	Orhan Sezal Yolu	37.5694	36.9173	0.32	44	0.25	0.07	21	0.09	0.02	2	0.03
77	Bridge	Ceyhan	37.6110	36.7963	0.18	33	0.17	0.10	36	0.20	0.01	2	0.02
78	Water, storage	100,000 Ton Field (Pipe Storage 1 (prestressed))	37.2157	37.3027	0.26	40	0.26	0.08	29	0.11	0.01	1	0.01
79	Water, source/pumps	Gaski Mizmilli İçme Suyu Tesisleri (Water Source Pumps)	37.2711	37.1146	0.44	76	0.46	0.06	15	0.05	0.01	1	0.01
80	Water, storage	Pipe Storage 2 (Steel)	37.1041	37.3967	0.20	28	0.21	0.08	33	0.17	0.01	1	0.01
81	Gen.	Liquefaction/tilting buildings	37.7888	37.6497	0.51	122	0.59	0.27	70	0.43	0.01	1	0.01
82	LPG, Plant	Hasgaz LPG Tank Facility	36.4494	36.2749	0.64	78	0.60	0.02	8	0.03	0.14	8	0.07
83	Dam	River Dam	37.8666	37.7744	0.40	83	0.36	0.26	56	0.40	0.00	0	0.00
84	Tunnel	Erkenek Tunnel	37.9236	37.8773	0.33	67	0.28	0.24	50	0.37	0.00	0	0.00

Site Information					M7.8			M7.5			M6.3		
ID	Site Category	Site Name (Facility or Structure)	Lat. (+)	Long. (+)	PGA (g)	PGV (cm/s)	Sa (1 s) (g)	PGA (g)	PGV (cm/s)	Sa (1 s) (g)	PGA (g)	PGV (cm/s)	Sa (1 s) (g)
85	Bridge	Göksu	37.8393	37.6977	0.41	90	0.41	0.29	69	0.45	0.00	1	0.01
86	Gen.	drive through damaged Antakya	36.2122	36.1599	0.62	133	1.70	0.03	12	0.08	1.02	105	0.80
87	Viaduct	Viaduct	37.1794	36.7056	0.48	62	0.65	0.04	8	0.03	0.01	1	0.01
88	Viaduct	Viaduct	37.1694	36.7315	0.63	118	1.54	0.07	17	0.09	0.02	3	0.03
89	Viaduct	Viaduct	36.7113	36.4993	0.65	131	1.00	0.05	25	0.16	0.06	3	0.04
90	Water, WWTP	WWTP Hassa	36.7928	36.5368	0.70	182	1.57	0.05	14	0.11	0.06	5	0.06
91	Water, WWTP	WWTP İskenderun	36.5879	36.1469	0.22	39	0.26	0.02	10	0.04	0.05	6	0.06
92	Silo	Granary 1 - Nurdağı	37.1815	36.7221	0.58	90	1.10	0.05	11	0.05	0.02	2	0.02
93	Silo	Granary 2 - Kırıkhan	36.5006	36.3730	0.70	95	0.77	0.02	14	0.05	0.10	7	0.12
94	Silo	Granary 3 - Kırıkhan	36.5010	36.3797	0.66	98	0.81	0.02	15	0.06	0.11	8	0.12
95	Airport	Gaziantep Airport	36.9459	37.4744	0.15	24	0.14	0.06	27	0.14	0.01	1	0.01
96	LPG, Terminal	Aygaz LPG Tank Facility	36.6914	36.2091	0.26	55	0.40	0.03	14	0.06	0.06	3	0.02
97	Water	KASKİ - Kahramanmaraş Su ve Kanalizasyon İdaresi Genel Müdürlüğü	37.5663	36.9527	0.35	52	0.34	0.07	18	0.09	0.02	3	0.03
98	LPG, Terminal	Milangaz LPG Tank Facility	36.8509	36.1550	0.21	41	0.39	0.04	17	0.09	0.06	4	0.03
99	University	Gaziantep University	37.0378	37.3134	0.22	30	0.26	0.08	32	0.18	0.01	2	0.01
100	Water/storage tower	KASKİ Water storage tower (damaged)	37.5124	36.9363	0.41	74	0.64	0.07	16	0.09	0.02	3	0.03
101	Substation	Narlı Substation	37.3829	37.1362	0.57	160	1.21	0.09	33	0.12	0.02	4	0.05

Site Information					M7.8			M7.5			M6.3		
ID	Site Category	Site Name (Facility or Structure)	Lat. (+)	Long. (+)	PGA (g)	PGV (cm/s)	Sa (1 s) (g)	PGA (g)	PGV (cm/s)	Sa (1 s) (g)	PGA (g)	PGV (cm/s)	Sa (1 s) (g)
102	Water/pipe repair	Water pipe repair	37.5732	36.9479	0.33	44	0.26	0.07	17	0.08	0.02	2	0.03
103	Water/pipe repair	Water pipe repair (2 leaks)	37.5739	36.9066	0.27	33	0.16	0.06	18	0.07	0.01	2	0.02
104	Industrial Facility	Kipas Starch Factory	37.4030	36.8721	0.53	107	0.77	0.08	17	0.07	0.02	3	0.02
105	Airport	Kahramanmaraş Airport	37.5395	36.9662	0.42	71	0.58	0.07	16	0.11	0.02	3	0.04
106	Water, TP	Ayvalık Su Arıtma Tesisi	37.5812	37.0279	0.37	53	0.32	0.09	16	0.08	0.01	2	0.01
107	University	KSU University (Eng Bldg and Physical Plant)	37.5874	36.8079	0.17	35	0.19	0.09	33	0.19	0.01	2	0.02
108	Hospital	KSU Hospital/Clinic	37.5875	36.8255	0.15	33	0.17	0.08	31	0.18	0.01	2	0.02
109	Water/storage tower	Antakya Water storage tower (damaged)	36.2941	36.1975	0.75	103	1.15	0.02	9	0.06	0.46	54	0.32
110	Substation	Substation 1 - Antakya	36.2408	36.1620	0.73	105	1.35	0.02	9	0.06	1.01	114	1.16
111	Substation	Substation 2 - Antakya	36.2399	36.1687	0.68	104	1.56	0.02	9	0.07	0.94	127	1.39
112	Substation	Substation 3 - Antakya	36.2280	36.1655	0.64	115	1.68	0.03	13	0.09	0.99	126	1.25
113	Substation	Substation 4 - Antakya	36.2094	36.1626	0.56	94	1.26	0.02	10	0.06	0.94	93	0.66
114	Substation	Substation 5 - Antakya	36.2076	36.1633	0.55	84	1.16	0.02	9	0.06	0.93	92	0.64
115	Substation	Substation 6 - Antakya	36.2074	36.1661	0.53	73	1.08	0.02	9	0.06	0.90	91	0.63
116	Substation	Substation 7 - Antakya	36.2200	36.1722	0.56	85	1.24	0.02	8	0.06	0.86	94	0.75
117	Readi-Mix Plant	Readi Mix Plant outside of Antep	37.3012	37.1504	0.45	80	0.49	0.07	18	0.06	0.01	1	0.01
118	Readi-Mix Plant	Tanks toppled	36.5010	36.3797	0.66	98	0.81	0.02	15	0.06	0.11	8	0.12

Site Information					M7.8			M7.5			M6.3		
ID	Site Category	Site Name (Facility or Structure)	Lat. (+)	Long. (+)	PGA (g)	PGV (cm/s)	Sa (1 s) (g)	PGA (g)	PGV (cm/s)	Sa (1 s) (g)	PGA (g)	PGV (cm/s)	Sa (1 s) (g)
119	Water, WWTP	WWTP Antakya	36.1881	36.1465	0.85	108	1.33	0.03	11	0.07	0.98	99	0.63
120	Silo	Granary - Antakya	36.3393	36.2082	0.82	101	0.95	0.02	9	0.05	0.43	39	0.28
121	Water	Transmission Pipeline (traveling along line)	37.3859	37.3130	0.48	57	0.32	0.11	31	0.08	0.01	1	0.01
122	Bridge	Bridge	37.0091	37.3763	0.19	26	0.21	0.07	31	0.18	0.01	1	0.01
123	Bridge	Mezarlık Yolu	37.0151	37.3981	0.16	22	0.15	0.06	25	0.13	0.01	1	0.01
124	Bridge	Bridge	37.0176	37.4068	0.18	25	0.19	0.07	30	0.17	0.01	1	0.01
125	Bridge	Bridge	37.0150	37.4301	0.16	23	0.16	0.06	28	0.15	0.01	1	0.01
126	Bridge	Bridge	37.0617	37.4602	0.18	29	0.21	0.08	38	0.22	0.01	2	0.01
127	Bridge	Bridge	37.0881	37.4342	0.17	24	0.17	0.07	29	0.15	0.01	1	0.01
128	Bridge	Bridge	37.0839	37.4240	0.19	28	0.22	0.08	36	0.20	0.01	2	0.01
129	Water	Water Pipe Fault crossing	37.6577	37.4507	0.69	152	0.87	0.18	50	0.23	0.01	1	0.01
130	Bridge	Bridge	37.0809	37.3148	0.22	29	0.24	0.08	29	0.15	0.01	1	0.01
131	Water/source	Düzbağ Water source	37.8173	37.4636	0.28	48	0.24	0.22	52	0.26	0.00	1	0.00
132	Water	Düzbağ water control structure	37.8171	37.4568	0.22	34	0.16	0.17	37	0.17	0.00	0	0.00
133	Water/tunnel	Tunnel: Water Pipe-entrance	37.7611	37.4718	0.30	49	0.23	0.15	33	0.15	0.00	0	0.00
134	Dam	Kılavuzlu Dam	37.6253	36.8010	0.18	35	0.18	0.11	40	0.21	0.01	2	0.02
135	Water/tunnel	Tunnel: Water Pipe- exit	37.7300	37.4702	0.43	77	0.39	0.17	38	0.18	0.00	1	0.00
136	Water	Pipeline vault-damaged	37.6885	37.4527	0.61	130	0.73	0.18	48	0.23	0.01	1	0.01
137	Dam	Menzelet Dam	37.6758	36.8493	0.18	26	0.12	0.12	33	0.14	0.01	1	0.01

Site Information					M7.8			M7.5			M6.3		
ID	Site Category	Site Name (Facility or Structure)	Lat. (+)	Long. (+)	PGA (g)	PGV (cm/s)	Sa (1 s) (g)	PGA (g)	PGV (cm/s)	Sa (1 s) (g)	PGA (g)	PGV (cm/s)	Sa (1 s) (g)
138	Substation	Substation 8 - Nurdağı	37.1644	36.7684	0.60	105	1.18	0.06	15	0.07	0.02	3	0.02
139	Substation	Substation 9 - Nurdağı	37.1713	36.7500	0.62	115	1.43	0.06	16	0.08	0.02	3	0.02
140	Substation	Substation 10 - İslahiye	37.0145	36.6247	0.66	94	0.70	0.04	11	0.07	0.04	3	0.04
141	Substation	Substation 11 - İslahiye	36.9437	36.5360	0.44	78	0.52	0.03	9	0.05	0.02	2	0.01
142	Substation	Substation 12 - Fevzipaşa	37.1028	36.6501	1.37	120	1.06	0.05	11	0.06	0.03	2	0.02
143	LPG	LPG Storage Facility	37.5711	36.9703	0.36	54	0.35	0.08	18	0.09	0.02	3	0.04
144	LPG	LPG Production Facility	37.3507	36.8194	0.55	83	0.54	0.06	10	0.04	0.01	1	0.01
145	Industrial Facility	Corn Oil Plant	37.1883	36.7608	0.59	101	1.17	0.06	13	0.06	0.02	3	0.02
146	Coal Plant	Afşin Coal Plant A	38.3470	37.0259	0.09	12	0.07	0.18	42	0.21	0.00	1	0.01
147	Bridge	Bridge	37.0809	37.3148	0.22	29	0.24	0.08	29	0.15	0.01	1	0.01
148	Bridge	Söğütlü Çay Köprüsü	38.2231	37.2108	0.13	19	0.12	0.24	66	0.34	0.00	1	0.01
149	Bridge	Tepebasi	38.2175	37.1973	0.13	19	0.12	0.25	68	0.36	0.00	1	0.01
150	Bridge	Şehit Jandarma Uzman Çavuş	38.2148	37.1870	0.12	16	0.09	0.25	64	0.32	0.00	1	0.01
151	Bridge	Esentepe	38.2098	37.1807	0.10	12	0.07	0.24	53	0.24	0.00	0	0.00
152	Bridge	Binali Yıldırım	38.2052	37.1804	0.10	12	0.07	0.24	54	0.25	0.00	0	0.00
153	Bridge	Hamid-i Veli	38.2006	37.1862	0.07	7	0.03	0.18	33	0.13	0.00	0	0.00
154	Bridge	Ulu Cami	38.1995	37.1877	0.10	13	0.07	0.25	55	0.25	0.00	0	0.00
155	Bridge	Pedestrian Bridge	38.1986	37.1879	0.10	13	0.07	0.25	56	0.25	0.00	0	0.00
156	Bridge	Pedestrian Bridge	38.1974	37.1895	0.10	13	0.07	0.25	56	0.25	0.00	0	0.00
157	Bridge	Köprübaşı	38.1972	37.1902	0.10	13	0.07	0.25	56	0.25	0.00	0	0.00
158	Bridge	Pedestrian bridge - support settlement	38.1972	37.1913	0.10	13	0.07	0.25	56	0.25	0.00	0	0.00

Site Information					M7.8			M7.5			M6.3		
ID	Site Category	Site Name (Facility or Structure)	Lat. (+)	Long. (+)	PGA (g)	PGV (cm/s)	Sa (1 s) (g)	PGA (g)	PGV (cm/s)	Sa (1 s) (g)	PGA (g)	PGV (cm/s)	Sa (1 s) (g)
159	Bridge	Bridge	38.1977	37.1927	0.10	13	0.07	0.25	56	0.25	0.00	0	0.00
160	Coal Plant	Afşin Coal Plant B	38.3534	36.9820	0.09	13	0.08	0.18	43	0.22	0.00	1	0.01
161	Bridge	Pedestrian Bridge	38.1982	37.1941	0.10	13	0.07	0.25	56	0.25	0.00	0	0.00
162	Bridge	Göktürk	38.1968	37.1953	0.10	13	0.07	0.25	56	0.25	0.00	0	0.00
163	Bridge	Kerkük	38.1962	37.2076	0.12	18	0.10	0.27	70	0.35	0.00	1	0.01
164	Fault Scars	First fault scar we reviewed in the open field	37.4703	37.0253	0.64	128	0.95	0.09	17	0.08	0.01	2	0.02
165	Fault Scars and Substation	Kapıçam Substation near first crossing we reviewed	37.4638	37.0187	0.62	114	0.81	0.08	14	0.07	0.01	2	0.01
166	Fault Scars	Second fault scar we reviewed on highway to Antep	37.4801	37.0422	0.63	111	0.77	0.08	14	0.07	0.01	2	0.01
167	Water, WWTP	WWTP Afşin	38.2558	36.9439	0.09	11	0.06	0.23	57	0.28	0.00	0	0.00

## 8.0 Performance of Flood/Irrigation Earth Dams

*Robb Moss, Onder Cetin, Umut Ayhan*

There are a number of earth dams located in the earthquake affected region that are used for irrigation and/or flood control. These dams were built between 1950's and the 2020's and consist of earthfill and rockfill composition. The advanced team (Phase 1) visited 7 dams at the request of the dam agency (State Hydraulic Works / Devlet Su İşleri), and made a preliminary assessment of their performance. Figure 8.1 shows the locations of these dams with respect to the surface fault rupture and the epicenters.



**Figure 8.1.** Showing locations of the earth dams visited by GEER and the surface fault rupture from both events (Google Earth).

Ground shaking estimates from the two main events are shown for the 7 dam locations. Estimates of peak ground acceleration (PGA), peak spectral acceleration at 1 second (PSA), and peak ground velocity (PGV) are given in Table 8.1. These were estimated based on the methods outlined in Chapter 3.

**Table 8.1.** Ground shaking estimates at each of the GEER visited earth dam locations.

Name	M7.8 Estimated PGA (g)	M7.8 Estimated Sa(1 s) (g)	M7.8 Estimated PGV (cm/s)	M7.7 Estimated PGA (g)	M7.7 Estimated Sa(1 s) (g)	M7.7 Estimated PGV (cm/s)
Sultansuyu	0.19	0.31	53.02	0.36	0.91	76.31
Surgu	0.19	0.22	44.16	0.50	0.92	125.47
Kartalkaya	1.16	0.61	101.82	0.12	0.07	26.95
Ariklikas	0.28	0.35	41.13	0.06	0.08	13.65
Yarseli	0.36	0.65	56.45	0.02	0.06	12.99
Reyhanli	0.24	0.43	43.13	0.03	0.06	16.08
Erkenek	0.54	0.75	160.01	0.25	0.53	64.81

### 8.1 Sultansuyu Dam

The Sultansuyu Dam (38.31854° N, 38.051208° E) is an earth-fill dam constructed between the years 1986-1992 in Malatya for irrigation purposes. The crest height from the stream level is almost 60 meters. Due to the earthquakes crest cracks formed with varying depths as well as large cracks on the upstream face. On the crest, cracks with upwards of 2 m lateral deformation with a 4 m depth were observed (Figure 8.2).



**Figure 8.2.** Left image shows crest cracking and deformations. Right image shows large face scarps on the upstream face rough half way down the face.



Large head scarps indicating rotational instability were observed on the upstream face roughly half way down the slope (Figure 8.2). Coincident with these scarps on the upstream face were deformations at the toe, along with evidence of liquefaction in the form of sand boils (Figures 8.3 and 8.4).

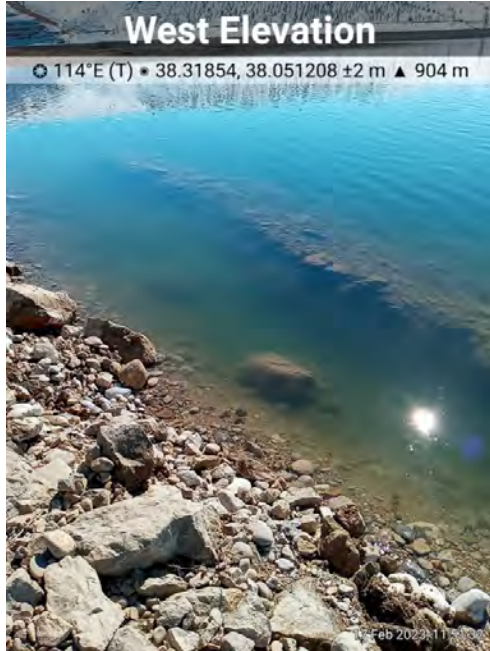


**Figure 8.3.** Lateral translation of the toe coincident with the location of the large face scarps.



**Figure 8.4.** Left image shows ground cracking indicating lateral spreading, and the right image shows sand boils at the skirts of the right abutment indicating liquefaction.

Based on these observations it appears that the foundation soils, which are granular in nature, liquefied during the strong ground shaking, destabilizing the upstream face of the earth dam leading to slope instability and crest cracking. No damage was observed on hydraulic structures (spillways, bottom outlets, etc).

## 8.2 Sürgü Dam

Sürgü dam (38.041488 N, 37.885133 E) was built in the late 50's and stands at 57 m high. It has a wholly separate outlet structure that is not connected with the earth dam. Crest cracks with 5 cm vertical with 10 to 15 cm horizontal displacement were observed. Slight bulging on the upstream face coincident with the crest cracks indicating seismic slope stability as the cause of the crest cracking. Only superficial damage was observed in the outlet structures, mainly concrete spalling/cracking along the top of the parapet walls in a few locations.

There exists a step over fault in the vicinity that did not appear to rupture in this event although there are aftershocks that align with it. The dam abuts very different geology on either side which may indicate the presence of a fault. It should be evaluated for future potential rupture.



**Figure 8.5.** Crest cracking observed looking both directions along the crest.



**Figure 8.6.** Bulging on the upstream face (circled) is coincident with the location of the crest cracking which may indicate seismic induced slope deformations.

### **8.3 Kartalkaya Dam**

Kartalkaya Dam (37.46874 N, 37.239213 E) is an clay core earthfill dam constructed between 1965-1972 in Kahramanmaraş for irrigation, fresh water supply and flood control purposes. The crest height from the stream level is 56 meters. The dam is located on Pazarcık, which is 3 km away from the epicenter of the first event. Consequently, moderate damage with crack widths varying in between 15-35 cm was observed along the crest of the dam. The earth dam was constructed upon a bedrock constricted channel and the rock abutments constrain the earthfill. The reservoir was already at low pool during the earthquakes due to the ongoing drought as reported by the dam operator. Wingwalls located at the water inlet through the gates had superficial damage due to intense shaking. One segment moved toward the earth dam. No cracking was observed in either the upstream or downstream faces. No trace of liquefaction was observed due to the rocky nature of the native materials. The crest damage, which was at its greatest at the center point of the dam, appears to be due to seismic compression of the earthfill.



**Figure 8.7** Left image, crest damage after the earthquakes, photo provided by dam operator. Right image, crest structure damaged by strong ground shaking.



**Figure 8.8.** Arrow points to the midpoint of the dam where the largest crest deformations were observed. The highwater line (aka bathtub ring) as indicated by the black line shows a “swayback” response due to seismic compression.

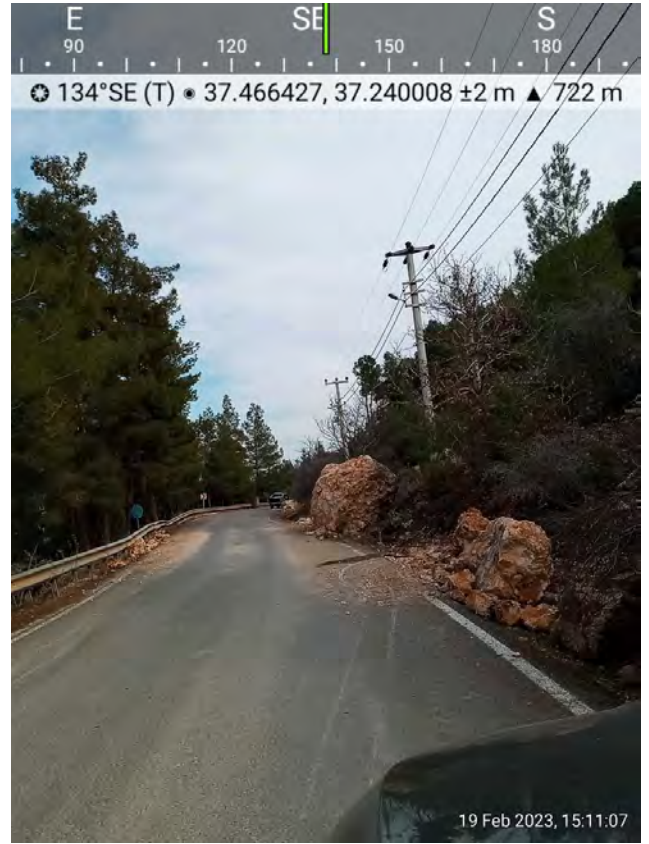


**Figure 8.9.** Left image, cracking of outlet structure that appears superficial. Right image, rock fall was prevalent in this area indicating intense high frequency shaking.



**Figure 8.10.** Auxiliary elements of the Kartalkaya Dam.

#### **8.4 Arıklıkaş Pond**

The Arıklıkaş pond (37.156133 N, 36.514218 E) is an earthfill dam constructed between 1994-1998 in Osmaniye for irrigation purposes. The crest height from the stream level is almost 32 meters. Observed crest cracking was very prominent with the crest widening horizontally up to 2.2 m from the deformations. Large scarps on the upstream face were observed in addition to sand boils towards the toe. No damage was detected on hydraulic structures except for minor cracks on the curtain walls of the spillway.



**Figure 8.11.** Significant crest cracking on Arıklıkış Pond earth dam.



**Figure 8.12.** Left image showing significant face cracks halfway down the upstream face. Right image showing sand boils at the toe of the earth dam.

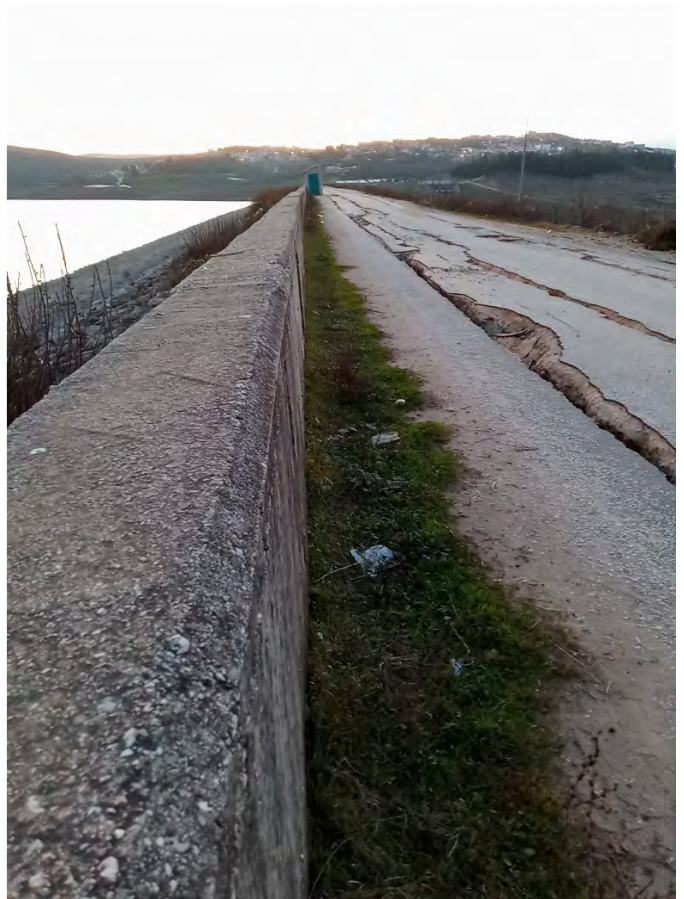


Figure 8.13. Earth dam specs for Arıklıkaş Pond.

## 8.5 Yarseli Dam

Yarseli Dam (36.194258 N, 36.326858 E) is a clay core sand-gravel fill dam constructed between 1985-1991 in Antakya for irrigation purposes. The crest height from the stream level is 43.5 meters. Crest cracking with lateral displacements varied between 15-25 cm. No cracking on the upstream or downstream slopes were observed. There were no observed sand boils on the earth dam face or the toe. The hydraulic structures had no obvious cracking or damage. Crest cracking is thought to be due to seismic compression. Surface manifestations of soil liquefaction were not observed on the earth dam body. However, sand boils and liquefaction-induced lateral spreading were mapped on the downstream side closer to the right abutment. The projection of surface cracking mapped on the crest coincides with these downstream manifestations (see Figure 8.14). Auxiliary elements are still functional and no damage was observed.





**Figure 8.14.** Left image shows crest cracking of Yarseli Dam. Right image shows slight tilt of the parapet wall and coincident crest cracking.



**Figure 8.15.** No observed cracking in the outlet structures.



**Figure 8.16.** Yarseli dam specifications.



**Figure 8.17.** Sand boils and liquefaction-induced lateral spreading downstream near the dam body.

## 8.6. Reyhanlı Dam

Reyhanlı Dam (36.336036 N, 36.548310 E) is located in Hatay. The construction was completed between 2013-2020, and its crest height is 20.2 meters above the minimum water level. The dam was constructed for flood control and irrigation purposes. It does not have a spillway. The crest length is more than 9 km. Due to the changes in topography, two cross-sections were designed. In between KM 0+000-6+000, it is a zoned earth-fill section; center clay-core sand-gravel fill between Km: 6+000-9+272.

Figure 8.18 visualizes the spatial distribution of the cracks mapped on the crest. The red color code emphasizes the significantly deformed section, along which 1.0 to 1.2 meter lateral deformations with up to 1 meter of settlement were mapped. The earthquake-induced permanent lateral deformations were observed to be towards the upstream side. The orange code indicates the moderate level of cracking, and as shown in Figure 8.19, their lateral extent was reported to be as high as 30 cm.

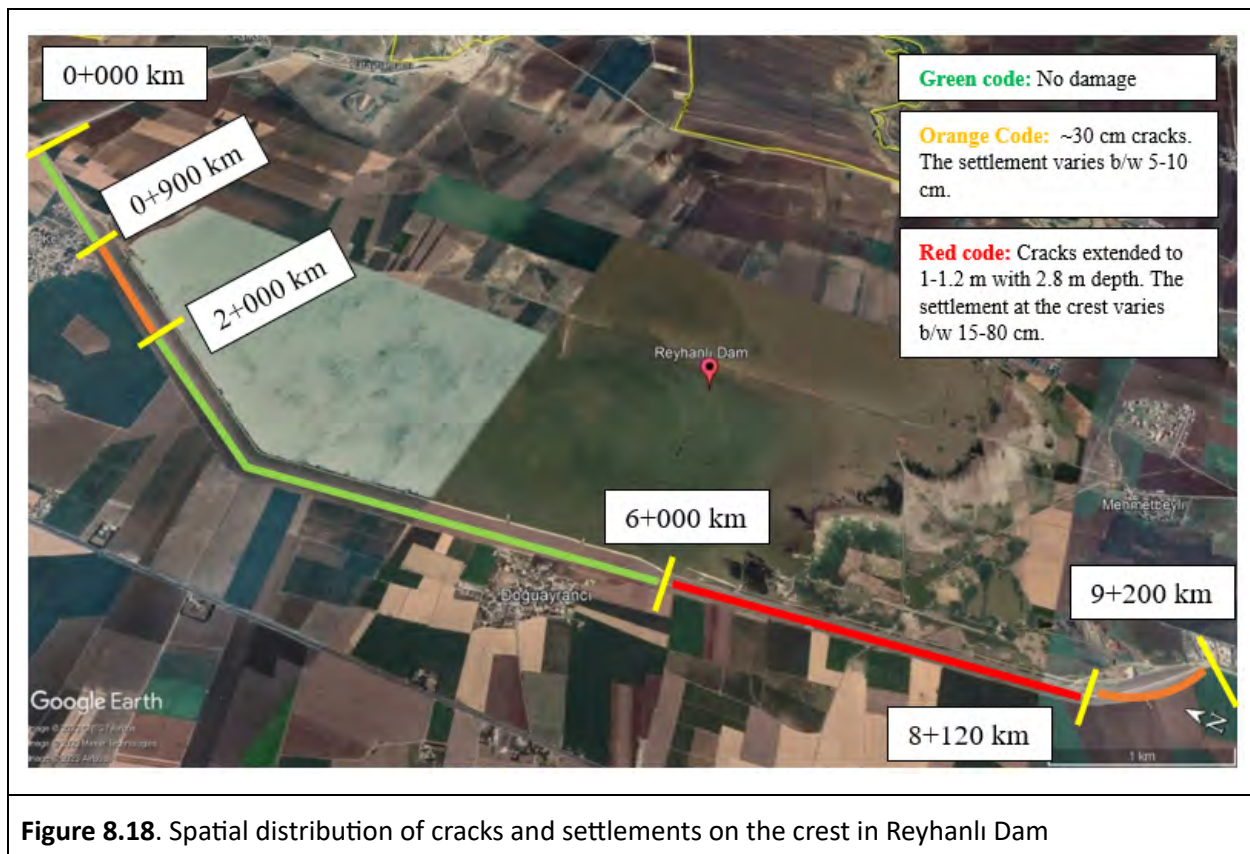


**Figure 8.18.** Spatial distribution of cracks and settlements on the crest in Reyhanlı Dam



**Figure 8.19.** Deformations reported on the crest of the Reyhanlı Dam

### **8.7. Erkenek Dam**

Erkenek Dam (37.934257 N, 38.035615 E) is a geomembrane faced earthfill dam with an approximately 10 cm thick concrete coating on the upstream face, located near Doğanşehir, Malatya. The dam was constructed for irrigation purposes, and its crest height is 41 meters from the thalweg. The surface rupture of the M7.8 event crossed the dam axis, producing a 3.4 m offset of the dam body. The left lateral offset was mapped along a 55 meter shear zone. The historical traces of the historical fault offsets and the fault plane were clearly visible at the dam site, as shown in Figure 8.20-8.21.



**Figure 8.20.** Left image shows the faulting in a cut near the dam. Right image shows evidence of the 3.4 meters of offset in the dam embankment.



**Figure 8.21.** Image showing the general trend of the surface fault rupture through the Erkenek dam.

No apparent deformations indicating global slope instability or failures were observed. The dam performed well against intense shaking despite being located on a ruptured fault. Some minor local lateral displacements and deformations were documented at the crest in the vicinity of the right and left abutments. The total lateral movement was reported as 10-30 cm. The appurtenant structures performed well during the event. The conduit of the bottom outlet was observed to be ruptured. Water level was low at the time of the events due to the ongoing drought. Springs were observed in the vicinity of the bottom outlet (see Figure 8.22).



**Figure 8.22.** Left image, outlet structure of Erkenek dam. Right image, water issuing from the base of the outlet structure that appeared after the events.

## 9.0 Landslides and Rock Falls

*Robb Moss, Rich Koehler, Umut Ayhan*

Landslides and rock falls were observed throughout the damage zone, however they were not as prevalent as was expected nor as was forecast using USGS shakemap predictions. Discussed are a few observations that were documented as part of the GEER reconnaissance, but overall mass wasting did not significantly impact the built environment in these events.

### 9.1 Landslides

A prominent landslide that was much in the media occurred near the village of Tepehan. This village was in ancient times known as Yarıklı Koy which translates to “village of the big cracks.” Several news programs had picked up on ground damage in this area, which has been photographed by broadcast images and drone footage. Figure 9.1 shows the feature, which includes large cracks, translated blocks, and mass wasting that intersected an olive grove (36.161688 N, 36.219966 E).

The chasm that opened up measured roughly 500m long by 300m wide by 30m deep. The geology consists of the Tepehan formation (Middle Miocene) comprised of sandstone, clayey limestone, claystone and marl. The layered beds were observed dipping downslope at 8 - 10 degrees, and the ground surface dips from 10 to 20 degrees steepening towards the toe. We found by climbing down to the base of the headscarp (Figure 9.2) that the claystone had weathered to a residual clay. In speaking with locals they reported heavy rainfall for a few days leading up to the seismic events. The earthquakes provided the lateral loading with values (Table 9.1) estimated from semivariogram fits to the nearby strong motions stations from the M7.8 as discussed in Chapter 3.

**Table 9.1** of strong ground shaking in the vicinity of the Tepehan landsliding.

PGA	0.40 g
Sa (1s)	0.54 g
PGV	48.2 cm/s



**Figure 9.1** Large ground cracks and translated blocks in an olive grove observed in Tepehan.

Closed-form solutions for wedge and block stability indicate that the static factor of safety ranges from 1.25 to 1.50. Estimating the seismic slope stability using Bray et al. (1998) indicates a  $k_y \sim 0.05$  to 0.10 and a  $k_y/k_{max} \sim 0.1$  to 0.3 which correlates to large deformations, and this assumes limited strength loss. In this particular case the strength loss from intact to residual clay most likely is more substantial resulting in larger deformation potential. Triaxial testing of the residual clay reported in a prior MS thesis (Kavuzlu, 2006) found the engineering parameters to be  $c=63$  kPa and  $\phi=7.5$  degrees.



**Fig 9.2.** Near the headscarp of the Tepehan ground cracks. Note the layered geologic units. These were observed to be dipping at roughly 8-10 degrees downslope.



## 9.2 Rock Fall

Countless rock falls were observed during the reconnaissance efforts. Earthquake induced rock falls appeared to be the most common form of mass wasting during the earthquakes. Several examples of rock falls are shown in Figures 9.3 through 9.5.

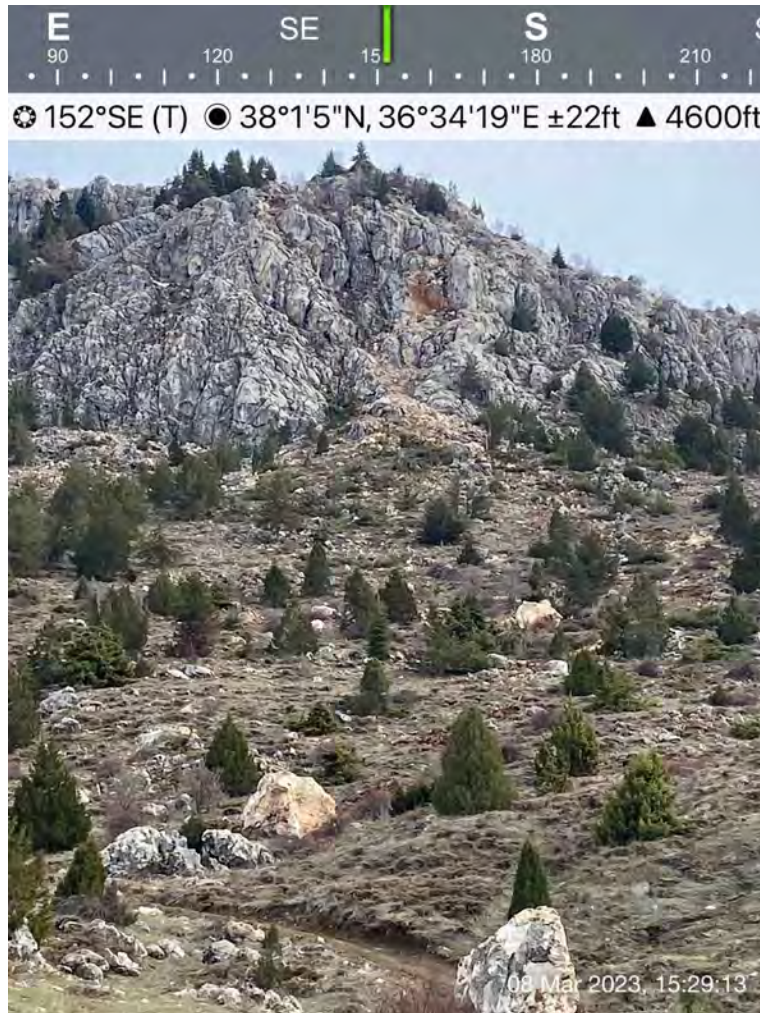


**Figure 9.3.** Earthquake induced rockfall from the M7.7 Sürgü-Çardak earthquake. Note: source and debris located near the town of Karaahmet.

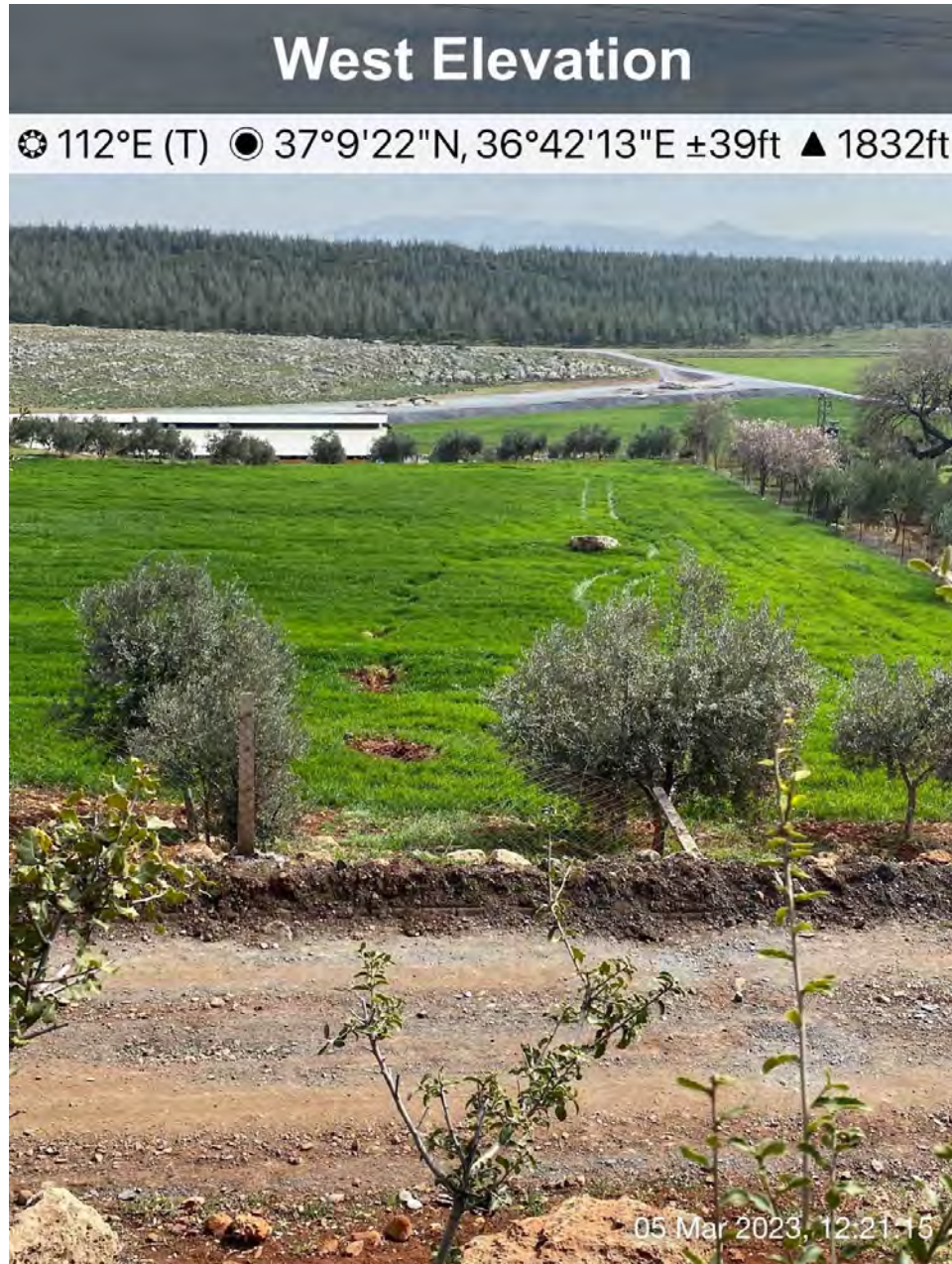


**Figure 9.4.** Rockfall runout south of the town of Gökçedere near the East Anatolian fault. Note the bouncing travel path of the several ton boulder, similar to a skipping stone.

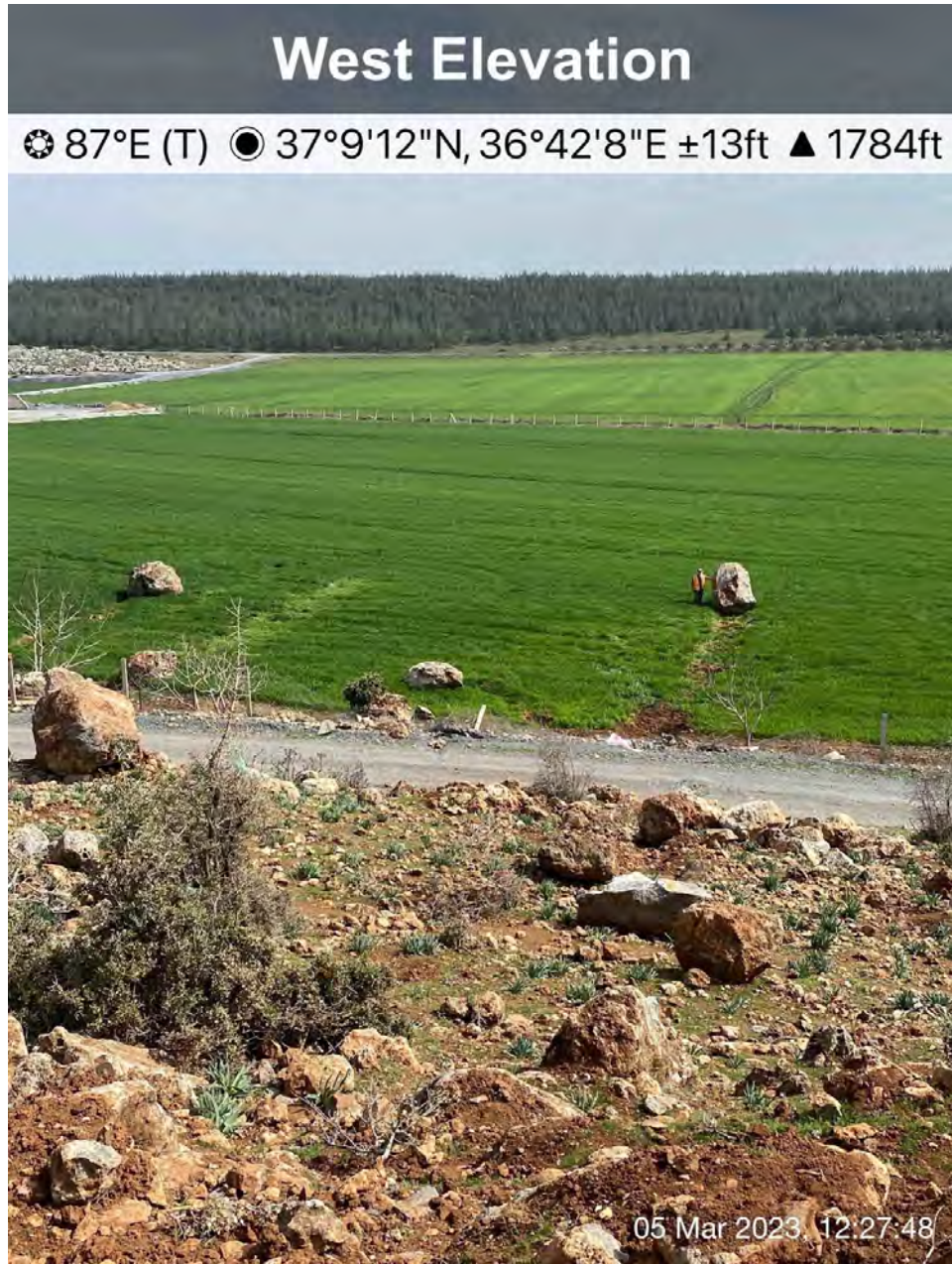


**Figure 9.5.** Rockfall runout south of the town of Gökçedere near the East Anatolian fault.

Rock fall has been reported throughout the main body of the report in conjunction with other observations. Rock fall was also observed or reported in the following locations:

- Around Kartalkaya Dam (37.46874 N, 37.239213 E)
- In the hills west of Gölbaşı (37.818237 N, 37.633028 E)
- In the EAF fault region West of Pazarcık (37.540783 N, 37.347587 E)
- In the fault adjacent region of Çelikhan (37.990623 N, 38.196125 E).
- Along the Malatya-Maraş highway downslope of the Erkenek tunnels (37.863212 N, 37.76272 E)

## 10.0 Impacts in Syria

*Youssef M.A. Hashash, Robb Eric S. Moss*

Surface fault rupture approached the border region between Syria and Türkiye, and extensive yet generally poorly documented damage occurred on the Syrian side. The shaking was felt all the way south to Lebanon including the city of Tripoli and the capital Beirut. Damage in Lebanon was sparse with some reported cracks in buildings in the north of the country. As indicated in Chapter 3, ground motion records Lebanon and Syria are not available at the time this report was prepared.

The GEER team had to rely on general news reports and personal connections via colleagues in Lebanon to collect damage reports. The situation in Syria was complicated by the security situation on the ground and hence no team members could be deployed due to safety concerns. An NGO report ([منسقو استجابة سوريا - Home | Facebook](#)) reported the statistics for northwestern Syria shown in Figure 10.1 with a focus on the humanitarian dimensions but also included damage statistics, which are translated below:

---

*“General population movement and the movement of displaced persons and arrivals: The number of registered affected families is 211,763 families, with a number of 1,164,805 individuals. The number of displaced persons affected by the earthquake reached 41,783 families, with a number of 229,747 individuals. The number of arrivals from Türkiye: 53,883 people.*

*General damage to buildings and facilities:*

*Various houses and residences: The immediate number of buildings destroyed during the earthquake: 1,812. The number of buildings that are not safe to return and cannot be supported: 3,817 buildings (severe damage, buildings urgently required to be demolished)*

*The number of buildings that need to be strengthened to make it safe to return is 11,733 buildings (moderate damage). The number of safe buildings that need maintenance is 17,927 buildings (light damage). The number of collapsed buildings that have been demolished after the earthquake is 112 buildings so far. Camps consisting of residential units have reported cases of cracks in 97 housing units, ranging between light and medium.*

*Facilities and service infrastructure sector: The service buildings and facilities previously designed according to certain standards have withstood more than the residential buildings, but the life of some of them has expired, particularly the facilities of the educational sector.*

- *Damages within educational facilities: 413 schools of various categories (partial damage, partial destruction, and moderate damage).*
- *Damages within the health sector facilities: it was recorded within 64 facilities.*
- *Damage within the camps: 97 housing units mentioned above.*
- *Damages within places of worship: 47.*
- *Damages within the high water tanks: 7.*
- *Damages within other facilities: 62.*

*General humanitarian needs: (The status of humanitarian needs remains in a state of periodic and continuous updating): Health sector: providing urgent support with medical consumables and general supplies to more than 18 hospitals and medical points (support is related to the location of the health facility, population density and cases received)*

*Shelter sector: initial provision of camp equipment (tents or permanent or temporary housing units) to 23,217 families as a first stage, pending the completion of a study of the reality of buildings in the area, which will allow a number of families to return to their homes. We previously estimated the urgent need for 20,000 tents to absorb a wave current displacement.*

- *Non-food items sector: providing shelter materials to 27,733 families as a first stage.*
- *Heating materials and consumables: It is necessary to provide heating materials and clothes to all registered and affected displaced persons within the areas of displacement.*
- *Foodstuffs: providing “dry” food baskets to more than 30,732 families, in addition to securing ready-to-eat emergency kits urgently for more than 60,000 families to ensure food stability, especially since the region witnessed an increase in the number of people suffering from food insecurity to 3.3 million.*
- *Water and sanitation: Providing clean and sterile water at a rate of 5 liters per day for an adult at a minimum, especially with the approaching end of the current winter season and the start of a gradual rise in temperature during the coming weeks, in addition to daily removal of waste at a rate of twice a day in shelter centers, residential gatherings, and camps that house the newly displaced.”*

*Additionally we have the following selected site specific damage reports:  
Embankment Failure: more to follow.”*

---

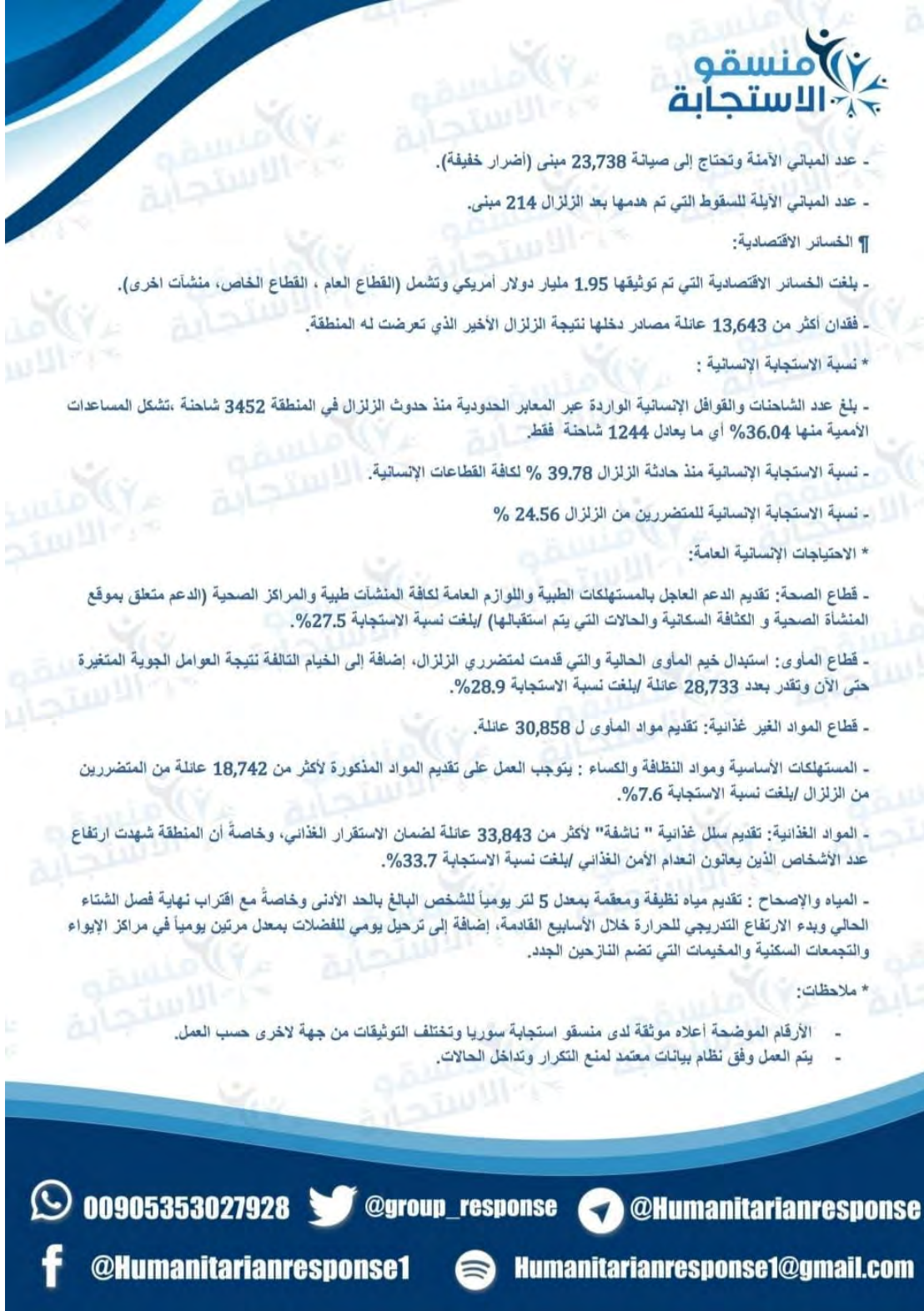


Figure 10.1. NGO report on the earthquake damage statistics in Syria.

## 11.0 Future Studies and Opportunities

### **Surface Fault Rupture:**

Surface fault rupture on the order of hundreds of kilometers was observed both in the free-field and through engineered infrastructure such as roads, buildings, earth dams, lifelines, and other systems. This provides an excellent source of data for augmenting existing surface fault rupture predictive models. These observations of performance also provide useful information to carefully evaluate which fared well, which did not, to then improve vulnerability and fragility models for assessment of the performance of engineered systems when subjected to surface fault rupture;

These earthquakes and their related aftershocks, especially those in the south west portion of the affected region, provide a reminder of the rupture potential along the Dead Sea fault and its branches. Studies of the potential increase of rupture risk further south due to this earthquake sequence would be important to better characterize seismic hazard impacting Syria, Lebanon, Israel, Palestinian Territories and Jordan.

### **Ground Motions:**

The most immediate task related to the ground motion data is to perform processing that preserves fling step for the records where these effects were observed. The procedures by which fling step is preserved are somewhat subjective and we anticipate engaging multiple investigators to examine user-to-user uncertainties. Once the fling step data is available, it can be compared to predictive models for fling. Additional data development efforts will include supplementing the data set with recordings from additional aftershocks and improvement of metadata as site investigations are performed and more refined finite fault models are developed.

The data sets from these earthquakes will surely be used in future ground motion model development efforts and as validation data for ground motion simulations, among other applications.

Ground motions recorded in Antakya and the associated diverse performance of structures in various parts of the city highlight the importance of site effects and the limitations of characterizing them through simplified parameters such as  $V_{s30}$ . This valley provides an excellent opportunity for conducting detailed studies of basin effects such as those that have been conducted at the EUROSITE-TEST in the Volvi basin in Greece.

Ground motion estimates at the facilities considered in these investigations would be improved by investigations of local site characteristics. The global research community may consider collaborating with local professionals to perform such investigations and develop improved local geologic maps.

### **Building Practices:**

The highway infrastructure performed very well overall in these events, whereas the residential and commercial building stock did not. Assessing the reasons that led to this large discrepancy in performance will be a difficult but productive endeavor. What engineering practices led to such well built highways, bridges, viaducts, tunnels, overpasses, and other roadway infrastructure? Was there federal or international design and construction oversight that resulted in such improved highway performance? What was missing in oversight, design, and construction that resulted in so many collapsed buildings? What is the interaction between hazard insurance, design/construction, and code-enforcement that led to such massive life loss and how can those be modified to mitigate seismic risks in future seismic events

The building stock in the affected region has been built over several decades, during which the building code has evolved over time. Working in collaboration with local professionals and building officials, a building inventory should be created that includes information on structure type (number of stories, material) and date of construction. The excellent performance of seismically isolated hospitals has provided further evidence of significant benefits of this technology. Its use should be expanded to more conventional residential buildings.

Future studies could evaluate the most effective evaluation methods to identify hazardous buildings. The result of those investigations could be a great benefit to ongoing efforts in Türkiye to identify hazardous structures to then seismically retrofit those that are identified to pose a substantial risk to human lives. Reconstruction should carefully evaluate successful programs in other seismic regions. While these earthquakes provide an invaluable set of ground motion records, very few structures were seismically instrumented. Such records would have provided equally invaluable information of the seismic performance of structures undergoing significant inelastic deformations.

### **Hospitals:**

Future research should expand the data collection effort to additional hospitals beyond those reported here. Future data collection should obtain detailed performance information about recently constructed hospitals that were evacuated, which the team was unable to access. It is also important to obtain clear information on post-earthquake safety evaluation procedures



used for hospitals, including government, university, and private hospitals. More information should be obtained about damage to MEP distribution systems, including water leaks.

We hope that in the future strong motion recordings from seismically isolated hospitals will be made available along with reliable estimates of movement across the plane of isolation as well as in the superstructure. Future data releases should also publish structural framing plans for hospitals to enable detailed analysis and study of the effects of ground shaking on buildings from different eras of the building code.

These research efforts would enable more specific criteria to be developed to target levels of inconvenience and damage that can be tolerated for different hospital functions and to achieve department-specific functional recovery criteria.

**Lifelines:**

This earthquake produced a wide range and large number of seismic interactions. Future research should explore seismic interactions between adjacent structures and between equipment and structures. Examples include impact loads on mechanical and electrical equipment from fallen infills and impacts on lifelines from rockfalls.

Some facilities (e.g., Afşin Plants A and B) were still recovering from the earthquakes at the time of the reconnaissance. A future reconnaissance investigation could re-visit these and other sites (e.g., damaged water treatment plants) after they have completed their testing and restarting efforts to gain additional insights on their asset performance and recovery activities.

Some lifelines systems were not investigated during the EERI reconnaissance, including natural gas transmission and distribution systems, wind, solar, and telecommunications. Documentation of the performance of these systems would be useful.

The progression of damage from the mainshock through various aftershocks requires further study. For example, the MKU University facilities were closed only after the **M6.3** aftershock inflicted additional damage to the structures. The Afşin plants reported most of the damage resulted from the second shock. Some structures may have performed up to the code during the mainshock but then experienced progressive damage from aftershocks, which by code standards might be considered a successful performance.

Damage to buried utilities, especially water and wastewater pipelines, was extensive in several regions. Repairs were ongoing in late March at the time of the EERI team visits, and the state of the wastewater systems in several cities was largely unknown. Continued documentation of

incurred damages, correlation with levels of transient and permanent ground deformations, and return-to-service metrics is strongly suggested.

**Liquefaction & Lateral Spreading:**

There were many many observations of liquefaction and lateral spreading at multiple locations throughout the affected region that require follow-up subsurface investigations to be useful for case histories and predictive modeling. SPT, CPT, VS and other subsurface measurements are required to learn the most from these ground failures. This will require external funding as in-country funding is generally not available for these investigations. Foundation performance related to soil plasticity can be augmented with the observations made in these events. Work that would complement the seminal research from the 1999 Adapazari earthquake.

**Ports & Harbors:**

The performance of port and harbor structures were observed. Follow-up work on characterizing the subsurface conditions would be useful in developing these observations into case histories. This will also require external funding as in-country funding is generally not available for these investigations along with agreements with the port authorities as they are privately held.

**Landslides and Rock Falls:**

The major landslide at Tepehan village would comprise an excellent case study for simplified (Newmark-type) and advanced methods for validation purposes.

Landsliding and rock fall was not as prevalent in areas where reconnaissance was performed as initially anticipated by predictive models

(e.g., <https://earthquake.usgs.gov/earthquakes/eventpage/us6000jllz/ground-failure/summary>).

Correlating rock fall with ground shaking parameters may provide some interesting results. Future research should consider the potential for additional landsliding in remote areas from remote sensing methods (e.g., using JPL/NASA resources).

## References

- ACI 318-19: Building Code Requirements for Structural Concrete and Commentary. American Concrete Institute, Farmington Hills, MI
- Address Based Population Registration System (2022). Available at <https://data.tuik.gov.tr/Bulten/Index?p=The-Results-of-Address-Based-Population-Registration-System-2022-49685&dil=2> (accessed April 24, 2023).
- AFAD (2023). PRESS BULLETIN-36 about the Earthquake in Kahramanmaraş. <https://en.afad.gov.tr/press-bulletin-36-about-the-earthquake-in-kahramanmaras> (accessed May 6 2023).
- Aki, K. and P.G. Richards (1980). *Quantitative Seismology*, 2nd Edition, W.H. Freeman, San Francisco, CA.
- ASCE/SEI 7-16. 2016. Minimum Design Loads and Associated Criteria for Buildings and Other Structures. American Society of Civil Engineers (ASCE), Reston, VA
- ASCE/SEI 41-17. 2017. Seismic evaluation and retrofit of existing buildings. American Society of Civil Engineers (ASCE), Reston, VA
- Baker, J.W., and Y. Chen (2020) "Ground motion spatial correlation fitting methods and estimation uncertainty." *Earthquake Engineering and Structural Dynamics* 49: 1662 – 1681.
- Baltzopoulos, G., R. Baraschino, E. Chioccarelli, P. Cito, I. Iervolino (2023). Preliminary Engineering Report on Ground Motion Data of the Feb. 2023 Turkey Seismic Sequence, Consortium of Italian Universities, Feb 24 2023.
- Boore, D.M. (2010) Orientation-independent, nongeometric-mean measures of seismic intensity from two horizontal components of motion. *Bull. Seismol. Soc. Am.*, 100 (4), 1830 - 1835.
- Boore, D.M., J.P. Stewart, E. Seyhan, and G.M. Atkinson, G.M.. (2014) NGA-West2 equations for predicting PGA, PGV, and 5%-Damped PSA for Shallow Crustal Earthquakes. *Bull. Seismol. Soc. Am.*, 30 (3), 1057-1085.
- Bray, J.D. and J.P. Stewart (2000). Damage patterns and foundation performance in Adapazari. Ch 8 from Kocaeli, Turkey, Earthquake of August 17, 1999 Reconnaissance Report. Youd, T.L., Bardet, J.P., and Bray, J.D., ed., *Earthquake Spectra*, 16 (Supp A), 163-189.
- Bray, J.D., E.M. Rathje, A.J. Augello, and S.M. Merry (1998). Simplified seismic design procedure for geosynthetic-lined, solid-waste landfills, *Geosynthetics International*, 5, 203-235.
- Buckreis, T., B. Güryuva, A. İçen, O. Okcu, A. Altındal, M. Aydin, R. Pretell, A. Sandikkaya, O. Kale, A. Askan, S. Brandenburg, T. Kishida, S. Akkar, Y. Bozorgnia, J. Stewart. (2023) "Ground Motion Data

from the 2023 Türkiye-Syria Earthquake Sequence." DesignSafe-CI.  
<https://doi.org/10.17603/ds2-t115-bk16>

- Cambaz, M.D., F. Turhan, M. Yilmazer, K. Kekovalı, K., Ö. Necmioğlu, D. Kalafat (2019). A Review on Kandilli Observatory and Earthquake Research Institute (KOERI) Seismic Network and Earthquake Catalog: 2008–2018, *Adv. Geosci.*, **51**, 15–23.
- Chiou, B. (2021) P4CF. GitHub repository, <https://github.com/bc88bc/P4CF>.
- Chiozzi, A., & Miranda, E. (2017). Fragility functions for masonry infill walls with in-plane loading. *Earthquake Engineering & Structural Dynamics*, **46**(15), 2831-2850.
- Contreras, V., J.P. Stewart, T. Kishida, R.B. Darragh, B.S.J. Chiou, S. Mazzoni, R.R. Youngs, N.M. Kuehn, S.K. Ahdi, K. Wooddell, R. Boroschek, F. Rojas, and J. Ordenes (2022). NGA-Sub source and path database. *Earthq. Spectra*, **38** (2), 799–840.
- Dakkak, R., M. Mreish, M. Daoud, G. Hade (2005). The Syrian National Seismological Network (SNSN): Monitoring A Major Continental Transform Fault. *Seismol. Res. Letters*, **76** (4), 437–445.
- Ekström, G., M. Nettles, and A.M. Dziewonski (2012) The global CMT project 2004-2010: Centroid moment tensors for 13,017 earthquakes, *Phys. Earth Planet. Inter.*, 200-201, 1-9.
- Emre, Ö., T.Y. Duman, S. Özalp, H. Elmacı, H., Ş. Olgun, F. Şaroğlu (2013). Açıklamalı Türkiye Diri Fay Haritası Ölçek 1/1.125.000: Maden Tetkik ve Arama Genel Müdürlüğü Özel Yayın Serisi 30. ISBN: 978-605- 5310-56-1.
- Erdik M. Report on 1999 Kocaeli and Düzce (Turkey) earthquakes (2001) Structural Control for Civil and Infrastructure Engineering: 149-86.
- Erdik M. et al. (2018) Seismic isolation code developments and significant applications in Turkey. *Soil Dynamics and Earthquake Engineering* **115**: 413-437
- Garini E. and G. Gazetas (2023). The Turkey-Syria Mw 7.8 Earthquake of February 6 2023, Recorded Accelerograms and their Response Spectra, National Technical University, Athens.
- Goulet C.A., T. Kishida, T.D. Ancheta, C.H. Cramer, R.B. Darragh, W.J. Silva, Y.M.A. Hashash, J. Harmon, G.A. Parker, J.P. Stewart, and R.R. Youngs (2021) PEER NGA-East database, *Earthq. Spectra*, **37** (1), 1331-1353.
- Gülerce, Z., A. Askan, Ö. Kale, A. Sandıkkaya, N. S. Işı, O. İlhan, G. Can, M. İlgaç, A.A. Ozacar, E. Sopacı, K.Ö. Çetin, B. Akbaş, A. Altındal, B. Guryuva, O. Kanun, K. Albayrak, G. Muratoglu, O. S. Okcu, A. Icen, M.F. Aydın (2023). Chapter 4: Preliminary Analysis of Strong Ground Motion Characteristics, February 6, 2023 Kahramanmaraş-Pazarcik (Mw=7.7) and Elbistan (Mw=7.5) Earthquakes, Report by Middle Eastern Technical University.

- Güvercin, S.E., H. Karabulut, A. Ö. Konca, U. Doğan, S. Ergintav (2022). Active seismotectonics of the East Anatolian Fault, *Geophysical Journal International*, 230 (1), 50–69.
- Jayaram, N., and J.W. Baker (2008) Correlation model for spatially distributed ground-motion intensities. *Earthquake Engineering and Structural Dynamics* 38: 1687 – 1708.
- Kaiser Family Foundation - Hospital Beds per 1,000 Population by Ownership Type (2021). Available at <https://www.kff.org/other/state-indicator/beds-by-ownership/> (accessed April 24, 2023).
- Kale, Ö., S. Akkar, A. Ansari, and H. Hamzehloo (2015) A ground-motion predictive model for Iran and Turkey for horizontal PGA, PGV, and 5% damped response spectrum: Investigation of possible regional effects. *Bull. Seismol. Soc. Am.*, 105 (2A), 963 - 980.
- Kale Ö, M.A. Sandikkaya, B. Akbaş, K. Albayrak, A. Altındal, A. Askan, M.F. Aydın, G. Can, K.Ö. Çetin, Z. Gülerce, B. Güryuva, M. İlgaç, N.S. Işık, A. İçen, O. İlhan, O. Kanun, G. Muratoğlu, O.S. Okçu, A.A. Özacar, E. Sopacı (2023). Analysis for Strong Ground Motion Characteristics from the 6 February 2023 Kahramanmaraş-Türkiye Earthquakes: Pazarcık Mw 7.8 and Elbistan Mw 7.7, *Bulletin of Earthquake Engineering* (in review).
- Kavuzlu, M. (2006) Tectono-Stratigraphical Investigations of Antakya and its Near Surrounding. MS Thesis. Department of Geological Engineering, Institute of Natural and Applied Sciences, University of Cukurova, Adana. <http://libratez.cu.edu.tr/tezler/5807.pdf>
- Leonard, M. (2014) Self-consistent earthquake fault-scaling relations: Update and extension to stable continental strike-slip faults. *Bull. Seismol. Soc. Am.*, 104 (6), 2953 - 2965.
- National Centre for Geophysical Research (2019). Provisional Seismological Bulletin from the National Seismic Network, Republic of Lebanon, National Council for Scientific Research.
- Pretell, R., S.J. Brandenberg, and J.P. Stewart. Global and regionalized spatial correlation models for ground motion intensity measures. *In progress*.
- Reitman, N.G., R.W. Briggs, W.D. Barnhart, J.A. Thompson Jobe, C.B. DuRoss, A.E. Hatem, R.D. Gold, J.D. Mejstrik, and S. Akçiz (2023) Preliminary fault rupture mapping of the 2023 M7.8 and M7.5 Türkiye Earthquakes. DOI: <https://doi.org/10.5066/P98517U2>
- Robinson, K., Cubrinovski, M., Kailey, P., Orense, R. (2010). "Field Measurements of Lateral Spreading following the 2010 Darfield Earthquake." Proc., Ninth Pacific Conference on Earthquake Engineering Building an Earthquake-Resilient Society, Auckland, New Zealand.
- Sadan, B. (2023). State of the Art in Application of Seismic Isolation and Energy Dissipation in Turkey. In: Cimellaro, G.P. (eds) *Seismic Isolation, Energy Dissipation and Active Vibration Control of Structures*. WCSI 2022. Lecture Notes in Civil Engineering, vol 309. Springer, Cham. [https://doi.org/10.1007/978-3-031-21187-4\\_2](https://doi.org/10.1007/978-3-031-21187-4_2)

- Shahi, S.K. and J.W. Baker (2014). An efficient algorithm to identify strong velocity pulses in multi-component ground motions. *Bull. Seismol. Soc. Am.*, 104(5), 2456–2466.
- TBEC. (2018). Turkish Seismic Earthquake Code (pp. 1-416). Retrieved from <https://www.resmigazete.gov.tr/eskiler/2018/03/20180318M1-2-1.pdf>
- Taghavi, S., and Miranda, E. (2003). Response assessment of nonstructural building elements, *PEER report 2003/05*. Pacific Earthquake Engineering Research Center, University of California, Berkeley, 1-96.
- Türkiye Earthquakes Recovery and Reconstruction Assessment. Available at <https://www.sbb.gov.tr/wp-content/uploads/2023/03/Turkiye-Recovery-and-Reconstruction-Assessment.pdf> (Accessed May 3, 2023)
- Wald, D.J. and T.I. Allen (2007). Topographic slope as a proxy for seismic site conditions and amplification. *Bull. Seismol. Soc. Am.*, 97 (5) 1379 - 1395.
- Yilmaz et al. (ongoing project), Production of GIS-based predicted-Vs30 maps at a scale of Turkey by using geological and topographical digital maps, Project ID; AFAD-UDAP-Ç-20-01, 2020-2023.
- Zhou, J. (2023) VS30 data of Turkey AFAD strong-motion network stations and VS30 map of Turkey and adjacent area related to the Feb. 2023 Turkey Earthquake Sequence. doi: 10.13140/RG.2.2.24389.12007.
- Zimmaro, P., G. Scasserra, J.P. Stewart, T. Kishida, G. Tropeano, M. Castiglia, and P. Pelekis (2018) Strong ground motion characteristics from 2016 central Italy earthquake sequence, *Earthq. Spectra*, 34, 1611-1637.